Characterization of Swirl-Driven Hybrid Rocket Engines

by

Timothy A. Marquardt

A dissertation submitted to the Graduate Faculty of
Auburn University
in partial fulfillment of the
requirements for the Degree of
Doctor of Philosophy

Auburn, Alabama
December 12, 2020

Keywords: hybrid rocket, regression rate, viscous correction, Beltramian, swirling flow, quadrupole vortex

Approved by

Joseph Majdalani, Chair, Professor and Francis Chair
Anwar Ahmed, Professor
Roy Hartfield, Walt & Virginia Woltosz Professor
David Scarborough, Assistant Professor

Abstract

Although hybrid rockets offer several potential benefits in terms of safety and performance, their use has mostly been limited to lab-scale motors and academic settings. Foremost among the factors contributing to this situation are the various drawbacks associated with the slow regression rates of the solid fuel that make hybrids less attractive for larger-scale launch vehicles. As a result, increasing the regression rate in hybrid rockets is probably the most active research area in the field of hybrid rocketry today. As new configurations and fuels are explored and tested, it is imperative that a physical understanding of the basic mechanisms behind these new designs is also properly developed. Thus, the creation or alteration of analytical models for regression rates in hybrid rockets is as important now as it ever has been and constitutes a critical but currently neglected component of the development cycle for novel hybrid concepts. After an introduction to hybrid rockets and their unique advantages in the first chapter, the next two chapters of this dissertation are devoted to literature reviews covering previous efforts to model regression rates in classical (axial-flow) hybrids as well as swirl-driven engines. A new, reduced-order model for predicting fuel regression in swirl-driven hybrids as a function of engine and injection geometry, propellant properties, and oxidizer mass flow is then presented and validated in the fourth chapter.

In addition to accurately modeling regression rates, understanding the internal flowfields of novel, swirl-driven engine concepts also produces valuable insight into their performance. In fact, modeling regression rates and understanding internal flowfields are typically co-requisite due to the nature of hybrid rocket combustion processes. Solutions for the internal velocity fields in two novel engines are described in the latter part of this work. The first is a detailed, axisymmetric solution, complete with viscous corrections, for incompressible flow within a bidirectional vortex engine such as the Vortex Injection Hybrid Rocket Engine developed by Orbital Technologies Corporation. This analysis identifies the parameters that define the velocity field and uncovers a new form of the vortex Reynolds number, which controls the

extent of the forced core region and wall boundary layers. The second solution describes, for the very first time, an untested concept dubbed the quadrupole vortex engine and is rudimentary by comparison. Nonetheless, the two-dimensional, potential-flow solution for the quadrupole vortex set permits an initial investigation into the hydrodynamic stability of such a configuration. With solutions for the velocity fields of these novel engines in hand, the regression rate model developed in the first half of the work is applied to both configurations in order to quantify their performance advantages.

Acknowledgments

As with any long-term endeavor, none of what I describe in this dissertation would have been possible if it were not for the combined support of my family, friends, teachers, and colleagues. It has truly been a blessing to benefit from the kindness of so many others throughout my life, and for that I thank first and foremost my Lord Jesus Christ.

To Mom and Dad: thank you for all of the love and opportunities you have given me. I couldn't ask for better parents, and I appreciate everything that you have done to help get me to this point. The love of learning that you instilled in me when I was little has carried me far, and you have been a steadfast source of guidance throughout my journey. My siblings have always encouraged me as well, and I am glad to have all of you in my family and on my side. In particular, I want to thank my sister, Elizabeth, for setting such a high standard of academic excellence for the rest of us. I spent many of my years in school trying to live up to your accomplishments, and that has helped propel me to where I am now. To my grandma Marie: thank you for loving and supporting me in all of my adventures. To Bob and Ditsie Scobie, who housed and fed me for a year so that I wouldn't have to give up on my goals: I will forever be grateful for your generosity. You were so much more than a place to stay, and I am striving to someday be the kind of example for someone else that you have been to me. To my in-laws, Pamela and Doug: thank you also for encouraging and enabling me to continue all the way to my doctorate.

To my advisor, Dr. Joe Majdalani: thank you for your loyal support throughout my time in graduate school. Your enthusiasm for research and mathematics is inspiring and your pursuit of excellence has often brought out the best in me. I am especially grateful for your work to secure high-quality research opportunities for me and for the funding that came with those projects, including the offer that brought me back to Auburn to work towards this degree. To the rest of my committee, Dr. Anwar Ahmed, Dr. Roy Hartfield, and Dr. David Scarborough: I owe you each a debt of gratitude for the material that I learned in your classes and for the discussions

that I have had with you regarding my research. Thank you for your willingness to review this document and the work that it represents. To Dr. Blake Melnick: you have been a pleasure to work with for the past two years. Thanks for making my job as a TA fun.

I owe a great deal to all of the other teachers at Auburn University and Cocoa Beach High School who helped get me to graduate school in the first place and, although I can't possibly mention them all here, I have always wanted to express my thanks to one in particular. To Mrs. Georgann Savage, who spent countless hours after school helping my classmates and me understand calculus: I am immensely grateful for your dedication and kindness. If you ever wondered about the impact you have on your students, I hope that a quick glance at Chapter 5 will convince you that the long hours have not been in vain.

To my fellow graduate students in the Advanced Propulsion Research Lab: it's been fun working with you all, and I wish you all the best as you work toward your own degrees and start your careers. My thanks in particular to Dr. Orie Cecil, Dr. Paul Kovacic, Langston Williams, Gaurav Sharma, and Dr. Lijun Xuan for all of the assistance you have offered over the years – and for being worthy table tennis opponents.

Although their contributions are duly cited throughout this work, a few researchers are also deserving of special recognition here. My sincere thanks to Dr. Marty Chiaverini and Dr. David Netzer for their previous efforts in compiling reviews of hybrid rocket regression rate modeling. Their works have contributed greatly to the field and made the preparation of this manuscript infinitely easier. Special thanks are also due to Dr. Arif Karabeyoglu, whose work I have frequently referenced and who provided valuable feedback on some of my ideas.

Additionally, I would like to acknowledge the people and organizations that kept me employed and enrolled while I worked toward my degree. My time as a graduate research assistant has been supported partly by the National Science Foundation, through Grant No. 1761675, partly by NASA/JPL, through RSA No. 1573777, partly by Jacobs Space Exploration Group, and partly by the Hugh and Loeda Francis Chair of Excellence, Department of Aerospace Engineering, Auburn University. I am particularly thankful to Dr. Ashley Karp and Dr. Beth Jens from the Jet Propulsion Laboratory for supporting elements of this work.

Finally, to my wife, Jenna: thank you so much for putting my graduate studies ahead of your own career aspirations. Your patience with my ever-slipping graduation date is deeply appreciated, along with everything else you have put up with over the years. You have been a steadfast source of encouragement through all of the frustrations that this research has brought me, and I am happy to share the triumph of completion with you now.

Table of Contents

Abstract ii

Acknowledgments iv

List of Abbreviations xvii

1 Introduction to Hybrid Rockets and Regression Rate Modeling 1

1.1 Advantages of Hybrid Rockets 1

1.2 Physical Processes in Hybrid Rockets 3

1.3 Advances in Hybrid Rocket Technology 4

1.4 Swirl Driven Hybrid Concepts 7

1.5 Outline of Dissertation 8

2 Review of Regression Rate Modeling in Traditional Hybrids 12

2.1 Background 12

2.2 Marxman's Diffusion-Limited Model 13

2.3 Radiation 22

2.4 Other Non-Ideal Considerations 25

2.5 Kinetics-Limited Models 25

2.6 Summary of Marxman's Theory 27

3 Review of Regression Rate Modeling in Swirling-Flow Hybrids 29

3.1 Orbital Technologies Corporation 30

3.2 Hybrid Rocket research Working Group 35

3.2.1 Early Experiments . . . 35
3.2.2 Yuasa and Coworkers . . . 38
3.2.3 Sakurai and Coworkers . . . 42
3.2.4 Ozawa and Shimada . . . 46
3.3 Wongyai and Greatrix . . . 51
3.4 Other Numerical and Experimental Studies . . . 56
3.4.1 Bellomo and Coworkers . . . 56
3.4.2 Paccagnella and Coworkers . . . 59
3.4.3 Franco and Coworkers . . . 64
3.5 Summary . . . 68

4 Diffusion-Limited Regression Rate Model for Swirling Flows . . . 70
4.1 Derivation . . . 70
4.2 Numerical Simulation Scheme . . . 75
4.2.1 Code Architecture . . . 75
4.2.2 Code Validation . . . 81
4.3 Model Validation . . . 82
4.3.1 Model Calibration . . . 84
4.3.2 Swirl Modifier Adjustments . . . 86
4.3.3 Evaluation of Swirling Model Using Space-Time-Averaged Data . . . 92
4.3.4 Evaluation of Swirling Model Using Locally-Resolved Data . . . 93
4.4 Summary . . . 98

5 Beltramian Solution for Cyclonically Driven Hybrids . . . 101
5.1 Problem Formulation . . . 103
5.1.1 Chamber Geometry . . . 103
5.1.2 Governing Equation . . . 104

5.1.3 Normalization . . . 105
5.1.4 Inviscid Solution . . . 105
5.2 Viscous Corrections . . . 106
5.2.1 Viscous Momentum Equations . . . 106
5.2.2 Tangential Corrections . . . 107
5.2.3 Axial Correction . . . 114
5.3 Boundary Layer Characterization . . . 117
5.3.1 Extent of Forced Vortex Region . . . 117
5.3.2 Boundary Layer Thickness . . . 118
5.4 Application of Regression Rate Model and Comparison to Experiments . . . 119
5.5 Summary . . . 125

6 Investigation of the Quadrupole Vortex Engine Concept . . . 127
6.1 Introduction . . . 127
6.2 Mean Flow Analysis . . . 129
6.2.1 Complex Potential Function . . . 129
6.2.2 Potential Flow Solution . . . 131
6.2.3 Piecewise Solution . . . 133
6.2.4 Equilibrium Points . . . 135
6.2.5 Pressure and Temperature Distributions . . . 136
6.3 Theoretical Simulation Results . . . 137
6.4 CFD Simulation Results . . . 141
6.5 Regression Rate Prediction . . . 143
6.6 Summary . . . 148

7 Summary and Conclusions . . . 150

Bibliography 155

A Derivation of Marxman's Blowing Correction 167

B Regression Rate Plots for Space-Time-Averaged Data 172

C Regression Rate Plots for Locally Resolved Data 177

List of Figures

1.1 Illustrative sketch of the diffusion combustion process in hybrid rockets. 3

1.2 Schematics of several swirl-driven combustors such as Orbitec's **a)** Vortex Injection Hybrid Rocket Engine (VIHRE) by Knuth et al. [36], **b)** Vortex Combustion Cold-Wall Chamber by Chiaverini et al. [40], **c)** Vortex Universal Stoichiometric Preburner (VUSP) for liquid rocket engines by Knuth et al. [41] and **d)** ISRU dual end-burning hybrid by Rice et al. [42]. 7

2.1 Comparison of blowing correction expressions derived by Lees [Eq. (2.17)] and Marxman [Eq. (2.15)] over a range of blowing parameter values and at several Reynolds numbers. Data is taken from Mickley and Davis [55] and Tewfick [56]. 20

2.2 Effect of thermal radiation on HTPB regression-rate behavior. Data is taken from Chiaverini et al. [62]. 24

3.1 Diagram of a typical inward-tangential swirl injector. This particular injector is sized to produce a geometric swirl number of 5. Reproduced from Fig. 3 a) of Yuasa et al. [3]. All units are in millimeters. 36

3.2 Plots and correlations characterizing the relation linking the average fuel regression rate, the oxidizer mass flux, and the geometric swirl number. Reproduced from Figs. 5-6 of Tamura et al. [29]. 37

3.3 Swirl number as a function of axial coordinate for a motor with inward-tangential injection and a calculated geometric swirl number of 9.17. Trends are shown for multiple flow conditions within the same geometry. Reproduced from Fig. 6 of Paccagnella et al. [30]. 60

3.4 Swirl number as a function of axial coordinate for a motor with inward-tangential injection and three different injector designs. Reproduced from Fig. 15 of Paccagnella et al. [30]. 63

3.5 Average regression rate plotted against the swirl-modified effective mass flux as represented by Eq. (3.15). Data from several simulation cases are shown alongside the regression law given by Eq. (3.48). Reproduced from Fig. 26 of Paccagnella et al. [30]. 64

3.6 Plots of negative axial velocity at the mid-section plane for a pair of simulated motors. The only difference between the two cases is the grain internal diameter, which is either **a)** 25mm or **b)** 50mm. Reproduced from Fig. 9 of Franco et al. [101]. 65

4.1 Graphical representation of the method of lines approach to the solution of the regression problem, with representative matrices shown after **a)** the first iteration and **b)** the second iteration of the procedure. Values in black represent known information at the start of each iteration. 76

4.2 Flowchart showing key steps in the main solver routine as well as its interactions with various subroutines and inputs. 77

4.3 Simplified representation of the core solver algorithm for the numerical simulation of a hybrid rocket burn. 78

4.4 Comparison of the prediction generated by the code described in this chapter with the data points at either end of the motor taken from Ref. [21]. 82

4.5 Comparison of the predictions generated by the code described in this chapter with the exact analytical solution for motors with $n = 0.5$ from Ref. [21] for a selection of burn times. 83

4.6 Regression rate prediction compared to "Tamura1999 Sg0" test data from four identical, axial-flow motors operating at different oxidizer mass flux conditions. This case is used to calibrate constants for the remainder of the data from [29] as well as data from [4] and [44]. Note that the swirling model is identical to Marxman's model when the swirl strength is zero. 87

4.7 Regression rate prediction compared to "Tamura1999 Sg7.1" test data with a geometric swirl number of 7.1. 88

4.8 Regression rate prediction compared to "Tamura1999 Sg9.7" test data with a geometric swirl number of 9.7. 88

4.9 Regression rate prediction compared to "Tamura1999 Sg19.4" test data with a geometric swirl number of 19.4. 89

4.10 Regression rate prediction compared to "Tamura1999 Sg32.3" test data with a geometric swirl number of 32.2. 89

4.11 Regression rate prediction compared to "Yuasa2012 L06" test data. 94

4.12 Regression rate prediction compared to "Sakurai2017 3-1" test data. Regions denoting the approximate extent of observed and hypothesized flow phenomena are denoted with dashed lines and roman numerals. 97

4.13 Regression rate prediction compared to "Tamura1999 L9.7A" test data. 97

4.14 Regression rate prediction compared to "Yuasa2001 L0" test data, as well as the regression model of Ozawa and Shimada [74]. 99

4.15 Regression rate prediction compared to "Yuasa2001 L9.7" test data, as well as the regression model of Ozawa and Shimada [74]. 99

4.16 Regression rate prediction compared to "Yuasa2001 L19.4" test data, as well as the regression model of Ozawa and Shimada [74]. 100

5.1 Notation and geometric sketch of a hybrid bidirectional vortex chamber. 103

5.2 Schematic of the boundary layer regions corresponding to inner, wall, and outer domains used in the matched-asymptotic expansion analysis. 109

5.3 Profiles of the tangential velocity at several values of κ and an injection Reynolds number of **a)** 10 and **b)** 100. In Part **c)** $u_\theta^{(c)}$ is shown at several values of $\mathrm{Re_w}$ and a fixed κ. Finally, Part **d)** compares $u_\theta^{(c)}$ to the previously published inviscid Beltramian solution as well as the complex-lamellar solution incorporating viscous corrections. 114

5.4 Variation of the axial velocity with the wall injection ratio for $\kappa = 0.01$ with **a)** $\mathrm{Re} = 10^3$ and **b)** $\mathrm{Re} = 10^4$. Here $\beta = \beta^*$ for both cases. 116

5.5 A comparison of the viscous Beltramian solution to the viscous complex-lamellar and inviscid Beltramian solutions using $\beta = \beta^*$. 117

5.6 Variation of the forced core thickness and maximum tangential velocity with $\mathrm{Re}\,\kappa^*$. 119

5.7 Locally-resolved regression rate prediction compared to "Knuth1998 Test2" test data. The prediction is manually adjusted to line up with this set of data so that the axial trends can be compared. 121

5.8 Locally-resolved regression rate prediction compared to "Knuth1998 Test2" test data for a rectified axial velocity profile. The prediction is manually adjusted to line up with this set of data so that the axial trends can be compared. 123

5.9 Locally-resolved regression rate prediction, computed using the complex-lamellar solution of Fleischmann and Majdalani [96], compared to "Knuth1998 Test2" test data for a rectified axial velocity profile. The prediction is manually adjusted to line up with this set of data so that the axial trends can be compared. 124

6.1 Four coaxial, counter-rotating vortices along the length of a right-cylindrical chamber. 127

6.2 Quad vortices with common downwash produced within **a)** a tall channel [135] and **b)** a shallow oval tray [137, 138]. In part **c)** , the mechanically analogous rotary drill used in surface digging is depicted. 128

6.3 Coordinate system used in a z-plane. 130

6.4 Potential flow solution for the quadrupole vortex engine. 137

6.5 Normalized velocity fields at stations located **a)** $2a$, **b)** $2.25a$, **c)** $2.5a$, and **d)** $2.75a$ downstream of the chamber headwall. 139

6.6 Streamlines of the flow corresponding to Fig. 6.5. 140

6.7 Normalized transverse velocity vectors for initial conditions representative of **a)** approximate quad symmetry and **b)** vortices induced by a pair of triangular vortex trippers. 140

6.8 Configuration used in the CFD simulation with **a)** surface rendering of the chamber and triangular vorticators and **b)** the unstructured polyhedral mesh used to capture the quadrupole vortex evolution. 141

6.9 Comparison between **a)** the CFD results at three different axial stations of 6, 8, and 10 radii from the headwall and **b)** the corresponding potential flow predictions at the same locations. The MATLAB predictions are initialized 4 radii from the headwall with $r_R = 0.18a$, $\Gamma = \pm 2\pi/5$, and $z_n = (\pm 0.32a, \pm 0.75a)$. 142

A.1 Sketch of the control volume for the momentum integral analysis. 169

B.1 Regression rate prediction compared to "Tamura1999 Sg0" test data. 173

B.2 Regression rate prediction compared to "Tamura1999 Sg7.1" test data. 173

B.3 Regression rate prediction compared to "Tamura1999 Sg9.7" test data. 174

B.4 Regression rate prediction compared to "Tamura1999 Sg19.4" test data. 174

B.5 Regression rate prediction compared to "Tamura1999 Sg32.3" test data. 175

B.6 Regression rate prediction compared to "Yuasa2001 Sg0" test data. 175

B.7 Regression rate prediction compared to "Yuasa2001 Sg9.7" test data. 176

B.8 Regression rate prediction compared to "Yuasa2001 Sg19.4" test data. 176

C.1 Regression rate prediction compared to "Sakurai2017 3-1" test data. 178

C.2 Regression rate prediction compared to "Sakurai2017 3-2" test data. 178

C.3 Regression rate prediction compared to "Sakurai2017 4-1,3" test data. 179

C.4 Regression rate prediction compared to "Sakurai2017 5-1" test data. 179

C.5 Regression rate prediction compared to "Sakurai2017 6-1" test data. 180

C.6 Regression rate prediction compared to "Tamura1999 L0A" test data. 180

C.7 Regression rate prediction compared to "Tamura1999 L0B" test data. 181

C.8 Regression rate prediction compared to "Tamura1999 L9.7A" test data. 181

C.9 Regression rate prediction compared to "Tamura1999 L9.7B" test data. 182

C.10 Regression rate prediction compared to “Yuasa2001 L0” test data. 182
C.11 Regression rate prediction compared to “Yuasa2001 L9.7” test data. 183
C.12 Regression rate prediction compared to “Yuasa2001 L19.4” test data. 183
C.13 Regression rate prediction compared to “Yuasa2012 L01” test data. 184
C.14 Regression rate prediction compared to “Yuasa2012 L02” test data. 184
C.15 Regression rate prediction compared to “Yuasa2012 L03” test data. 185
C.16 Regression rate prediction compared to “Yuasa2012 L04” test data. 185
C.17 Regression rate prediction compared to “Yuasa2012 L05” test data. 186
C.18 Regression rate prediction compared to “Yuasa2012 L06” test data. 186
C.19 Regression rate prediction compared to “Yuasa2012 L07” test data. 187
C.20 Regression rate prediction compared to “Yuasa2012 L08” test data. 187

List of Tables

4.1 Summary of axially-resolved SOFT motor data for model validation 84

4.2 Summary of space-time-averaged SOFT motor data for model validation 85

4.3 Zero-swirl calibration constants for Marxman's model for each dataset 86

4.4 Average error between Eq. (4.15), with $n_1 = 0.3$, and test data 86

4.5 Average relative error [%] between Eq. (4.19) and space-time-averaged test data for a variety of swirl modifier a_1 and n_1 pairs. All other constants remain unchanged from their values in Table 4.3 91

4.6 Average error between Eq. (4.19), with $a_1 = 3.75$ and $n_1 = 0.18$, and space-time-averaged test data. All other constants remain unchanged from their values in Table 4.3 92

4.7 Average error between Eq. (4.19), with $a_1 = 3.75$ and $n_1 = 0.18$, and locally resolved test data. All other constants remain unchanged from their values in Table 4.3 93

5.1 Motor information for experimental tests from Knuth et al. [25] 120

5.2 Average regression rate improvement for the bidirectional vortex engine configuration as compared to equivalent axial-injection motors. VIHRE test data and predictions from Knuth et al. [25] are compared to the results of numerical simulations based on the new swirl model presented in Chapter 4 . . 123

List of Abbreviations

a	coefficient in regression rate model; chamber radius (Chapters 5-6)
A_i	total injector or inlet area
A_s	surface area
$\bar{B}$	tangential angular momentum
B	blowing parameter
b	chamber exit radius
c^*	characteristic velocity
C_f	skin friction coefficient
c_p	specific heat at constant pressure
D	port diameter
D_h	hydraulic diameter
f	Darcy-Weisback friction factor
$F(z)$	complex potential function with a circular boundary (Chapter 6)
$f(z)$	complex potential function with no boundary (Chapter 6)
G	mass flux

$\bar{H}$ total pressure head per unit mass

h enthalpy; convective heat transfer coefficient (Chapter 3)

H_f heat of reaction

h_v heat of gassification

J_n nth order Bessel function of the first kind

K species concentration

k thermal conductivity; vortex strength (Chapter 6)

Le Lewis number

L chamber length

l aspect ratio, L/a

$\dot{m}$ mass flow rate

$\dot{m}''$ mass flux

MW molecular weight

M momentum

m exponent on axial distance in regression rate model

Nu Nusselt number

n exponent on mass flux in regression rate model

n_{inj} number of injector slits

Pr Prandtl number

P pressure

$\dot{Q}$ heat flux

$\dot{r}$ regression rate of solid fuel

Re Reynolds number

r radial coordinate

r_R vortex core radius

R_s specific gas constant

R_x radius of port at injector exit

R_{inj} radius of injector slit

Sg geometric swirl number

St Stanton number

S swirl number

T temperature

t stretched radial coordinate, r/λ or $(1-r)/\lambda$

t_b burn time

U tangential injection velocity

u axial velocity component (Chapters 1-4, Appendix A)

u_r, u_θ, u_z normalized velocities in cylindrical coordinates, $(\bar{u}_r, \bar{u}_\theta, \bar{u}_z)/U$ (Chapter 5); local polar velocity components relative to the vortex centers (Chapter 6)

u_x, u_y cartesian velocity components in the x and y directions (Chapter 6)

v radial velocity component (Chapters 1-4, Appendix A)

X normalized tangential momentum, ru_θ (Chapter 5)

x axial distance from leading edge of grain (Chapters 1-4, Appendix A)

y radial distance inward from grain surface (Chapters 1-4, Appendix A)

z normalized axial coordinate, $\bar{z}/a$ (Chapter 5); complex position, $x + iy$ (Chapter 6)

z_n vortex center location

Greek

β open outlet fraction, b/a

β^* mantle location where $u_z = 0$

Γ vortex circulation

δ boundary layer thickness

δ_c forced core thickness

ε turbulent eddy diffusivity; emissivity (Chapter 1); small perturbation parameter, U_w/U (Chapter 5)

ε_R surface roughness

ζ constant, $\lambda_1 c J_2(\lambda_1) - \sqrt{\mathrm{Re}/\kappa^*}\varepsilon$

η nondimensional radial distance in boundary layer

θ tangential coordinate; momentum thickness of boundary layer (Appendix A)

κ tangential inflow parameter, $(2\pi\sigma l)^{-1}$

κ^* modified tangential inflow parameter, $\kappa + \varepsilon$

Λ nondimensional vortex position, $a^2/(x_1^2 + y_1^2)$

λ_1 first positive root of $\kappa^* J_1(\lambda_1) = \varepsilon\beta J_1(\beta\lambda_1)$

μ dynamic viscosity

ν kinematic viscosity

ξ constant, $-\lambda_1 c J_0(\lambda_1)$

ρ density

σ swirl number for the bidirectional vortex engine, a^2/A_i; Stefan-Boltzmann constant (Chapter 1)

τ shear stress

ϕ nondimensional axial velocity in boundary layer

Φ velocity potential function

ψ streamfunction (Chapter 6); normalized streamfunction (Chapter 5)

ω angular velocity

Abbreviations and Acronyms

AMROC American Rocket Company

BHE Bragg-Hawthorne equation

BV bidirectional vortex

CFD computational fluid dynamics

GOX gaseous oxygen

HRrWG Hybrid Rocket research Working Group

HTPB hydroxyl-terminated polybutadiene

JAXA Japan Aerospace Exploration Agency

LOX liquid oxygen

O/F oxidizer to fuel

Orbitec Orbital Technologies Corporation

PMMA polymethyl methacrylate (acrylic)

PP polypropylene

QpV quadrupole vortex

RMS root-mean-squared

SOFT swirling-oxidizer-flow-type (unidirectional swirling flow)

UTC United Technology Center

VIHRE Vortex Injection Hybrid Rocket Engine

Subscripts and Superscripts

0 reference value

avg average value

b flame zone (burned gas) value

(c) denotes a composite approximation

c convective

e boundary layer edge (core flow) value

f solid fuel value

g reference value

(i) denotes an inner, viscous core approximation

inj value at injector

(o) denotes an outer, inviscid approximation

opt optimum value

ox oxidizer value

rad	radiative
sw	swirling value
T	total
t	value at nozzle throat
(w)	denotes a wall-region approximation
w	wall value
$\bar{}$	overbars denote dimensional quantities (Chapter 5); or complex conjugates (Chapter 6)
$'$	primes denote derivatives with respect to radial coordinate r
$*$	zero-transpiration (non-blowing) value
$\dot{}$	overdots denote derivatives with respect to stretched coordinate t

Chapter 1

Introduction to Hybrid Rockets and Regression Rate Modeling

1.1 Advantages of Hybrid Rockets

Hybrid rockets are defined by having their fuel and oxidizer stored separately and in different phases; a typical hybrid rocket consists of a liquid oxidizer that is injected into a cylindrical chamber whose walls are composed of a solid fuel. This design philosophy has numerous potential advantages over the traditional solid and liquid rocket concepts. Hybrid rockets are less complex and, therefore, less costly than liquid rockets, because they require half of the plumbing and turbo-machinery. They offer the flexibility of throttling and are capable of non-destructive aborts, which cannot be achieved by solid motors. Combustion in hybrid rockets is generally independent of the chamber pressure and not sensitive to cracks in the fuel grain as are solid rockets; the combustion process is in fact somewhat self-limiting in the event of a malfunction. Although a dangerous over-pressure event may occur in the thrust chamber of any chemical rocket, hybrid rockets are fundamentally nonexplosive. In fact, hybrids offer unique safety advantages during all phases of their life cycle, including fabrication, storage, and handling, since the propellants are generally inert and non-toxic while separated.

Hybrid engines typically possess specific impulse values (a measure of propulsive efficiency) between those of solids and liquids but can equal the performance offered by common liquid propellant combinations, such as LOX-RP1, when designed properly [1]. Common fuels include rubber-like compounds such as hydroxyl-terminated polybutadiene (HTPB) [2], everyday polymers such as acrylic and polypropylene [3, 4], and waxes [5–7], while the two most common oxidizers are oxygen (O_2, often referred to as GOX when in gaseous form or

LOX as a liquid) and nitrous oxide (N_2O) [1]. Solid fuels used in hybrid rocket applications will not boil off in storage or cause problems by freezing within feed lines in the cold environment of space. The resultant reduction in thermal insulation requirements makes them attractive for use on interplanetary or other long-term extra-terrestrial missions, where any inert mass (or the need to divert power to an electrical heater) reduces the payload and maneuvering capabilities of the vehicle. When combined with a high density specific impulse and an ability to perform multiple engine restarts, the suitability of hybrids for space applications becomes especially clear. Furthermore, medium-performance hybrids can be constructed cheaply and easily using storable oxidizers and a wide range of materials; this opens up the possibility of using recycled waste plastics as fuel and of efficiently producing optimally designed fuel grains through additive manufacturing. One lighthearted anecdote recounted by Altman [8] even involves an edible fuel grain:

> In a further demonstration of the wide range of acceptable fuels for the hybrid, AMROC [the American Rocket Company] recently hollowed out the center of an Italian salami, fitted it to the demonstrator unit and fired it. The combustion proceeded smoothly, was throttled over a range greater than 5/1, and provided the spectators with a pleasant aroma. After the firing, the spectators munched on slices of the "rocket fuel" which had acquired a delicious BBQ flavor.

Combined with their relative safety during operation, the accessible nature of hybrids has made them the rocket of choice for academic purposes, both as lab-scale research motors and to propel sounding rockets.

Clearly, hybrid rockets possess unique advantages and a great deal of potential for a variety of propulsion applications. Unfortunately, the physical separation of the fuel and oxidizer also results in a different and less vigorous combustion behavior when compared to the essentially premixed burning of solid and liquid motors. Details of the physical interactions involved in hybrid rocket combustion are the subject of the next section.

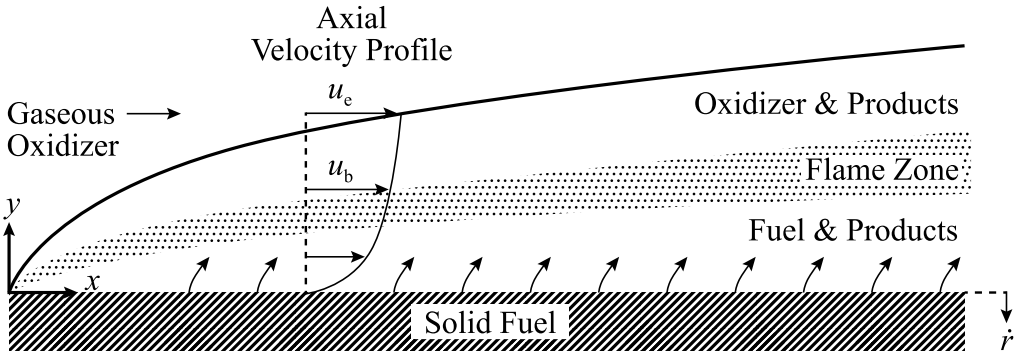

Figure 1.1. Illustrative sketch of the diffusion combustion process in hybrid rockets.

1.2 Physical Processes in Hybrid Rockets

Hybrid combustion involves the balance of many different aerodynamic, chemical, and thermal processes. An illustrative sketch of the diffusion flame in a hybrid rocket is provided in Fig. 1.1. When an oxidizer is injected uniformly into a combustion chamber, a turbulent boundary layer forms as the flow passes over the solid fuel grain. It should be noted that in nearly all real hybrids, oxidizer injection is not uniform and injector effects dominate at the head end. These effects tend to greatly increase the local burning rate and often demand special care be taken in preventing burn-through of the grain and casing near the injectors. When injection is not uniform, the boundary layer assumes its classical structure downstream of the flowfield generated by the injectors.

Heat from an ignition source reaches the wall and vaporizes a thin layer of fuel, which then enters the boundary layer flow. At some small distance from the wall the local mixture ratio due to diffusion between the oxidizer and fuel is conducive to combustion and a thin flame appears. This location is typically about 10-20% of the boundary layer thickness (δ) from the wall and may be around 0.1δ thick [9]. Interestingly, chemical combustion in the boundary layer of hybrids was observed in some early experiments to occur at fuel rich conditions [9–11], thus leading to flame temperatures that were considerably lower than the adiabatic flame temperature of the reacting propellants. This situation is not universal, and its report immediately generated significant debate which, while informative regarding the validity of diffusion-limited models, is

beyond the scope of this overview [12]. A fraction of the vaporized fuel flows axially below the flame zone; this fuel typically must be mixed with excess oxidizer in a post-combustion chamber in order to recover the full performance potential of a hybrid motor. Once the motor has been ignited, the combustion process is self-sustaining and somewhat self-regulating. Increasing the oxidizer flow increases the convective heat transfer to the wall because of the increased velocity, which in turn increases the vaporization rate of the fuel. The increased mass of fuel blowing inward from the wall has a blocking effect on further convective heat transfer outward from the flame, reducing the vaporization rate until an equilibrium is achieved. For this reason, and because increasing the oxidizer flow also pushes the motor further away from an ideal overall oxidizer-to-fuel ratio, throttling the oxidizer alone as a means of control in a hybrid motor is more complicated than throttling both propellants together as in a liquid rocket. Too much oxidizer too fast will blow the engine out as the mixture ratio shifts into a region that cannot support combustion or as residence times become insufficient for chemical reactions to complete. Not enough oxidizer will also extinguish combustion. Operating just above the lower flammability limit can "cook" the motor as low flame temperatures cause charring of the fuel instead of complete combustion; moreover, low heat transfer and regression rates allow heat to soak deeper into the fuel grain, thus altering its mechanical properties. Chemical kinetics can be quite important in either of these extremes, but combustion is generally accepted to be a diffusion-limited process at the moderate operating conditions that are typical of most hybrid motors.

1.3 Advances in Hybrid Rocket Technology

Advancements in propellant composition, injection technology, auxiliary equipment, chamber design, and fabrication processes over the past two decades have brought hybrid rocket propulsion further than ever before. No longer confined to the test stand or target drones, notable examples of newsworthy hybrids in just the past few years include the HTPB/N_2O hybrid motor used on the Ansari X-prize winner, SpaceShipOne, and its successor, Virgin Galactic's SpaceShipTwo [13], the Nucleus rocket flown by Norwegian company Nammo [14], and the planned use of another Nammo hybrid motor for the Bloodhound supersonic car project

based in the United Kingdom [15]. In years past, the propulsion industry refrained from seriously considering hybrid propellants as viable alternatives to liquids or solids because of four principal deficiencies: (i) low combustion efficiency, (ii) low regression rate, (iii) low volumetric loading, and (iv) combustion instability [16]. All four impediments are at least somewhat related to the slow diffusion flames that are sustained at the interface between the solid fuel and gaseous oxidizer. In fact, polymeric fuels associated with hybrids burn away approximately one order of magnitude more slowly than solids [17].

At this point in the exposition, a short note on terminology is in order. The speed at which the solid surface of the fuel grain recedes is commonly known as the *regression rate*. Because this rate represents the single most important parameter for characterizing the performance of a hybrid rocket, "regression rate" and "regression model" are phrases that will be repeated often throughout this dissertation. It should be noted that these terms refer to "regression" in the sense of "moving back" and have no connection to the statistical meaning of the word. Practically speaking, the regression rate is simply the time rate of change of the fuel surface position. Since hybrid rockets most often have cylindrical ports where the distance from the centerline to the fuel surface is measured by the radial coordinate r, the regression rate is designated by the symbol $\dot{r}$ in this work, although it is also referred to elsewhere as r (without the dot).

Even when hybrids have been seriously considered for use in prominent missions, they have often fallen short of the system performance offered by solids or liquids [18]. To compensate for the sluggish mass burning rate of the vaporizing fuel, bulky, multi-port, high-pressure casings have often been required. These heavy casings are designed to hold complex grain shapes comprising wide ports with wetted surface areas that are sufficiently large to produce the desired thrust level. In addition to their heavy cases, multi-port designs tend to necessitate that significant amounts of fuel remain as unburnt slivers at the termination of motor operation. In the absence of innovative design features, the manufacturing costs and mediocre system performance of large hybrids often makes them impractical for first stage use on launch vehicles. This is illustrated best by the demise of the American Rocket Company (AMROC), which sought to develop hybrid boosters for full-scale launch vehicles but went bankrupt before any of its large motors could be put into production. Despite these long-standing impediments, the

four-pronged problem affecting hybrids is gradually fading away. As shown by Casillas et al. [19], cost effectiveness of hybrids can be achieved through a three-to-four fold increase in fuel regression rate as compared to a typical motor at the time of their study. In the modern era of hybrid rocketry, two main advances have allowed the creation of motors that fulfill this criterion. The first is the development and use of fast-burning paraffin-based fuels, whose combustion process is described by Karabeyoglu and Cantwell [5, 20–22], and whose use has even led to the creation of motors with regression rates that needed to be intentionally reduced in order to better fit mission requirements [23, 24].

The second major advancement toward increasing hybrid regression rates has been the use of swirling oxidizer injection or other swirl-driven flowfields. The main reason for the growing interest in producing swirling flowfields in hybrid rocket engines is simple: when compared to traditional, axial-injection configurations, swirling flows have been shown to increase the regression rate and combustion efficiency while still offering a great deal of flexibility in propellant choice and motor design. Specifically, the introduction of swirl provides an additional degree of freedom for independent control of the O/F ratio and the total oxidizer mass flux [25], which can lead to a much wider range of practical throttling than would be available with a traditional hybrid [26] and improved performance compared to motors without this additional control method [27]. In a diffusion flame environment, species mixing is crucial and, according to Boardman and Sutton [28], the performance of a hybrid motor "depends critically on the degree of flow mixing attained in the combustion chamber" because heat from combustion products must be transferred to the solid fuel in order to sustain motor operation. Given the increased shear stress at the grain and the enhanced mixing levels within the main stream, the diffusion-limited combustion process, which is characteristic of hybrids, is substantially accelerated by the introduction of swirl [29, 30]. Furthermore, vortex-driven motors also exhibit elevated acoustic and hydrodynamic stability margins, which seem to accompany the introduction of coherent swirling structures [31–34].

1.4 Swirl Driven Hybrid Concepts

W. H. Knuth developed the first vortex hybrid rocket engine in the mid-nineties and performed the initial laboratory tests to establish the foundation of this technology, which was based on a cyclonic flow concept [35]. His experimental work, confirmed theoretically and computationally by Majdalani [36], led to the creation of the innovative Vortex Injection Hybrid Rocket Engine (VIHRE) in 1996. A key achievement of VIHRE was its ability to produce a seven-fold increase in regression rates versus a classic hybrid with the same propellant combination and oxidizer flow rate [25, 37–39]. Thus, the VIHRE project proved that vortex hybrid engines were likely to offer a feasible alternative to liquid propulsion systems.

The improved performance granted by VIHRE has been attributed to its unique internal flowfield that is dominated by a strongly swirling bidirectional motion (Fig. 1.2(a)). The moniker "bidirectional" refers to the fact that oxidizer, which is injected tangentially at the aft end of the engine, first proceeds along the fuel grain toward the headwall before reversing direction

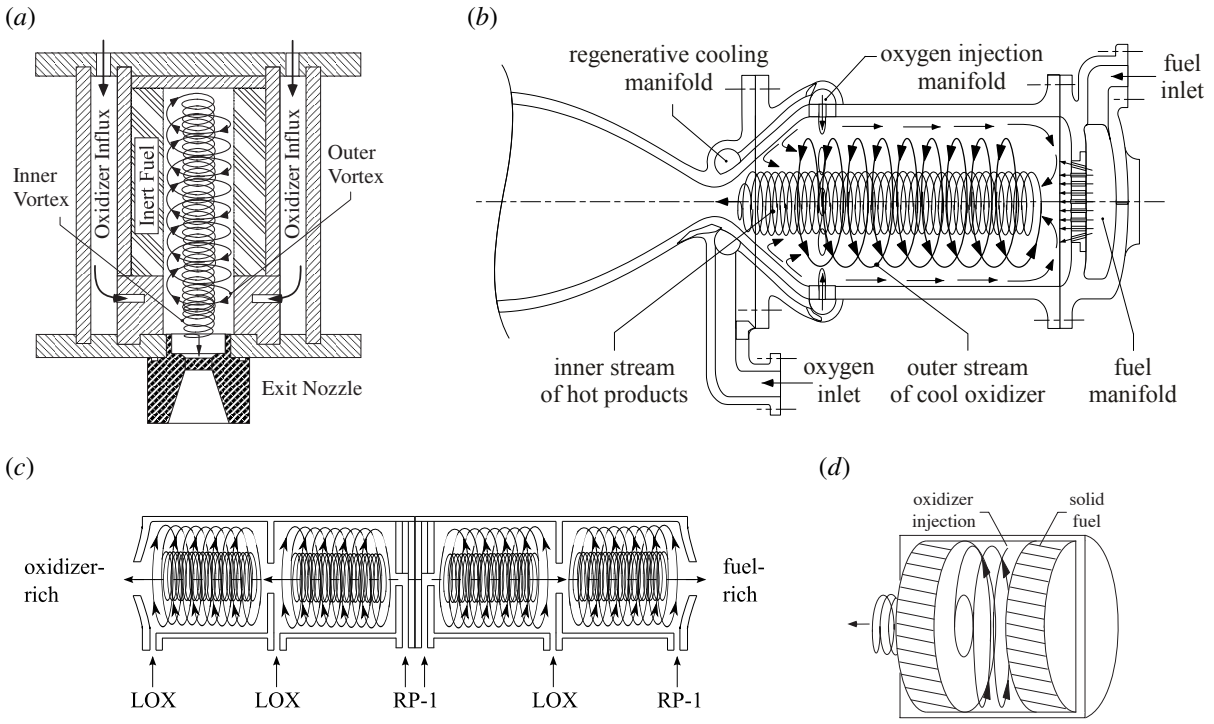

Figure 1.2. Schematics of several swirl-driven combustors such as Orbitec's a) Vortex Injection Hybrid Rocket Engine (VIHRE) by Knuth et al. [36], b) Vortex Combustion Cold-Wall Chamber by Chiaverini et al. [40], c) Vortex Universal Stoichiometric Preburner (VUSP) for liquid rocket engines by Knuth et al. [41] and d) ISRU dual end-burning hybrid by Rice et al. [42].

and exiting through a nozzle opening in the center of the chamber's base. The swirling motion is consistent in direction throughout the chamber, although its magnitude varies as the flow moves inward toward the centerline. The specifics of this flow configuration are the subject of Chapter 5. The vortex motion increases surface erosion while promoting mixing and residence time [25, 37–39]. The success of VIHRE also led to the development of the self-cooling Vortex Combustion Cold Wall Chamber (VCCWC) and the Vortex Universal Stoichiometric Preburner (VUSP) liquid rocket engines by Chiaverini et al. [40] and Knuth et al. [41] (Fig. 1.2(*b*)–1.2(*c*)). Another common hybrid motor configuration with swirling oxidizer injection at the head end of a simple cylindrical fuel grain has been studied extensively by the Hybrid Rocket research Working Group (HRrWG) in Japan [3, 4, 43–45] and will be discussed in greater detail in Chapter 3. Other swirl injection configurations employ spirally fluted tubes [46, 47] or helical ports built into a cylindrical grain [48]. A radial [49] or dual end-burning hybrid grain [42] that is driven by unidirectional vortex motion is also possible. For the dual end-burner, two cylindrically shaped fuel cartridges are placed a small distance apart on both ends of the chamber (Fig. 1.2(*d*)). Forward swirl injectors are then employed to produce a spiraling stream that sweeps across the exposed fuel surfaces before flashing out of the chamber. In this configuration, gas expulsion is achieved through a perforated orifice in the aft cartridge, while the circular surfaces burn and regress axially (Fig. 1.2(*d*)).

Clearly, there are a multitude of possible configurations that harness the power of swirl in order to improve engine performance. As these new configurations are explored and tested, it is imperative that a physical understanding of the basic mechanisms behind these new designs is also properly developed. Thus, the creation or alteration of analytical models for internal flowfields and regression rates in hybrid rockets is as important now as it ever has been and constitutes a critical but currently neglected component of the development cycle for novel hybrid concepts.

1.5 Outline of Dissertation

Now that hybrid rockets and their advantages have been introduced, the remainder of the dissertation will dive into a series of related investigations that seek to better characterize

the benefits of incorporating swirling flow into this type of propulsive technology. Since the regression rate of the fuel is of major consequence to the performance of hybrid rockets, and especially because the primary objective of introducing swirl is to increase the regression rate, the first half of the dissertation is devoted to the development of a model that is capable of predicting the regression rate in hybrid rockets with swirl injection. As a prerequisite to this effort, Chapter 2 consists of a thorough exposition on regression rate modeling in traditional hybrid rockets. This primer introduces the assumptions and concepts that underlie the existing diffusion-limited model, which in turn forms the basis for the new model that is introduced later in the work. All of the necessary derivations are retraced so that the treatment is self-contained. Chapter 3 continues to pave the way with a review of previous investigations into modeling regression rates in swirl-driven hybrid rockets. It focuses on analytical and semi-empirical models, although a few numerical and experimental studies that stand to inform future analytical models are covered as well. While the predictions of several research groups are presented and discussed, the review largely serves to identify the various phenomena that must be included in a regression rate model in order to ensure its effectiveness.

Informed by the efforts of previous researchers, a new model for the regression rate in swirl-driven hybrid rockets is derived and validated in Chapter 4. The new model takes the form of a modifier to the expression developed by Marxman and his colleagues so that it serves to generalize the existing theory to both swirling and non-swirling motors. In a nutshell, the new modifier posits that the regression rate may be predicted in a straightforward manner by modeling the ratio of the tangential (swirling) velocity to the axial velocity. While the dependence of propulsive performance on this ratio – known essentially as the swirl number – has long been recognized, only a few previous studies have accounted for its variation throughout the chamber. When other researchers have attempted to adjust the regression rate based on changes in axial position or port diameter, the resulting expressions have been tied to a particular engine configuration. Therefore, two novel contributions offered by the model presented in Chapter 4 are its ability to accurately reproduce the axial regression trends observed in experiments and its general applicability to different engine designs. After the model is presented, it is validated against experimental data that have been reported by other researchers and that have

been repeatedly used to validate or calibrate other models. Due to the coupled nature of fuel regression and mass flow rates within hybrid rockets, a numerical simulation scheme based on the method of lines algorithm is used to evaluate the regression formulation so that detailed predictions can be generated. Once the model is appropriately calibrated to a few sets of experimental data, it proves capable of predicting regression rates with high accuracy across all of the validation cases.

While the engines used for model validation in Chapter 4 are of a relatively simple design with unidirectional swirl, Chapter 5 examines the properties of another proven configuration, the bidirectional vortex. This design stands out on the basis of its unconventional flowfield, which was introduced in Sec. 1.4. Analytical solutions for flow patterns within various bidirectional vortex engine concepts exist, but the set of solutions is incomplete for the hybrid configuration. To rectify this situation, the majority of the chapter is devoted to deriving viscous corrections for an existing Beltramian solution for the velocity field in a hybrid bidirectional vortex engine such as VIHRE. Without these corrections, the analytical model predicts a pair of physical impossibilities: the velocity at the centerline becomes infinite, and the boundary layer is completely neglected so that flow slips along the wall with non-zero velocity. Adding frictional effects to the original inviscid solution not only removes these inconsistencies, but it also allows for the extent of the viscous regions and the maximum velocity within the chamber to be predicted. Once the velocity field solution is improved, it is then incorporated into the regression rate model from Chapter 4. Comparisons to data from VIHRE test firings show that the model is quite accurate for this engine type in an average sense.

Finally, Chapter 6 introduces another unconventional, swirl-enhanced hybrid rocket configuration known as the quadrupole vortex (QpV) engine. Since this design is almost entirely unstudied, the tone of the chapter is more properly described as an exploration of the concept than a quest for high accuracy. A potential flow solution for the velocity in a cross-sectional plane allows for an evaluation of the general flow characteristics and hydrodynamic stability of the arrangement. A basic CFD simulation confirms that the potential flow solution constitutes a reasonable representation of the in-plane velocity pattern, while the application of the new

regression rate model allows for quantitative predictions of the regression rate improvement afforded by a quadrupole vortex engine.

Chapter 2

Review of Regression Rate Modeling in Traditional Hybrids

2.1 Background

By the early 1960s, the advent of the space race had renewed industrial interest in hybrid rockets. Previous experimentation in 1947 by the Pacific Rocket Society had established that the chamber pressure of a hybrid rocket was not strongly influenced by the exposed fuel surface area and that hybrids were thus insensitive to cracks in the fuel grain [8]; this safety feature essentially nullified the risk of an explosion due to defects in the motor fabrication process and presented hybrids as an attractive alternative to the more universally-accepted solid propellant boosters. Unfortunately, there was much about the physical processes involved in the operation of hybrid rockets that was not yet understood, such as the details of the combustion process or the effects of scaling on motor performance. The search for answers both quantitative and qualitative to these fundamental questions was undertaken throughout the 1960s at the United Technology Center (UTC) in California where Marxman, Gilbert, Wooldridge, and Muzzy carried out several elegant experimental and theoretical investigations into the nature of hybrid motor burning. Although this group was by no means alone in its line of investigation, its members published a number of landmark papers that are routinely cited to this day and which helped to establish them at the forefront of the field. For a more thorough perspective on the efforts of this and other contemporaneous groups, the history by Altman [8], who led the hybrid research group at UTC, is highly recommended.

The effort to describe the internal ballistics of hybrid motors continues into the present day, especially as novel engine configurations that are not accurately described by the traditional

models become commonplace. Furthermore, the continuous growth in modern computing power and numerical techniques has allowed for computational investigations into hybrid rocket combustion in greater detail than ever before. The subject of classical diffusion-limited regression rate models is cursorily reviewed in the introduction of numerous articles on hybrid rockets, but these treatments are of course not intended or sufficient to elucidate the finer points of the models. Although other comprehensive reviews of the subject matter exist [50, 51], they are lengthier and have a generally broader focus. While their value remains unquestionable, they can require great effort on the part of the reader to gather all the details necessary for a complete re-construction of Marxman's model.

This chapter is particularly intended for readers who have not been acquainted with the history of analytical, boundary-layer-based regression rate modeling in hybrid rockets. It aims to complement the existing literature by providing the reader with a concise but sufficiently detailed review of classical diffusion-limited regression models for the purpose of establishing a firm foundation before regression rate modeling in the context of swirl-driven flows is discussed in subsequent sections.

2.2 Marxman's Diffusion-Limited Model

The first step in the review of classical regression rate models is a reconstruction of the model developed at UTC by Marxman and his colleagues. Their model describes the heat transfer within a hybrid motor and leans heavily on earlier work by Lees [52]; the latter performed a similar analysis in a chemically reactive environment with blowing. The model assumes that the flow is developing along the entire length of the grain (i.e. the boundary layers on either side of the motor have not yet merged at the centerline and a core flow of nearly pure oxidizer exists). Thus, the model does not accurately portray motors whose flow becomes fully developed in the port or is dominated by injector effects over a large segment of the head-end region. The foundational relationship of Marxman's model consists of an equivalence between the heat transferred from the gas to the wall and the energy absorbed in vaporizing the solid fuel:

$$\dot{Q}_\mathrm{w} = \dot{m}''_\mathrm{f} h_v = \rho_\mathrm{f} \dot{r} h_v \tag{2.1}$$

where $\dot{Q}_\mathrm{w}$, $\dot{m}''_\mathrm{f}$, h_v, ρ_f, and $\dot{r}$ represent the total heat flux at the wall, the fuel mass flux leaving the surface, the effective heat of gasification (which combines the heat of vaporization and melting, the heating of the solid fuel grain, and the heat of reaction associated with polymer degradation), the solid fuel density, and the grain regression rate, respectively. Note that the fuel is assumed to pyrolyze and vaporize, as is the case with most polymers, and that Marxman's model is not accurate for liquefying fuels such as paraffin wax. These fuels characteristically form a low-viscosity melt layer at the surface, from which droplets of liquid fuel are entrained into the flow before combusting outside the boundary layer. The grain regression rate is represented by $\dot{r}$ in keeping with most other authors despite some later simplifications that assume a planar configuration. Implicit in Eq. (2.1) is the assumption that there are no heat losses through the grain to the motor casing or outside environment. Experiments and theory have both shown that this is an accurate portrayal of normal operation for most hybrid motors, with the thermal wave penetrating only a short distance below the grain surface at moderate regression rates [10]. Although simple and fairly obvious, Eq. (2.1) represents one of a few fundamental concepts that are essential to the model.

In the original derivation by Marxman, a more specific expression for the heat transferred from the gas to the wall by convection is given by

$$\dot{Q}_\mathrm{c} = -\left(\frac{k}{c_p}\frac{\partial h}{\partial y}\right)_\mathrm{w} \tag{2.2}$$

where $\dot{Q}_\mathrm{c}$, k, c_p, h, and y represent the convective heat flux (including the effect of partial enthalpies transport by species diffusion), thermal conductivity of the gas, specific heat of the gas, enthalpy of the gas, and normal distance into the flow from the fuel surface, respectively. Here the subscript "w" refers to properties evaluated at the wall. The introduction of this expression is not necessary for the derivation, although its reproduction here provides an opportunity to comment on some underlying assumptions of the model. Firstly, Eq. (2.2) appears as a conductive expression although it is not explicitly labeled as such in Marxman and Gilbert's [9] original paper. Applying such a simple conductive heat transfer relation to combusting flow implies the assumption that $\mathrm{Le} = \mathrm{Pr} = 1$ and that the Reynolds analogy is valid

for turbulent flow. As for the radiative component of the total heat flux, it represents a smaller contribution than convection in most hybrids. Whether the effect of radiation is small enough to be safely neglected, as in Eq. (2.2), depends on the propellants and motor operating conditions: although the PMMA-O_2 systems studied by Marxman and his colleagues display very little radiation dependence, this is not true of some practical hybrid motors. The importance of radiation is discussed at greater length in Sec. 2.3.

In most historical derivations, the Stanton number is also introduced at this point to simplify the notation since it arises naturally in many problems involving heat transfer in fluids. It is a non-dimensional ratio of the heat transferred into a fluid to the thermal capacity of that fluid:

$$\mathrm{St} = \frac{\dot{Q}_\mathrm{c}}{\rho_\mathrm{b} u_\mathrm{b} \Delta h} \tag{2.3}$$

where for the problem at hand the difference in gas sensible enthalpy Δh is evaluated between the flame zone, denoted by a subscript "b" for "burned gas," and the gas at the wall. In the above, the axial velocity at the flame sheet is denoted by u_b. Writing the wall energy balance, Eq. (2.1), in terms of the Stanton number produces

$$\rho_\mathrm{f} \dot{r} = \frac{\dot{Q}_\mathrm{c}}{h_v} = \frac{\dot{Q}_\mathrm{w}}{h_v} = \mathrm{St}\, \rho_\mathrm{b} u_\mathrm{b} \frac{\Delta h}{h_v} \tag{2.4}$$

so that $\dot{Q}$ is eliminated from the expression in favor of a dimensionless parameter.

The primary challenge at this stage remains the question of how to determine the amount of convective heat transfer at the wall based on other known characteristics of the turbulent flow. The answer is to invoke the Reynolds analogy in order to establish an approximate relationship between the unknown heat flux and the better-understood shear stress within the boundary layer. In this process, the Prandtl and Lewis numbers between the wall and the flame zone are taken to be unity. Accordingly, the thermal and molecular diffusion mechanisms associated with the energy and momentum transfers within the boundary layer are assumed to be driven by similar turbulent mixing processes. It should be noted that since real hybrids often experience conditions that differ from the idealized assumptions made here, the Chilton-Colburn analogy

may replace the Reynolds analogy for cases where Pr ≠ 1 or in the presence of an axial pressure gradient. In fact, it may be shown that the difference in the final regression rate relation is rather small when these effects are taken into account (see Marxman [11]). In practical terms, the Reynolds analogy is written as an equivalence between the ratio of the heat flux to the radial gradient of total enthalpy h_T and the ratio of the shear stress τ to the radial gradient of the axial velocity:

$$-\frac{\dot{Q}}{\partial h_T/\partial y} = \frac{\tau}{\partial u/\partial y} \tag{2.5}$$

The expression may then be integrated from the wall to the flame zone since the object of invoking the analogy is to link values at these two points. Integrating yields

$$\frac{\dot{Q}_\mathrm{w}}{\Delta h_T} = \frac{\tau_\mathrm{w}}{u_\mathrm{b}} \tag{2.6}$$

If no combustion occurs in the low-speed region below the flame, $\Delta h_T = \Delta h$ and dividing Eq. (2.6) by $\rho_\mathrm{b} u_\mathrm{b}$ leads to an alternative expression for the Stanton number in terms of the wall shear stress τ_w or the skin friction coefficient C_f viz.

$$\mathrm{St} = \frac{\tau_\mathrm{w}}{\rho_\mathrm{b} u_\mathrm{b}^2} = \frac{1}{2} C_f \frac{\rho_\mathrm{e} u_\mathrm{e}^2}{\rho_\mathrm{b} u_\mathrm{b}^2} \tag{2.7}$$

Finally, substituting Eq. (2.7) into Eq. (2.4) gives

$$\rho_\mathrm{f} \dot{r} = \frac{1}{2} C_f \rho_\mathrm{e} u_\mathrm{e} \frac{u_\mathrm{e}}{u_\mathrm{b}} \frac{\Delta h}{h_v} \tag{2.8}$$

Note that $\dot{Q}$ is now replaced in the energy balance by C_f, which is more straightforward to estimate. Also note that it would have been possible to arrive at Eq. (2.8), without the introduction of the Stanton number or an explicit form of the heat flux, i.e., by combining Eq. (2.1) and Eq. (2.6) directly. This serves as a reminder that the solution is fundamentally based on framing the regression rate in terms of the energy absorption rate of the fuel and then approximating this rate by assuming that the transfer of energy and momentum are analogous in the region between the flame and the wall.

From this point onward, the derivation essentially concerns itself with how to describe the transfer of momentum (represented by the friction coefficient) in the context of a turbulent boundary layer with additional mass injection at the wall. Toward that end, the skin friction coefficient may be estimated using a suitable empirical relation. Marxman uses the well-known expression for turbulent flow over a flat plate with no blowing, as taken from Schlichting [53],

$$\frac{C_{f_0}}{2} = 0.03\mathrm{Re}_x^{-0.2} \tag{2.9}$$

Here the reference flat-plate value for the skin friction coefficient is given a zero subscript to distinguish it from the value applicable to the combusting flowfield. The local Reynolds number in this expression is defined in terms of the freestream properties at the boundary layer edge, denoted with a subscript "e," and the axial distance x from the grain leading edge:

$$\mathrm{Re}_x \equiv \frac{\rho_\mathrm{e} u_\mathrm{e} x}{\mu_\mathrm{e}} \tag{2.10}$$

Making use of this relationship involves two significant assumptions: first, that the presence of blowing does not change the nature of the flow so much that a standard value of the friction coefficient modified by a correction factor would be invalidated; and, second, that the result for a flat plate will adequately describe flow in a typical cylindrical center-perforated grain. The validity of the first assumption largely depends on the complexity or degrees of freedom offered by the correction factor applied. The flat-plate assumption is generally accepted for axially-injected hybrid motors — the grain curvature is not germane to the analysis in the absence of swirl, i.e., when the motion lacks a significant tangential component. In such configurations, the boundary layer length scales remain at least one order of magnitude smaller than those associated with the radius of curvature so that the combustion process may be safely modeled using a flat-plate assumption. The combined effect of both assumptions has been revisited in the context of swirl-driven motors by at least one researcher [54].

Substituting the skin friction coefficient expression given by Eq. (2.9) into the energy balance in Eq. (2.8) produces

$$\rho_{\mathrm{f}}\dot{r} = 0.03\rho_{\mathrm{e}}u_{\mathrm{e}}\frac{C_f}{C_{f_0}}\mathrm{Re}_x^{-0.2}\frac{u_{\mathrm{e}}}{u_{\mathrm{b}}}\frac{\Delta h}{h_v} \tag{2.11}$$

All that remains is to find a "blowing correction," $C_f/C_{f_0} = \mathrm{St}/\mathrm{St}_0$, that will account for the difference in heat flux between the combusting (blowing) and non-combusting cases.

For convenience, the blowing parameter B is first defined as

$$B \equiv \frac{u_{\mathrm{e}}}{u_{\mathrm{b}}}\frac{\Delta h}{h_v} \tag{2.12}$$

so that

$$\rho_{\mathrm{f}}\dot{r} = 0.03\rho_{\mathrm{e}}u_{\mathrm{e}}\frac{C_f}{C_{f_0}}\mathrm{Re}_x^{-0.2}B \tag{2.13}$$

The blowing parameter thus appears as a thermochemical parameter that depends on the flame location within the boundary layer and that can be specified for a particular propellant combination. That the heat of gasification and difference in enthalpies are determined by the propellants and mixture ratio is evident, but the dependence of the velocity ratio $u_{\mathrm{e}}/u_{\mathrm{b}}$, which is closely linked to the flame height, on these same parameters is less obvious. The dependence may be verified by integrating the oxidizer and fuel mass fluxes through a pair of control volumes separated by the flame zone and comparing the results to the integral momentum equation to obtain

$$\frac{u_{\mathrm{e}}}{u_{\mathrm{b}}} = \frac{K_{\mathrm{ox_e}} + \left(\mathrm{O/F} + K_{\mathrm{ox_e}}\right)(\Delta h/h_v)}{(\mathrm{O/F})(\Delta h/h_v)} \tag{2.14}$$

where $K_{\mathrm{ox_e}}$ is the oxidizer concentration in the free stream and O/F is the local oxidizer-to-fuel ratio at the flame. For further detail, the reader is referred to Marxman et al. [10]. For the equi-diffusive case, the blowing parameter also proves to be a similarity parameter of the boundary layer. In other words, when Le = Pr = 1 and B = const., the velocity, species concentration, and enthalpy profiles become similar everywhere [10, 50]. Because the diffusivities cannot always be assumed equal, some researchers maintain a distinction between the aerodynamic

blowing parameter, $B' = 2(\rho_w v_w)/(\rho_e u_e C_f)$, and the thermochemical blowing parameter as defined above.

In a follow-up paper, Marxman [11] derives the following expression for the blowing correction

$$\frac{C_f}{C_{f_0}} = \left[\frac{\ln(1+B)}{B}\right]^{0.8} \left[\frac{1 + \frac{13B}{10} + \frac{4B^2}{11}}{(1+B)(1+B/2)^2}\right]^{0.2} \tag{2.15}$$

which he simplifies by curve fit to

$$\frac{C_f}{C_{f_0}} = 1.2B^{-0.77} \tag{2.16}$$

Much academic debate has surrounded the proper representation of the blowing correction. In his original derivation, Marxman [11] acknowledges the form derived by Lees [52] using a thin-film theory approach,

$$\frac{C_f}{C_{f_0}} = \ln(1+B)/B \tag{2.17}$$

Marxman concludes that since mass addition is neglected in the derivation of Eq. (2.17), it can only be expected to produce reasonable results for low values of the blowing parameter B. Marxman [11] then derives the equations most often used in the context of hybrids, namely, Eq. (2.15) and Eq. (2.16), using the Prandtl mixing length hypothesis combined with a momentum integral analysis. Details of this derivation may be found in Appendix A. These expressions lead to better agreement with experiments at high mass injection rates. The improvement in accuracy when moving from Eq. (2.17) to Eq. (2.16) is displayed against experimental data from Mickley and Davis [55] and Tewfick [56] in Fig. 2.1.

Lengellé [57] revisits some of Marxman's assumptions regarding eddy diffusivity and develops his own blowing correction, but both derivations are shown to display inconsistencies with experimental results and an exact solution developed by Karabeyoglu [20] under similar conditions. Specifically, Marxman's expression for the skin friction does not reduce to the accepted value in the case of no blowing, but his analysis yields a blowing correction trend that stands in better agreement with experiments. Meanwhile, Lengellé's expressions fall closer to the analytical solution for skin friction but overestimate the blowing correction when compared to experiments. Based on this realization, Karabeyoglu derives a new expression that does

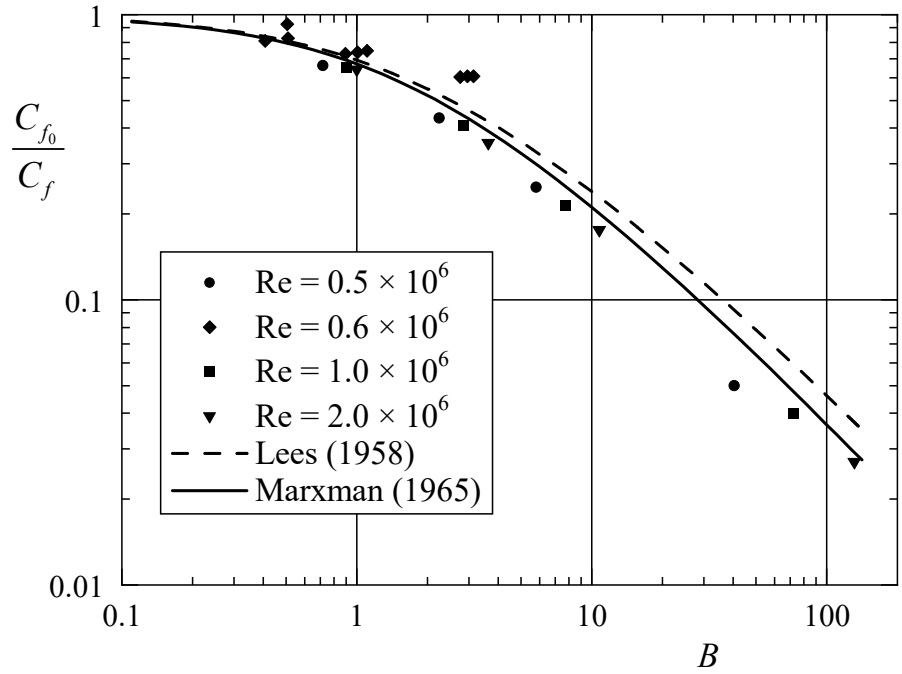

Figure 2.1. Comparison of blowing correction expressions derived by Lees [Eq. (2.17)] and Marxman [Eq. (2.15)] over a range of blowing parameter values and at several Reynolds numbers. Data is taken from Mickley and Davis [55] and Tewfick [56].

not rely on the same assumptions drawn from Prandtl's mixing length hypothesis. He arrives at an expression for the blowing correction that is nearly identical to that of Marxman [11], Eq. (2.15), albeit with a more self-consistent expression for the skin friction coefficient. In the end, Karabeyoglu also suggests the use of a simplified exponential expression and points out that Altman [1] has already shown that a simple power-law relation remains a more accurate representation than Eq. (2.16) over a practical range of interest. This relation is simply

$$\frac{C_f}{C_{f_0}} = B^{-0.68} \tag{2.18}$$

Nonetheless, by substituting Marxman's simplified blowing correction, Eq. (2.16), into the regression rate expression given by Eq. (2.13), one gets

$$\rho_f \dot{r} = 0.036 \rho_e u_e \mathrm{Re}_x^{-0.2} B^{0.23} \tag{2.19}$$

or, in terms of the mass flux $G \equiv \rho_e u_e$,

$$\rho_f \dot{r} = 0.036 G \left(\frac{Gx}{\mu_e} \right)^{-0.2} B^{0.23} \tag{2.20}$$

This is the classical form of the local regression rate derived by Marxman in the absence of radiation, although a more commonly seen result may be obtained by collecting the constant terms in Eq. (2.20) to produce the simplified result

$$\dot{r} = a G^{0.8} x^{-0.2} \tag{2.21}$$

where a is approximately constant for a given propellant. The space-time averaged equivalent is also often used by researchers reporting experimental data:

$$\dot{r} = a_2 G^n \tag{2.22}$$

Combining B with the other constants is justified by noting that, as long as $\Delta h / h_v$ does not change with Re_x, the distribution of the regression rate will be such that B remains spatially constant [10]. Even if this is not strictly true, B is expected to display very little variation. The small exponent of B further ensures that even large changes in Δh or h_v will produce negligible effects on the overall regression rate. One infers from this relationship that values of B calculated for one propellant can be expected to produce reasonable results for other propellants if they have similar compositions and radiation is unimportant. The relationship also suggests that any possible oxidative reactions at the fuel surface that alter $\Delta h / h_v$ from the idealized value would have a minor effect on the rate of fuel regression (see the reply to Dr. Rosner's comment at the end of [11] for context and elaboration on the importance of this implication).

Before leaving this subject, it may be helpful to reflect on several characteristics of hybrid rocket combustion that may be gleaned from Eq. (2.20). First and foremost, one notes the absence of any pressure dependence in the expression for $\dot{r}$. While this behavior remains contingent on discarding radiative effects, an assumption which will be later examined in more depth, it proves to be surprisingly accurate for many systems. Physically, the lack of a pressure dependence is

a result of the diffusion-flame burning behavior that is the defining characteristic of hybrids. Practically, one may argue that a mass-flux-controlled motor offers distinct advantages over a pressure-dependent solid motor. Designers are permitted more freedom in choosing a motor operating pressure that helps to achieve a desired target performance or meet certain safety requirements, which can be particularly useful in research and academic settings. Another feature captured in Eq. (2.20) is the axial variation in regression rate, which encompasses both a positive correlation with axial distance as fuel injection increases the local mass flux (i.e., the flux increases at locations further downstream as more fuel mass is added to the flow), and a negative correlation with axial distance, which is associated with boundary layer growth and the corresponding decrease in the skin friction coefficient and thus heat flux according to the Reynolds analogy. These competing factors result in an equilibrium location for the minimum regression rate that shifts downstream with the passage of time. This axial trend is not always born out in practice; researchers have noted that the exponent on x is very close to zero for some motors [21, 58] and that the effects of non-uniform or non-axial oxidizer injection commonly overshadow those due to boundary layer variation [4, 44, 59].

2.3 Radiation

Up to this point, several pressure-dependent phenomena that may have significant effects on the regression rate in a hybrid motor have been ignored. Foremost among these is radiative heat transfer, which can contribute significantly to the overall fuel regression depending on the motor operating conditions and fuel composition. Although some researchers find that the purely convective classical equations are the most accurate for hydrocarbon fuels [60], Marxman and Gilbert immediately recognize the potential importance of radiative heat transfer and include a crude treatment in their initial publication [9] by adding a grey-body radiation term to the regression rate expression just described. The relation is

$$\rho_\mathrm{f}\dot{r} = 0.036G\left(\frac{Gx}{\mu_\mathrm{e}}\right)^{-0.2} B^{0.23} + \frac{\sigma\varepsilon_\mathrm{w}\left(\varepsilon_\mathrm{g}T_\mathrm{b}^4 - T_\mathrm{w}^4\right)}{h_v} \tag{2.23}$$

where ε_g denotes the emissivity of the gas while ε_w refers to the emissivity of the wall and σ stands for the Stefan-Boltzmann constant. However, since this expression neglects the strong coupling between radiation and the blocking effect, it does not agree well with experiments. Marxman et al. [10] later attempt to address this coupling by providing a correction factor of the form

$$\frac{B_{\text{rad}}}{B} = 1 + \frac{\dot{Q}_{\text{rad}}}{\dot{Q}_c}\left(\frac{B_{\text{rad}}}{B}\right)^{0.77} \tag{2.24}$$

where

$$\dot{Q}_c = 0.036 G h_v Re_x^{-0.2} B^{0.23} \qquad \text{and} \qquad \dot{Q}_{\text{rad}} = \sigma \varepsilon_w \left(\varepsilon_g T_b^4 - T_w^4\right)$$

This equation cannot be solved explicitly, but its solution can be approximated adequately by

$$B_{\text{rad}}/B = \exp\left(1.3 \dot{Q}_{\text{rad}}/\dot{Q}_c\right) \tag{2.25}$$

which leads to

$$\rho_f \dot{r} = \left[\dot{Q}_c \exp\left(-\dot{Q}_{\text{rad}}/\dot{Q}_c\right) + \dot{Q}_{\text{rad}}\right]/h_v \tag{2.26}$$

For systems with low values of $\dot{Q}_{\text{rad}}/\dot{Q}_c$, the tradeoff between the new terms in Eq. (2.26) is "nearly exact, and $\dot{r}$ can be calculated with little error by using $\dot{Q}_c$ alone" [10]. If $\dot{Q}_{\text{rad}} = \dot{Q}_c$, then Eq. (2.26) predicts that approximately three quarters of the heat actually transferred to the wall will be due to radiation and that $\dot{r}$ will be only 35% higher than the case without any radiation. While useful for illustrative purposes, this result should be treated with care: if the majority of heat transferred is radiative, the dependencies on geometry will not be the same as those already considered for the purely convective case.

In a paper published three years later, Marxman [61] adds more qualitative thoughts on the radiation problem. Particularly, he classifies three general situations where radiation is important: grains containing particles that react incompletely in the flame to the extent of producing solid or liquid products (e.g. metallized fuels), grains that naturally produce solid or liquid products beyond the flame (e.g. carbon-heavy or sooty fuels), and propellants whose gas-phase combustion products produce appreciable radiation. All three cases may be described by similar expressions with the primary difference being in how the number density of radiating

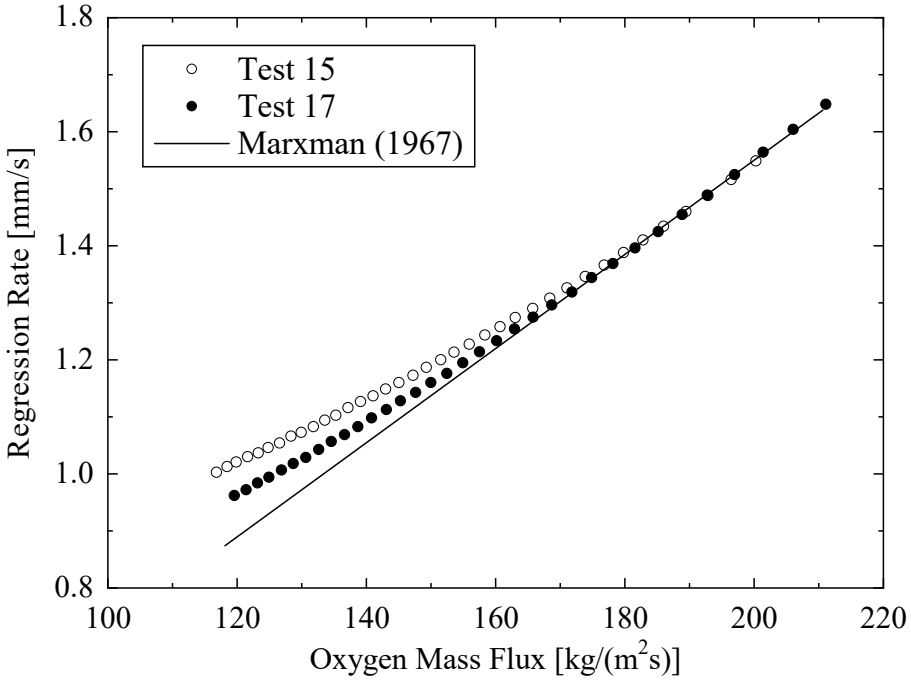

Figure 2.2. Effect of thermal radiation on HTPB regression-rate behavior. Data is taken from Chiaverini et al. [62].

particles is defined. In any case, the heat transfer becomes dependent on the chamber pressure through the density of radiating particles. Marxman notes that for the first two cases the most appropriate effective optical path length is probably the distance from the surface to the flame zone since the particle phase absorptivity will be high beyond that point. For the third case, he posits that the optical path length will depend on a characteristic chamber dimension such as the diameter. Although Marxman's group works primarily with PMMA-O_2 sytems with negligible radiation, other experiments with HTPB grains confirm that radiation effects become significant at higher motor pressures and lower oxidizer mass fluxes. Figure 2.2 displays the radiation dependence obtained in one such investigation by Chiaverini et al. [62]. Note that test 15 is performed at a higher pressure than test 17 and thus displays a stronger variance from the values predicted by Marxman's diffusion-limited, convection-driven model. Both sets of data agree with the theory at higher mass fluxes where convection dominates the heat transfer process and radiation proves to be unimportant.

2.4 Other Non-Ideal Considerations

In his 1965 paper, Marxman [11] provides a derivation for the regression rate, which parallels that of Marxman et al. [10] just described in detail, where the fundamental work of Lees [52] is revisited by relaxing the assumption that Pr = 1 to that of Pr = const. In this case, the thermochemical blowing parameter B differs from the aerodynamic similarity parameter B' according to

$$B = B' \mathrm{Pr}^{0.67} \tag{2.27}$$

and Eq. (2.20) becomes

$$\rho_\mathrm{f} \dot{r} = 0.036 G \left(\frac{Gx}{\mu_\mathrm{e}} \right)^{-0.2} B^{0.23} \mathrm{Pr}^{-0.15} \tag{2.28}$$

Since Pr is close to unity for most gases even at high temperatures, the effect of $\mathrm{Pr}^{-0.15}$ remains sufficiently small to render the correction unnecessary in most cases. The same study by Marxman [11] also addresses the assumption of uniform gas density between the flame and the wall by using a Howarth-Dorodnitsyn variable transformation to relate the actual, variable-property turbulent boundary layer to an equivalent incompressible boundary layer, viz.

$$\rho_\mathrm{f} \dot{r} = 0.036 G \left(\frac{\rho_0}{\rho_\mathrm{e}} \right)^{0.6} \left(\frac{Gx}{\mu_\mathrm{e}} \right)^{-0.2} B^{0.23} \tag{2.29}$$

The reference state ratio ρ_0/ρ_e is determined from a semi-empirical relation described in terms of previously defined parameters and the boundary layer thickness δ, which must be measured experimentally. Because of the added complexity, the variable-density correction is seldom used.

2.5 Kinetics-Limited Models

The importance of kinetics, both homogeneous and heterogeneous, has long been a subject of debate. As previously mentioned, in response to criticism received for neglecting heterogeneous surface reactions, Marxman [11] argues that the effects of reactions below the flame on the values of Δh and h_v remain of secondary importance. However, many researchers promote models and

correlations in which kinetics play an appreciable role. A selection of these, loosely grouped by dominant physical mechanism, is overviewed here as a starting point for further reading. This cursory coverage is not intended to be comprehensive in scope nor in detail.

The first group of researchers are those who are primarily concerned with gas-phase kinetics. For example, Wooldridge et al. [63] study pressure sensitivity at low pressures in an attempt to characterize the stability characteristics of hybrids. This effort entails the development of an analytical expression for the regression rate as a function of several kinetic parameters and length scales. Miller [64] performs an analysis that incorporates both the diffusion rate of fuel and the chemical reaction rates, which he uses to successfully correlate data taken by Smoot and Price [65–67]. Kosdon and Williams [68] later note that Miller's analysis is only applicable to systems with low pressure and moderate oxidizer fluxes and derive a new expression that incorporates a flame zone of finite thickness. Wooldridge and Muzzy [69] examine the effects of scaling and pressure on motor performance in the context of throttling. In his 1972 article, Muzzy [70] points out that even simple PMMA-O_2 motors behave differently at low pressures and also that combustion likely becomes kinetically-limited as the motor approaches a flooding condition. By reviewing existing test data, he constructs an explicitly pressure-dependent correlation which is quite similar to that of Wooldridge et al. [63], namely, where

$$\dot{r} \propto P^{0.5} G^{0.3} x^{-0.2} \tag{2.30}$$

Another group of researchers focuses more on heterogeneous surface reactions as the source of kinetics dependence. Smoot and Price [65–67] perform numerous tests using a slab burner and find that above a threshold value of G, the regression rate becomes nearly independent of G and instead varies with P and the oxidizer composition. They define a low mass flux regime where the normal $G^{0.8}$ dependence holds, an intermediate mass flux regime where both P and G play a role, and a third regime at very high mass fluxes where the regression rate varies like that of a solid rocket:

$$\dot{r} \propto P^{n} \tag{2.31}$$

Kumar and Stickler [71] cite discrepancies between hybrid motor data measurements and pyrolysis tests in an inert environment for PMMA to support their hypothesis that heterogeneous reactions must play a significant role in regression rate. They additionally argue that the gas-phase kinetics cannot be slow enough to play an important role. They develop a correlation that normalizes the regression rate by the flux-limited value for the purpose of predicting whether a particular set of conditions is kinetically or diffusively limited in and to more effectively match experimental data. More recently, Favaro et al. [72] perform experiments designed to elucidate the role of heterogeneous reactions and offer a corresponding semi-empirical model.

Despite the number of investigations into kinetically-limited operating regimes, Marxman's model and the assumptions that it prescribes have become the de facto standard for normal applications. This does not mean, however, that experts in the field have reached a definitive agreement on how to properly model regression in all situations. While modern computational studies are increasingly contributing to the community's understanding of diffusion-limited combustion in ways that may be less restricted by simplifying assumptions, Marxman's model is still commonly used to guide designs of hybrid systems and as a basis for the development of further analytical treatments in more complicated hybrids, such as those incorporating swirl or liquefying fuels.

2.6 Summary of Marxman's Theory

In closing this discussion, several key points regarding hybrid rocket regression rate modeling and its practical implementation may be summarized as follows:

- Marxman's theory is based on the assumption that the diffusion of oxidizer and fuel into the flame is the rate-limiting process in hybrid combustion and leads to adequate predictions for the moderate pressures and mass fluxes typically seen at steady-state operation in most hybrid motors.

- For classical, non-metallized hybrids, the fuel regression rate theoretically depends on $G^{0.8}$ but not on pressure.

- Radiation is generally of secondary importance, but should not be neglected at low mass fluxes or for metallized or other heavily sooting fuels.
- Most of the improvements to the initial diffusion-limited model (other than the treatment of radiation) lead to rather small corrections to the end result and can often be ignored.
- Numerous alternative regression rate models have been designed to be more accurate for kinetically-limited operating conditions.

For those seeking more information or a deeper understanding of classical regression rate models, the seminal reviews of the subject by Netzer [50] and Chiaverini [51] are highly recommended along with Marxman's 1965 paper [11]. Many relatively recent advances in hybrid design, such as the use of paraffin fuels, nanoparticles, energetic ingredients, or swirl injection, and other long-standing considerations, such as the sensitivity of motor performance to the oxidizer injection scheme, lie outside the scope of traditional regression rate models but must be taken into account when predicting the operation of a real system. Considerations related to swirling oxidizer injection are covered in detail in the next chapter.

Chapter 3

Review of Regression Rate Modeling in Swirling-Flow Hybrids

Despite the increasing interest in the use of swirl to enhance grain regression in hybrid motors, few studies exist that attempt to quantitatively model the explicit relations between swirl parameters and the regression rate. These mainly consist of separate groups of investigators who introduce both semi-empirical and analytical models to describe test data taken from their working engines [4, 44] or to use as an input to a larger study [27, 73–76]; it also comprises a further attempt by another team [77–79] to develop a theoretical model that is not directly motivated by any particular in-house experiment. These investigations and their relevant findings will be reviewed and discussed in the sections that follow. It should be noted that other groups have contributed greatly to the understanding of fuel regression in the presence of swirl injection by carrying out both experimental and numerical studies. Although a small selection of these studies will be briefly presented, effort will be made to maintain the focus of this review on theoretical modeling approaches to avoid an excessively long exposition. Several of the studies covered here have already been summarized in an earlier review of swirling-hybrid regression rate modeling by Roy and Frederick [80]; however, the main groups working in this area have made considerable progress in the intervening years. The purpose of this chapter is twofold: first, it will serve to identify and discuss new developments in theoretical approaches for modeling fuel regression rates impacted by swirl injection in hybrid rockets and, secondly, it will seek to revisit some of the earlier models with a focus on what each study reveals about the controlling parameters for this class of engine.

3.1 Orbital Technologies Corporation

The first analytical regression rate expression to take into account swirl effects in a hybrid motor may be traced back to William H. (Bill) Knuth, Martin J. (Marty) Chiaverini, and their coworkers[see Ref. 36, for example]. It is aimed at describing the Vortex Injection Hybrid Rocket Engine (VIHRE), a novel cyclonic-flow concept pioneered in the mid 1990s by Orbital Technologies Corporation (Orbitec), which is now part of Sierra Nevada Corporation (SNC). As shown in Fig. 1.2(*a*), VIHRE employs a bidirectional vortex configuration, wherein the oxidizer is injected tangentially into a simple cylindrical motor, just upstream of its nozzle. The incoming oxidizer sweeps across the grain surface, reacts with the fuel, and the resulting mixture spirals around while traversing the chamber length in what is known as the *outer vortex*. Upon reaching the headwall region, the products then turn around, drawn into the cyclonic funnel, and continue to spin around while crossing the chamber length for the second time, namely, through its *inner vortex* core region. This configuration has been introduced with an illustration in Sec. 1.4 and is described in greater detail in Chapter 5.

It may prove informative to examine the empirical correlations reported by Knuth et al. [54] before moving on to their semi-analytical model. A least-squares fit to the test data results in an empirical relationship of $\dot{r} = 0.189G^{0.55}$ with a coefficient of determination (R-squared value) of 0.952, where $\dot{r}$ is given in mm/s and G in kg/(m^{2}s). This, of course, represents a significant departure from the traditional dependence on $G^{0.8}$. Knuth et al. [54] note that many classical hybrids also display dependencies on G with powers significantly less than 0.8, but that such a departure from theory is usually attributed to pressure or radiation effects (or, more recently, to the use of liquefying fuels). In the case of VIHRE, the departure is definitively ascribed to the cyclonic flow configuration. This hypothesis is supported by another empirical correlation drawn from the same set of data measurements that encompass results from VIHRE experiments at three different scales, ranging over 20-200 lbf of motor thrust. Accordingly, a least-squares fit of the data to geometrical engine properties and operating conditions gives rise

to the following correlation:

$$\dot{r} = 0.0085 \left(\frac{D_{\text{avg}}}{D_{\text{t}}}\right)^{0.45} \left(\frac{L}{D}\right)^{-0.59} G_{\text{inj}}^{0.45} G^{0.37}, \quad R^2 = 0.997 \tag{3.1}$$

A larger contraction ratio, $D_{\text{avg}}/D_{\text{t}}$, between the port and throat corresponds to a wider radial gap between the tangential injectors and chamber outlet. A proportionally wider engine allows more space for the establishment of a coherent outer vortex and so the contraction ratio carries a positive exponent. The inverse dependence on aspect ratio could be due to either a more pronounced decrease in O/F ratio for longer, slimmer motors or vortex strength decay. Knuth et al. [54] attribute the relation mostly to swirl decay based on the results of a parallel CFD study[38] that also predicts significantly decreasing swirl strength with increasing aspect ratio. The importance of swirl strength to regression rates in hybrids has since been demonstrated by numerous experiments (including several that are discussed later in this work); they further affirm that a shift in O/F ratio alone is not capable of accounting for the magnitude of the exponent on L/D in Eq. (3.1). The regression rate still depends on the port mass flux G as in a traditional hybrid, although the dependence is weakened. A stronger dependence is observed on the injection mass flux G_{inj}, which has a larger bearing on the overall port mass flux. Interestingly, the combined effect of the two mass fluxes aligns well with traditional theory since the exponents on G and G_{inj} add to 0.82. This result may be more coincidental than meaningful because the combined fluxes in Eq. (3.1) do not have the same physical basis as the port flux alone. Moreover, engine pressure does not appear to influence the correlation given that the high swirl velocities produced in VIHRE ensure that the various modes of heat transfer remain convection-dominated.

Next, Knuth et al. [54], with the expertise of M. J. Chiaverini, turn to an analysis that consolidates the results of Marxman and Gilbert [9], written for VIHRE as

$$\frac{\rho \dot{r}}{G} = 0.023 \text{Re}_D^{-0.2} \text{Pr}^{-0.7} \left(\frac{\text{St}}{\text{St}_0}\right) B \tag{3.2}$$

with the experimental results of Dhir and Chang [81], who study the enhancement of heat transfer caused by swirl in solid pipes. After some effort, they arrive at the correlation

$$\frac{\mathrm{Nu_{sw}}}{\mathrm{Nu_0}} = \frac{\mathrm{St_{sw}}}{\mathrm{St_0}} = 1 + 1.93 \left(\frac{M_\theta}{M}\right)^{0.6} \mathrm{Pr}^{-\frac{1}{7}} \exp\left[-m \left(\frac{x}{D_h}\right)^{0.6}\right] \tag{3.3}$$

where $m = 0.89\,(M_\theta/M)^{0.2}\,\mathrm{Re}_D^{-0.18}\mathrm{Pr}^{-0.083}$ can be used to describe this enhancement. Note that this experimental result accounts for the effects of swirl but excludes wall blowing and combustion.

While Eq. (3.2) may not appear to match the exact form of Marxman's model given by Eq. (2.20), comparing it to Eq. (2.13) shows that it does indeed agree if the form of the blowing correction, $\mathrm{St}/\mathrm{St_0}$, is left undetermined. Here, $\mathrm{Pr} = 0.7$ is assumed rather than $\mathrm{Pr} = 1$, and the Reynolds number in both Eq. (3.2) and Eq. (3.7) is calculated using the hydraulic diameter instead of the axial location, as is done by Marxman. The Reynolds number appears in the classical regression rate expression because the shear stress depends on it, as discussed in Sec. 2.2. The expression for the skin friction coefficient used by Marxman, Eq. (2.9), applies for developing flow, where the boundary layer has not yet grown to the point of filling the pipe. On the other hand, the expression for fully-developed flow depends on the hydraulic diameter and is therefore used by Knuth and coworkers to describe VIHRE, whose flow characteristics differ significantly from those driven by axial injection.

Next, these investigators proceed to define a vortex-hybrid-specific Stanton number $\mathrm{St_v}$ such that the "real" Stanton number for VIHRE can be broken down into the product of a reference value, the effects of swirl, and the remaining effects due to wall blowing and unique geometry:

$$\mathrm{St_v} = \mathrm{St_0} \frac{\mathrm{St_{sw}}}{\mathrm{St_0}} \frac{\mathrm{St_v}}{\mathrm{St_{sw}}} \tag{3.4}$$

Thus, the term $\mathrm{St}/\mathrm{St_0}$ in Eq. (3.2) may be replaced by $(\mathrm{St_{sw}}/\mathrm{St_0})(\mathrm{St_v}/\mathrm{St_{sw}})$ to produce

$$\frac{\rho \dot{r}}{G} = 0.023 \mathrm{Re}_D^{-0.2} \mathrm{Pr}^{-0.7} \left(\frac{\mathrm{St_{sw}}}{\mathrm{St_0}}\right) \left(\frac{\mathrm{St_v}}{\mathrm{St_{sw}}}\right) B \tag{3.5}$$

The first ratio is given by Eq. (3.3) so that, if the propellant properties, geometry, and operating conditions are known, only $\dot{r}$ and $\mathrm{St_v}/\mathrm{St_{sw}}$ have to be determined. In keeping with previous studies, Knuth et al. [54] use experimental data to empirically derive an expression for $\mathrm{St_v}/\mathrm{St_{sw}}$ in terms of B,

$$\frac{\mathrm{St_v}}{\mathrm{St_{sw}}} = 0.55B^{-0.97} \tag{3.6}$$

It is suspected that the presence of blowing causes the velocity profile near the wall to become much steeper than in the non-combusting reference case. That this steepening effect is due to the presence of a reaction zone is confirmed by the fact that Eq. (3.6) exceeds unity for small values of B. This particular behavior is verified numerically by Merkle and Venkateswara [82] and experimentally by Chiaverini et al. [83]. Possible effects of swirl on the boundary layer structure, on the other hand, are not specifically addressed by Knuth et al. [54].

With the final relationship in hand, $\dot{r}$ can be estimated directly from

$$\frac{\rho\dot{r}}{G} = 0.016\mathrm{Re}_D^{-0.2}\frac{\mathrm{St_{sw}}}{\mathrm{St_0}}B^{0.03} \tag{3.7}$$

Equation (3.7) shows that for VIHRE, fuel regression is nearly independent of the blowing parameter and, instead, relies primarily on the mass flux G, as in the classical case, and the fraction of tangential momentum, as alluded to by Eq. (3.3).

At 0.868, the coefficient of determination for Eq. (3.6) is the lowest reported by Knuth et al. [54]. They attribute this result to slightly different trends in the data at different motor scales. The relation between $\mathrm{St_v}$ and $\mathrm{St_0}$ is also plotted but not expressed as a correlation, possibly because the corresponding data measurements do not display a consistent logarithmic trend as compared to Eq. (3.6). Two further correlations are introduced to validate the form of Eq. (3.5): first, a statistical analysis tool is allowed to vary the pre-constant in Eq. (3.5), which, for an assumed Prandtl number of 0.7, returns

$$\frac{\rho\dot{r}}{G} = 0.023\mathrm{Re}_D^{-0.2}\left(\frac{\mathrm{St_{sw}}}{\mathrm{St_0}}\right)\left(\frac{\mathrm{St_v}}{\mathrm{St_{sw}}}\right)B \tag{3.8}$$

with $R^2 = 0.938$. Note that the constant coefficient of 0.023 compares favorably to the value of 0.030 predicted by Eq. (3.5), whereas the relatively high R^2 value confirms the soundness of the model. Clumping of data suggests that Eq. (3.5) does not properly account for scaling differences and so the same analysis tool is next permitted to vary both the constant and the power on the Reynolds number. This results in

$$\frac{\rho \dot{r}}{G} = 0.082 \mathrm{Re}_D^{-0.33} \left(\frac{\mathrm{St_{sw}}}{\mathrm{St_0}} \right) \left(\frac{\mathrm{St_v}}{\mathrm{St_{sw}}} \right) B \tag{3.9}$$

with $R^2 = 0.992$. The improvement in the regression correlation with a stronger Reynolds number dependence suggests that boundary layer behavior in a vortex hybrid motor probably differs from pipe flow or that the hydraulic diameter may not be the most appropriate reference length in this context. The usefulness of theoretical modeling is highlighted by the fact that Eq. (3.9) more faithfully represents the data than does Eq. (3.1).

The discussion of Knuth et al. [54] can now be summarized by a few key points. Firstly, a correlation of experimental data for $\dot{r}$ solely in terms of G results in a much lower exponent, thus indicating that the oxidizer mass flux plays a smaller role in the presence of a swirling motion. Presumably, some aspect or aspects of the new flowfield must then act as controlling factors in addition to those described by Marxman. Potential parameters identified empirically include the chamber aspect ratio, contraction ratio, and the total mass flux of oxidizer injected both tangentially and axially. Nonetheless, analytical models based on Marxman's theory perform well and even outperform empirical data regression techniques in accurately predicting fuel regression rates in VIHRE. This reinforces the position that heat transfer inside swirl-driven hybrid motors will be dominated by convection and remains essentially diffusion-limited. A critical factor in the success of this semi-empirical model stands in its ability to account for the increase in heat transfer due to swirl. The model depends primarily on the ratio of tangential to total momentum at the injection location as well as the downstream distance, which provides an estimate of swirl strength decay. These two parameters, along with the port mass flux and Reynolds number, control the regression behavior in VIHRE. Finally, the Reynolds

number dependence appears to be somewhat different from that predicted by Marxman, which is unsurprising given that the flowfield is substantially dissimilar in character and orientation.

3.2 Hybrid Rocket research Working Group

The Hybrid Rocket research Working Group (HRrWG), which represents a collaborative endeavor between the Japan Aerospace Exploration Agency (JAXA) and several Japanese universities, constitutes another team of researchers who have sought to analytically describe the underlying factors affecting experimental results. Most of their studies concentrate on improving regression rates in hybrids with uni-directional swirl injection of oxidizer at the grain's fore end. Several studies performed by the HRrWG are of particular relevance to this review.

3.2.1 Early Experiments

The concept of head-end swirl injection is introduced in a pair of papers by Yuasa et al. [3] and Tamura et al. [29]. Although the VIHRE concept predates these studies, it is focused on the bidirectional vortex configuration rather than the potential benefits of swirl in a broader sense. The first paper, by Yuasa et al. [3], introduces the general concept and details of the experimental apparatus. The test motors contain cylindrical PMMA fuel grains with internal diameters of 40 mm and lengths of 150 mm. Gaseous oxygen is introduced into the head end of the chamber at a rate of 22 kg/s using one of three special swirl injectors. The injectors consist of annular disks, each with four thin passages that are cut through at an angle so that oxygen from the plenum is forced tangentially into the combustion chamber. For the reader's convenience, a diagram of the $Sg = 5.0$ injector originally presented as Fig. 3 a) by Yuasa et al. [3] is reproduced here as Fig. 3.1.

The strength of the swirling effect produced by the injector shown is measured by the geometric swirl number, namely,

$$Sg = \frac{\left(R_x - R_{\text{inj}}\right) R_x \pi}{n_{\text{inj}} R_{\text{inj}}^2 \pi} \approx \frac{\dot{m}_{\text{ox}} u_{\theta,\text{ox}} R}{\dot{m}_{\text{ox}} u_{x,\text{ox}} R} = \frac{u_{\theta,\text{ox}}}{u_{x,\text{ox}}} \tag{3.10}$$

Three different injectors are used in this study: the first contains injector slits that are directed radially inwardly to produce a non-swirling reference case, while the other two designs make use of tangential slits of differing sizes to produce geometric swirl numbers of 1.94 and 5.0. The nominal burning time for the engine is fixed at 10 s so that the geometric swirl number becomes the only variable. About 50 successful burning tests confirm that swirl-injection hybrids are viable and capable of stable operation with improved performance and efficiency. Notably, adjusting the swirl intensity of oxidizer injection provides the means to control engine performance independently of the O/F ratio, at least as compared to throttling.

The swirl injectors used by Yuasa et al. [3] are modified by Tamura et al. [29] to reduce the non-uniform impingement of the oxidizer on the fuel grain. The primary adjustment consists of increasing the number of injector slits from four to eight. A new set of five injectors is produced with geometric swirl numbers ranging from 0 to 32.3. The experimental apparatus of Tamura et al. [29] is otherwise largely identical to that of Yuasa et al. [3]. Multiple tests with different oxidizer mass fluxes allow the sensitivity of regression on the injector design and mass flux to be investigated. The results are best presented graphically, and so Figs. 5-6 from Tamura et al. [29] are combined and reproduced here as Fig. 3.2. Based on this graph, it may be easily inferred that increasing the swirl strength leads to an increase in regression rate. Furthermore, the data readily admit a correlation in the form of Eq. (2.22), as given in the upper right of Fig. 3.2. The exponent on G_{ox} remains lower than the theoretically predicted value of 0.8 and relatively consistent across all swirl strengths. In other words, increasing the geometric

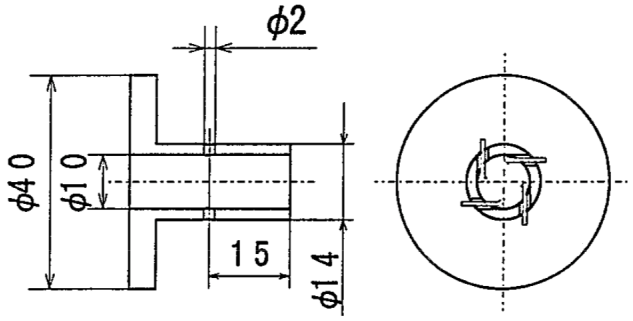

Figure 3.1. Diagram of a typical inward-tangential swirl injector. This particular injector is sized to produce a geometric swirl number of 5. Reproduced from Fig. 3 a) of Yuasa et al. [3]. All units are in millimeters.

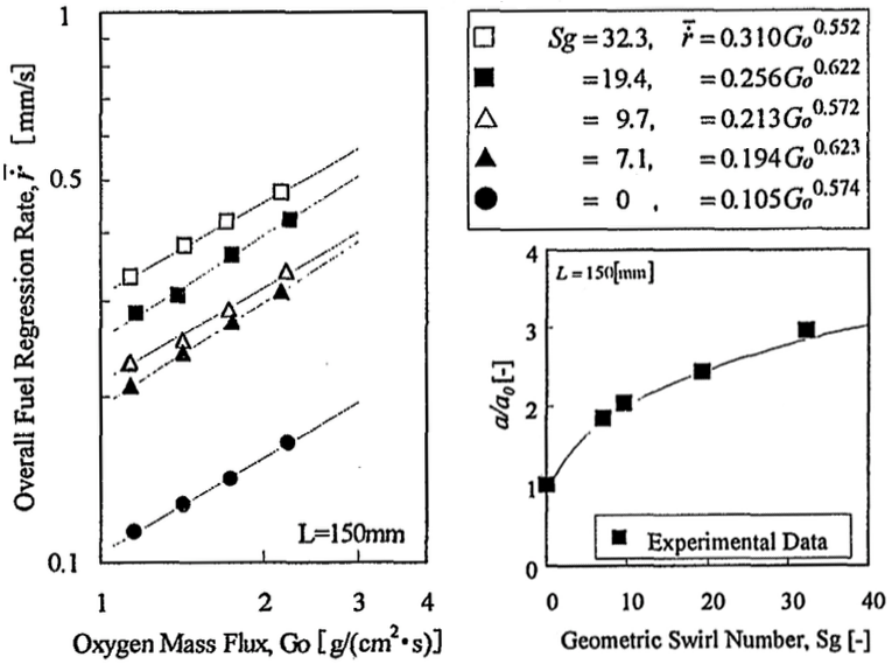

Figure 3.2. Plots and correlations characterizing the relation linking the average fuel regression rate, the oxidizer mass flux, and the geometric swirl number. Reproduced from Figs. 5-6 of Tamura et al. [29].

swirl number seems to have the effect of increasing the coefficient in Marxman's model without greatly affecting its form. This is functionally equivalent to increasing the mass flow rate, which is a promising discovery. The exact dependence of a on Sg is shown graphically on the right side of Fig. 3.2, where the regression coefficient normalized by its zero-swirl value is plotted against the geometric swirl number. Clearly, increasing swirl strength leads to diminishing returns as it will, at some point, become limited by practical considerations such as pressure losses in the injector. It is nevertheless gratifying to see that the impact of swirling oxidizer injection can be accurately described using existing theory, at least for the motor scale examined here.

In addition to providing useful correlations, Tamura et al. [29] note that the increase in regression rate can be explained by considering that the mass flux is equivalent to the axial momentum per unit volume. Injecting with additional tangential momentum increases the effective mass flux, a concept that is refined by several subsequent investigators. Furthermore, Tamura et al. [29] find that the optimum grain length of a hybrid motor decreases significantly with the application of swirl injection, which could allow for much more compact and mass-efficient motors. They also estimate that an optimized motor with swirling injection may be

capable of achieving a specific impulse within three percent of the theoretical maximum. The impact and importance of these initial papers published by Yuasa et al. [3] and Tamura et al. [29] cannot be overstated. By demonstrating that the concept of a swirl-injected hybrid is sound and ripe with potential, they open up the door for the technology to be further developed and matured.

3.2.2 Yuasa and Coworkers

Next is an investigation conducted by Yuasa et al. [4]. By collecting and organizing data from previous HRrWG tests, these researchers are able to carry out additional experiments aimed at elucidating the effects of swirl injection on hybrid combustion. Most of the experiments are performed using a hybrid test rig consisting of a cylindrical combustion chamber lined with polypropylene fuel that has an inner diameter of 40–48 mm, and a length of either 600 or 1000 mm. An interchangeable graphite nozzle at the aft end of the chamber allows for tests to be conducted at various chamber pressures. Gaseous oxygen is introduced into the head end of the chamber using one of two special swirl injectors that are similar in design to those used in the earlier investigation by Tamura et al. [29]. The injectors have geometric swirl numbers of 19.4 and 32.2, thus implying two cases of strong swirl where the tangential momentum dominates over the axial momentum at the injectors. The oxidizer mass flow rates are varied here from 10 to 400 g/s. A second, slightly modified test rig with transparent chamber walls is also employed to visualize the flame structure in the fuel grains. Further details of both experimental setups may be found in[4]. Regression rates are measured as spatially averaged values over both the entire grain and at various axial locations. All values are time averaged since they are obtained by immersing the grain in water before and after burning.

Several interesting phenomena appear upon testing, particularly regarding the disparity between upstream and downstream regions of the grain. On the one hand, $\dot{r}$ taken in the vicinity of the injector remains independent of grain diameter and thus burn time. On the other hand, $\dot{r}$ decreases with increasing burn time at axial stations further downstream as predicted by classical theory. Previous experiments with globally averaged data admit a curve fit with G as the single controlling parameter, in conformance with Marxman's theory, but with an

exponent of 0.582, which constitutes a significant departure from the predicted value of 0.8. It is interesting to note that this decreased value is similar to the number reported by Knuth et al. [54], which is discussed in Sec. 3.1. It seems, then, that the influence of oxidizer mass flux is markedly diminished in favor of swirl intensity in both unidirectional and bidirectional swirling flows. In fact, Yuasa et al. [4] report that regression in the leading edge region, defined in their study as the 100 mm of grain closest to the injector, remains completely independent of mass flux. Moreover, photos taken both during and after combustion show flames that remain attached to the wall near the injectors but separate downstream. These observations prompt the researchers to subdivide their analysis of the grain into two sections: the leading edge and the rear.

The leading edge analysis starts with the assertion that grain regression depends on the heat transferred to the wall, expressed at $\dot{r} \propto \mathrm{d}T/\mathrm{d}y$. Yuasa et al. [4] argue that since the flame and wall temperatures do not vary appreciably for a particular propellant combination and mixture ratio, the heat transfer must primarily depend on the flame height above the wall, $\mathrm{d}y = y_\mathrm{b}$. Next, it is recognized that for the injector configuration used in their experiments, the flow at the head end of the chamber is best described as a turbulent wall jet. A turbulent wall jet is defined as "a shear flow directed along a wall where, by virtue of the initially supplied momentum, at any station, the streamwise velocity over some region within the shear flow exceeds that in the external stream"[84]. Wall jets exhibit different velocity profiles near the wall as compared to typical flat-plate boundary layers and are traditionally thought to consist of a lower region near the wall, which behaves similarly to a conventional boundary layer, and an upper region, which more closely resembles an unbounded free-shear flow[85]. Some researchers also identify an intermediate mixing layer separating the aforementioned two in the region of maximum streamwise velocity[86]. To make further headway, Yuasa et al. [4] speculate that the thickness of a turbulent wall jet must be inversely proportional to the injection velocity U which, for the case of tangential injection, may be written in terms of the geometric swirl number:

$$U = u_{x,\mathrm{ox}}\sqrt{1 + Sg^2} \tag{3.11}$$

In the above, for $Sg \gg 1$, Eq. (3.11) may be approximated by $U \approx u_{x,\mathrm{ox}} Sg$. The assertion of a one-to-one inverse proportionality between δ and U remains unproven; this is discussed further in Sec. 3.2.3. Nevertheless, if $\delta \propto 1/U$ is assumed, then

$$\dot{r} \propto \frac{1}{y_\mathrm{b}} \propto \left(\frac{\dot{m}_\mathrm{ox}}{\rho} \frac{1}{A_\mathrm{i}} Sg \right)^n \tag{3.12}$$

Here continuity is used to rewrite $u_{x,\mathrm{ox}} = \dot{m}_\mathrm{ox} Sg / \rho A_\mathrm{i}$ and the exponent n is unknown. It should be noted that ρ in the denominator of Eq. (3.12) is instead replaced by a μ by Yuasa et al. [4], which could be due to a typographical error. Furthermore, A_i must be measured normal to $u_{x,\mathrm{ox}}$ in order for continuity to be maintained and, therefore, should not be the area of the injector slits as reported by Yuasa et al. [4]. The cumulative effect of these discrepancies calls the accuracy of the resulting correlation into doubt. Nonetheless, for the sake of completeness, it is cited here. A fit of the experimental data to the form of Eq. (3.12) results in

$$\dot{r} = 4.85 \times 10^{-6} \left(\frac{\dot{m}_\mathrm{ox}}{\mu} \frac{1}{A_\mathrm{i}} Sg \right)^{0.668} \tag{3.13}$$

where the expression in parentheses must have units of m^{-1} to yield $\dot{r}$ in mm. This expression does correlate the test data very well for swirl numbers of 19.4 and 32.3 and several chamber pressures. The satisfactory results produced by Eq. (3.13) can be reconciled with the uncertainty regarding its derivation by noting that the the primary drivers of regression are well represented one way or another. In either case, an oxidizer mass flux modified by the geometric swirl number makes up the bulk of the correlation. Dividing by the oxidizer viscosity is functionally equivalent to changing the coefficient in Eq. (3.13) since all of the tests are performed under similar conditions. Similarly, defining the oxidizer mass flux using the injector area rather than the cross-sectional area at the entrance to the port will uniformly shift the magnitude of the prediction for all tests performed using the same injector. Simply put, resolving the discrepancies in the derivation of Eq. (3.13) would likely lead to a similar result with a slightly different combination of coefficient and exponent since the actual values of the viscosity and areas do not vary significantly from one test to another. The exception to this statement is the

effect of changing the reference area across multiple injectors. It is thus interesting to see that the lone result for a different injector included in the data set used to derive Eq. (3.13) is also one of the furthest from the trend line.

In the rear region, photographs show that the angle of the swirl visible in the flames decreases considerably. This indicates that the turbulent wall jet no longer dominates the flow and so an attempt is made to correlate the regression rate with the oxidizer mass flux as in Marxman's theory, although the presence of swirl necessitates a key modification that may be elucidated by referring back to the derivation of Marxman's theory in Sec. 2.2. A close examination of the derivation reveals that the mass flux originally appears in the form of a momentum ratio [Eq. (2.7)] before one of the velocities is grouped into the blowing parameter. Thus, the $G^{0.8}$ term in the final expression proves to be a combination of momentum, which always coincides with the flow direction, and Reynolds number with respect to distance from the leading edge. In a swirling flow, the relevant length for boundary layer development should remain the distance traveled, even if it is not aligned with the axial coordinate. Thus, a Reynolds number defined in terms of the fluid pathline rather than the axial distance seems more appropriate. In general, Yuasa et al. [4] posit that the axial mass flux should be modified by the ratio of the swirl velocity to the axial velocity: $G_{\mathrm{sw}} = (u_{\mathrm{sw}}/u_x)\, G_x$. To develop this correction, they write the total swirl velocity as

$$u_{\mathrm{sw}} = \sqrt{u_x^2 + u_\theta^2} = u_x \sqrt{1 + \left(\frac{D}{D_0} Sg\right)^2} \tag{3.14}$$

where D_0 represents the initial diameter of the port. The diameter ratio does not appear in Eq. (3.11) because the radial location of the injectors is fixed, but it must be taken into account here in order to satisfy conservation of angular momentum and conservation of mass. For high swirl numbers, Eq. (3.14) simplifies to $u_{\mathrm{sw}} \approx u_{\mathrm{x}} SgD/D_0$. Thus,

$$G_{\mathrm{sw}} \approx \frac{\dot{m}_{\mathrm{ox}}}{A} \frac{D}{D_0} Sg \tag{3.15}$$

This expression becomes the controlling parameter for grain regression in the rear region of the motor. A comparison with their data leads Yuasa et al. [4] to the correlation

$$\dot{r} = 0.00339 \left(\frac{\dot{m}_{\mathrm{ox}}}{A} \frac{D}{D_0} Sg \right)^{0.734} \tag{3.16}$$

Here, the quantity in parentheses should have units of $\mathrm{kg}/(\mathrm{m}^2\ \mathrm{s})$ to give a regression rate in mm/s. This result agrees well with the exponent of 0.8 for the mass flux predicted by Marxman's theory and falls well within the range of values often encountered in practical applications. Equation (3.16) is also shown to correlate the same varied data set as Eq. (3.13) with very good agreement. More importantly, it proves to be a much more consistent predictor of the actual regression rate when compared to the unmodified axial mass flux.

Despite possible inconsistencies in the implementation of the leading edge expression, the realization that swirl injectors produce turbulent wall jets represents an important milestone in explaining the physics of swirl-driven hybrid rocket regression. Furthermore, establishing that Marxman's theory can simply be modified by a swirl number to produce reasonable predictions in regions of lower swirl strength is a fundamental accomplishment that should not be overlooked. The treatment of both the leading edge and rear sections by Yuasa et al. [4] points the way forward for refinements and corrections that are introduced by Sakurai et al. [44], as detailed in the next section.

3.2.3 Sakurai and Coworkers

In the wake of Yuasa et al. [4], the Hybrid Rocket research Working Group has continued its journey to develop practical, head-end-injection, swirl-driven hybrid rockets, coined *swirling-oxidizer-flow-type* (SOFT) hybrids. In 2017, this effort has culminated in the design, fabrication, and testing of a 5 kN hybrid rocket motor described by Sakurai et al. [44]. The fundamental design of the motor mirrors the style of earlier lab-scale (1.5 kN) HRrWG SOFT motors, such as the one described in Sec. 3.2.2. In this configuration, the oxidizer is introduced into the chamber at the head end through a swirl injector with a geometric swirl number of 19.4. The chamber has an initial inner diameter of 56 mm and a length of 970 mm. Following the analysis

of Yuasa et al. [4], the grain is once again divided for regression rate prediction into a 100 mm leading edge segment and a rear segment comprising the remainder of the motor. Further details of the chamber design and performance may be found in the paper by Sakurai et al. [44]; the present discussion will be limited to findings directly relevant to the problem of regression rate modeling.

Upon actual testing, the peak thrust levels produced by the motor are reported at 4.4 kN rather than the expected 5 kN. After examination of the data, these workers attribute this deficit to an over-prediction of the regression rate, particularly in the rear region. The assumed over-prediction leads to the engine operating at an equivalence ratio between 1.12 and 1.26, well below the intended equivalence ratio of 1.42. The fuel-lean operation results in lower flame temperatures and decreased performance, thus underscoring the importance of accurate regression rate modeling and the challenges that are often encountered in scaling up existing models.

Comparisons of the 1.5 kN tests to the lab-scale motor studied by Yuasa et al. [4] show that regression rates agree in the leading edge section but are lower by about 0.3 mm/s for the larger motor in the rear section. This difference cannot be ascribed to oxidizer mass flux values or grain lengths, which are similar for both motors; nor can it be tied to the chamber pressure, which does not affect regression rates in any of the cases examined. Rather, the discrepancy is attributed to a difference in initial port diameter. Data from both motors is plotted against the expected controlling parameters, given by Eq. (3.13) for the leading edge region and Eq. (3.16) for the rear. Over the rear portion, both sets of 1.5 kN test results agree well with the correlation whereas the 5 kN data falls below the predicted value by at least 17% in every case. Near the leading edge, both sets of 1.5 kN test results are once again in accord with the correlation while the 5 kN data consistently exceeds the predicted value. An additional comparison between the motor at the 1.5 kN and 5 kN operating conditions reveals a significant difference in regression rate trends in the leading edge segment, with the injection effects remaining important past the 100 mm mark for the 5 kN case. This behavior helps to explain the over-performance in the leading edge region and suggests that the original 100 mm distinction between regions is not accurate at larger motor scales. Thus, two differences between the lab-scale and 5 kN motors

become apparent: an axial elongation of injector influence and a decrease of regression rate in the region beyond that influence.

Sakurai et al. [44] address the first difference, i.e., the elongation of the leading edge region, by reexamining the properties of turbulent wall jets. The regression rate near the injectors is again assumed to depend on the flame height, with a transition to mass-flux dominated regression once the turbulent wall jet has given way to fully developed flow. Whereas Yuasa et al. [4] estimate the development length to be 100 mm (based on observation at one motor scale), Sakurai et al. [44] show that it is possible and preferable to calculate the development length for each motor individually. The only relation needed is the one linking the boundary layer thickness to the axial distance, as is commonly reported for all types of boundary layer flows. For a turbulent wall jet, the boundary layer thickness is given by

$$\delta = 0.37x\mathrm{Re}_\theta^{-0.2} = 0.37x\left(\frac{\nu_{\mathrm{ox}}}{xu_\theta}\right)^{0.2} \approx 0.37x\left(\frac{\nu_{\mathrm{ox}}}{xu_x Sg}\right)^{0.2} \tag{3.17}$$

The development length then corresponds to the axial distance at which the boundary layer thickness becomes equal to the chamber radius:

$$L_{\mathrm{front}} \propto D_0^{0.75}\left(\frac{\dot{m}_{\mathrm{ox}}Sg}{\mu_{\mathrm{ox}}}\right)^{0.25} \tag{3.18}$$

Here, the axial velocity is replaced by the oxidizer mass flow and initial port area in order to consolidate terms and reveal the strong dependence on port diameter. Sakurai et al. [44] identify the transition points in the experimental data, defined as the points at which the local regression rate first equals the axially averaged regression rate from the rear segment; they find that Eq. (3.18) is an accurate predictor of the leading edge length in all three motors under consideration. They then correlate the regression rate data from all motors using Eq. (3.12) and obtain the modified relation

$$\dot{r} = 5.63 \times 10^{-5}\left(\frac{\dot{m}_{\mathrm{ox}}}{\mu}\frac{1}{A_{\mathrm{i}}}Sg\right)^{0.541} \tag{3.19}$$

which has the same units as Eq. (3.13). It is somewhat intriguing that these researchers opt not to update the form of their correlation to reflect the more widely accepted expression for boundary layer thickness, Eq. (3.17). Nonetheless, Eq. (3.19) proves to be accurate to within the 10% uncertainty in the data measured in the forward segment of all tests except for one run of the 5 kN engine, which is found to differ by 15.3% from its prediction. It is also noted that Eq. (3.19) is only applied to motors with a single swirl intensity and should be validated for other cases.

The discrepancy in the rear segment of the motor is also addressed and ascribed to the initial port diameter as previously mentioned. Sakurai et al. [44] introduce this dependency by including the fuel mass flux and substituting the total mass flux into the existing regression model rather than the oxidizer mass flux alone. They note that while the oxidizer mass flux is commonly used as a stand-in for the total mass flux, Marxman and Gilbert [9] specify that the total mass flux at the boundary layer edge is the quantity on which the regression rate theoretically depends. Sakurai et al. [44] further note that for the case of constant oxidizer mass flow, the oxidizer mass flux depends on $1/A \propto 1/r^2$, whereas the fuel mass flux G_f remains proportional to both the regression rate and the area: $G_\mathrm{f} \propto r/A \propto r/r^2 \propto 1/r$. Using Eq. (3.15) with the fuel mass flow taken into account, an improved correlation is obtained, specifically:

$$\dot{r} = 2.33 \times 10^{-3} \left(\frac{\dot{m}_\mathrm{ox} + m_\mathrm{f}}{A} \frac{D}{D_0} Sg \right)^{0.729} \tag{3.20}$$

The maximum error in the rear regment improves from 17.1% to 14.5% by the addition of fuel mass flux. However, although this addition has the effect of making the regression rate prediction more accurate, it becomes less convenient *a priori* since $\dot{r}$ now effectively appears on both sides of the equation, necessitating a solution by iteration or numerical integration.

In summary, the improvements to the earlier model of Yuasa et al. [4] made by Sakurai et al. [44] are notable and lead to better precision at multiple motor scales. The general notion behind the choice of controlling parameters remains essentially unchanged, as do the parameters themselves. The most significant improvement can be seen, perhaps, in the development of a

physically-based, scale-dependent determination of the extent of the jet effects that dominate near the injectors.

3.2.4 Ozawa and Shimada

Next, Ozawa and Shimada [73, 74] investigate the stability characteristics of SOFT motors. In particular, they aim to determine whether the intrinsic low-frequency instabilities that characterize axial-injection hybrid rockets similarly appear in swirl-injection motors or whether swirl injection bestows a measure of inherent stability. On the one hand, swirling the oxidizer tends to push the flame closer to the fuel surface and thereby reduces the time lag of fuel vaporization in response to increased combustion. On the other hand, the blocking effect from the vaporizing fuel is predicted to affect the heat transfer more significantly. A major part of this effort is the development of an analytical model for the response of solid fuel vaporization to heat flux; that is, a model for the fuel regression rate in response to flow conditions. In their first paper on the subject, Ozawa and Shimada [73] extend the work of Karabeyoglu et al. [87] to account for swirl effects. The same methodology and results are also presented in a 2016 paper by the same authors [75]. Several important simplifications are hypothesized; among them are statements that the axial velocity remains uniform except in the boundary layer, that the tangential velocity mimics that of solid-body rotation except in the boundary layer, and that the swirl decays exponentially in the axial direction. The general philosophy of Ozawa and Shimada [73] mirrors that of Marxman and Gilbert [9] and invokes the Reynolds analogy to establish an equivalence between heat transfer and skin friction terms. Starting with the axisymmetric Navier-Stokes equations, they arrive at

$$\dot{Q} = \frac{C_f}{2} \frac{\rho_\mathrm{e} u_\mathrm{e}^2}{u_\mathrm{b}} \Delta h = \rho_\mathrm{f} \dot{r} h_v \tag{3.21}$$

which is familiar from Marxman's original derivation for axial flow. Ozawa and Shimada [73] point out that the absence of any explicit tangentially-dependent variable is consistent with the zero-balance circumferential heat flux required by axisymmetry.

The first noteworthy addition is an expression for the axial skin friction coefficient in a form that incorporates a dependence on the swirl number. Specifically, they find that

$$\frac{C_f}{2} \approx (0.01538S + 0.0233)\,\mathrm{Re}_\delta^{-0.125}\frac{\ln(1+B)}{B} \tag{3.22}$$

Note that all quantities in Eq. (3.22) are defined in terms of the axial velocity component only, with the obvious exception of the swirl number. This simplified equation for the skin friction incorporates the assumptions of a 1/7 power law profile for the boundary layer and a specific value of the mixing length constant. Ozawa and Shimada [73] provide a more general equation for the skin friction coefficient as well as the details of its derivation in their 2014 paper, but Eq. (3.22) should provide a sufficient appreciation for their result. In short, the skin friction coefficient increases linearly with the local swirl number of the flow while retaining its traditional dependence on the Reynolds number and blowing parameter.

Next, Ozawa and Shimada [73] derive a blowing correction, C_f/C_{f_0}, that accounts for the change in skin friction coefficient due to the presence of blowing from the wall when both axial and tangential velocity components are present. This blowing correction is then approximated in the traditional power law form as

$$\frac{C_f}{C_{f_0}} = 0.7275B^{0.965} \tag{3.23}$$

Here, the blowing parameter B is still defined using the axial velocity. Note that the coefficient and exponent in Eq. (3.23) differ significantly from the generally accepted values for rockets with axial flow only. To make further headway, the assumption of an exponentially decaying swirl strength is specified by

$$S \approx S_{\mathrm{inj}} \exp\left(-0.569\mathrm{Re}_D^{-0.277}\frac{x}{D}\right) \tag{3.24}$$

Equation (3.24), while simpler, mirrors Eq. (3.3) in its primary dependencies since both are based on cold flow experiments in solid pipes. By combining Eqs. (3.22–3.24), Ozawa and

Shimada [73] arrive at a final equation for the regression rate in a swirl-injected hybrid rocket:

$$\dot{r} = 0.0218 \left(\frac{\mu_e^{0.2}}{\rho_f} \right) G_x^{0.8} x^{-0.2} B^{0.035} \left[1 + 0.66Sg \frac{\exp\left(-0.569 \mathrm{Re}_D^{-0.277} \frac{x}{D}\right) - 1}{-0.569 \mathrm{Re}_D^{-0.277} \frac{x}{D}} \right]^{-\frac{1}{9}} \left[1 + 0.66Sg \exp\left(-0.569 \mathrm{Re}_D^{-0.277} \frac{x}{D}\right) \right] \quad (3.25)$$

Note that this equation retains the traditional form of Marxman's model with two important modifications. First, the dependence on the blowing parameter is lessened as a result of the addition of tangential velocity. Secondly, the axial mass flux is modified by a term that adjusts for the second velocity component in a manner reminiscent of Eq. (3.14).

Ozawa and Shimada [73] remark that while their model is largely consistent with experimental results by Yuasa et al. [43] for engines with large swirl numbers, the accuracy is not satisfactory. In a subsequent presentation of the material devoted entirely to modeling fuel regression rather than the question of stability [75], these researchers admit that even in cases where the averaged values are accurate, the axial trends predicted by Eq. (3.25) do not agree with the data. Furthermore, their model predicts a decrease in regression rate relative to the axial case when the swirl number is less than 3. This situation arises from simplifications made in the derivation of the model, and may be attributed to the separate formulations used for the blowing correction and skin friction coefficient and the assumption of an exponential swirl decay. The neglect of radial pressure gradients is also identified as a factor capable of reducing the accuracy of the model at higher swirl numbers.

In order to improve the accuracy associated with their model, Ozawa and Shimada [74] revisit the assumption of an exponential swirl strength decay. Citing the work of Motoe and Shimada [88, 89], they note that flow acceleration due to mass addition and combustion heat release dominates the effects of friction in real hybrid rockets and that this axial acceleration causes the swirl strength to decay according to the inverse of the axial distance and not exponentially. They therefore proceed to develop a new model for the swirl decay rate based on tracking the gas properties throughout the port. The axial temperature and molecular weight profiles are approximated based on the assumption that the flow is a mixture of gases

in equilibrium at each axial position. The local flow properties are referenced to an optimal equivalence ratio and temperature in order to track their relative changes:

$$T = T_{\text{inj}} + \frac{\left(\frac{\text{F}}{\text{O}}\right)_{\text{opt}} \left(1 + \frac{\text{F}}{\text{O}}\right) c_{p_{\text{opt}}} \left(T_{\text{opt}} - T_{\text{ox}}\right)}{c_{p_{\text{opt}}} \left[1 + \left(\frac{\text{F}}{\text{O}}\right)_{\text{opt}}\right] \frac{\text{F}}{\text{O}} + c_{p_{\text{ox}}} \left[\left(\frac{\text{F}}{\text{O}}\right)_{\text{opt}} - \frac{\text{F}}{\text{O}}\right]} \tag{3.26}$$

$$MW = \frac{\left(\frac{\text{F}}{\text{O}}\right)_{\text{opt}} \left(1 + \frac{\text{F}}{\text{O}}\right) MW_{\text{ox}}\, MW_{\text{opt}}}{MW_{\text{ox}} \left[1 + \left(\frac{\text{F}}{\text{O}}\right)_{\text{opt}}\right] \frac{\text{F}}{\text{O}} + MW_{\text{opt}} \left[\left(\frac{\text{F}}{\text{O}}\right)_{\text{opt}} - \frac{\text{F}}{\text{O}}\right]} \tag{3.27}$$

Thus, the details of the combustion reactions are omitted in favor of a greatly simplified treatment. By solving the one-dimensional Euler equations in terms of the O/F ratio as well, the swirl number can be written as a function of the initial flow properties and the equivalence ratio at any axial position:

$$S = S_{\text{inj}} \frac{MW\, T_{\text{inj}}}{MW_{\text{inj}}\, T} \frac{1}{\left(1 + \frac{\text{F}}{\text{O}}\right)^2} \tag{3.28}$$

Ozawa and Shimada [74] compare the predictions of Eq. (3.28) with a simulation carried out by Motoe [88] and find the agreement to be excellent except near the injectors, where the O/F ratio is greater than 20. In this region, the recirculation zone present in the numerical simulation increases the average temperature further upstream than analytically predicted, thus leading to a more rapid drop in swirl strength.

With an improved model for the swirl strength decay in hand, Ozawa and Shimada [74] present an abbreviated derivation of a regression model that mirrors that of [73]. After some algebra, they obtain

$$\dot{r} = 0.036 \left(\frac{\mu_{\text{e}}^{0.2}}{\rho_f}\right) G_x^{0.8} x^{-0.2} B^{0.23} \left(1 + 0.66Sg\right) \left(0.18 B^{0.23} \text{Re}_x^{-0.2} \frac{x}{D}\right)^{0.125} \left(1 + \frac{\text{F}}{\text{O}}\right) \left[\ln\left(1 + \frac{\text{F}}{\text{O}}\right)\right]^{-0.125} \tag{3.29}$$

In Eq. (3.29), the thermochemical and aerodynamic blowing parameters are equated and the radial distribution of tangential velocity is taken to be that of a solid body. Although these

simplifications by Ozawa and Shimada [74] are made for the purpose of validating their model, they also provide more detailed forms of their equations in the absence of these assumptions. Equation (3.29) compares favorably to axially-resolved regression rate data from Yuasa et al. [43] for tests performed with geometric swirl numbers of 9.7 and 19.4, except at the tail end of the motor where the analytical prediction begins to overshoot the experimental measurements. Plots of these comparisons are available in Sec. 4.3.4. Ozawa and Shimada [74] attribute this overshoot to approximations made in their development of the skin friction correlation. Moreover, when applied to the same motor with $Sg = 0$, Eq. (3.29) overpredicts the experimental data universally and does not represent the axial trend. Instead, a form of Marxman's model with a modified mass flux shows better agreement, although it does not fully capture the axial trend either:

$$\dot{r} = 0.036 \left(\frac{\mu_e^{0.2}}{\rho_f} \right) G_x^{0.8} x^{-0.2} B^{0.23} \exp\left(0.18 B^{0.23} \mathrm{Re}_x^{-0.2} \frac{x}{D} \right) \tag{3.30}$$

Ozawa and Shimada [74] also note that the use of Eq. (3.29) results in a mismatch between the initial value of the O/F ratio that is supplied to the equation and the value that can then be obtained based on the resulting regression rate. This disagreement grows with increasing swirl numbers and may be attributed to an inherent inconsistency. Ozawa and Shimada [74] speculate that calculating Karman's momentum integral in the axial direction only, while ignoring any effects of tangential velocity on the boundary layer thickness, is the root of the inconsistency. In any case, the predictions provided by Eq. (3.29) are deemed to be fairly reliable at intermediate swirl strengths and represent a significant improvement in accuracy over Eq. (3.25). In fact, Eq. (3.29) provides what may be the most accurate axially-resolved predictions demonstrated by any analytical model to date.

Subsequently, Ozawa and Shimada [90] note that, in general, the increase in regression rate as a result of swirl injection can be written in the form

$$\frac{a_{\mathrm{sw}}}{a_0} = \left(1 + Sg^2 \right)^{n_1 \pm N_1 \sigma_1} \tag{3.31}$$

where n_1 is an exponent determined by fitting experimental data and $N_1 \sigma_1$ represents the uncertainty of n_1. Later, they make use of a simplified regression rate model in studies of O/F

shifts on hybrid rocket performance [27, 76]; they get

$$\dot{r}(t) = a_0 G_{\text{ox}}(t)^n \left[1 + Sg(t)^2\right]^{n_1} \tag{3.32}$$

In Eq. (3.32), a_0 and n are the coefficient and exponent from Marxman's model for axial flow so that the second half of the equation serves as a modifier to account for swirl. As usual, G_{ox} in $\text{kg}/(\text{m}^2\,\text{s})$ will produce $\dot{r}$ in mm/s. By fitting Eq. (3.32) to data for axially-injected paraffin-GOX motors [21] and swirl-injected PMMA/GOX motors from within the HRrWG [91], Ozawa and Shimada [76] obtain a nominal regression rate for swirl-injected, paraffin-GOX motors:

$$\dot{r} = \exp(-2.22) G_{\text{ox}}^{0.640} \left(1 + Sg^2\right)^{0.156} \tag{3.33}$$

As an input to a larger model for comparing motor performance under different O/F control conditions, Eq. (3.33) is not the focus of the paper in which it is presented. It is assumed to be accurate and no further verification or comments regarding its validity are offered by Ozawa and Shimada [76]. Even so, that this simple form of a regression rate correction is apparently capable of fitting data for swirl-driven motors is noteworthy on its own. The next chapter of this dissertation will demonstrate that a similar expression may indeed provide a path toward unifying the modeling of fuel regression in swirling and non-swirling hybrid rockets in a manner that is both practical and physically justified.

3.3 Wongyai and Greatrix

An entirely different approach is taken by Wongyai and Greatrix [79]. Rather than referencing Marxman's work and concerning themselves with details of the boundary layer aerodynamics, these researchers adopt a heat-transfer-based scheme evolving from the thin-film theoretical work of Mickley et al. [92]. The central equality of this model sets the energy absorbed in heating and vaporizing an element of fuel equal to the heat of the flame transferred to the wall

through convection:

$$\rho_{\mathrm{f}} \dot{r} A_s \left[c_{p\mathrm{f}} \left(T_{\mathrm{w}} - T_{\mathrm{f}} \right) - \Delta H_{\mathrm{f}} \right] = \left(h_x + h_\theta \right) A_s \left(T_{\mathrm{b}} - T_{\mathrm{w}} \right) \tag{3.34}$$

Here, A_s denotes the surface area of the grain element, ΔH_{f} represents the net heat of reaction of the fuel, h_x and h_θ stand for the axial and tangential heat transfer coefficients, and the other terms carry their usual meaning. Note that the temperature of the fuel surface T_{w} refers to the steady-state value during burning, while the solid fuel temperature T_{f} designates the state of the fuel before it has been exposed to heat from combustion. As for T_{b}, it reflects the temperature of the burned gas at the flame. Equation (3.34) is quite similar to Eq. (2.1) in substance, but Wongyai and Greatrix's approach focuses the regression rate problem on obtaining an expression for the convective heat transfer coefficients. This strategy leads by no means to a trivial solution, but it can be less arduous than that of Marxman.

The first step in solving for h_x and h_θ is to revisit the one-dimensional heat equation, which is a statement of energy conservation between the fuel surface and the flame. Recalling that the regression rate is defined as the change in position of the fuel surface with time, the heat equation may be written as[93]

$$\frac{\mathrm{d}T}{\mathrm{d}y} = \frac{k}{\rho_{\mathrm{f}} \dot{r} c_{p\mathrm{g}}} \frac{\mathrm{d}^2 T}{\mathrm{d}y^2} \tag{3.35}$$

Equation (3.35) states that the rate of heat transfer from the gas must equate to the rate of heat absorbed by vaporizing the solid fuel, both rates being expressed on a per-volume basis. Practically, this differential equation can be used to describe the temperature profile in the gas between the flame and the wall. Solving Eq. (3.35) over $T_{\mathrm{w}} < T < T_{\mathrm{b}}$ and $0 < y < y_{\mathrm{b}}$ results in an expression for the gas temperature as function of height[77],

$$T\left(y\right) = T_{\mathrm{w}} + \left(T_{\mathrm{b}} - T_{\mathrm{w}} \right) \frac{\exp\left(\rho_{\mathrm{f}} \dot{r} c_{p\mathrm{g}} y / k - 1 \right)}{\exp\left(\rho_{\mathrm{f}} \dot{r} c_{p\mathrm{g}} y_{\mathrm{b}} / k - 1 \right)} \tag{3.36}$$

which, when differentiated, leads to the gas temperature gradient at the wall:

$$\left. \frac{\mathrm{d}T}{\mathrm{d}y} \right|_{y=0} = \frac{\left(T_{\mathrm{b}} - T_{\mathrm{w}} \right) \rho_{\mathrm{f}} \dot{r} c_{p\mathrm{g}} / k}{\exp\left(\rho_{\mathrm{f}} \dot{r} c_{p\mathrm{g}} y_{\mathrm{b}} / k \right) - 1} \tag{3.37}$$

The heat transfer into the fuel can now be expressed in two different ways: firstly, as conduction at the wall given by Fourier's law and, secondly, in the convective heat transfer form,

$$\dot{Q}_{\mathrm{w}} = k \left.\frac{\mathrm{d}T}{\mathrm{d}y}\right|_{y=0} = (h_x + h_\theta)\,(T_{\mathrm{b}} - T_{\mathrm{w}}) \tag{3.38}$$

Rearranging and substituting Eq. (3.36), the total heat transfer coefficient becomes[78]

$$h_x + h_\theta = \frac{\rho_{\mathrm{f}} \dot{r} c_{p\mathrm{g}}}{\exp\left(\rho_{\mathrm{f}} \dot{r} c_{p\mathrm{g}} y_{\mathrm{b}}/k\right) - 1} \tag{3.39}$$

In the limiting case of no transpiration, the total heat transfer coefficient may be represented as $h_x^* + h_\theta^* = k/y_{\mathrm{b}}$; this enables us to combine Eq. (3.39) with Eq. (3.34) to extract a solution for $\dot{r}$ in a form that depends on parameters that are either known or easily estimated by available correlations:

$$\dot{r} = \frac{\left(h_x^* + h_\theta^*\right)}{\rho_{\mathrm{f}} c_{p\mathrm{g}}} \ln\left[1 + \frac{c_{p\mathrm{g}}}{c_{p\mathrm{f}}} \frac{T_{\mathrm{b}} - T_{\mathrm{w}}}{\left(T_{\mathrm{w}} - T_{\mathrm{f}} - \Delta H_{\mathrm{f}}/c_{p\mathrm{f}}\right)}\right] \tag{3.40}$$

If the Reynolds analogy is invoked, the zero-transpiration convective heat transfer coefficients may be found as functions of the Darcy-Weisbach friction factor[79]:

$$h_x^* = \frac{k^{2/3} c_{p\mathrm{g}}^{1/3}}{\mu^{2/3}} \frac{G_x f_x^*}{8} \quad \text{and} \quad h_\theta^* = \frac{k^{2/3} c_{p\mathrm{g}}^{1/3}}{\mu^{2/3}} \frac{G_\theta f_\theta^*}{8} \tag{3.41}$$

The zero-transpiration friction factors are given for fully-developed flow by

$$\frac{1}{\sqrt{f_x^*}} = -2\log_{10}\left[\frac{2.51}{\mathrm{Re}_{d,x}\sqrt{f_x^*}} + \frac{\varepsilon_R}{3.7 D_x}\right] \text{ and } \frac{1}{\sqrt{f_\theta^*}} = -2\log_{10}\left[\frac{2.51}{\mathrm{Re}_{d,\theta}\sqrt{f_\theta^*}} + \frac{\varepsilon_R}{3.7 D_\theta}\right] \tag{3.42}$$

where ε_R is the surface roughness and the Reynolds numbers are defined in terms of the effective hydraulic diameters $D_x = D$ and $D_\theta \approx 4\delta_\theta$, if δ_θ is the thickness of the swirling flow layer along the wall. Wongyai and Greatrix [79] caution that this approximation for D_θ is restricted to the outward-swirl injection pattern under consideration in their treatment and would require re-evaluation for other types of injector geometries. Similar expressions for f^* applicable to developing flow may also be used to bring the model more in line with that of Marxman, if needed. In addition to the appropriate length scales, the axial and tangential velocity components

are required to evaluate the Reynolds numbers. These velocity components are often derived from a reported swirl number.

The geometric swirl number is discussed earlier in this work in the context of the HRrWG. However, unlike the efforts described earlier, Wongyai and Greatrix [79] use the standard version of the swirl number, such that it can be approximated for a simplified plug flow by

$$S \approx \frac{2}{3}\frac{u_\theta}{u_x} \tag{3.43}$$

A standard swirl number greater than approximately 0.6 is typically considered to represent "strong" swirl and roughly corresponds to the development of a recirculation zone near the injectors[94]. A vast difference seems to exist in commonly reported swirl intensity magnitudes between studies that use the traditional swirl number S, usually for outwardly-directed swirl injection, and those that represent the swirl strength of purely-tangential, inwardly-directed swirl injection; the latter are customarily expressed as a function of area ratios only, using the geometric swirl number Sg or the similar swirl number σ that appears in the analysis of the bidirectional vortex engine[95–97]. In a short paper dedicated to the subject, Greatrix [98] discusses the differences between these metrics. The primary point of his discussion is that these alternative forms of the swirl number, while conceptually related, are not equivalent or interchangeable. An additional point is that swirl decay seems to affect inward-injection configurations much more severely, thereby complicating the use of the injector-geometry-referenced geometric swirl number as a global representation of the relative values of the axial and tangential velocities in these motors. This point is further illustrated in the discussion of the HRrWG motors found in Sec. 3.2.

It should be noted here that even if the "true" swirl numbers of the HRrWG and Orbitec engines are only a fraction of their reported geometric swirl numbers, these designs still make use of significantly stronger swirl than most outward-injection designs. A modified geometric swirl number proposed by Greatrix [98] proves illustrative:

$$Sg_{\text{mod}} = \frac{2}{3}\frac{\left(r - 2R_{\text{inj}}\right)^2}{n_{\text{inj}}R_{\text{inj}}^2} \tag{3.44}$$

According to this metric, Greatrix points out that the $Sg = 5$ motor presented by Yuasa et al. [3] yields a "true" swirl number closer to 1.5; this correction brings the reported regression rate improvement more in line with the values published for other, outward-injection swirl motors. In this context, the previously discussed motors studied by Yuasa et al. [4] and Sakurai et al. [44] with geometric swirl numbers of 19.4 lead to modified values of approximately 10 instead. In comparison, the highest swirl number among the eight tests used to validate the model by Wongyai and Greatrix [79] is 1.156, with all of the other tests having swirl numbers that remain less than unity. Clearly, the comparison between inward-injection and outward-injection swirl generation is, at least historically, a comparison of flows with tangential and axial velocity components on the same order of magnitude to flows that are altogether dominated by tangential motion. At the time of this writing, however, the extent to which a description of one flow will apply to the other remains uncertain.

Because their model is not based on data from a specific test campaign, Wongyai and Greatrix [79] make use of test data from Hikone et al. [99], Pucci [34], and Lee and Potapkin [100] to validate their model. All of these test firings employ outwardly-injected swirl and no attempt is made to account for any swirl decay effects when applying the regression rate model. For simplicity, the net surface heat release, ΔH_f, of all fuels is assumed to be zero. Agreement is found to be fair for all data considered, although it may be generally viewed to be less compelling than results obtained by the foregoing studies. When considering the amount of estimation that is necessary to implement the model (as evidenced by the multitude of values in Table 1 of Ref. [79] that are used as inputs to the model), the wider variety of independent test data employed, and the lack of any explicit curve fitting, even a low level of accuracy must be regarded as being satisfactory.

In summary, then, the model presented by Wongyai and Greatrix [79] stands somewhat on its own in comparison to the others discussed here. It relates to a different injection configuration than the others, and it may be the only model not built on top of the foundation constructed by Marxman and his contemporaries. The potential applicability of this new model to motors with inward-injection swirling motion depends on reconciling the differences between the traditional and geometric swirl numbers. In a more general sense, this work highlights the need to identify

the relative strengths of the axial and tangential velocity components not just at the oxidizer injectors but throughout the port, as the flow evolves in space and time. In fact, understanding the decay in swirl strength that accompanies strong, inwardly-directed swirl injection is identified as a major part of this effort. It can be seen that besides their modeling effort itself, Wongyai and Greatrix [79] contribute a fresh perspective on the subject of swirl-driven and swirl-enhanced hybrid rocket regression rate modeling.

3.4 Other Numerical and Experimental Studies

In addition to the studies already presented, which each carry a notable analytical component, a few recent efforts that are primarily numerical or experimental can help to illuminate the nature of swirl-regression interactions and may be worth summarizing here. In particular, these studies contribute greatly to the understanding of swirl number trends within hybrid motors in ways that are likely to influence future theoretical pursuits.

3.4.1 Bellomo and Coworkers

The first of these is the 2013 study by Bellomo et al. [59], who numerically simulate combustion in a hybrid rocket with both swirl and axial injection in addition to performing laboratory-scale test firings of a physical motor. For the swirling case, the oxidizer is injected through openings in the headwall at a 45° angle with respect to the central axis of the cylindrical port in an outward-injection configuration. The propellants, nitrous oxide and paraffin, are chosen to investigate the potential for high regression rates offered by the combination of the exothermic decomposition of NO_2 and the entrainment of liquid paraffin in the oxidizer stream. This choice of propellants is especially worthy of investigation in light of a study by Hikone et al. [99] who show a doubling of regression rate for paraffin fuels when the oxidizer is swirled. The same study suggests that the use of paraffin fuels with swirl injection may also alleviate the non-uniform fuel regression that afflicts nearly all swirl-driven motors with traditional fuels. Nitrous oxide is also chosen by Bellomo et al. [59] to study the swirl injection of an oxidizer in liquid form. For the numerical simulations, both the oxidizer and fuel enter the chamber as decomposed gas mixtures at representative temperatures in order to avoid the complexity

of simulating multi-phase flow. Moreover, the injectors for the simulations are oversized with respect to those used in the experiments in order to better replicate the true mass flow and velocity conditions. The vortex injector in the numerical simulation has a geometric swirl number of 22 for the modified case of gaseous injection, although Bellomo et al. [59] note that if the oxidizer is injected as a liquid, the phase change and accompanying reduction in density will cause a marked drop in swirl intensity as the gas accelerates in the axial direction. In light of this, they suggest modifying the gaseous-injection swirl number by the density ratio of vaporized to condensed oxidizer in order to approximate the swirl number after the oxidizer has evaporated and dispersed. Using this method, they estimate the true swirl number of the motor under consideration to be closer to 1.7, which is more in line with other studies that consider similar injector designs. Once the numerical solution method and mesh are prepared, the simulation is then carried out repeatedly, with each iteration adding or modifying an additional component. In this manner, the influence of each component on the solution can be better characterized. The major iterations consist of a non-combusting simulation of the oxidizer injection alone, another non-combusting simulation that incorporates mass injection from the wall, a simulation that adds combustion and its effects on the flowfield, and, finally, a complete simulation of combusting flow that includes a converging-diverging nozzle in the simulation domain.

In all cases considered, vortex injection creates a recirculation region in the center of the port near the injectors. The strength of recirculation in this region and its size are both reduced by combustion. It is also confirmed that vortex injection enhances the mixing of hot and cold gases within the chamber which, in turn, increases the combustion efficiency. This mixing is partially due to the pressure and density gradients caused by the swirling motion: the cold, denser oxidizer is forced to the edges of the chamber while simultaneously displacing the lighter products of combustion toward the center. The magnitude of these gradients is determined to be

$$\ln\left(\frac{P}{P_{\text{center}}}\right) = \ln\left(\frac{\rho}{\rho_{\text{center}}}\right) = \frac{\omega^2 r^2}{2R_s T} \tag{3.45}$$

Specifically, Eq. (3.45) may be obtained by simplifying the Navier-Stokes equations in cylindrical coordinates under the assumption of steady-state, axisymmetric flow with a

negligible variation of the tangential velocity in the axial direction and a negligible radial velocity. The additional assumption of an ideal gas and forced vortex behavior leads to

$$\frac{\partial P}{\partial r} = \rho \frac{u_\theta^2}{r} = \frac{\omega^2 r P}{R_s T} \tag{3.46}$$

Equation (3.46) may then be separated and integrated between the center of the chamber and an arbitrary radial position r if any radial gradients in temperature or species composition are ignored.

Bellomo et al. [59] also note a large decrease in swirl angle (the angle between the local streamline and the motor axis) as the flow proceeds downstream when combustion is included in the simulation; they identify the axial acceleration of the flow, in keeping with the requirements of mass conservation, as the cause. This trend is crucial to the understanding of swirl strength in vortex injection hybrid rockets and is discussed at greater length in the next section's review of Paccagnella et al. [30], who present an almost identical result in additional detail and in terms of both the swirl number and swirl angle. For now, it may be sufficient to remark that, with combustion included, the swirl angle drops precipitously from about 70 degrees near the start of the fuel grain to roughly 15 degrees in the space of 25 mm, which is equivalent to approximately 10% of the motor length. In addition to the decrease in swirl angle that accompanies fuel injection and gas expansion, Bellomo et al. [59] report a rapid 30% decrease in swirl angle before the flow has even reached the fuel grain. All told, the initial swirl angle of 100 degrees decays to 10 degrees by the time the flow reaches the nozzle.

Specifics of the experimental results are generally beyond the scope of this review, but summarizing a few key points may be appropriate. Firstly, vortex injection is found to boost regression rates by an average of 51% when the propellant tank is actively pressurized and 36% when the NO_2 is self-pressurized. The relative improvement is noted especially at lower oxidizer mass flow rates. The c^* efficiency of the motor increases from 76% to 92% of the ideal value for the actively pressurized vortex injection case over the axial one, although the difference in actual characteristic velocities between the two setups is much lower due to the lower theoretical c^* for the vortex injection case. Similarly to Yuasa et al. [4], an examination of the grain post-firing

reveals obvious swirl patterns on the surface downstream of a bulging impingement region near the injectors. Finally, vortex injection using either pressurization scheme results in burns with a reduced shift in the mean motor pressure as well as a significantly damped combustion instability.

The analysis performed by Bellomo et al. [59] illustrates the fact that, barring the use of an exotic port geometry or flowfield design, the relative strength of swirl will drop off for nearly all hybrid rockets as the motor burns, even in the absence of explicit injector effects. In view of this, the desired benefits of swirl may often be overshadowed by an increasingly prepotent axial velocity downstream of the injection region. The explicit identification of the dominant mechanism of swirl decay as being mass conservation is a major step towards realizing the potential of swirl injection for hybrids. It is also somewhat disheartening because the barrier to maintaining consistent swirl strength is intrinsic to the operation of the motors. Some encouragement may be taken from the fact that the exact axial trends reported in Ref. [59] and Ref. [30] no doubt depend on the geometrical and operational scalings of the motor, and that unidirectional flows in cylindrical ports are not the only options for implementing swirl-driven hybrids.

3.4.2 Paccagnella and Coworkers

Several of the lines of inquiry that begin with Bellomo et al. [59] are pursued again by Paccagnella et al. [30]; the latter conduct a numerical investigation into the performance of a swirl-injected hybrid rocket. Their focus rests on scaling several different parameters independently in order to ascertain the effects of each on overall performance. In particular, they are interested in understanding the results of scaling the swirl number and the oxidizer mass flux, which are widely accepted to be the two most influential control parameters for swirl-augmented hybrids. A commercial CFD code is used to solve the Reynolds-averaged Navier-Stokes equations for a geometrical domain based on the motor built by Lee and Potapkin [100], albeit with a different injector design. The shear stress transport $k-\omega$ model is used to model turbulence and an eddy dissipation model is employed to approximate the net reaction rate for a single-step combustion process of oxygen with HTPB that results in eight product species. Following the lead of

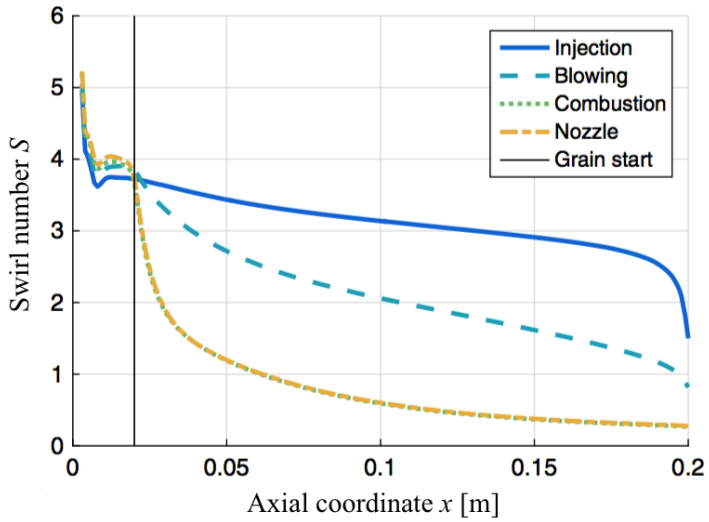

Figure 3.3. Swirl number as a function of axial coordinate for a motor with inward-tangential injection and a calculated geometric swirl number of 9.17. Trends are shown for multiple flow conditions within the same geometry. Reproduced from Fig. 6 of Paccagnella et al. [30].

Bellomo et al. [59], multiple simulations are undertaken to identify the distinct sources of these effects. Subsequent iterations largely mirror those of Bellomo et al. [59], the primary difference being that a post-combustion chamber is added along with a supersonic nozzle for the final set of simulations. After building up the swirling simulation piece by piece, the results of the complete simulation are compared to those with axial injection in the same motor. By proceeding in this fashion, Paccagnella et al. [30] leverage the highly-controlled nature of numerical simulations to provide detailed insights into the relative importance of various phenomena as well as the results of scaling the controlling parameters.

One of the first notable results presented by Paccagnella et al. [30] concerns the variation of both the swirl number and the swirl angle as a function of axial distance. A plot by Paccagnella et al. [30] of the swirl number S (SN in their notation) as a function of the axial coordinate provides a succinct summary of their relevant findings and is repeated as Fig. 3.3 for convenience. The first important feature illustrated by Fig. 3.3 is that, despite the injector having a geometric swirl number of 9.17, the maximum swirl number actually achieved at the injector is only slightly above 5 and drops below 4 by the time flow reaches the fuel grain. This observation supports the discussion at the end of Sec. 3.3 regarding the differences between the two metrics.

Figure 3.3 also shows that the role of friction is minor in relation to the role of mass conservation, with the injection-only case displaying a steady but moderate decrease in swirl strength – roughly 25% of the original swirl number – over nearly the entire length of the grain. The addition of mass from the sidewall produces a noticeable reduction of approximately 75% over the grain length, while the rapid heating and expansion of the gas due to combustion reduces the swirl number from its starting value of approximately 3.75 by an entire order of magnitude, to ~ 0.3. The addition of a nozzle does not meaningfully alter the swirl strength over the fuel grain. In all cases, a significant drop in swirl intensity also occurs in the injector region. The magnitude of this drop is not greatly affected by the addition of model components and is not included in the trends just described. These comparisons clearly indicate that it is largely the effects of continuity that drive the reduction of the swirl number in a hybrid motor. The acceleration of the flow in the axial direction by the addition of mass and, particularly, by the expansion of the gases, drives down the relative strength of the tangential velocity component without decreasing its absolute value in a significant way. To the contrary, blowing from the wall is actually shown to decrease the retardation of the tangential velocity by friction and can lead to a modest increase in the tangential velocity as energy is added to the flow [30].

As mentioned earlier, some versions of the VIHRE motor with aspect ratios close to one can prevent an extreme drop in swirl strength for a given combination of the bidirectional vortex flowfield and the scaling of the injectors, which effectively ensure that the entire length of the grain is dominated by injector effects. As Bellomo et al. [59] point out, acceleration in the axial direction depends on an essentially one-dimensional statement of the continuity equation, which is applicable to uni-directional (swirling or axial) flow in a straight port. In plain terms, the flow must accelerate in the axial direction as it expands because it cannot escape the chamber any other way. For a bidirectional vortex configuration, however, the flow in the outer vortex is free to expand radially inwardly in order to satisfy the mass conservation requirement. In fact, combining aft-end injection with an inert headwall means that *all* of the flow must accelerate radially inwardly as it turns to exit through the nozzle. Thus, bidirectional vortex engines should be expected to display much lower levels of swirl decay when velocities are measured near the fuel grain.

The assertion by Wongyai and Greatrix [79] that outward-injection motors are less affected by swirl decay is, at first glance, perplexing in the context of the results of Paccagnella et al. [30] since continuity is expected to affect either type of motor in equal measure. In fact, the trend is merely masked by the difference in injection conditions typical of the two. Firstly, the relative decrease in swirl strength is lower for a motor with a smaller initial swirl number. More to the point, all of the outward-injection designs considered by Wongyai and Greatrix [79] have a significant axial component at the injectors themselves: this feature leads to a smaller relative increase in the axial contribution to the resultant velocity vector as the flow accelerates axially. It should not come as a surprise that inwardly-oriented swirl injectors, which rely on continuity to establish any axial velocity at all, exhibit a drastic decrease in the ratio of tangential to axial velocity (that is, a decrease in swirl number) as the value of the axial velocity in the denominator diverges from zero. It is entirely consistent with all of the studies examined so far to say that the values of the swirl number, geometric or otherwise, measured locally at the injector in a motor with inward-tangential injection and unidirectional flow are not representative of the actual swirl number experienced by the majority of the grain. This situation exists because the initial swirl strength is artificially inflated by a low initial axial velocity that cannot be reasonably maintained over the length of the fuel grain during motor operation. In support of this assertion, Fig. 15 of Paccagnella et al. [30], reproduced here as Fig. 3.4, shows that the actual swirl numbers over the grain for injection geometric swirl numbers of 4.39, 5.97, and 9.17 are much closer than would be expected based on the clear differences calculated and observed at the injector. While the higher injection swirl numbers do indeed lead to higher swirl numbers throughout the motor, the difference is vastly reduced as the flow accelerates axially. It would be informative to disentangle the regression trends attributed to the radially non-uniform oxidizer distribution and boundary layer structure of a turbulent wall jet by Yuasa et al. [4] and Sakurai et al. [44] from the increased head-end residence times and effective mass fluxes caused by an exponential or inverse-distance axial velocity distribution as observed by Bellomo et al. [59] and Paccagnella et al. [30].

Next, Paccagnella et al. [30] move on to examine the dependence of motor performance on oxidizer mass flux by performing a series of simulations for each swirl number while setting

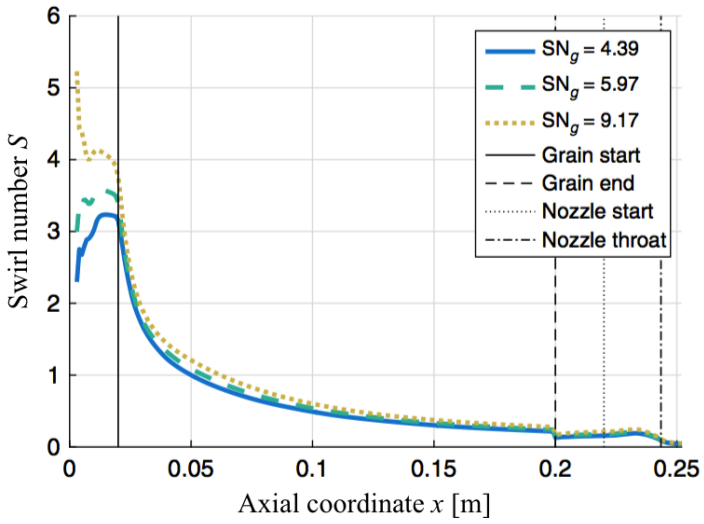

Figure 3.4. Swirl number as a function of axial coordinate for a motor with inward-tangential injection and three different injector designs. Reproduced from Fig. 15 of Paccagnella et al. [30].

the mass injection to 100, 67, and 33 percent of the design value. The shape and intensity of the flowfield are not affected by throttling because the pathlines depend only on the injector geometry and velocities. The decrease in chamber pressure as a result of reduced mass flow maintains the injection velocity at a constant level across all cases. In general, the swirl strength, temperature, and axial velocity all display only minor variations over the range of throttling. These differences are attributed to the change in mass addition due to increased fuel regression rates at higher oxidizer mass fluxes. Using data from the simulation, Paccagnella et al. [30] produce expressions for the average regression rate at each swirl number in the form of Eq. (2.22): $\dot{r} = 0.053 G_{\text{ox}}^{0.56}$ for $Sg = 4.39$, $\dot{r} = 0.044 G_{\text{ox}}^{0.64}$ for $Sg = 5.97$, and $\dot{r} = 0.038 G_{\text{ox}}^{0.71}$ for $Sg = 9.17$. In these correlations, G_{ox} must have units of kg/(m^2 s) to produce a regression rate in millimeters per second.

Finally, a unified regression rate law is developed by combining the simulation results with the approach of Yuasa et al. [4]. In this process, the geometric swirl number is assumed to be approximately equivalent to the ratio of the velocity components, $Sg \approx u_\theta / u_x$, and this ratio is further assumed to vary with the port diameter so that, for large Sg,

$$u_{\text{sw}} \approx u_x \frac{D}{D_0} Sg \tag{3.47}$$

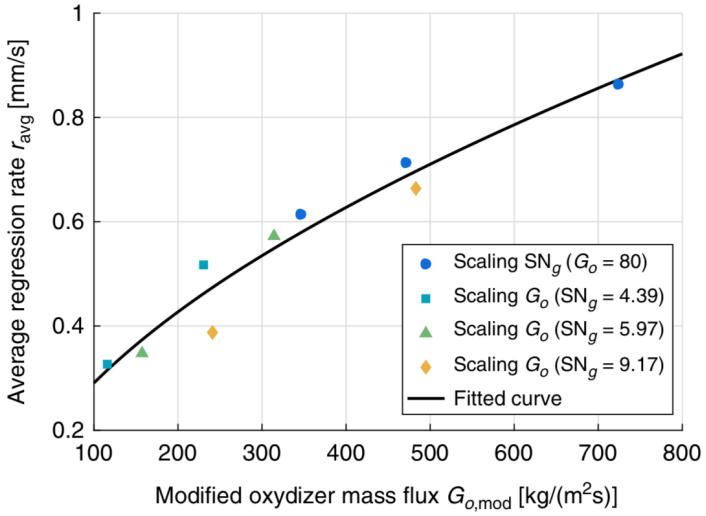

Figure 3.5. Average regression rate plotted against the swirl-modified effective mass flux as represented by Eq. (3.15). Data from several simulation cases are shown alongside the regression law given by Eq. (3.48). Reproduced from Fig. 26 of Paccagnella et al. [30].

This once again leads to Eq. (3.15). When correlated to the simulation data, this form of the effective mass flux leads to

$$\dot{r} = 0.023 G_{\mathrm{sw}}^{0.56} \tag{3.48}$$

As shown in Fig. 3.5, which is recreated from [30], the methodology adopted by Yuasa et al. [4] in the rear segment of their grain allows Paccagnella et al. [30] to develop an accurate regression rate law for their motor. Comparing Eq. (3.16) and Eq. (3.48), which are both established using the same process and equation with two different data sets, shows that while this approach is promising, the resulting coefficients are highly dependent on the scale and operating conditions. This dependency is attributed in particular to the scaling of the oxidizer mass flux by Paccagnella et al. [30]. In light of the preceding discussion in Sec. 3.3 on the fidelity of the geometric swirl number and the corroborating findings in Ref. [30], it seems likely that a modified dependency on this parameter will also improve the portability of the regression rate law.

3.4.3 Franco and Coworkers

Franco et al. [101] keep treading the same line of research with a recent article that examines the effects of swirl intensity and postchamber length on the effectiveness of vortex injection hybrid rockets. Once again, the investigation comprises both numerical and experimental parts, with

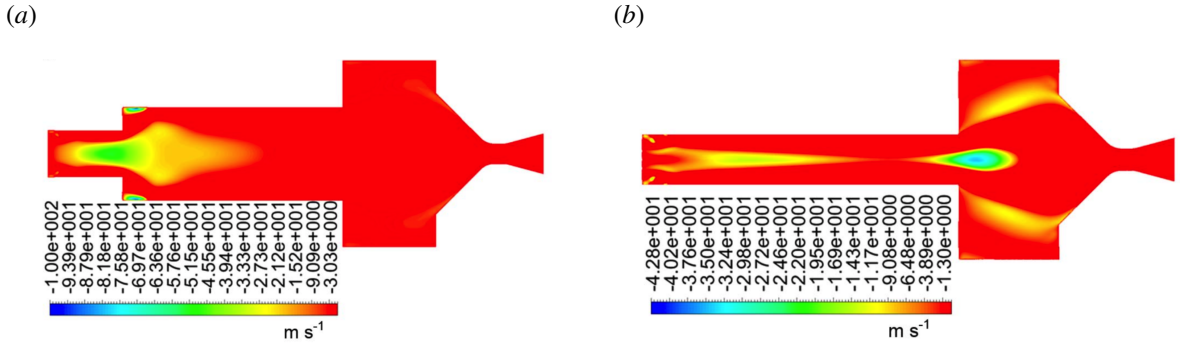

Figure 3.6. Plots of negative axial velocity at the mid-section plane for a pair of simulated motors. The only difference between the two cases is the grain internal diameter, which is either a) 25mm or b) 50mm. Reproduced from Fig. 9 of Franco et al. [101].

the CFD simulations informing the design of the experiments and interpretation of results. This investigation is somewhat unique regarding the swirl injectors: all three of the designs studied are of the inward-tangential type, but the number and diameter of the injection holes are both increased relative to all of the other inward-injection experiments that have been discussed so far. These changes are made in order to reduce the geometric swirl number of the injectors to values of 2, 2.53, and 3.33. They require introducing a second rank of injection holes, separated by a small axial distance, to the two injectors with the lowest swirl intensities in order to fit the necessary total injection area into the available internal diameter of 25 mm. This axial stacking of injection jets may slightly alter the development of the swirling flowfield, but the procurement of data for inward-tangential-injection swirling hybrids with low swirl strengths is a welcome addition to the literature.

The numerical simulations confirm that swirl injection leads to recirculating flow in the low-pressure core near the injectors for all cases, even over the range of comparatively small geometric swirl numbers studied. Figure 3.6, which is a partial reproduction of Fig. 9 from Franco et al. [101], clearly displays this recirculation zone. When the port diameter is greater than the injection plate diameter, recirculation is also observed on the back sides of the step at their interface, as shown in Fig. 3.6(*a*). On the one hand, the presence of a diameter increase and accompanying recirculation at the injector-grain interface increases the temperature in the head end of the grain. On the other hand, Fig. 3.6(*b*) illustrates the formation of a kernel of reverse flow at the entrance to the postchamber for the combination of a 25 mm fuel grain with

the 100 mm diameter postchamber. A larger diameter ratio between the two sections results in a more uniform temperature at the nozzle entrance, indicating improved mixing. In short, sudden cross-sectional area increases have the expected effect of increasing fluid mixing. More noteworthy is their effect on the swirl strength. As previously discussed, the swirl number is theoretically proportional to the chamber radius in order to conserve angular momentum and axial mass flow. The simulations carried out by Franco et al. [101] show that the swirl number does in fact increase when the chamber radius is increased, but the effect is not immediate for discontinuous changes in radius. Rather, a sudden expansion leads to a similarly sudden drop in swirl number; this is followed by a more gradual increase as the flow moves downstream. The ensuing behavior is attributed to the disruptive effects of recirculation zones that dominate the flowfield in the vicinity of sharp steps. The flow recovers its idealized structure further downstream, which allows the swirl number to recover as well. In discussing these trends, it is important to keep in mind that the swirl number is simply a ratio of velocity components. It does not necessarily correspond to the coherence of any flow structure. As an example, consider the results for the wider-grain motor simulation in Fig. 3.6(a). The complete lack of any reverse flow kernel at the postchamber entrance for this configuration demonstrates that while a grain diameter wider than the injector diameter will cause the swirl number to increase beyond its starting value as the flow slows axially, the axial recirculation and turbulent mixing near the injector-grain step will, on the whole, reduce the coherence of the swirling flow structure even some distance downstream.

On the experimental side, Franco et al. [101] perform a matrix of test firings based on a combination of three injector designs, three postchamber lengths, and three different conditions for the initial chamber diameter. Rather than being fixed at particular values, these conditions set the baseline grain diameter to 25 mm and then adjust the actual diameter for each motor to represent the expected internal diameter after 0, 10, and 20 seconds of burning. Thus, the starting grain diameters vary more widely for the motors using stronger swirl injection. Franco et al. [101] acknowledge the familiar trend of excessive regression in the injector region and measure the post-burn fuel regression using a weighted average of the near-injector and downstream port sections.

With the average regression rates calculated, several trends are observed. Firstly, a log-log plot of regression rate vs oxidizer mass flux for different port diameters results in a straight line for each motor when all other aspects of the configuration are held constant. These trends are then unified by accounting for the geometric swirl number to produce a correlation for the coefficient in Eq. (2.22):

$$a_2 = 0.0261Sg + 0.0154 \tag{3.49}$$

The exponent on G_{ox} is taken to be $n = 0.5$ for all swirl numbers, which is a good approximation of the measured average values of 0.5217, 0.4851, and 0.4706 at swirl numbers of 2, 2.53, and 3.33, respectively. The slight downward trend in n with increasing swirl number and the small range of swirl strengths investigated leaves open the possibility of a more significant dependence of n on Sg at other operating conditions. For the set of data under consideration though, a virtually constant value of n and a linear relationship between Sg and a_2 allow for easy prediction of motor performance at other similar design points. Another finding of Franco et al. [101] is that the diameter of the postchamber relative to the grain is more important than its length. In fact, longer postchambers made of the same fuel material as the grain can cause a decrease of up to 25% in the global O/F ratio as additional chamber material is burned away before the flow reaches the nozzle. Even if the postchamber is constructed of a non-combustible material, mixing will occur in a short space as long as the change in diameter is sufficiently large and so a longer chamber is unnecessary.

The effects studied by Franco et al. [101] help to address some of the questions that have been left open by previous researchers. In particular, a better understanding of the response of swirling flow in combusting hybrid rockets to discontinuities in chamber diameter will be useful for the design of non-academic motors. While most regression rate models to date assume that the flow velocities will behave in an idealized way, achieving increased accuracy will inevitably require some recognition of the three-dimensional disruption caused by features such as sharp corners.

3.5 Summary

In this chapter, the current state of solid fuel regression rate modeling for hybrid rockets with swirling oxidizer injection is reviewed. In the process, several prominent research groups that are active in the field are identified. These groups have a variety of methods, objectives, and outcomes associated with their investigations, but the synthesis and comparison of each permits some general conclusions. First and foremost, a few obvious findings can be stated. Describing regression in swirl-injected hybrids of any type requires the quantification of the swirl strength using a swirl number that is adequately specified. Arguments in favor of one version or another are ongoing, but it seems that these could be largely resolved by a mutual understanding of the nuance involved in using a single number to characterize a phenomenon that undoubtedly depends on the axial position, port geometry, and injection configuration at a minimum. That is to say, it would perhaps be more constructive to focus on how to accurately describe the velocity ratio over the entire length of the grain, at different scales and with different injection configurations, than to become overly attached to any one existing metric. Additionally, there is unanimous agreement that heat transfer in swirl-injection hybrids is driven by turbulent convection to an even greater extent than in axial-flow hybrids. Diffusion-limited regression rate models prove to be accurate, and radiation and pressure can generally be neglected, barring the deliberate introduction of metal particles. There also seems to be a loose consensus that, at least for regions where the flow can be assumed relatively uniform in cross-section and the axial and tangential velocity components are on the same order, Marxman's model can produce accurate predictions when modified with some form of "effective" mass flux.

Beyond these generalizations lie a host of more specific observations, whose reconciliation and implications would benefit from further research. Knuth et al. [54] demonstrate that the axial oxidizer mass flux abdicates its role as the primary driver of fuel regression in favor of a swirling equivalent, while Tamura et al. [29] show that increasing the swirl strength is tantamount to augmenting the coefficient on a traditional regression rate expression in terms of the axial mass flux, such that increasing the swirl number is somewhat akin to increasing the mass flux itself. Yuasa et al. [4] confirm that an effective mass flux treatment of Marxman's

model can produce accurate results under some conditions but identify non-uniformly distributed flow in the injector region as cause for a departure from this rule. Sakurai et al. [44] affirm these findings and supplement them with additional insight into the effect of motor scaling on injector influence. Meanwhile, Ozawa and Shimada [74, 75] develop a more rigorous analytical model by following the approach established by Marxman and Gilbert [9] and reveal differences that accompany swirling flow in the individual dependencies that comprise their model. Wongyai and Greatrix [79] offer a new perspective on convection-driven regression, while a series of numerical and experimental studies by Motoe and Shimada [102], Bellomo et al. [59], Paccagnella et al. [30], and Franco et al. [101] highlight the mechanisms by which swirl decays or grows within a hybrid rocket.

Although there is much yet to be explored and better understood about predicting fuel regression in swirl-driven motors, the efforts of the aforementioned researchers ensure that the potential benefits of swirl injection will make their way out of the lab to be realized in practical hybrid rockets. The findings summarized in this chapter establish a baseline for new models and point to numerous opportunities for further improvements. As the community's grasp of the various dependencies underpinning fuel regression rates improves, so too will the capabilities of hybrid rockets.

Chapter 4

Diffusion-Limited Regression Rate Model for Swirling Flows

The key points summarized at the conclusion of the previous chapter point the way toward a simple, unified expression for regression rates in swirling and non-swirling hybrids. The development and validation of such a model is the focus of this chapter. In contrast to the already-discussed researchers who have approached the problem from a semi-empirical perspective to describe experimental results [4, 44, 54] or who have attempted a completely analytical solution from first principles [75, 79], the present model is developed as a modification to the commonly used, classical regression rate expression of the form $\dot{r} = aG^n x^m$. It is hoped that this approach will provide a generally applicable model for swirling hybrid motors while remaining simpler to implement than some of the foregoing correlations.

4.1 Derivation

Encouraged by the successes of Yuasa et al. [4] and Paccagnella et al. [30] in applying a modification to the mass flux that accounts for swirl, this model is based on the same concept of an effective mass flux. As an extension to these two prior efforts, careful consideration is given to the spatial and temporal variations in the swirl number.

The first step in developing a swirl modifier, namely, the inclusion of a tangential velocity component in Marxman's model, is fairly straightforward. It may be accomplished by substituting the swirling velocity $u_{\mathrm{sw}} = \sqrt{u_x^2 + u_\theta^2}$ in place of the axial velocity u_x and, where appropriate, the path length $s_{\mathrm{sw}} = \sqrt{s_x^2 + s_\theta^2}$ in place of the axial distance x. A convenient starting point is the completed form of Marxman's model written in terms of velocity rather

than mass flux:

$$\rho_f \dot{r} = 0.036 \rho_e u_e \mathrm{Re}_x^{-0.2} B^{0.23} \tag{2.19 Revisited}$$

It is then a simple matter to make the proper substitutions:

$$\rho_f \dot{r} = 0.036 \rho_e \sqrt{u_{x_e}^2 + u_{\theta_e}^2} \left(\frac{\rho_e \sqrt{u_{x_e}^2 + u_{\theta_e}^2} \sqrt{s_x^2 + s_\theta^2}}{\mu_e} \right)^{-0.2} B^{0.23} \tag{4.1}$$

Recognizing that $\sqrt{u_{x_e}^2 + u_{\theta_e}^2} = u_{x_e} \sqrt{1 + \left(u_{\theta_e}/u_{x_e}\right)^2}$ and $\sqrt{s_x^2 + s_\theta^2} = s_x \sqrt{1 + \left(u_{\theta_e}/u_{x_e}\right)^2}$, Eq. (4.1) may be further reduced and written in terms of the traditional axial variables:

$$\rho_f \dot{r} = 0.036 \rho_e u_{x_e} \sqrt{1 + \left(u_{\theta_e}/u_{x_e}\right)^2} \left(\frac{\rho_e u_{x_e} x \left[1 + \left(u_{\theta_e}/u_{x_e}\right)^2\right]}{\mu_e} \right)^{-0.2} B^{0.23} \tag{4.2}$$

$$\dot{r} = 0.036 \frac{\mu_e^{0.2}}{\rho_f} G^{0.8} x^{-0.2} B^{0.23} \left[1 + \left(\frac{u_{\theta_e}}{u_{x_e}} \right)^2 \right]^{0.3} \tag{4.3}$$

Accounting only for the second component in distance and velocity terms results in an expression that resembles the traditional form, but changes to the blowing parameter dependence and boundary layer structure are ignored by making a direct substitution as in Eq. (4.1) instead of a careful derivation from the governing equations. These detailed effects are treated by Ozawa and Shimada [75], who find that slight differences do exist. A discussion of these changes and their effect on the final result may be found in Sec. 3.2.4. Ultimately, these are neglected here in favor of a further simplification to a more generic form of the regression rate expression that is capable of absorbing various discrepancies:

$$\dot{r} = a G^{0.8} x^{-0.2} \left[1 + \left(\frac{u_{\theta_e}}{u_{x_e}} \right)^2 \right]^{0.3} \tag{4.4}$$

It may be instructive to remark that the exponent on the swirl modifier term of 0.3 in Eq. (4.4) is unlikely to be perfectly corroborated by experimental measurements, much like the theoretical mass flux exponent of 0.8 and the axial exponent of −0.2, although all three values serve to

anchor the model for practical use. In particular, the exponent of 0.3 stems from the questionable simplification of a boundary layer structure that remains unchanged by the swirl velocity and whose thickness increases in proportion to the total distance traveled by the flow. To avoid becoming snared in the details, it is sufficient to note that this exponent should possess a value somewhere between zero and one half. In general, this modified Marxman model predicts that regression in a hybrid rocket, with or without swirl injection, can be represented by

$$\dot{r} = aG^n x^m \left[1 + \left(\frac{u_{\theta_e}}{u_{x_e}}\right)^2\right]^{n_1} \tag{4.5}$$

This form is ideally suited for application to existing motors whose traditional propellant parameters (coefficient a and exponents n and m) are already well characterized, since it provides a "net swirl modifier" to the original, non-swirling case. It is also preferable for validation since it allows the data to be calibrated to a zero-swirl case, if one is available, thus ideally removing any error introduced by inaccuracies in Marxman's model. Although the correction term is derived based on Marxman's model, it could potentially be applied to any expression that describes the regression rate of a non-swirling motor. This possibility has not yet been investigated and may require further exploration.

The validity of Eq. (4.5) depends in large part on how faithfully the velocity ratio term is represented. To that end, it is convenient to replace the velocity ratio with a swirl number, defined here simply as the ratio of the bulk velocities:

$$S \equiv \frac{u_\theta}{u_x} \tag{4.6}$$

Note that this notation is a departure from the classical definition of the swirl number and is specific to this problem. There are two phenomena that must now be addressed. The first is the disparity between the assumption of bulk, cross-sectional averaged velocity values and the radial gradient in velocity values that must exist as a consequence of the swirling motion. Under the assumption of a forced vortex structure with a uniform axial velocity, such as would be found in an idealized, unidirectional SOFT motor, the swirl number can be related to the

velocity at the boundary layer edge according to

$$2S \approx \frac{u_{\theta_e}}{u_{x_e}} \tag{4.7}$$

Numerical simulations performed by Paccagnella et al. [30] establish that this idealized assumption is reasonable for cold flowfields but is substantially affected by the presence of combustion. Their results suggest that a proper scaling between the velocity ratio at the boundary layer edge and the bulk velocity ratio could be as low as 1.3 when the radial density gradient in a swirl-driven motor, the acceleration due to heating, and the viscosity of the fluid are taken into account. For now, the theoretical value of 2 will be retained.

The next and most important component of the swirl number model is a recognition of the sharp decay in swirl strength that is exhibited in nearly all swirl-injected hybrid motors. An initial attempt to address this effect is inspired by the successful use of Eq. (3.3) by Knuth et al. [54] to model regression rates in the VIHRE and employs a similar correlation from Chang and Dhir [103]:

$$S = 1.48 \left(\frac{M_\theta}{M_{\text{tot}}} \right)^{0.93} \exp \left[-0.113 \left(\frac{M_\theta}{M_{\text{tot}}} \right)^{0.35} \left(\frac{x}{D} \right)^{0.7} \right] \tag{4.8}$$

where M_θ and M_{tot} represent the tangential and total fluid momentum at the injector exit, respectively. This expression may be appropriate for the application of Eq. (4.5) to bidirectional vortex engines, but as discussed at length in Chapter 3, the vast majority of the swirl decay in SOFT motors with purely tangential injection occurs as a result of flow acceleration rather than viscous damping. Thus, another method of estimating the swirl decay is required for motors of this type, namely, one that is based on the conservation of mass and momentum. One option is to describe the temperature, molecular weight of the mixture, and swirl number in terms of the local O/F ratio using the expressions provided by Ozawa and Shimada [74] [Eqs. (3.26–3.28)]. A more transparent solution may be obtained by solving the quasi-one-dimensional, compressible form of the continuity equation for the axial velocity at an arbitrary location downstream of the injectors:

$$\dot{m}_2 = \dot{m}_1 + \Delta\dot{m}_{12} \tag{4.9}$$

$$\dot{m}_2 = \dot{m}_1 \left(1 + \frac{\dot{m}_2 - \dot{m}_1}{\dot{m}_1}\right) \tag{4.10}$$

$$u_{x2} = u_{x1} \frac{A_1 \rho_1}{A_2 \rho_2} \left(1 + \frac{\dot{m}_2 - \dot{m}_1}{\dot{m}_1}\right) \tag{4.11}$$

For a circular port and a constant chamber pressure, Eq. (4.11) is equivalent to

$$u_{x2} = u_{x1} \frac{r_1^2 R_{s2} T_2}{r_2^2 R_{s1} T_1} \left(1 + \frac{\dot{m}_2 - \dot{m}_1}{\dot{m}_1}\right) \tag{4.12}$$

where, as defined in the nomenclature, r, R_s, T, and $\dot{m}$ represent the port radius, specific gas constant of the fluid mixture, temperature of the fluid, and total mass flow rate. The subscripts 1 and 2 refer to conditions at the first (upstream) and second (downstream) stations, respectively. Meanwhile, the average tangential velocity can be assumed to vary so as to satisfy conservation of angular momentum:

$$u_{\theta 2} = u_{\theta 1} \frac{r_1}{r_2} \tag{4.13}$$

Combining Eqs. (4.12–4.13) – while taking stations one and two to be the injector exit and an arbitrary point further downstream – results in a simple expression for the swirl number as a function of the chamber conditions.

$$S = S_{\text{inj}} \frac{r T_{\text{inj}} R_{s\,\text{inj}}}{r_{\text{inj}} T R_s} \left(1 + \frac{\dot{m} - \dot{m}_{\text{inj}}}{\dot{m}_{\text{inj}}}\right) \tag{4.14}$$

By combining Eq. (4.5) with Eq. (4.7) and Eq. (4.14), the completed equation for regression in a motor with unidirectional, swirling flow is obtained:

$$\dot{r} = a G^n x^m \left\{1 + \left[2 S_{\text{inj}} \frac{r T_{\text{inj}} R_{s\,\text{inj}}}{r_{\text{inj}} T R_s} \left(1 + \frac{\dot{m} - \dot{m}_{\text{inj}}}{\dot{m}_{\text{inj}}}\right)\right]^2\right\}^{n_1} \tag{4.15}$$

Thus, the regression rate for a swirl-driven motor depends not only on the mass flux and axial distance, as in a traditional motor, but also on the swirl number at the injectors and the changes in port radius, temperature, specific gas constant, and total mass flow rate as these properties evolve from their values at the injectors.

4.2 Numerical Simulation Scheme

As may be clearly seen, a solution to Eq. (4.15) requires knowledge of the motor state throughout the engine and over the entire course of the burn. To obtain detailed results from the model, and to allow for comparison to data reported in a variety of formats, a MATLAB routine is written to numerically solve the regression problem. In general, this consists of the coupled set of equations

$$\frac{\partial r}{\partial t} = f\left(r, \dot{m}, x\right) \tag{4.16}$$

$$\frac{\partial \dot{m}}{\partial x} = g\left(r, \frac{\partial r}{\partial t}\right) = 2\pi r \rho_{\mathrm{f}} \frac{\partial r}{\partial t} \tag{4.17}$$

Here, the general function $f\left(r, \dot{m}, x\right)$ represents a regression rate model, such as that given by Eq. (4.15), that must be integrated concurrently with the mass flow rate at each axial station and timestep. The form of the general mass flow rate gradient function $g\left(r, \dot{r}\right)$ depends only on the port geometry and is specified above for a cylindrical chamber.

4.2.1 Code Architecture

Due to the coupled nature of Eqs. (4.16–4.17), a method-of-lines-type solution is required. This solution method relies on the fact that, although the two equations are coupled at each point, the mass flow starts with a boundary value and propagates downstream while the chamber radius has an associated initial condition and grows with time. As such, the condition on one of these variables may be used to initiate a solution for the other, with the solution proceeding step by step for all of one time (or spatial) value before moving to the next. This scheme is illustrated graphically in Fig. 4.1, using the same organizational convention as the data matrices in the solver.

If the matrices are arranged so that a row contains each data point from a single time step and each column consists of all times at a single location, then the top row is initialized with known boundary values while the leftmost column is populated with known initial values. The cell in the upper left corner (at the initial time and initial location) then contains values for both $\dot{m}$ and r, and so the governing equations may be integrated forward to the next time step (for

the fuel position) and the next x step (for the mass flow rate). When the end of one column is reached, the solver moves to the next axial step and repeats the process. This solution method does come with one limitation: in passing vaporized mass information downstream at a single

(a)

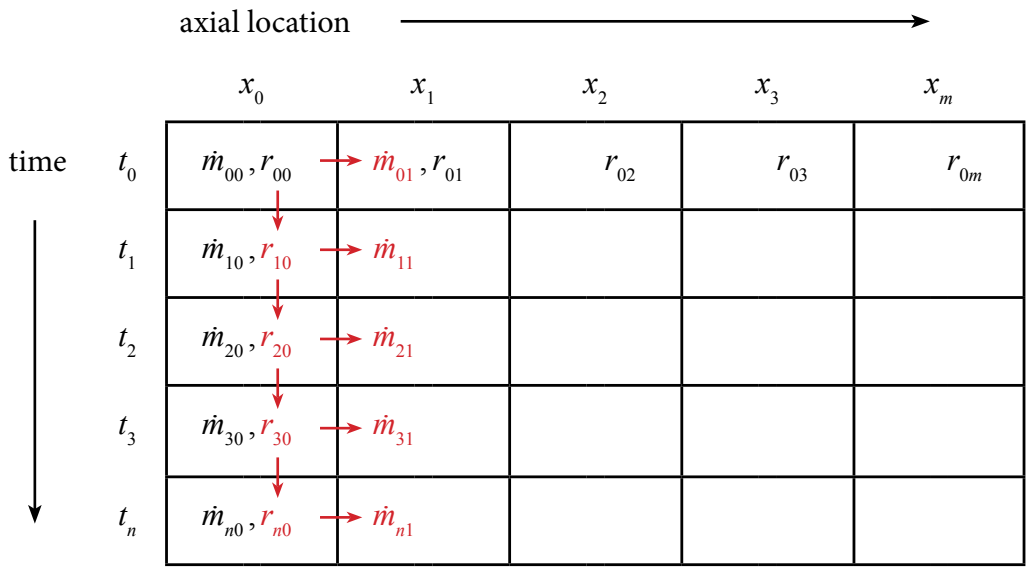

(b)

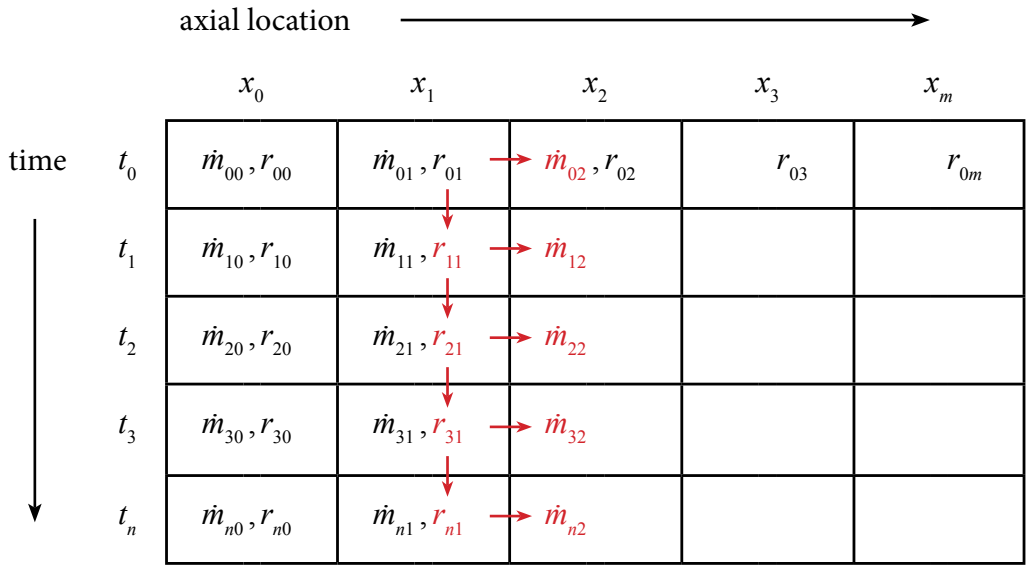

Figure 4.1. Graphical representation of the method of lines approach to the solution of the regression problem, with representative matrices shown after a) the first iteration and b) the second iteration of the procedure. Values in black represent known information at the start of each iteration.

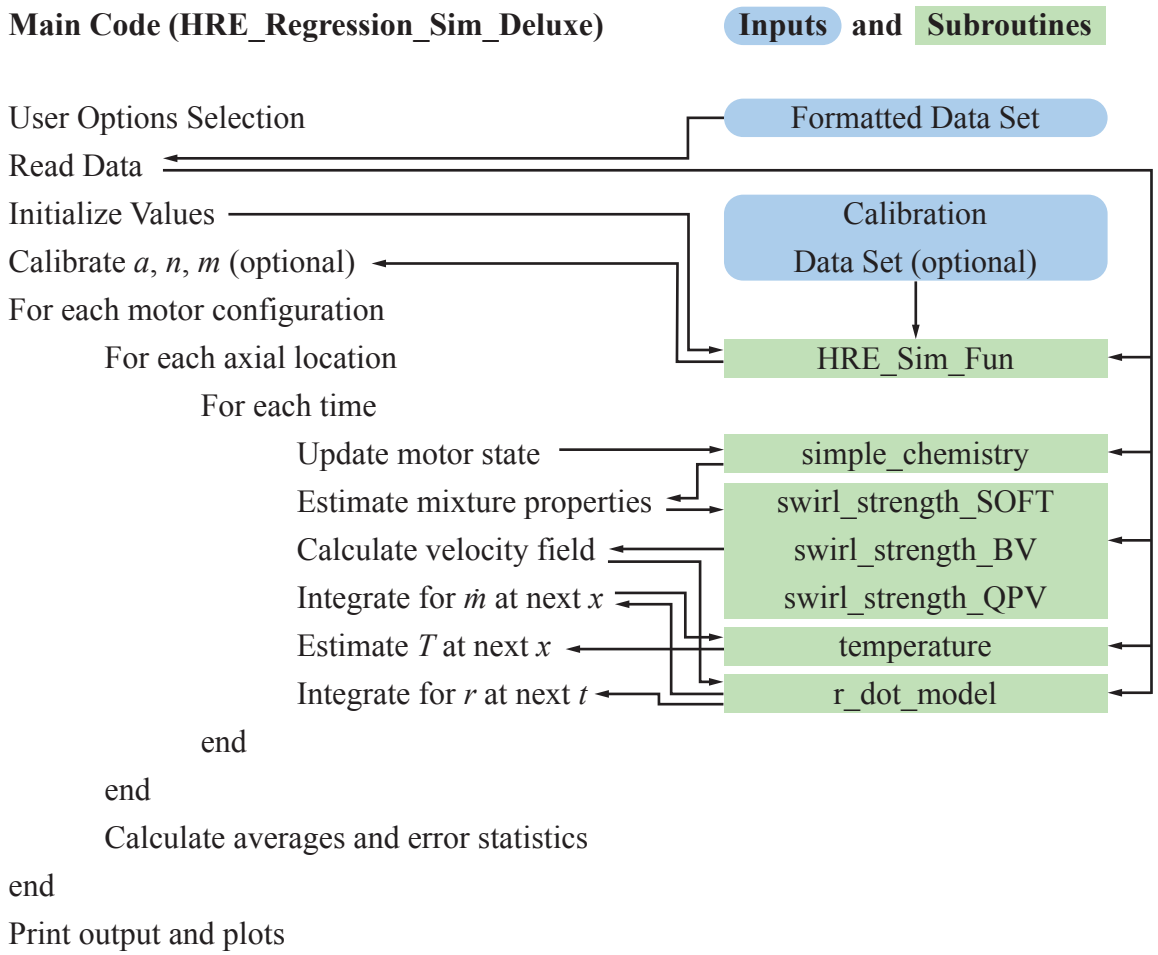

Figure 4.2. Flowchart showing key steps in the main solver routine as well as its interactions with various subroutines and inputs.

timestep, the flow is treated as being quasi-steady. The natural evolution of the mass flow rate with changes to the port geometry in both space and time is captured, and gradual throttling of the injected mass flow with time is permitted with a sufficiently resolved timestep, but the solver described in this section is not capable of accurately representing startup and shutdown transients. Thus, it is expected that the results of a simulation may become questionable for burns lasting less than a few seconds. On the whole, this restriction is not limiting for the purposes of the present investigation since none of the regression rate models being examined account for transient phenomena either.

Figure 4.2 provides a better overview of the overall code architecture by displaying the major steps in the main solution routine as well as its interactions with the various required

```
for j=1:num_x_grid %Step downstream
  for i=1:num_t_grid %Step forward in time
    %Update current mass flow rate
    m_dot(i,j)=m_dot_ox_inj(i)+m_dot_f_vaporized(i,j);

    %Evaluate mixture properties
    [R_mix(i,j),Cp_mix(i,j),Y_O2(i,j),...]=simple_chemistry(...)

    %Evaluate velocity field depending on motor type
    if strcmp(motor_type,'SOFT')
      [S(i,j),u_x(i,j),u_theta(i,j)]=swirl_strength_SOFT(...);
    elseif strcmp(motor_type,'BV')
      [S(i,j),u_x(i,j),u_theta(i,j)]=swirl_strength_BV(...);
    elseif strcmp(motor_type,'QPV')
      [S(i,j),u_x(i,j),u_theta(i,j)]=swirl_strength_QPV(...);
    end

    %RK44 spatial integration for fuel mass flow rate (total fuel
  vaporized; ignores reactions)
    m_dot_f_vap_increment(i,j)=...
    m_dot_f_vaporized(i,j+1)=m_dot_f_vaporized(i,j)+m_dot_f_vap_increment
  (i,j);

    %Calculate temperature at next station based on incremental amount of
   vaporized fuel
    T_mix(i,j+1)=temperature(...);

    % RK44 time integration for fuel postition (r and r_dot)
    r_dot(i,j)=...
    r(i+1,j)=r(i,j)+r_dot(i,j)*t_step;
  end %End of timestep
end %End of spatial step
```

Figure 4.3. Simplified representation of the core solver algorithm for the numerical simulation of a hybrid rocket burn.

inputs and subroutines. The integration itself is accomplished using the well-known 4th order Runge-Kutta algorithm, and a single motor simulation with 10,000 by 1000 grid resolution (ten million elements in each data matrix) runs in approximately 40 s on a personal computer. For a typical academic hybrid motor with a length of less than one meter and a burn duration under ten seconds, this grid size provides at least millimeter spatial and millisecond temporal resolution; this is more than sufficient and provides grid independence. Given the speed with which the code is capable of simulating a burn, super fine grid resolutions are adopted in lieu of performing a rigorous study on the trade-off between run time and accuracy. Similarly, the numerical error of the code is far exceeded by the uncertainty associated with the regression rate models and the scatter in the reference data.

While the inputs to the regression model are being integrated, the code also calculates and stores a variety of other motor information at each step. Figure 4.3 provides a simplified look at

the core simulation algorithm. Thermochemical parameters that are stored include temperature, specific heat, gas constants, and species mass fractions. Furthermore, the velocity components and swirl numbers are evaluated using subroutines specific to the motor type being simulated. The wealth of data available for analysis at the conclusion of a simulation is invaluable for a thorough examination and visualization of the various interdependencies affecting the regression process.

The various subroutines mentioned in Figs. 4.2–4.3 merit further discussion. The swirl strength subroutines are called from the main code based on the motor type indicated in the data file. Each accepts flow conditions and location information and evaluates the local velocity components and resultant swirl number. For SOFT motors, the function evaluates Eqs. (4.12–4.13) so that the final regression rate law is given by Eq. (4.15). The relevant flowfield solutions for bidirectional vortex or quadrupole vortex engines are the subject of Chapter 5 and Chapter 6, respectively. Simulation results for these engine types are presented in those chapters following the derivation of expressions for the fluid motion within each engine. A crucial function not explicity shown in Fig. 4.3 is the $\dot{r}$ model. It is simply a statement of Eq. (4.5) that may be called as often as necessary during the integration processes.

The simple chemistry function works in tandem with the temperature function to estimate the flow composition and integrated heat release within the motor as the flow moves downstream. In its current state, this aspect of the numerical simulation is accomplished using a set of crude, 4-species C-H-O-N reaction models for a representative fuel element undergoing complete combustion. For example, PP is represented by a single propylene molecule, whose reaction proceeds directly to the idealized products in stoichiometric proportion with pure oxygen:

$$C_3H_6 + \frac{1}{2}\,O_2 \longrightarrow 3\,CO_2 + 3\,H_2O$$

Similarly, the combustion of PMMA is represented by

$$C_5H_8O_2 + 6\,O_2 \longrightarrow 5\,CO_2 + 4\,H_2O$$

The simple chemistry routine invokes these simplified chemical reactions to compute the total quantity of products that are present in the flow based on the amount of fuel that has been vaporized, thus providing a way to estimate the local composition of the flow. Based on the flow composition, current temperature, and thermochemical tables, the bulk gas constant and specific heat are then evaluated. The temperature function relies on a similar knowledge of chemical reactions to estimate the incremental heat release of the burned fuel. Since the assumption of stoichiometry is an obvious idealization, the heat release is adjusted by a tuning constant to better approximate a realistic temperature rise, such as that displayed in Fig. 16 a) of Paccagnella et al. [30]. Furthermore, the simplified reaction models greatly overpredict the maximum temperature attained in the motor. This is once again largely attributable to the assumption of universally stiochiometric reactions, which does not reflect the reality of combustion in hybrid rockets. In order to prevent exessive temperatures from undermining the validity of the velocity calculations, this problem is addressed by further modifying the tuning constant on the temperature increment with the inclusion of a negative exponential term that tapers off as the flow approaches a pre-defined maximum temperature.

The treatment of the temperature profiles remains perhaps the most apparent weakness of the numerical simulation scheme, although it can be readily justified. A detailed chemical simulation of the motor would greatly increase the complexity and solution time of the simulations and, since the temperature and species profiles are merely inputs to the larger regression rate problem, any reasonable representation of these values will produce the desired results. In other words, it would be equally valid to simply require a representative temperature profile as a model input, although it is, of couse, preferable to reduce the *a priori* knowledge required to make a prediction. Reduced-order modeling requires a balance of accuracy with simplicity. The present arrangement of the numerical code strikes this balance by allowing the fuel choice and regression rate to inform the heating rate of the flow, albeit imperfectly; it also circumvents a more computationally expensive chemical simulation while improving upon the predictive capabilites offered by simply importing a pre-defined temperature profile. As a secondary benefit, the code is already structured to easily allow for the incorporation of a more detailed chemical reaction model, either internally or through interface with an external

program, should a higher degree of precision be required. As a final note, it should be recognized that any reaction model that does not account for dissociation cannot be representative of the motor conditions as the temperature approaches its maximum value above 3000 K. Improving the fidelity of the species model at high temperatures would be a welcome addition to the simulation package. Previous modeling by Lengellé [104] suggests that simply invoking an equilibrium reaction solver to determine the heat output in the presence of dissociation may be sufficiently accurate for predicitve purposes, even when the simple, one-step, stoichiometric reaction model is retained.

4.2.2 Code Validation

The solver itself is validated against a series of non-swirling engine tests run at NASA Ames Research Center for which all model parameters are reported [21] and a similar, but less general, numerical solver that is described by Karabeyoglu et al. [105]. The agreement between the two solvers is compelling. Furthermore, the present solver reproduces the experimental measurements as shown in Fig. 4.4, indicating that the core functionality of the code is correct. Auxiliary functionalities of the code, such as the curve-fitting subroutine or the ability to process multiple space-time averaged data sets in addition to locally-resolved data from a single motor firing, are also verified by running calibration cases and examining all of the outputs to check for consistency with the baseline data.

In addition to the numerical solutions published by Karabeyoglu et al. [105], a closed-form analytical solution to the regression problem that is presented in the same paper and later generalized by Cantwell [26] provides another point of comparison. For a traditional motor whose regression rate may be described by Marxman's model with a mass flux exponent of $n = 0.5$ exactly, the regression rate may be integrated analytically to produce an expression for the fuel position as a function of axial distance only:

$$r = \left[r_0^2 + \frac{8a}{\sqrt{\pi}} x^m t_b \left(\sqrt{\dot{m}_{\mathrm{ox}}} + \frac{\sqrt{\pi} a \rho_{\mathrm{f}}}{m+1} x^{2m+1} \right) \right]^{\frac{1}{2}} \tag{4.18}$$

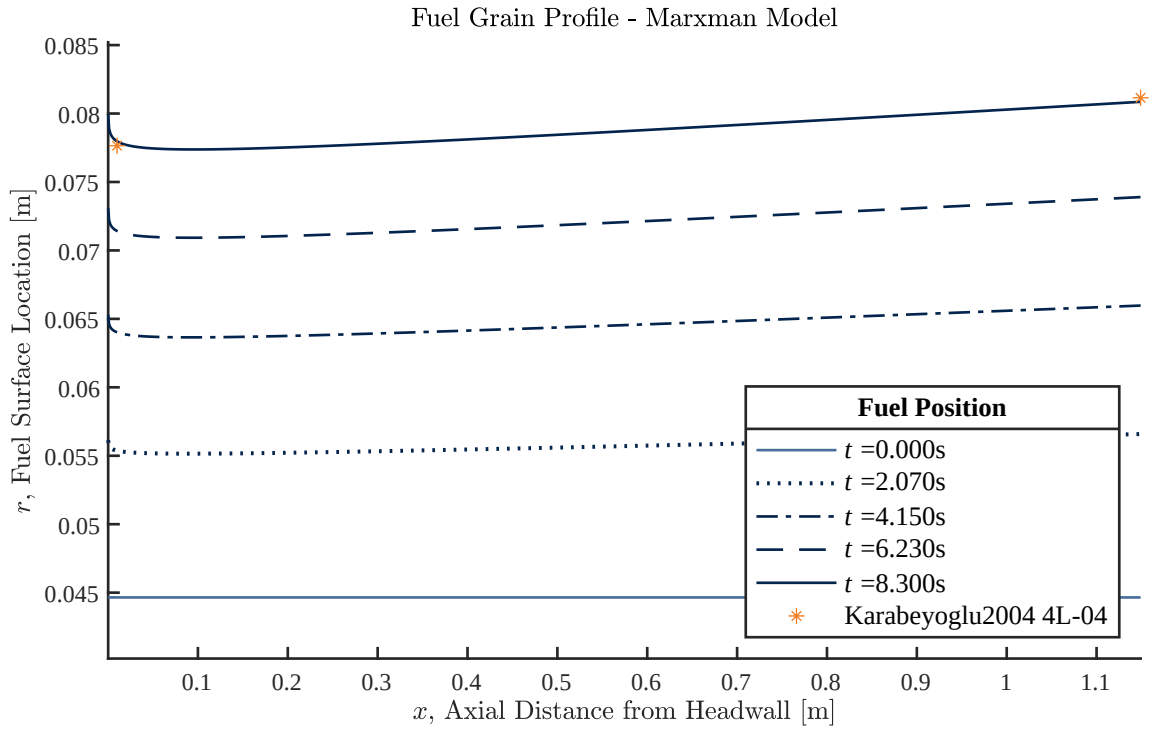

Figure 4.4. Comparison of the prediction generated by the code described in this chapter with the data points at either end of the motor taken from Ref. [21].

where r_0 denotes the initial inner radius of the fuel grain in the above. Figure 4.5 compares the output of the numerical solver to this analytical solution for a hypothetical motor with an initial inner diameter of 0.10 m, a length of 1.149 m, a constant oxidizer mass flow rate of 4.5 kg/s, a total burn time of 20 s, and coefficients $a = 9.36 \cdot 10^{-5}$, $n = 0.5$, and $m = -0.015$.

4.3 Model Validation

With a working numerical solver in hand, it is now possible to evaluate the model given by Eq. (4.15) by comparing its predictions to test data reported in the open literature by Tamura et al. [29], Yuasa et al. [43], Yuasa et al. [4], and Sakurai et al. [44]. Table 4.1 summarizes the relevant motor characteristics for the locally-resolved data, where each data set consists of a paired set of x and $\dot{r}$ or r values for a single motor. Table 4.2 describes the averaged data sets, where average G_{ox} versus average $\dot{r}$ values are reported for motors at different mass flux conditions. Because all of the data stems from measurements by the HRrWG, the scale and swirl strength of the motors are generally quite similar for the locally resolved data. However, these

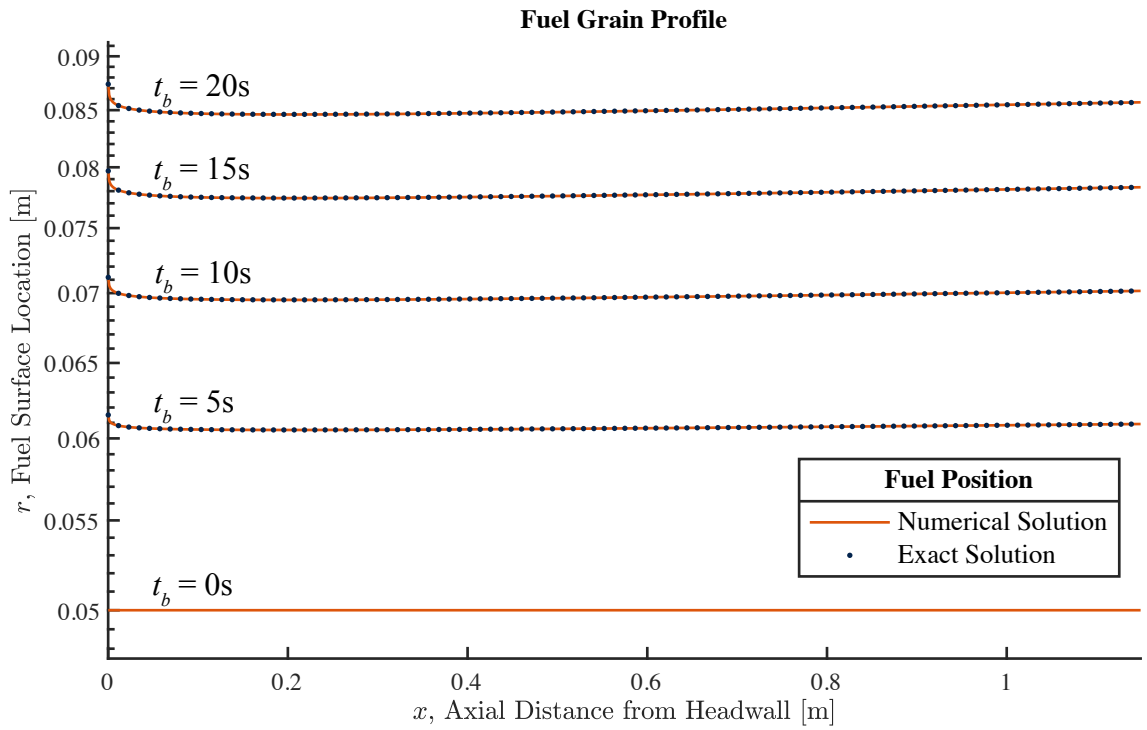

Figure 4.5. Comparison of the predictions generated by the code described in this chapter with the exact analytical solution for motors with $n = 0.5$ from Ref. [21] for a selection of burn times.

measurements provide the opportunity to evaluate the local trends predicted by the regression rate model. As will be seen, the overall averaged data provide a clear reference for the effect of increasing swirl number or oxidizer mass flux.

Operating parameters are taken directly from the published sources when possible. When a necessary value is not disclosed, it is calculated or estimated from other reported values and the corresponding entry in Tables 4.1–4.2 is preceded by a "∼" to indicate the estimation. Data sets that require the estimation of multiple critical parameters are discarded to improve confidence in the validation process, although some error is undoubtably still introduced through the estimation of any parameter. In particular, broad statements about typical burn times lead to what is probably the largest source of uncertainty in the values used to replicate the test results. In general, the results of any simulation based on the data presented in Tables 4.1–4.2 are expected to have precision no better than several percent. This situation arises not just from the errors introduced in estimating values, but also from simplifications in the regression model and from significant scatter in the data themselves. By way of example, the local data sets from

Table 4.1. Summary of axially-resolved SOFT motor data for model validation

Dataset Name	Fuel	$\dot{m}_{ox}$ [kg/s]	L [m]	D_0 [m]	Sg	t_b [s]	P_c [MPa]
Sakurai2017 3-1	PP	0.459	0.970	0.056	19.4	8.8	1.43
Sakurai2017 3-2	PP	0.417	0.970	0.056	19.4	19.6	1.26
Sakurai2017 4-1,3	PP	1.325	0.970	0.056	19.4	6.0	2.76
Sakurai2017 5-1	PP	1.208	0.970	0.056	19.4	4.4	2.58
Sakurai2017 6-1	PP	1.140	0.970	0.056	19.4	9.3	2.13
Tamura1999 L0A	PMMA	0.022	0.150	0.040	0	~8	~0.52
Tamura1999 L0B	PMMA	0.022	0.450	0.040	0	~8	~0.52
Tamura1999 L9.7A	PMMA	0.022	0.150	0.040	9.7	~8	~0.52
Tamura1999 L9.7B	PMMA	0.022	0.450	0.040	9.7	~8	~0.52
Yuasa2001 L0	PMMA	0.090	0.500	0.040	0	~8	3.30
Yuasa2001 L9.7	PMMA	0.090	0.500	0.040	9.7	~8	3.30
Yuasa2001 L19.4	PMMA	0.090	0.500	0.040	19.4	~8	3.30
Yuasa2012 L01	PP	~0.314	1.000	0.040	19.4	4.7	3.90
Yuasa2012 L02	PP	~0.306	1.000	0.040	19.4	6.8	3.90
Yuasa2012 L03	PP	~0.211	0.600	0.040	19.4	7.9	2.12
Yuasa2012 L04	PP	~0.217	0.600	0.040	19.4	12.0	2.12
Yuasa2012 L05	PP	~0.212	0.600	0.040	19.4	15.9	2.12
Yuasa2012 L06	PP	~0.115	0.600	0.040	19.4	6.8	1.18
Yuasa2012 L07	PP	~0.119	0.600	0.040	19.4	14.8	1.18
Yuasa2012 L08	PP	~0.117	0.600	0.040	19.4	25.0	1.18

Yuasa et al. [4] and Sakurai et al. [44] display average, normalized root-mean-squared errors of around 10-15% when compared to self-calibrated lines of best fit.

4.3.1 Model Calibration

The validation process begins by calibrating the model to a zero-swirl case, so that the values of a, m, and n in Marxman's model can be determined. While it is difficult to identify a single, unique set of parameters that describes a motor in an objectively "best" sense, some valid sets are nonetheless manifestly better than others. A combination of automatic curve-fitting with manual guidance and adjustment proves useful in finding these values. Automatic curve-fitting is used with a locally-resolved data set in order to determine the general range of acceptable values for each parameter, and then the parameters are tuned manually so that they accurately reproduce the calibration data while avoiding potential pitfalls. One frequent issue is that the calibration routine tries to reduce the *average* error and does not always capture local trends very well. In addition, it will occasionally select values that, despite producing a good fit to the

Table 4.2. Summary of space-time-averaged SOFT motor data for model validation

Dataset Name	Fuel	G_{ox} [kg/(m^{2}s)]	L [m]	D_0 [m]	Sg	t_b [s]	P_c [MPa]
Tamura1999 Sg0	PMMA	11.5 - 22.2	0.150	0.040	0	~8	~0.52
Tamura1999 Sg7.1	PMMA	11.4 - 21.6	0.150	0.040	7.1	~8	~0.52
Tamura1999 Sg9.7	PMMA	11.3 - 22.1	0.150	0.040	9.7	~8	~0.52
Tamura1999 Sg19.4	PMMA	11.6 - 22.5	0.150	0.040	19.4	~8	~0.52
Tamura1999 Sg32.3	PMMA	11.4 - 21.6	0.150	0.040	32.3	~8	~0.52
Yuasa2001 Sg0	PMMA	43.0 - 63.4	0.500	0.040	0	~8	3.30
Yuasa2001 Sg9.7	PMMA	37.9 - 55.3	0.500	0.040	9.7	~8	3.30
Yuasa2001 Sg19.4	PMMA	36.9 - 55.6	0.500	0.040	19.4	~8	3.30

data, are physically unlikely or even impossible. In general, the process for manually adjusting the calibration coefficients proceeds as follows: the parameters are initialized based on values from an automated curve fit, and then the length exponent m is set to a fixed value, typically between -0.2 and 0, since the numerical fitting routine often provides unrealisticly large negative values for m. At this point, the muliple operating conditions represented by a single zero-swirl G_{ox} versus $\dot{r}$ dataset are leveraged to adjust the mass flux exponent n, since the slope of the data points on a logarithmic plot roughly corresponds to the correct exponent. With m fixed and n adjusted to match the slope of the data, a is determined based on the $\dot{r}$ intercept so that the prediction is anchored in the right place. Finally, the calibration is compared to a set of local data from an identical motor, if possible, to judge whether the axial trend is acceptable. If it is not, m is adjusted appropriately and the process is repeated.

Owing to the similarity in design and fuel of most of the test motors, only a few calibrations are required. Most of the data is based on calibration to space-time-averaged data from Tamura et al. [29]. It is worth noting that a pair of zero-swirl axially-resolved tests are also reported in Ref. [29], and these require a different value of a that is significantly higher. The axially-resolved data from Sakurai et al. [44] use the same values of n and m as that from [29], but with a larger coefficient. The data from Yuasa et al. [4] are adequately described using the same set of calibration constants as that of Sakurai et al. [44] but display a flatter axial trend. Reducing the value of m to -0.10, with a corresponding increase in a, halves the average error and cuts the RMS error by nearly a third. The data from Yuasa et al. [43] display markedly different axial trends and requires a unique set of calibration constants. In fact, these data are

Table 4.3. Zero-swirl calibration constants for Marxman's model for each dataset

Dataset Source	a	n	m
Sakurai et al. [44]	$1.81 \cdot 10^{-5}$	0.63	−0.20
Tamura et al. [29]	$1.25 \cdot 10^{-5}$ (Averaged), $1.61 \cdot 10^{-5}$ (Local)	0.63	−0.20
Yuasa et al. [43]	$1.07 \cdot 10^{-5}$ (Averaged), $1.13 \cdot 10^{-5}$ (Local)	0.8	0.00
Yuasa et al. [4]	$1.95 \cdot 10^{-5}$	0.63	−0.10

Table 4.4. Average error between Eq. (4.15), with n_1 = 0.3, and test data

Dataset Name	Average Relative Error [%]	Average Relative RMS Error [%]
Tamura1999 Sg0	0.01	1.27
Tamura1999 Sg7.1	0.20	2.43
Tamura1999 Sg9.7	5.35	6.59
Tamura1999 Sg19.4	13.76	14.15
Tamura1999 Sg32.3	23.18	23.64

not particularly well represented by Marxman's model using any reasonable set of constants. This situation underscores the usefulness of a correction-type swirl model, where the influence of the swirl strength can be explored independently of the base model. Table 4.3 enumerates the various calibration constants used and the datasets that they describe. The units assigned to the constants are such that all model inputs and outputs correspond to base SI units; for example, providing a mass flux in $\mathrm{kg}/(\mathrm{m}^2\ \mathrm{s})$ and a length in meters returns a regression rate in m/s.

4.3.2 Swirl Modifier Adjustments

With the model constants calibrated for zero-swirl cases, evaluating the efficacy of the new regression rate model for swirl-driven rockets is as simple as changing the data input files for the code to those of known swirling cases. Figure 4.6 shows the baseline zero-swirl case (Tamura1999 Sg0) that is used to calibrate the majority of the test data, while Figs. 4.7–4.10 show the results of applying Eq. (4.15) to similar motors with geometric swirl numbers ranging from 7.1 to 32.3. In each of these figures, the solid line represents Eq. (4.15), where the values of a, n, and m are set by calibration to the zero-swirl case and n_1 is set to the theoretically predicted value of 0.3.

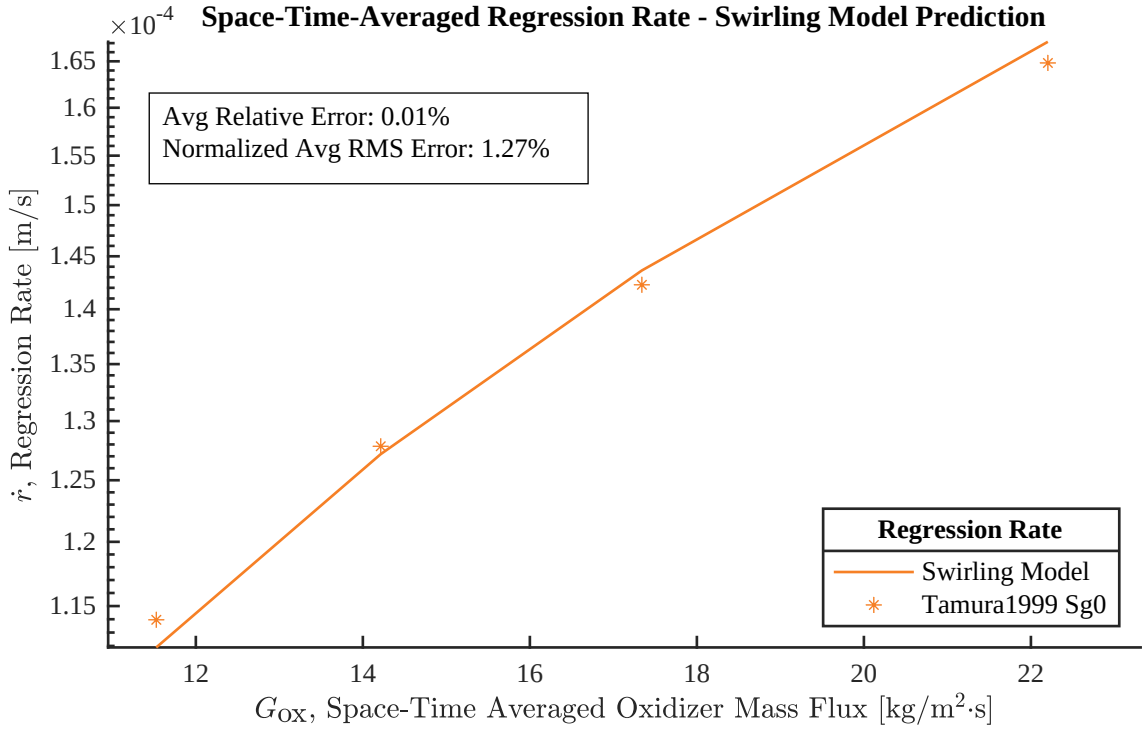

Figure 4.6. Regression rate prediction compared to "Tamura1999 Sg0" test data from four identical, axial-flow motors operating at different oxidizer mass flux conditions. This case is used to calibrate constants for the remainder of the data from [29] as well as data from [4] and [44]. Note that the swirling model is identical to Marxman's model when the swirl strength is zero.

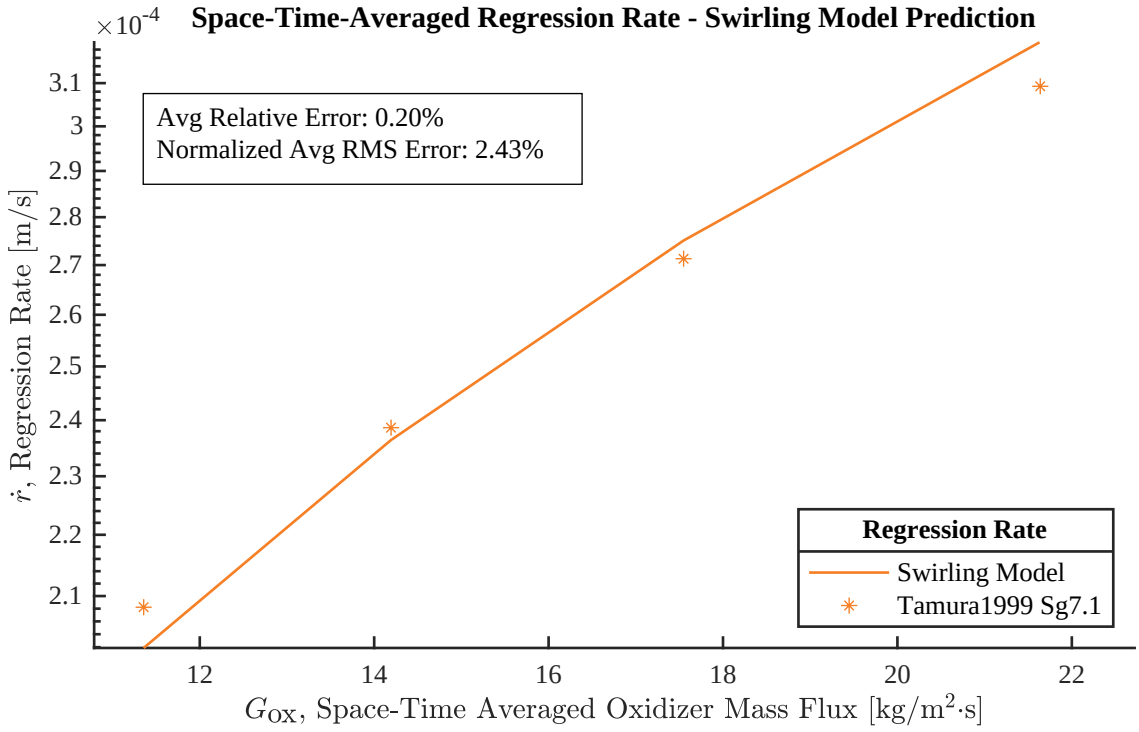

Figure 4.7. Regression rate prediction compared to "Tamura1999 Sg7.1" test data with a geometric swirl number of 7.1.

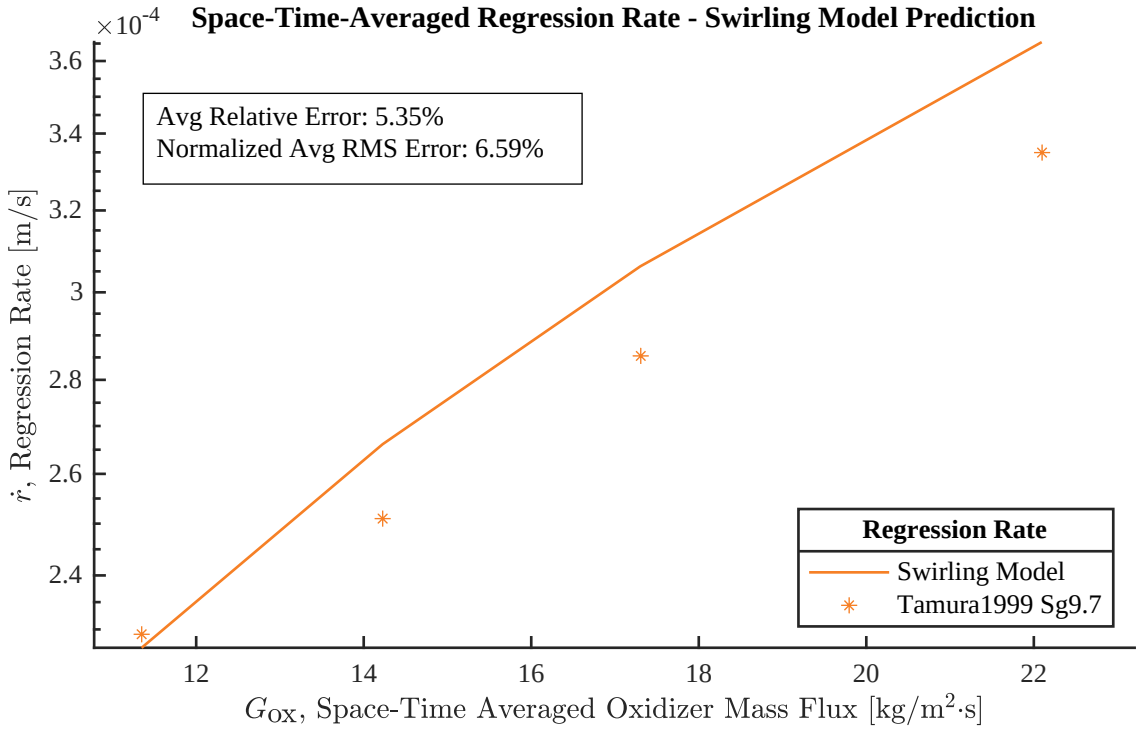

Figure 4.8. Regression rate prediction compared to "Tamura1999 Sg9.7" test data with a geometric swirl number of 9.7.

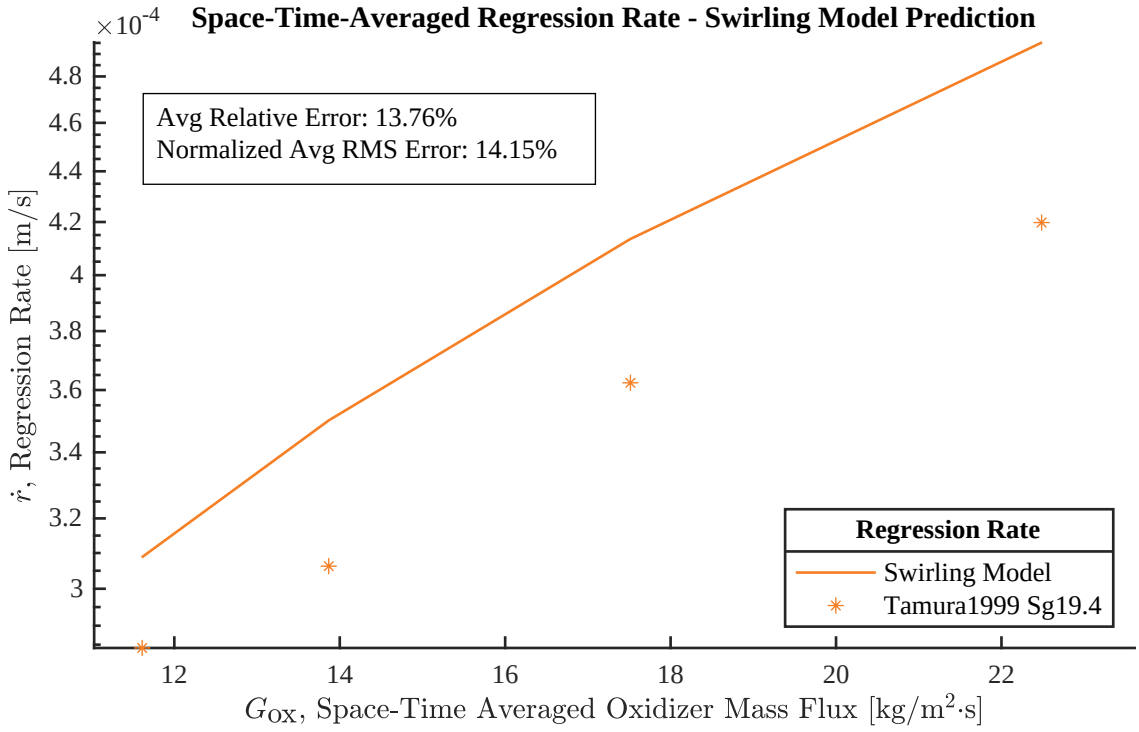

Figure 4.9. Regression rate prediction compared to "Tamura1999 Sg19.4" test data with a geometric swirl number of 19.4.

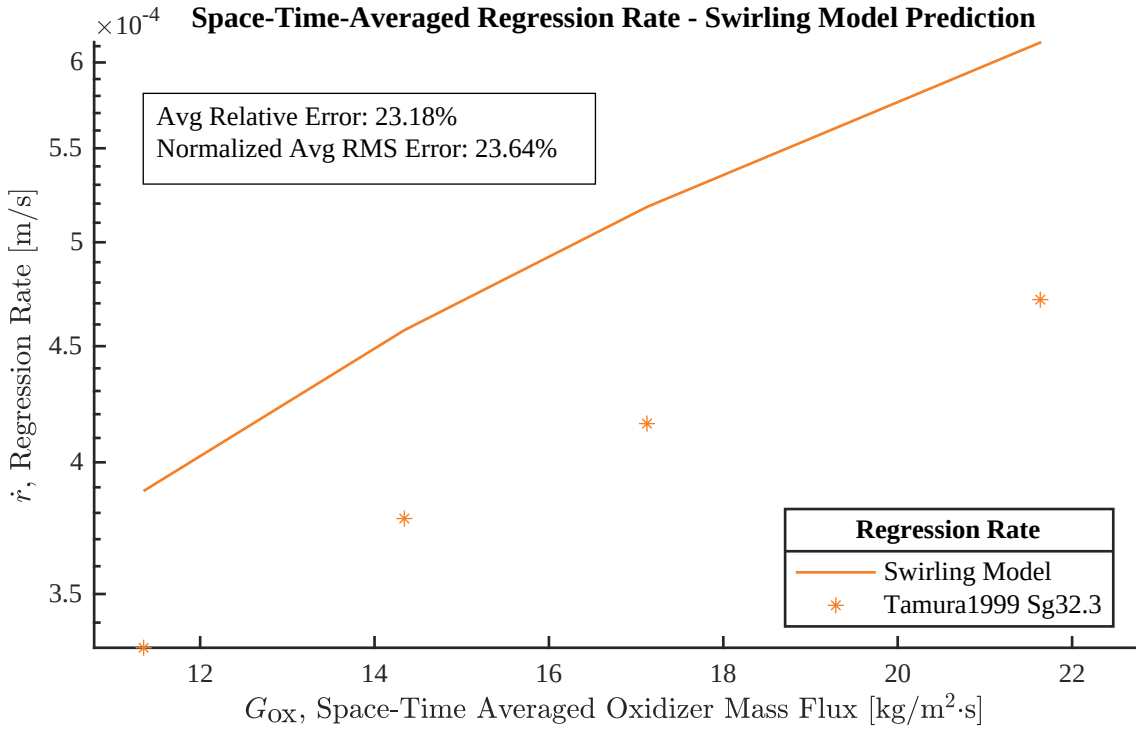

Figure 4.10. Regression rate prediction compared to "Tamura1999 Sg32.3" test data with a geometric swirl number of 32.2.

Table 4.4 summarizes the error statistics for all five of the space-time-averaged data, but it is clear from even a cursory glance at the accompanying figures that the model in its present form overpredicts the regression rate in a systematic fashion. For motors with a geometric swirl number of 7.1, the prediction is impressively accurate, but the average error grows to 23% for the motors with the strongest swirl injection. It is encouraging, however, that in every case plotted the slopes of the predictions align with the data on logarithmic scales. More importantly, the error grows in a generally linear relationship with the swirl number. This behavior suggests that a modification to the swirl-sensitive portion of the regression rate model may yet provide accurate predictions across a wide range of swirl strengths. In short, the regression model demonstrates dependence on the correct parameters, albeit with slightly skewed scaling. This situation is easily resolved if, as is commonplace with the traditional Marxman model, the constants are altered from their analytically predicted values to bridge the gap between theory and practice. In its most general form, Eq. (4.15) is fairly simple, since the bulk of the detail is absorbed in the formulation of the local swirl number:

$$\dot{r} = aG^n x^m \left[1 + (a_1 S)^2\right]^{n_1} \tag{4.19}$$

Note that the second coefficient a_1, which multiplies the swirl number, can be shown to be equal to $a_1 = 2$ when the assumption of solid-body rotation is made. The deviation of this constant to values with $a_1 < 2$ has already been discussed in the context of the computational simulations by Paccagnella et al. [30]. The latter show that the axial velocity is also affected by the radial pressure gradient, thereby reducing the relative difference between the two components. In practice, the swirl number coefficient a_1 will actually exceed a value of 2 for all of the data considered. This behavior can be attributed to the swirl number's definition as a ratio of velocities in relative rather than absolute terms and the difficulties of modeling a complex, three-dimensional flowfield using a quasi-one-dimensional relation. Marxman's model assumes that the regression rate depends on the mass flux at the boundary layer edge, which, in a traditional axial-flow hybrid, is effectively the bulk, core-flow axial velocity. The swirl modifier term in Eq. (4.19) is based on the assumption that the addition of a tangential velocity component does

Table 4.5. Average relative error [%] between Eq. (4.19) and space-time-averaged test data for a variety of swirl modifier a_1 and n_1 pairs. All other constants remain unchanged from their values in Table 4.3

Dataset Name	$\left[1 + (2S)^2\right]^{0.3}$	$\left[1 + (2S)^2\right]^{0.2}$	$\left[1 + (3S)^2\right]^{0.2}$	$\left[1 + (3.75S)^2\right]^{0.18}$
Tamura1999 Sg0	0.01	0.01	0.01	0.01
Tamura1999 Sg7.1	0.20	-14.85	-3.85	-2.12
Tamura1999 Sg9.7	5.35	-13.11	-1.32	-0.09
Tamura1999 Sg19.4	13.76	-13.53	-0.81	-1.12
Tamura1999 Sg32.3	23.18	-13.18	0.22	-1.45

not change the physics of heat transfer and mass diffusion between the flame and the wall, except by altering the effective mass flux within the port proportionally to the swirl number. While this assumption generally holds true, it remains valid only to the extent that the assumptions underlying the velocity model are upheld. In the case of strong swirl injection, it is well-documented that a recirculation zone forms at the center of the chamber where the pressure is relatively low. With reverse flow occupying the center of the chamber, the bulk of the mass flow must pass through an area-restricted annular zone in the vicinity of the wall, thus increasing the effective mass flux at the boundary layer edge. This increase, while critical to the fuel regression rate, is not properly reflected in the swirl number formulation since both velocity components adjust simultaneously to the changing area. Neither is it readily incorporated into the present, quasi-one-dimensional form of the SOFT motor velocity model itself, as is the flow acceleration due to heating. Thus, there is a sound theoretical justification for a second coefficient that increases the effective mass flux in a swirling motor in much the same way as the swirl number itself. As for the variance in n_1, it stems from the same myriad of real-world considerations that rarely produce an axial motor with a mass flux exponent of precisely 0.8 and a length exponent of -0.2. In short, neither Marxman's model nor the proposed swirl correction can offer reliably accurate predictions of the regression rate in a motor when based solely on theoretical values, nonetheless, this limitation has not prevented the traditional model from becoming the gold standard for casting regression rate expressions for over five decades.

The results shown earlier in Figs. 4.7–4.10 for the Tamura1999 datasets are therefore revisited in Table 4.5 along with several other choices for a_1 and n_1 that incrementally improve upon the accuracy of the model. Decreasing the exponent on the modifier from 0.3 to 0.2

Table 4.6. Average error between Eq. (4.19), with $a_1 = 3.75$ and $n_1 = 0.18$, and space-time-averaged test data. All other constants remain unchanged from their values in Table 4.3

Dataset Name	Average Relative Error [%]	Average Relative RMS Error [%]
Tamura1999 Sg0	0.01	1.27
Tamura1999 Sg7.1	-2.12	2.75
Tamura1999 Sg9.7	-0.09	3.04
Tamura1999 Sg19.4	-1.12	2.46
Tamura1999 Sg32.3	-1.45	3.36
Yuasa2001 Sg0	0.42	1.18
Yuasa2001 Sg9.7	-11.61	11.64
Yuasa2001 Sg19.4	-10.39	10.44

produces a consistent underprediction, as shown in the middle column. Subsequently increasing the coefficient from 2 to 3 returns the predictions to the proper range of values. The final set of constants, $a_1 = 3.75$ and $n_1 = 0.18$, offer a small improvement and bring the overall average error across all swirl numbers to around one percent. Further improvement is undoubtedly possible, but the error displayed by this form of the correction term drops to a level that falls well within the estimated uncertainty of the model.

4.3.3 Evaluation of Swirling Model Using Space-Time-Averaged Data

Table 4.6 contains error information for all eight of the space-time-averaged data available, and a full set of accompanying plots are available in Appendix B. The swirl model employed with great success for the Tamura et al. [29] data underpredicts the space-time-averaged data from Yuasa et al. [43] by approximately 12.5%. Encouragingly, it is consistent in its underprediction across both of the available non-zero swirl numbers. This behavior seems to suggest that the swirl modifier's exponent is correct for these datasets as well, or nearly so. The difference could be made up either by an increase in the coefficient a_1 or with a fixed increase to the swirl modifier term. By way of example, increasing a_1 from 3.75 to 5.3, while leaving all other constants fixed, leads to average simple and RMS errors of -0.27% and 0.96% for the case of $Sg = 9.7$. This produces simple and RMS errors of 2.07% and 2.36% for the case of $Sg = 19.4$. On the other hand, retaining $a_1 = 3.75$ and augmenting the swirl modifier by a fixed 12.5% yields error values of -0.24% and 0.92% for $Sg = 9.7$; and 1.57% and 1.93% for $Sg = 19.4$. It is thus difficult to state with certainty which of these methods is more appropriate based on the

Table 4.7. Average error between Eq. (4.19), with $a_1 = 3.75$ and $n_1 = 0.18$, and locally resolved test data. All other constants remain unchanged from their values in Table 4.3

Dataset Name	Average Relative Error [%]	Average Relative RMS Error [%]
Sakurai2017 3-1	5.70	17.59
Sakurai2017 3-2	-0.64	16.57
Sakurai2017 4-1,3	-0.21	15.96
Sakurai2017 5-1	-6.51	11.14
Sakurai2017 6-1	1.95	22.13
Tamura1999 L0A	0.35	13.20
Tamura1999 L0B	25.95	37.32
Tamura1999 L9.7A	0.33	4.29
Tamura1999 L9.7B	-7.55	10.20
Yuasa2001 L0	-0.29	14.95
Yuasa2001 L9.7	-1.68	6.92
Yuasa2001 L19.4	-1.24	2.94
Yuasa2012 L01	-7.61	14.85
Yuasa2012 L02	-6.42	12.36
Yuasa2012 L03	0.23	17.12
Yuasa2012 L04	2.74	18.99
Yuasa2012 L05	0.06	9.87
Yuasa2012 L06	17.35	44.07
Yuasa2012 L07	8.29	18.57
Yuasa2012 L08	4.24	11.54

data alone. One way or another, there must be some effect that is either not incorporated in the present regression model at all or that differs significantly from one motor configuration to the other. This behavior, which is still unexplained, further underscores the difficulties of describing different motors with a unified expression and the importance of understanding the source of the constant a_1. On the bright side, the consistency of the exponent n_1 between different motors strengthens the argument in favor of a unified swirl modifier in the form of Eq. (4.19).

4.3.4 Evaluation of Swirling Model Using Locally-Resolved Data

It is now time to test the swirl correction term on locally-resolved data, where the extra effort that has gone into modeling the velocity field can prove its worth. Table 4.7 lists the normalized, average errors and the normalized, average RMS errors for the full range of locally-resolved data available. Two of the tests ("Tamura1999 L0A" and "Yuasa2001 Sg0") correspond to axial-flow cases used for calibrating the axial exponent m. Sixteen of the remaining eighteen

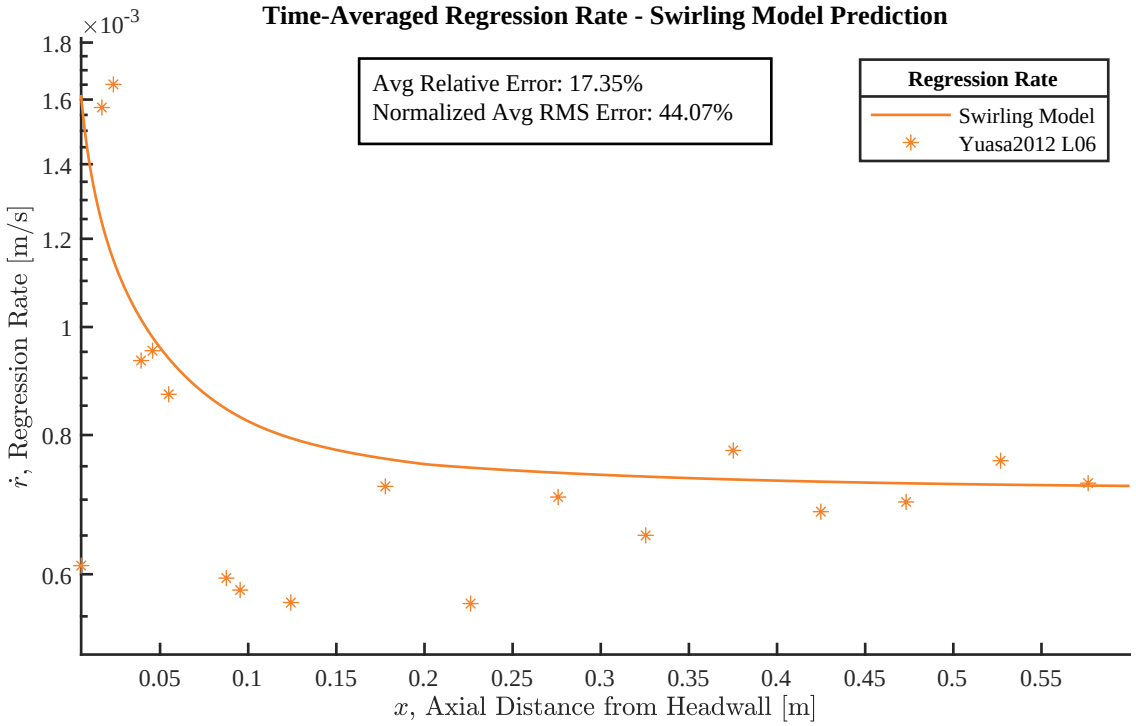

Figure 4.11. Regression rate prediction compared to "Yuasa2012 L06" test data.

predictions possess single-digit average relative errors, with eight of the cases falling under 2% (excluding those used for calibration). This is a definite improvement over existing locally-resolved regression models for swirl driven motors, especially considering the conceptual simplicity of the present swirl modifier and the greater number of data points employed in comparison to other studies. Interestingly, the case with the highest error is actually an axial-flow test ("Tamura1999 L0B") that is not self-calibrated, where the proposed swirl modifier plays no role in the regression prediction whatsoever. It may thus be ignored as unimportant for the purposes of validating the new swirl modifier term.

The other predicition with an above-average error, "Yuasa2012 L06" is shown in Fig. 4.11. Qualitatively, the prediciton is not unreasonable. It splits the difference between the two clusters of higher regression values near the injector before flattening out at the correct level in the aft region. The high error stems from a handful of outliers in the upstream half of the grain that are bypassed by the prediction. It is difficult to ascertain with certainty whether these points are genuine representations of the wider trend on account of the highly-scattered nature of the data. Certainly, the surface of this test motor post-firing is quite irregular. In fact, removing the four

data points with regression rate values below 0.65 mm/s results in a prediction with average simple and RMS errors of −0.70% and 11.97%, respectively. It is therefore encouraging to note that even the least precise prediction made by the proposed regression rate model leads to an acceptable error margin.

Overall, the trends predicted by Eq. (4.19) are fair qualitatively as well as quantitatively, with some cases matching very well while others exhibit localized deficiencies. A full set of the $\dot{r}$ versus x plots for every dataset in Table 4.7 may be found in Appendix C, but several are reproduced here for convenience. Figure 4.12 is representative of the results for data from Sakurai et al. [44], which is generally less scattered with a steep axial drop across the chamber that flattens to about half of the initial value. These data, along with many of those from Yuasa et al. [4], display a characteristic dip in values 20-30% of the way down the chamber. The source of this dip is not definitively established and it appears in some data sets while remaining absent from others. One possibility is that the structure of the flow is disrupted immediately downstream of the central recirculation zone similarly to the effect noted by Franco et al. [101] in the wake of expansions in the actual port or casing geometry.

According to this theory, the variation of the local flow and regression rate are outlined as follows. The flow enters the chamber with a very high swirl number imparted by the injectors, producing the high regression rates that typify the head end. The swirl number begins to drop immediately as the flow accelerates due to heating and the axial velocity diverges from zero, leading to a steep decline in regression rates over the first quarter of the port as seen in region II of Fig. 4.12. Meanwhile, the pressure gradient due to swirl injection leads to a central recirculation zone that occupies the area near the injectors, forcing the majority of the flow through a smaller, annular area. This is assumed to account for the independent scaling constant a_1 in Eq. (4.19), since this side effect of swirl modifies the effective mass flux outside of the swirl-number-resultant-velocity framework that defines the rest of the regression model. At the rear of the recirculation zone, the flow moves radially inward as the swirl velocity begins to decrease, reducing the centrifugal effect on the fluid. Some of the flow is drawn back to the head end of the motor by the pressure difference, while the majority continues downstream. While the effect at the termination of the recircualtion zone is unlikely to be nearly as sudden or severe

as that observed in the wake of a solid bluff body, it may be sufficient to locally interrupt the swirling structure of the flow, as in region III of Fig. 4.12. As the flow continues downstream past the disturbance and regains coherence, the swirl number briefly increases in response to the increase in available cross-sectional area, leading to the sudden rise in regression rate seen in region IV of Fig. 4.12. As flow progresses beyond this point to region V of Fig. 4.12, the assumption of a radially uniform flow is more applicable, explaining the consistent match between the trendlines of the theoretical predicitions and experimental data in the aft of nearly all of the locally-resolved cases studied. This also accords well with the findings of Yuasa et al. [4] and Sakurai et al. [44], who are able to correlate a simple mass flux modification only in the aft region. In fact, their focus on the turbulent wall jet structure in the injection region can be viewed as an alternative interpretation of the same influence of the mass concentration near the walls in this zone. As a final note, the lower regression rate value often encountered as an obvious outlier at the leading edge of the grain likely develops as the grain regresses beyond the injection plate with time, creating a small backward-facing step and another, much smaller recirculation zone. The leading edge of the grain, which now occupies the corner of this low-velocity pocket, sees a severely reduced mass flux compared to the flow just beyond. This is represented by region I in Fig. 4.12. The regression rate in this pocket may still be higher than the average value due to a high oxygen concentration and the entrainment of hot gasses – or it may be lower, depending on the local flow structure, motor design, and burn time.

The results shown in Fig. 4.13 for the "Tamura1999 L9.7A" test data exemplify the strength of the model from the standpoint of predicting axially-resolved data in addition to averaged values. Since this data comes from a test campaign that produces ample calibration data, it is gratifying to see that the overall error is so low and that the axial prediction trend stands in perfect agreement with that of the data. This case demonstrates that, when the model is well-calibrated, it performs admirably.

The last set of data that merit special attention here are those from Yuasa et al. [43]. These measurements are also used by Ozawa and Shimada [74] to validate their model, which is among the best that are presently available in the open literature. Their model is notable for also relying on a temperature distribution along the port in order to approximate the change in local

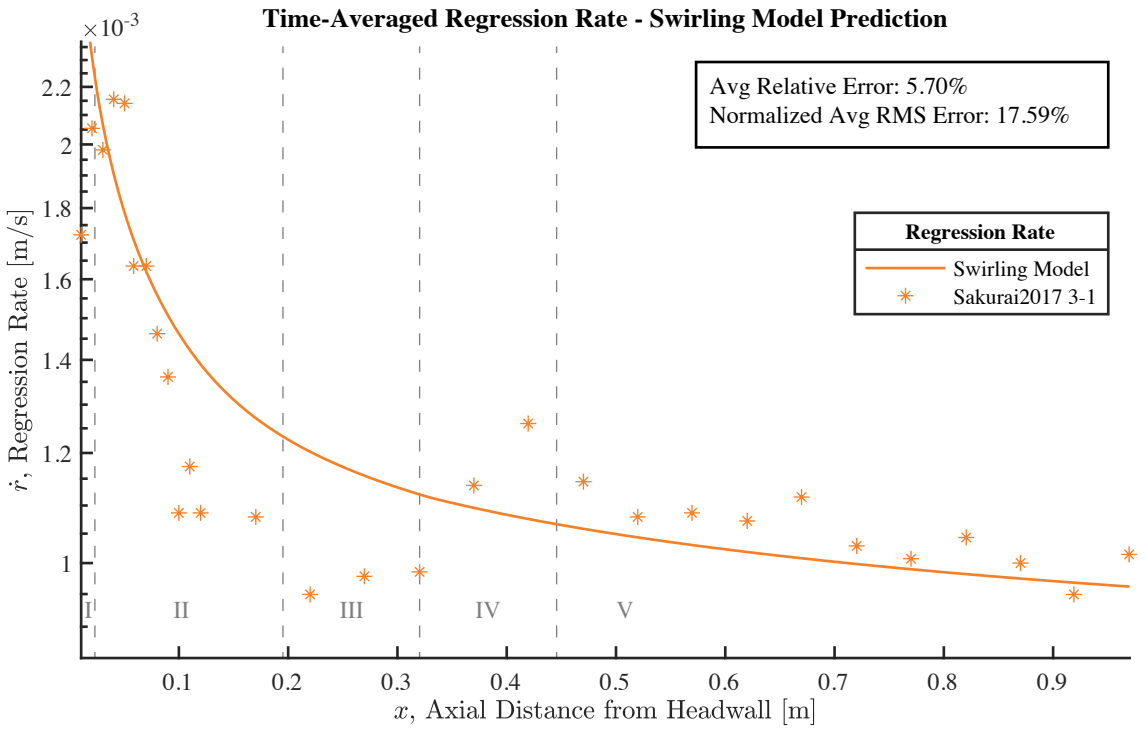

Figure 4.12. Regression rate prediction compared to "Sakurai2017 3-1" test data. Regions denoting the approximate extent of observed and hypothesized flow phenomena are denoted with dashed lines and roman numerals.

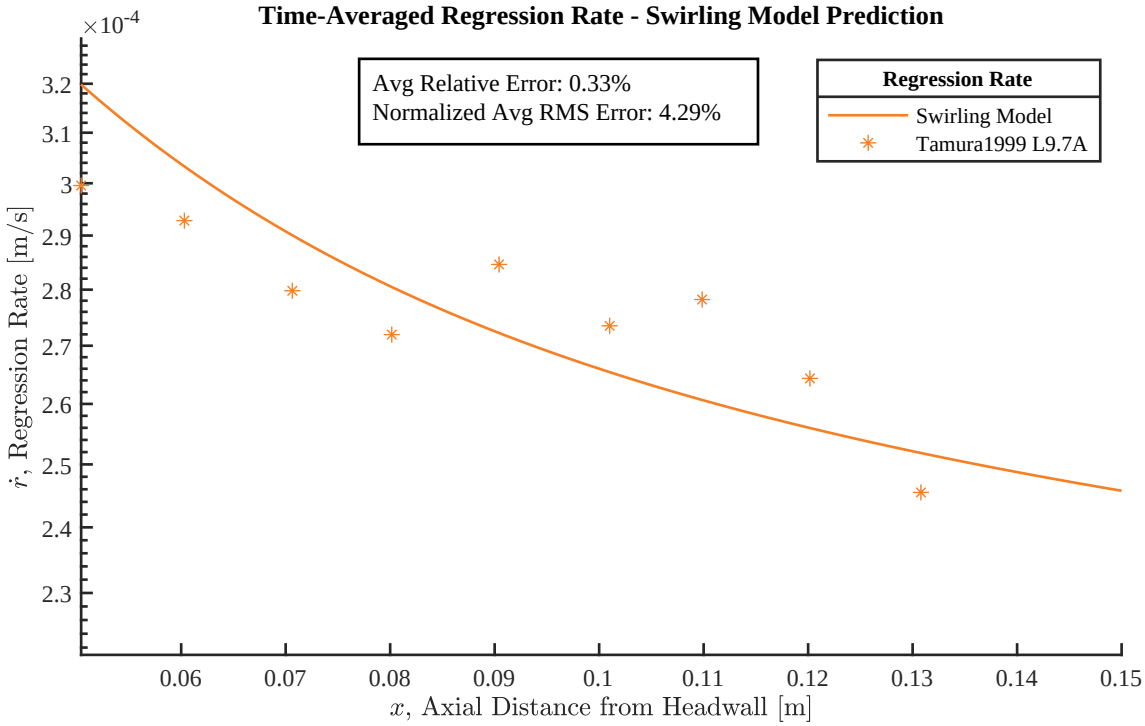

Figure 4.13. Regression rate prediction compared to "Tamura1999 L9.7A" test data.

regression rate. A more in-depth discussion of their model, including a simplified statement of the final result, may be found in Sec. 3.2.4. For the present study, the zero swirl "Yuasa2001 L0" test is used to calibrate Marxman's model, with the resulting constants directly applied to the prediction of the remaning two tests. Neither Marxman's model nor Ozawa and Shimada's model predict the axial test data very well, although the latter does produce a more reasonable trend, as shown in Fig. 4.14. Considering how poorly Marxman's model characterizes the axial trend of the zero-swirl case, the results of applying the swirling flow model to the swirling test data are incredible. At both swirl strengths, the average error is less than 2%. Figure 4.15 demonstrates that at the intermediate swirl strength, both the proposed modifier and the model by Ozawa and Shimada produce good trends, with the former being slightly more accurate over the first half of the grain and the latter showing a slight edge in accuracy afterward. The prediction by Ozawa and Shimada is quite impressive in this case, with an overall error just under 1% and an RMS error below that of the new swirl modifier formulation. For the stronger swirl case shown in Fig. 4.16, the proposed swirl model displays a better trend throughout the port as evidenced objectively by the significantly lower RMS error. Overall, Figs. 4.14–4.16 demonstrate that the proposed model is at least as reliable as the current state of the art, and Appendix C provides proof that the model shows favorable agreement with a much wider variety of data than has been demonstrated by almost any other swirl-sensitive model.

4.4 Summary

In summary, the proposed swirl modifier term for regression rate modeling in SOFT motors is based on the concept that introducing swirl to a hybrid motor merely augments the effective mass flux in the port. This framework allows for a description based on the traditional model developed by Marxman and his colleagues, which continues to find widespread use due to its simplicity and utility. By treating the swirling regression problem as a question of effective mass flux, the difficulty of describing the heat transfer rate is transmuted into a requirement that the velocity field must be characterized throughout the chamber. At a high level, this results in a simple swirl modifier term that is largely independent of the base regression model employed and highly adaptable to the flowfields associated with a variety of motor configurations. The application

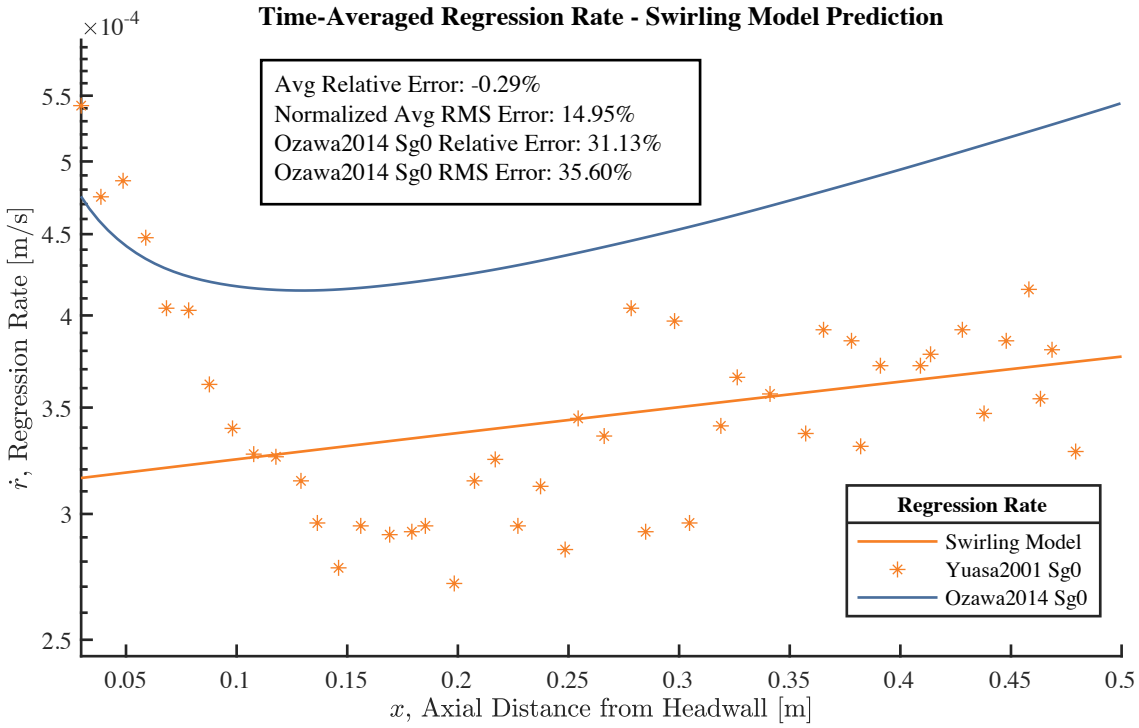

Figure 4.14. Regression rate prediction compared to "Yuasa2001 L0" test data, as well as the regression model of Ozawa and Shimada [74].

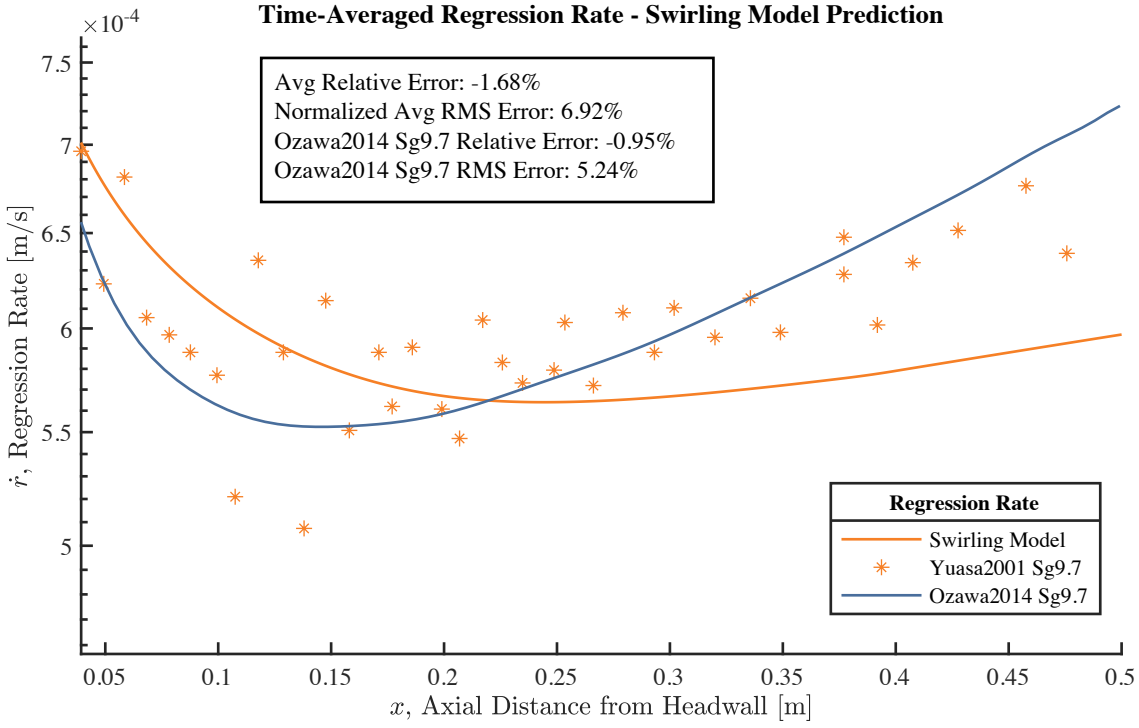

Figure 4.15. Regression rate prediction compared to "Yuasa2001 L9.7" test data, as well as the regression model of Ozawa and Shimada [74].

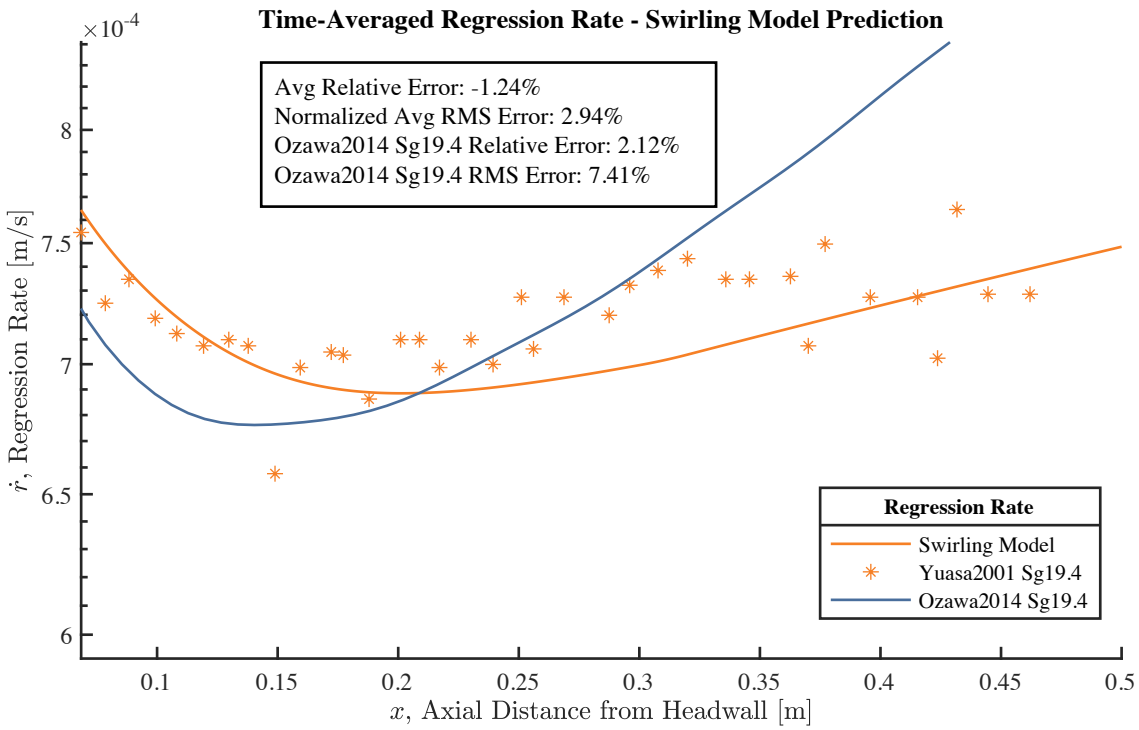

Figure 4.16. Regression rate prediction compared to "Yuasa2001 L19.4" test data, as well as the regression model of Ozawa and Shimada [74].

of the compressible continuity equation, combined with a rudimentary set of chemical reaction models, proves sufficient to create a satisfactory flowfield model for engines with unidirectional swirling flow. A numerical simulation scheme then enables detailed predictions of the regression rate for a variety of motor operating conditions. These simulations show that when Marxman's model is properly calibrated to an appropriate non-swirling test firing, the addition of the swirl modifier term produces predictions that agree remarkably well with experimental data collected by several other researchers. Finally, the proposed swirl modifier is compared directly to the leading regression rate model in the literature and compares favorably, matching or even outperforming the existing predictions in each of the cases examined. With the new regression rate model thoroughly validated for a common motor configuration, it is now time to extend its application to other swirl-dominated hybrid rocket engines.

Chapter 5

Beltramian Solution for Cyclonically Driven Hybrids

Despite early research being rooted in industrial cyclonic separation processes [106–110], bidirectional vortex flowfields have been of particular interest to the propulsion community for nearly three decades. Prominent examples of specifically bidirectional vortex engine configurations include the Vortex Injection Hybrid Rocket Engine (VIHRE) [36] and the Vortex Combustion Cold-Wall Chamber (VCCWC) [40]. Several other vortex-fired engine and burner designs have been explored, including the Vortex Universal Stoichiometric Preburner [37] and the In-Situ Resource Utilization propellant end burner [42]. In addition to these specialized vortex designs, several investigations have been undertaken to characterize the effects of swirled injection of oxidizers in both novel and conventional hybrid motor configurations (see, for example, Lee et al. [46] and Yuasa et al. [43]).

This chapter draws on the cumulative progress of a series of bidirectional vortex models that began with Vyas and Majdalani [111] and their formal solution for the bulk gaseous motion of a cyclonically-driven, wall-bounded flowfield. This profile was derived in the absence of either sidewall or headwall mass addition. Nonetheless, the resulting flowfield gave rise to several sequels that presented both linear and nonlinear solutions in spherical geometry [112] as well as inner core corrections to the original solution [113, 114]. The latter two investigations employed either viscous boundary layer or constant shear stress models to overcome the problem's intrinsic singularity at the chamber's centerline. Several related studies followed, and these extended the analysis of bidirectional vortices to incorporate the effects of sidewall injection [17] as well as small viscosity [115]. These were based on the traditional use of the vorticity-streamfunction approach in concert with the viscous momentum equations.

Then using the Bragg-Hawthorne equation as a starting point, a new class of Beltramian solutions was developed by Majdalani [116, 117]; the corresponding models would immediately form the basis of a dedicated series of studies aimed at investigating the so-called Trkalian and Beltramian types of motions, namely, those exhibiting velocity vectors parallel to their corresponding vorticities. Among them were models that captured the effects of small viscosity[118–120], arbitrary headwall injection [121, 122], compressibility [123, 124], conical wall tapering [125, 126], and the presence of air entrapment [127]. These differed from earlier solutions, which proved to be nearly complex lamellar, having orthonormal velocity and vorticity vectors.

From a practical standpoint, although both complex-lamellar and Beltramian families of solutions describe similar flow configurations, they exhibit noteworthy differences. Foremost among them are a relative increase in speed for the linear Beltramian case and a shift in the mantle location, i.e., the interface between the outer and inner vortex regions along which the axial velocity vanishes [116, 117]. For example, the complex-lamellar solution predicts a normalized mantle location of approximately 0.707, whereas the linear Beltramian solution returns a value of 0.628. Interestingly, classical experiments by Smith [128, 129] report a duality of mantle positions that correspond quite convincingly to the two values just given, thus underscoring the potential usefulness and complementary nature of these two families of solutions. Furthermore, the availability of refined velocity field solutions will aid in other related research efforts that require such expressions, such as the study of multiple concentric vortices in rocket combustion chambers conducted by Wall [130].

In this chapter, the inviscid Beltramian hybrid solution of Majdalani [116] is extended to incorporate the role of viscous effects in the sidewall and core regions. The analysis mirrors that of Fleischmann and Majdalani [96], who performed a comparable analysis of the complex-lamellar flowfield with sidewall mass addition. After a brief review of the former work, a perturbation expansion of the incompressible Navier-Stokes equations is methodically pursued with the aim of producing a simplified set of ordinary differential equations for the motion in the viscous regions. Subsequently, the method of matched-asymptotic expansions is applied to obtain uniformly valid, composite solutions in all spatial directions.

5.1 Problem Formulation

5.1.1 Chamber Geometry

The idealized motor used in this work consists of a cylindrical chamber of length L and inner radius a such that the aspect ratio may be written $l = L/a$. The cylindrical coordinates describing the chamber consist of a z-axis running along the centerline, with positive z in the direction of the outflow or nozzle, a radial coordinate r pointing perpendicularly away from the z-axis, and an azimuthal coordinate θ, which captures the angular rotation about the z-axis according to the right-hand rule. A sketch of the geometry is furnished in Fig. 5.1. The boundary of the chamber at $z = 0$ is impermeable in order to simulate an inert headwall in the analogous hybrid engine while the opposing end has a smaller circular outlet of radius b, which is left open to permit the exhaust products to escape the chamber through a straight nozzle, thus leading to an open fraction of $\beta = b/a$. The flow behavior beyond the exit plane at $z = L$ will not be considered here.

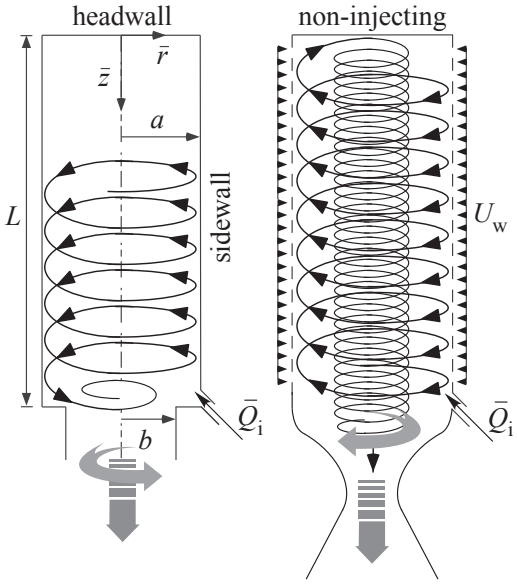

Figure 5.1. Notation and geometric sketch of a hybrid bidirectional vortex chamber.

In this configuration, fluid representing vaporized fuel enters the chamber in the negative r direction through the sidewall with a mass average injection velocity of U_w. Although the regression rate, and hence ejection velocity of gaseous mixtures, varies in an actual hybrid motor, a suitable average may be used for the purpose of estimating the velocity field. Just upstream of the fictitious nozzle, the simulated oxidizer enters the chamber along the outer edge of the exit plane in a purely tangential direction, i.e., as an idealization of the nearly tangential injection that may be accomplished through the use of multiple and evenly spaced oxidizer inlets. The oxidizer's injection, which takes place around the entire circumference of the chamber rather than at discrete azimuthal locations, ensures that the fluid motion remains

axisymmetric and hence enables the implementation of regular boundary conditions. Note that the tangential injection velocity is denoted by U and will be used as the normalizing value for all other velocities because its magnitude is the largest among the pre-defined velocities. In fact, the effective ratio of the fuel and oxidizer injection velocities, $\varepsilon \equiv U_{\mathrm{w}}/U$, which should be corrected for density variations in combusting motors, is of particular interest here since its emergence as a small parameter will prove useful in the upcoming asymptotic analysis. In addition to specifying the injection velocities, the areas for the injected gases are also defined as A_{i} in the case of the tangential inflow and $2\pi aL$ for the radial inflow. Specifying the inflow area and velocity has the effect of prescribing the volumetric flow rates of the fluids entering the chamber; these rates are designated as $\bar{Q}_{\mathrm{i}} = A_{\mathrm{i}}U$ and $\bar{Q}_{\mathrm{w}} = 2\pi aLU_{\mathrm{w}}$ in their dimensional forms. Lastly, under the assumption of incompressible motion, volumetric flow rates become interchangeable with mass flow rates and may hence be incorporated into the conservation equations.

5.1.2 Governing Equation

The inviscid solution for the Beltramian velocity field within a bidirectional vortex engine[116] begins with the Bragg-Hawthorne equation [131], which is a more compact statement of the axisymmetric Euler equations for steady and inviscid flow [132]:

$$\frac{\partial^2\bar{\psi}}{\partial\bar{r}^2} - \frac{1}{\bar{r}}\frac{\partial\bar{\psi}}{\partial\bar{r}} + \frac{\partial^2\bar{\psi}}{\partial\bar{z}^2} = \bar{r}^2\frac{\mathrm{d}\bar{H}}{\mathrm{d}\bar{\psi}} - \bar{B}\frac{\mathrm{d}\bar{B}}{\mathrm{d}\bar{\psi}} \tag{5.1}$$

where $\bar{B} = \bar{r}\bar{u}_\theta$ stands for the tangential angular momentum and $\bar{H} = \bar{p}/\rho + \bar{\boldsymbol{u}}\cdot\bar{\boldsymbol{u}}/2$ represents the total pressure head per unit mass. To derive a Beltramian solution in accordance with the assumption of isentropic flow, the pressure head may be taken to be constant along streamlines [133]. In this vein, a pair of new relationships is realized in such a manner as to grant the angular momentum dependence on the Stokes streamfunction. These are

$$\frac{\mathrm{d}\bar{H}}{\mathrm{d}\bar{\psi}} = 0 \qquad \text{and} \qquad \bar{B} = \sqrt{\bar{C}_n^2\bar{\psi}^2 + B_1} \quad \text{so that} \quad \bar{B}\frac{\mathrm{d}\bar{B}}{\mathrm{d}\bar{\psi}} = \bar{C}_n^2\bar{\psi}$$

Substituting these expressions into Eq. (5.1) yields a partial differential equation that may be solved using a product solution of the form $\bar{\psi}(\bar{r},\bar{z}) = \bar{F}(\bar{r})\bar{G}(\bar{z})$. By choosing a zero separation constant, the resultant streamfunction becomes

$$\bar{\psi} = \bar{F}\bar{G} = (C_1\bar{z} + C_2)[C_3\bar{r}J_1(\bar{C}_n\bar{r}) + C_4\bar{r}Y_1(\bar{C}_n\bar{r})] \tag{5.2}$$

The boundary conditions may be directly connected to the geometric model laid out in Sec. 5.1.1. These are:

(a) no axial flow through the headwall: $\bar{u}_z(\bar{r},0) = 0$

(b) no radial flow across the centerline (axisymmetry): $\bar{u}_r(0,\bar{z}) = 0$

(c) uniform injection through the chamber walls: $\bar{u}_r(a,\bar{z}) = -U_{\mathrm{w}}$

(d) tangential injection at the exit plane: $\bar{u}_\theta(a,L) = U$

(e) a mass balance between the inflow and outflow:
$\int_0^{2\pi}\int_0^b \bar{\boldsymbol{u}}\cdot\hat{\bar{\boldsymbol{n}}}\,\bar{r}\mathrm{d}\bar{r}\mathrm{d}\theta = 2\pi\int_0^b \bar{u}_z\bar{r}\mathrm{d}\bar{r} = \bar{Q}_{\mathrm{in}} = \bar{Q}_{\mathrm{i}} + \bar{Q}_{\mathrm{w}} = UA_{\mathrm{i}} + 2\pi aLU_{\mathrm{w}}$

5.1.3 Normalization

In the process of solving for the velocities, it is desirable to normalize all variables in order to facilitate comparisons to previously published material. The sensible choices for reference values are the chamber radius a for distances and the oxidizer injection speed U for velocities. Thus, the nondimensional variables are defined by:

$$\begin{gathered} r = \frac{\bar{r}}{a};\quad z = \frac{\bar{z}}{a};\quad u_r = \frac{\bar{u}_r}{U};\quad u_\theta = \frac{\bar{u}_\theta}{U};\quad u_z = \frac{\bar{u}_z}{U};\quad p = \frac{\bar{p}}{\rho U^2}; \\ H = \frac{\bar{H}}{U^2};\quad B = \frac{\bar{B}}{aU};\quad \mathrm{Re} = \frac{Ua}{\nu};\quad C_n = a\bar{C}_n;\quad \sigma = \frac{a^2}{A_{\mathrm{i}}} \end{gathered} \tag{5.3}$$

5.1.4 Inviscid Solution

The solution of Eq. (5.2) using the boundary conditions listed in Sec. 5.1.2 has been previously described by Majdalani [117]. The non-dimensional form of the corresponding streamfunction

is $\psi = c\kappa^* z r J_1(\lambda_1 r)$, where $c \equiv 1/[\beta J_1(\beta\lambda_1)]$ and $\kappa^* \equiv \kappa + \varepsilon$ are defined for convenience. For an engine with fixed open fraction β, sidewall injection ratio ε, and tangential inflow parameter κ, the quantity $\lambda_n = C_n$ may be retrieved from the eigencondition $\kappa^* J_1(\lambda_n) = \varepsilon\beta J_1(\beta\lambda_n)$. The lowest positive solution for λ_n, which corresponds to a bidirectional vortex with a single mantle, is designated λ_1. It may be worth mentioning that this notation differs from that used by Majdalani [117], who uses λ_0 for models both with and without wall injection. The notation λ_1 appears to be more in line with a later and more comprehensive review of swirling flows [133]. It is used here to emphasize that in opposition to the non-blowing solution, λ_1 is not identically a root of J_1. In addition, κ^* is used instead of κ_ε to be consistent with the nomenclature of Fleischmann and Majdalani [96]. With this notation in place, the velocity associated with the streamfunction becomes

$$\boldsymbol{u} = -c\kappa^* J_1(\lambda_1 r)\,\hat{\boldsymbol{e}}_r + \frac{1}{r}\sqrt{1 + \lambda_1^2 c^2 \kappa^{*2} z^2 r^2 J_1^2(\lambda_1 r)}\,\hat{\boldsymbol{e}}_\theta + c\kappa^* \lambda_1 z J_0(\lambda_1 r)\,\hat{\boldsymbol{e}}_z \tag{5.4}$$

5.2 Viscous Corrections

Due to the assumption of inviscid flow being inherent to the BHE formulation, Eq. (5.4) cannot account for the no-slip condition at the wall. Furthermore, the tangential velocity continues to exhibit free-vortex behavior that becomes unbounded at the centerline. Both of these regions must be treated separately in order to accurately capture the effects of viscous shear.

5.2.1 Viscous Momentum Equations

The treatment of the viscous regions starts with the normalized equations for momentum in the r, θ, and z directions. These are written under the assumptions of incompressible, steady, viscous flow with constant transport properties and negligible body forces. Written in cylindrical coordinates:

$$\frac{\partial P}{\partial r} = -u_r\frac{\partial u_r}{\partial r} - u_z\frac{\partial u_r}{\partial z} - \frac{1}{r}\left(u_\theta\frac{\partial u_r}{\partial \theta} - u_\theta^2\right) + \frac{1}{\mathrm{Re}}\left(\frac{\partial^2 u_r}{\partial r^2} + \frac{1}{r}\frac{\partial u_r}{\partial r} + \frac{1}{r^2}\frac{\partial^2 u_r}{\partial \theta^2} + \frac{\partial^2 u_r}{\partial z^2} - \frac{u_r}{r^2} - \frac{2}{r^2}\frac{\partial u_\theta}{\partial \theta}\right) \quad (5.5)$$

$$\frac{\partial P}{\partial \theta} = -ru_r\frac{\partial u_\theta}{\partial r} - ru_z\frac{\partial u_\theta}{\partial z} - u_\theta\frac{\partial u_\theta}{\partial \theta} - u_r u_\theta + \frac{r}{\mathrm{Re}}\left(\frac{\partial^2 u_\theta}{\partial r^2} + \frac{1}{r}\frac{\partial u_\theta}{\partial r} + \frac{1}{r^2}\frac{\partial^2 u_\theta}{\partial \theta^2} + \frac{\partial^2 u_\theta}{\partial z^2} - \frac{u_\theta}{r^2} + \frac{2}{r^2}\frac{\partial u_r}{\partial \theta}\right) \quad (5.6)$$

$$\frac{\partial P}{\partial z} = -u_r\frac{\partial u_z}{\partial r} - u_z\frac{\partial u_z}{\partial z} - \frac{1}{r}u_\theta\frac{\partial u_z}{\partial \theta} + \frac{1}{\mathrm{Re}}\left(\frac{\partial^2 u_z}{\partial r^2} + \frac{1}{r}\frac{\partial u_z}{\partial r} + \frac{1}{r^2}\frac{\partial^2 u_z}{\partial \theta^2} + \frac{\partial^2 u_z}{\partial z^2}\right) \quad (5.7)$$

5.2.2 Tangential Corrections

With expressions for the radial and tangential momentum in hand, both may be differentiated with respect to the opposite variable in order to equate the mixed derivatives of pressure. One gets

$$\frac{\partial}{\partial \theta}\left[\frac{1}{\mathrm{Re}}\left(\frac{\partial^2 u_r}{\partial r^2} + \frac{1}{r}\frac{\partial u_r}{\partial r} + \frac{1}{r^2}\frac{\partial^2 u_r}{\partial \theta^2} + \frac{\partial^2 u_r}{\partial z^2} - \frac{u_r}{r^2} - \frac{2}{r^2}\frac{\partial u_\theta}{\partial \theta}\right) - u_r\frac{\partial u_r}{\partial r} - u_z\frac{\partial u_r}{\partial z} - \frac{1}{r}\left(u_\theta\frac{\partial u_r}{\partial \theta} - u_\theta^2\right)\right] = \frac{\partial}{\partial r}\left[-ru_r\frac{\partial u_\theta}{\partial r} - ru_z\frac{\partial u_\theta}{\partial z} - u_\theta\frac{\partial u_\theta}{\partial \theta} - u_r u_\theta + \frac{r}{\mathrm{Re}}\left(\frac{\partial^2 u_\theta}{\partial r^2} + \frac{1}{r}\frac{\partial u_\theta}{\partial r} + \frac{1}{r^2}\frac{\partial^2 u_\theta}{\partial \theta^2} + \frac{\partial^2 u_\theta}{\partial z^2} - \frac{u_\theta}{r^2} + \frac{2}{r^2}\frac{\partial u_r}{\partial \theta}\right)\right] \quad (5.8)$$

Since the problem is axisymmetric, all derivatives with respect to θ may be discarded;

$$\frac{\partial}{\partial r}\left[\frac{r}{\mathrm{Re}}\left(\frac{\partial^2 u_\theta}{\partial r^2} + \frac{1}{r}\frac{\partial u_\theta}{\partial r} + \frac{\partial^2 u_\theta}{\partial z^2} - \frac{u_\theta}{r^2}\right) - ru_r\frac{\partial u_\theta}{\partial r} - ru_z\frac{\partial u_\theta}{\partial z} - u_r u_\theta\right] = 0 \quad (5.9)$$

Furthermore, axial variations have little bearing on the tangential motion for the type of problem under consideration. Thus, terms containing $\partial u_\theta/\partial z$ may be suppressed and one is left with

$$\frac{\partial}{\partial r}\left[\frac{r}{\mathrm{Re}}\left(\frac{\partial^2 u_\theta}{\partial r^2} + \frac{1}{r}\frac{\partial u_\theta}{\partial r} - \frac{u_\theta}{r^2}\right) - ru_r\frac{\partial u_\theta}{\partial r} - u_r u_\theta\right] = 0 \quad (5.10)$$

Upon closer inspection, Eq. (5.10) may be condensed by rewriting it in terms of the tangential momentum, which then serves as a more convenient proxy for the unknown tangential velocity. Defining $X = ru_\theta$ so that $X' = r\,\partial u_\theta/\partial r + u_\theta$ and grouping terms in Eq. (5.10) leads to a more compact relation, namely,

$$\frac{\partial}{\partial r}\left\{\frac{r}{\mathrm{Re}}\frac{\partial}{\partial r}\left[\frac{1}{r}\frac{\partial X}{\partial r}\right] - u_r\frac{\partial X}{\partial r}\right\} = 0 \tag{5.11}$$

Then using primes to denote differentiation with respect to r, Eq. (5.11) becomes

$$\mathrm{Re}^{-1}\left(X''' - r^{-1}X'' + r^{-2}X'\right) - u_r X'' - u_r' X' = 0 \tag{5.12}$$

The outcome represents a simplified boundary layer equation in the tangential direction for flow in the viscous regions. To make further headway, boundary conditions are needed. These may be readily translated to the angular momentum expression as

$$\begin{array}{llll} X^{(i)}(0,z) = 0 & \text{(Forced vortex core)} & X^{(w)}(1,z) = 0 & \text{(No slip)} \\ \lim\limits_{r\to 1} X^{(i)} = \lim\limits_{r\to 0} X^{(o)} & \text{(Matching)} & \lim\limits_{r\to 0} X^{(w)} = \lim\limits_{r\to 1} X^{(o)} & \text{(Matching)} \end{array} \tag{5.13}$$

The superscripts (i), (o), and (w) refer to the inner (core), outer (inviscid), and wall regions, respectively.

Core Region

Since the angular momentum exhibits a steep gradient in the core region, it is necessary to introduce a stretched spatial scale in the form of $t = r/\lambda$, as shown in Fig. 5.2 where λ denotes a scaling factor whose value may be determined in such a manner to achieve a balance between the most prominent terms in the viscous region. The "stretched" governing equation becomes

$$\mathrm{Re}^{-1}\left[\lambda^{-2}\dddot{X}^{(\mathrm{i})} - t^{-1}\lambda^{-2}\ddot{X}^{(\mathrm{i})} + t^{-2}\lambda^{-2}\dot{X}^{(\mathrm{i})}\right] - u_r\lambda^{-1}\ddot{X}^{(\mathrm{i})} - u_r'\dot{X}^{(i)} = 0 \tag{5.14}$$

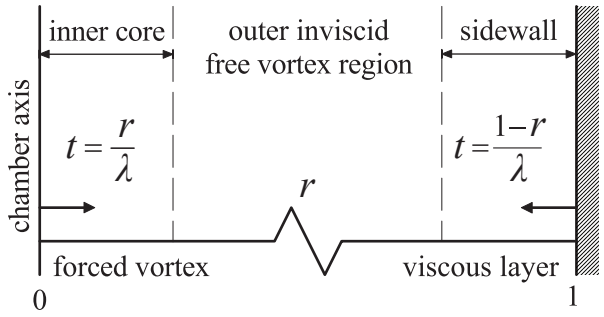

Figure 5.2. Schematic of the boundary layer regions corresponding to inner, wall, and outer domains used in the matched-asymptotic expansion analysis.

where overdots denote derivatives with respect to t.

Before integration, it is convenient to rewrite Eq. (5.14) in terms of $X^{(\mathrm{i})}$ and t only. To this end, the expression for u_r presented in Eq. (5.4) along with its derivative is first substituted. To avoid unnecessary complexity, these expressions are asymptotically expanded in the region of interest, namely as $r \to 0$, so that

$$J_0(\lambda_1 r) = 1 + \frac{\lambda_1^2 r^2}{4} + O(r^4); \quad J_1(\lambda_1 r) = \frac{\lambda_1 r}{2} - \frac{\lambda_1^3 r^3}{16} + O(r^5); \quad J_2(\lambda_1 r) = \frac{\lambda_1^2 r^2}{8} - \frac{\lambda_1^4 r^4}{96} + O(r^6)$$

Thus, the velocity expressions may be rewritten as

$$\begin{aligned} u_r &= -c\kappa^* \tfrac{1}{2}\lambda_1 r + O(r^3) = -\tfrac{1}{2}c\kappa^*\lambda_1 \lambda t + O(\lambda^3) \\ u_r' &= -\tfrac{1}{2}c\kappa^*\lambda_1 \left(1 - \tfrac{3}{8}\lambda_1^2 r^2\right) + O(r^4) = -\tfrac{1}{2}c\kappa^*\lambda_1 \left(1 - \tfrac{3}{8}\lambda_1^2 \lambda^2 t^2\right) + O(\lambda^4) \end{aligned} \tag{5.15}$$

Subsequently, inserting Eq. (5.15) into Eq. (5.14) yields

$$\lambda^{-2}\mathrm{Re}^{-1}\left[\ddot{X}^{(\mathrm{i})} - t^{-1}\dot{X}^{(\mathrm{i})} + t^{-2}\dot{X}^{(\mathrm{i})}\right] + \tfrac{1}{2}c\kappa^*\lambda_1\left[t\ddot{X}^{(\mathrm{i})} + \dot{X}^{(\mathrm{i})} - \tfrac{3}{8}\lambda_1^2\lambda^2 t^2 \dot{X}^{(\mathrm{i})}\right] + O(\lambda^3) = 0 \tag{5.16}$$

Since λ is small, and in keeping with the precision of the one-term matched-asymptotic expansion that is pursued, Eq. (5.16) may be further truncated to order $O(\lambda)$:

$$\lambda^{-2}\mathrm{Re}^{-1}\left[\ddot{X}^{(\mathrm{i})} - t^{-1}\dot{X}^{(\mathrm{i})} + t^{-2}\dot{X}^{(\mathrm{i})}\right] + \tfrac{1}{2}c\kappa^*\lambda_1\left[t\ddot{X}^{(\mathrm{i})} + \dot{X}^{(\mathrm{i})}\right] + O(\lambda) = 0 \tag{5.17}$$

For the remainder of this chapter, the trailing order relation will be omitted and all subsequent equations will be assumed to be accurate to $O(\lambda)$ or $O(\varepsilon)$, unless stated otherwise.

At this juncture, the value of λ must be determined such that Eq. (5.17) remains physically meaningful in the viscous region. This will be accomplished when a balance between the terms representing viscous (first term) and convective (second term) forces is established. To this end, it is necessary to determine which of the coefficients are not of order unity. Since the Reynolds number is large, its reciprocal certainly falls into this category. In addition, κ^* will be of order κ (ε being small), which contains the product of several parameters that can vary considerably. The other coefficients may be assumed to be of $O(1)$ and hence neglected.

With the relevant coefficients identified, division of Eq. (5.17) in its entirety by κ^* makes it clear that the distinguished limit of $\lambda = (\mathrm{Re}\,\kappa^*)^{-1/2}$ will ensure that the viscous and convective terms will be of like order. The result is

$$\dddot{X}^{(\mathrm{i})} + \left(\tfrac{1}{2}c\lambda_1 t - t^{-1}\right)\ddot{X}^{(\mathrm{i})} + \left(\tfrac{1}{2}c\lambda_1 + t^{-2}\right)\dot{X}^{(\mathrm{i})} = 0 \tag{5.18}$$

This third-order, ordinary differential equation is linear and contains no unknown coefficients; it may be readily integrated into

$$X^{(\mathrm{i})}(t) = K_0 + K_1 e^{-\frac{1}{2}\left(\frac{1}{2}c\lambda_1\right)t^2}\left[K_1 \ln\left[\tfrac{1}{2}\left(\tfrac{1}{2}c\lambda_1\right)t^2 - \mathrm{Ei}\left(\tfrac{1}{2}\left(\tfrac{1}{2}c\lambda_1\right)t^2\right)\right]\right] + K_2 e^{-\frac{1}{2}\left(\frac{1}{2}c\lambda_1\right)t^2} \tag{5.19}$$

where Ei denotes the elliptic integral function. To obtain the remaining coefficients, one may apply the boundary condition at the centerline and write

$$X^{(\mathrm{i})}(0) = K_0 + K_1(\infty) - K_1(\infty) + K_2(1) = 0 \tag{5.20}$$

This reveals that $K_1 = 0$ and $K_2 = -K_0$. Next, the matching condition may be used after conversion to the stretched scale: the second component of Eq. (**??**) becomes $\lim_{t\to\infty} X^{(\mathrm{i})} = \lim_{r\to 0} X^{(\mathrm{o})}$ where $X^{(\mathrm{o})} = B$. Thus,

$$\lim_{t\to\infty} K_0\left(1 - e^{-\frac{1}{4}c\lambda_1 t^2}\right) = \lim_{r\to 0}\sqrt{1 + c^2\kappa^{*2}\lambda_1^2 z^2 r^2 J_1^2(\lambda_1 r)} = 1 \tag{5.21}$$

and so $K_0 = 1$. In this fashion, one may extract $X^{(\mathrm{i})}(t) = 1 - \exp\left(-\frac{1}{4}c\lambda_1 t^2\right)$ which, in terms of r, returns the inner approximation

$$X^{(\mathrm{i})}(r) = 1 - \exp\left(-\tfrac{1}{4}c\lambda_1 \mathrm{Re}\,\kappa^* r^2\right) \qquad \text{or} \qquad u_\theta^{(\mathrm{i})}(r) = r^{-1} - r^{-1}\exp\left(-\tfrac{1}{4}c\lambda_1 \mathrm{Re}\,\kappa^* r^2\right) \tag{5.22}$$

Wall Region

The boundary layer near the wall now requires attention. Once again, the steep gradient in the boundary layer necessitates the introduction of a locally stretched spatial scale. Since the wall demarcates the right side of the domain, a suitable coordinate transformation will be $t = (1 - r)/\lambda$ where, as before, λ represents an unknown quantity that must be determined from the act of balancing the key forces in the transformed momentum equation. In this vein, Eq. (5.12) and Eq. (**??**) may be modified so that the relevant equation and boundary conditions in the wall region become

$$\begin{gathered} \mathrm{Re}^{-1}\lambda^{-2}\left[\ddot{X}^{(\mathrm{w})} + (1-\lambda t)^{-1}\lambda\ddot{X}^{(\mathrm{w})} + (1-\lambda t)^{-2}\lambda^2\dot{X}^{(\mathrm{w})}\right] + \lambda^{-1}u_r\ddot{X}^{(\mathrm{w})} - u_r'\dot{X}^{(\mathrm{w})} = 0 \\ \text{with} \qquad X^{(\mathrm{w})}(0) = 0 \qquad \text{and} \qquad \lim_{t\to\infty} X^{(\mathrm{w})} = \lim_{r\to 1} X^{(\mathrm{o})} \end{gathered} \tag{5.23}$$

As before, u_r and its derivative may be expanded asymptotically near $r = 1$. The coefficients of the viscous terms may be similarly simplified. Bearing in mind that $\lambda \to 0$ as $r \to 1$, the approximations are

$$\begin{gathered} (1-\lambda t)^{-1} = 1 + O(\lambda); \qquad (1-\lambda t)^{-2} = 1 + O(\lambda) \\ u_r = -\varepsilon + \lambda\left[\lambda_1 c\kappa^* J_2(\lambda_1) - \varepsilon\right] + O(\lambda^2); \qquad u_r' = -\lambda_1 c\kappa^* J_0(\lambda_1) + O(\lambda) \end{gathered} \tag{5.24}$$

After introducing these simplifications into Eq. (5.23), the balancing act will once again dictate the use of $\lambda = (\mathrm{Re}\kappa^*)^{-1/2}$, which proves identical to the distinguished limit in the core region. It follows that

$$\ddot{X}^{(\mathrm{w})} + \left[\lambda_1 c J_2(\lambda_1) - \sqrt{\mathrm{Re}/\kappa^*}\varepsilon\right]\ddot{X}^{(\mathrm{w})} + \lambda_1 c J_0(\lambda_1)\dot{X}^{(\mathrm{w})} = 0 \tag{5.25}$$

For convenience, let $\zeta = \lambda_1 c J_2(\lambda_1) - \sqrt{\mathrm{Re}/\kappa^*}\varepsilon$ and $\xi = -\lambda_1 c J_0(\lambda_1)$ so that Eq. (5.25) becomes

$$\dddot{X}^{(\mathrm{w})} + \zeta \ddot{X}^{(\mathrm{w})} - \xi \dot{X}^{(\mathrm{w})} = 0 \tag{5.26}$$

A direct solution may hence be obtained, namely,

$$X^{(\mathrm{w})}(t) = K_0 + \exp\left[-\tfrac{1}{2}t\left(\sqrt{\zeta^2 + 4\xi} + \zeta\right)\right]\left[K_1 \exp\left(t\sqrt{\zeta^2 + 4\xi}\right) + K_2\right] \tag{5.27}$$

At this point, application of the matching requirement in Eq. (5.23) leads to

$$K_0 + (+\infty)K_1 + K_2(0) = \sqrt{1 + \lambda_1^2 z^2 \varepsilon^2} \tag{5.28}$$

and so $K_0 = 1$ and $K_1 = 0$. Moreover, the velocity-adherence condition may be used to retrieve $K_2 = -1$ in fulfillment of $1 + K_2(1) = 0$. With these constants in hand, the tangential momentum in the wall region may be written as

$$X^{(\mathrm{w})}(t) = 1 - \exp\left[-\tfrac{1}{2}t\left(\sqrt{\zeta^2 + 4\xi} + \zeta\right)\right] \tag{5.29}$$

or, in terms of r,

$$X^{(\mathrm{w})}(r) = 1 - \exp\left[-\tfrac{1}{2}\left(\sqrt{\zeta^2 + 4\xi} + \zeta\right)\sqrt{\mathrm{Re}\,\kappa^*}(1 - r)\right] \tag{5.30}$$

and so, the wall tangential velocity is given by

$$u_\theta^{(\mathrm{w})}(r) = r^{-1} - r^{-1}\exp\left[-\tfrac{1}{2}\left(\sqrt{\zeta^2 + 4\xi} + \zeta\right)\sqrt{\mathrm{Re}\,\kappa^*}(1 - r)\right] \tag{5.31}$$

Composite Solution

So far, three solutions have been identified for the tangential momentum in three flow regions. The outer, core, and wall approximations correspond to Eq. (5.4), Eq. (5.22), and Eq. (5.31), respectively. According to the theory of matched-asymptotic expansions, a composite solution

may be obtained by combining the three locally valid approximations into one solution that will remain uniformly valid over the entire domain of $0 \leq r \leq 1$. This may be achieved by adding the solutions and subtracting their overlapping parts, viz.

$$X^{(\mathrm{c})} = X^{(\mathrm{i})} + X^{(\mathrm{o})} + X^{(\mathrm{w})} - \left[X^{(\mathrm{i})}\right]^{(\mathrm{o})} - \left[X^{(\mathrm{w})}\right]^{(\mathrm{o})} \tag{5.32}$$

The common parts correspond to the same values that are determined using Prandtl's matching principle [134]. Specifically,

$$\left[X^{(\mathrm{i})}\right]^{(\mathrm{o})} = \lim_{t\to\infty} X^{(\mathrm{i})} = \lim_{r\to 0} X^{(\mathrm{o})} = 1 \qquad \text{and} \qquad \left[X^{(\mathrm{w})}\right]^{(\mathrm{o})} = \lim_{t\to\infty} X^{(\mathrm{w})} = \lim_{r\to 1} X^{(\mathrm{o})} = 1 \tag{5.33}$$

Thus, the composite angular momentum may be compacted into

$$X^{(\mathrm{c})}(r) = \sqrt{1 + c^2\kappa^{*2}\lambda_1^2 z^2 r^2 J_1^2(\lambda_1 r)} - \exp\left[-\tfrac{1}{4}c\lambda_1 \mathrm{Re}\,\kappa^* r^2\right] - \exp\left[-\tfrac{1}{2}\left(\sqrt{\zeta^2 + 4\xi} + \zeta\right)\sqrt{\mathrm{Re}\,\kappa^*}(1 - r)\right] \tag{5.34}$$

which results in the composite tangential velocity expression

$$u_\theta^{(\mathrm{c})}(r) = r^{-1}\sqrt{1 + c^2\kappa^{*2}\lambda_1^2 z^2 r^2 J_1^2(\lambda_1 r)} - r^{-1}\exp\left[-\tfrac{1}{4}c\lambda_1 \mathrm{Re}\,\kappa^* r^2\right] - r^{-1}\exp\left[-\tfrac{1}{2}\left(\sqrt{\zeta^2 + 4\xi} + \zeta\right)\sqrt{\mathrm{Re}\,\kappa^*}(1 - r)\right] \tag{5.35}$$

Equation (5.35) is plotted for several values of κ and Re in Fig. 5.3. For all cases considered, the open fraction β is set to the idealized β^* such that the mantle location and outlet radius coincide. In this manner, the flow is unimpeded as it exits the chamber and the corresponding motion remains as described in Fig. 5.1, i.e., without additional wall interactions or recirculation zones. The value of β^* may be determined by setting the axial component of Eq. (5.4) equal to zero and solving for $r = \beta^*$. The resultant relation, $\beta^* = j_0/\lambda_1$, where j_0 is defined by $J_0(j_0) = 0$, suggests that, in order to ensure smooth outflow, the value of λ_1 must be set using β^*, thus leading to a refined expression for λ_1 that must be solved numerically: $\lambda_1 J_1(\lambda_1) = \varepsilon j_0 J_1(j_0)/\kappa^*$.

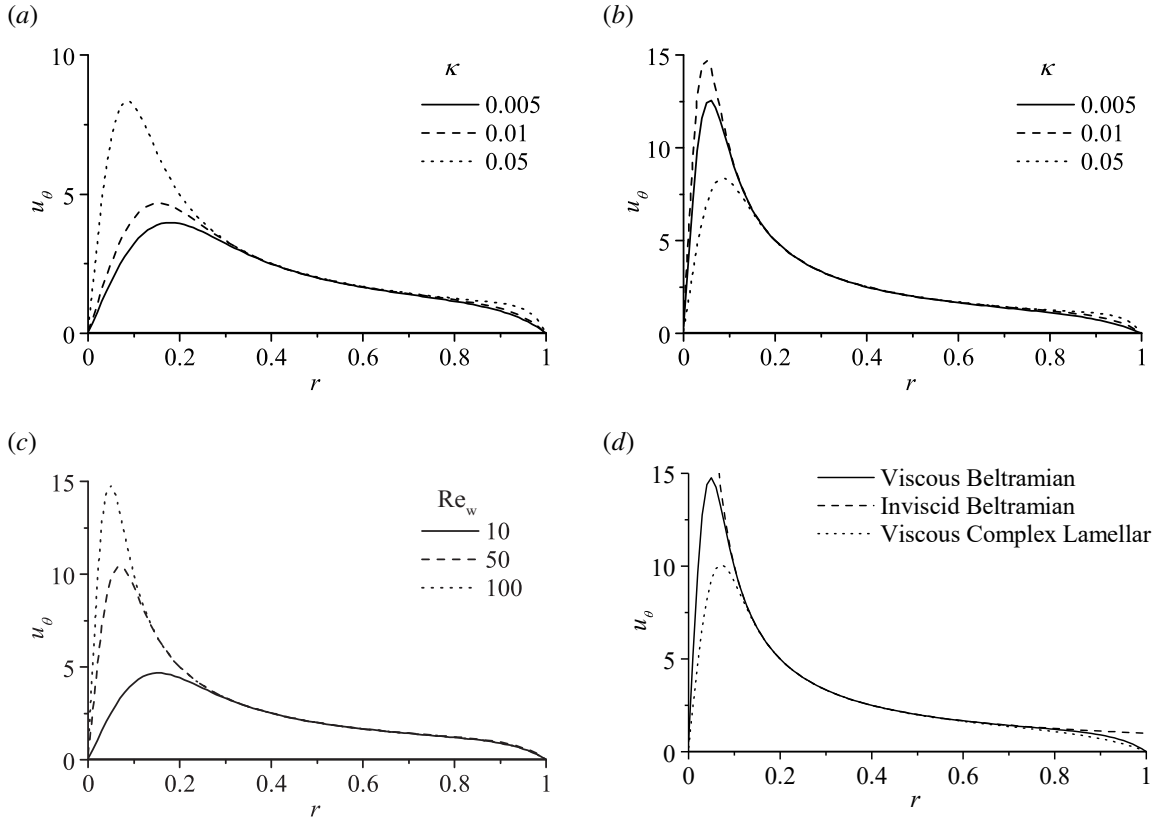

Figure 5.3. Profiles of the tangential velocity at several values of κ and an injection Reynolds number of a) 10 and b) 100. In Part c) $u_\theta^{(c)}$ is shown at several values of $\mathrm{Re_w}$ and a fixed κ. Finally, Part d) compares $u_\theta^{(c)}$ to the previously published inviscid Beltramian solution as well as the complex-lamellar solution incorporating viscous corrections.

Hence, the ideal open fraction is prescribed by the swirl number, aspect ratio, and ratio of injection velocities.

5.2.3 Axial Correction

In a manner similar to that of the preceding section, the normalized expressions for the axial and radial momentum given by Eq. (5.5) and Eq. (5.7) may be differentiated with respect to the opposite variable in order to equate the mixed derivatives of the pressure. Axisymmetry may also be employed to simplify the resulting equation. Furthermore, the assumption that velocity gradients in the r-direction significantly outweigh their counterparts in the z-direction can be used to eliminate all terms containing derivatives with respect to z. One is left with

$$\mathrm{Re}^{-1}\left(u_z''' + r^{-1}u_z'' - r^{-2}u_z'\right) - u_r u_z'' - u_r' u_z' = 0 \tag{5.36}$$

As before, the introduction of the stretched scale, $t = (1 - r)/\lambda$, enables the capture of the fast changes that affect the velocity near the sidewall. Realizing that t does not differ from the tangential wall case, the same conversion formulas apply. The result is

$$\lambda^{-2}\mathrm{Re}^{-1}\left[\ddot{u}_z^{(\mathrm{w})} - \lambda(1-\lambda t)^{-1}\ddot{u}_z^{(\mathrm{w})} - \lambda^2(1-\lambda t)^{-2}\dot{u}_z^{(\mathrm{w})}\right] + \lambda^{-1}u_r\ddot{u}_z^{(\mathrm{w})} - u_r'\dot{u}_z^{(\mathrm{w})} = 0 \tag{5.37}$$

After replacing u_r, u_r', and the $(1 - \lambda t)$ terms with their asymptotic approximations given by Eq. (5.24), Eq. (5.37) becomes

$$\lambda^{-2}\mathrm{Re}^{-1}\ddot{u}_z^{(\mathrm{w})} + \lambda^{-1}\left[-\varepsilon + \lambda\lambda_1 c\kappa^* J_2(\lambda_1)\right]\ddot{u}_z^{(\mathrm{w})} + \lambda_1 c\kappa^* J_0(\lambda_1)\dot{u}_z^{(\mathrm{w})} = 0 \tag{5.38}$$

Here too, balancing relevant terms leads to the same distinguished limit, $\lambda = (\mathrm{Re}\,\kappa^*)^{-1/2}$, along with a simpler form of Eq. (5.38),

$$\ddot{u}_z^{(\mathrm{w})} + \left[\lambda_1 c J_2(\lambda_1) - \sqrt{\mathrm{Re}/\kappa^*}\varepsilon\right]\ddot{u}_z^{(\mathrm{w})} + \lambda_1 c J_0(\lambda_1)\dot{u}_z^{(\mathrm{w})} = 0 \tag{5.39}$$

In terms of the previously defined constants ζ and ξ, Eq. (5.39) becomes

$$\ddot{u}_z^{(\mathrm{w})} + \zeta\ddot{u}_z^{(\mathrm{w})} - \xi\dot{u}_z^{(\mathrm{w})} = 0 \tag{5.40}$$

Equation (5.40) is now ready to be solved in conjunction with the auxiliary conditions,

$$u_z(t = 0, z) = 0 \qquad \text{and} \qquad \lim_{t\to\infty} u_z^{(\mathrm{w})} = u_z^{(\mathrm{o})} = c\kappa^*\lambda_1 z J_0[\lambda_1(1 - \lambda t)] \tag{5.41}$$

While the solution to Eq. (5.40) in its present form is straightforward – indeed, it is identical in form to Eq. (5.26) – the application of the matching condition uncovers an inconsistency associated with the assumption that, unlike $u_z^{(\mathrm{o})}$, $u_z^{(\mathrm{w})}$ does not depend on z explicitly. To circumvent this inconsistency, one may introduce another intermediate transformation,

$$\eta(t, z) \equiv \frac{u_z^{(\mathrm{w})}(t, z)}{u_z^{(\mathrm{o})}(t, z)} \tag{5.42}$$

Consequently, $u_z^{(\mathrm{w})} = \eta u_z^{(\mathrm{o})}$ and Eq. (5.40) may be rewritten at leading order without changing form:

$$\dddot{\eta} + \zeta\ddot{\eta} - \xi\dot{\eta} = 0 \tag{5.43}$$

At this point, straightforward application of Eq. (5.42) to Eq. (5.41) returns to transformed boundary conditions

$$\eta(0, z) = 0 \qquad \text{and} \qquad \lim_{t\to\infty} \eta = 1 \tag{5.44}$$

One thus retrieves the solution to Eq. (5.43) with three undetermined constants,

$$\eta(t, z) = K_0 + \exp\left[-\tfrac{1}{2}t\left(\sqrt{\zeta^2 + 4\xi} + \zeta\right)\right]\left[K_1 \exp\left(t\sqrt{\zeta^2 + 4\xi}\right) + K_2\right] \tag{5.45}$$

Applying the matching condition shows that in order for $\lim_{t\to\infty} \eta = K_0 + (\infty)K_1 + (0)K_2 = 1$ to be true, K_1 must vanish and K_0 must be equal to one. Moreover, enforcing the velocity adherence at the sidewall requires that $\eta(0, z) = 1 + K_2 = 0$ such that $K_2 = -1$. What remains is

$$\eta = 1 - \exp\left[-\tfrac{1}{2}t\left(\sqrt{\zeta^2 + 4\xi} + \zeta\right)\right] \tag{5.46}$$

or, in terms of the original variables,

$$u_z(r, z) = c\kappa^*\lambda_1 z J_0(\lambda_1 r)\left\{1 - \exp\left[-\tfrac{1}{2}\left(\sqrt{\zeta^2 + 4\xi} + \zeta\right)\sqrt{\mathrm{Re}\,\kappa^*}(1 - r)\right]\right\} \tag{5.47}$$

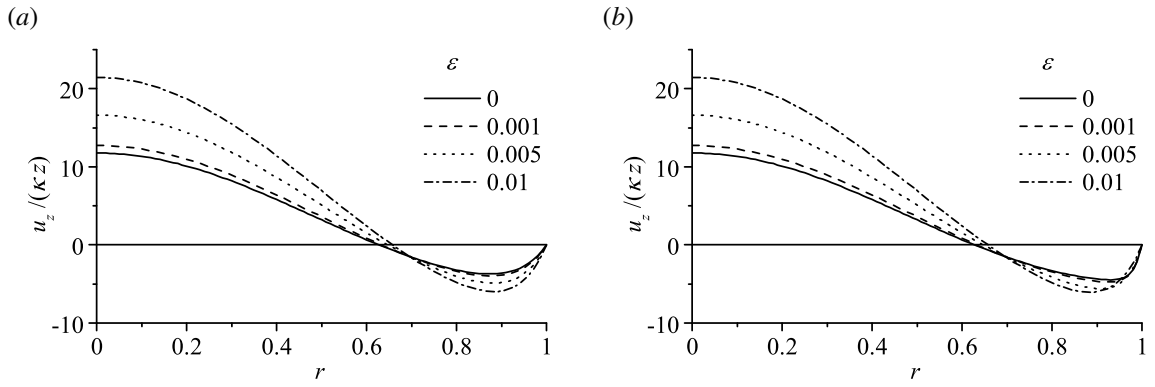

Figure 5.4. Variation of the axial velocity with the wall injection ratio for $\kappa = 0.01$ with a) $\mathrm{Re} = 10^3$ and b) $\mathrm{Re} = 10^4$. Here $\beta = \beta^*$ for both cases.

The outcome is an expression that remains valid over the entire domain, as illustrated in Fig. 5.4 at two dissimilar Reynolds numbers and a range of ε. Note that the case of $\varepsilon = 0$ restores the solution by Majdalani [117]. Indeed, the first term of Eq. (5.47) captures the outer solution while the second term may be seen to be significant only near the wall. In the absence of the viscous correction, slippage along the wall cannot be prevented as shown in Fig. 5.5, where the spatially normalized axial velocity is compared to its inviscid counterpart as well as its complex-lamellar flow analog at a representative set of control parameters.

As a result of the mathematical model employed in developing the inviscid solution, a boundary layer analysis in the radial direction may be viewed as being practically unnecessary. At the wall, the leading-order behavior is fully prescribed by the mass injection condition while the radial flow approaching the centerline is similarly constrained by the inability to cross the chamber axis. While higher-order analyses have been conducted for analogous problems [118], the corresponding formulations have only unraveled a minor smoothing effect on the radial velocity profile in the wall boundary layer. In fact, the corrective effect is so miniscule that it will be neglected here in order to retain the same level of accuracy as in the remainder of this work.

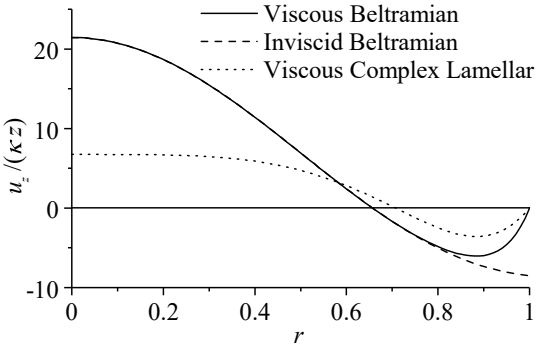

Figure 5.5. A comparison of the viscous Beltramian solution to the viscous complex-lamellar and inviscid Beltramian solutions using $\beta = \beta^*$.

5.3 Boundary Layer Characterization

5.3.1 Extent of Forced Vortex Region

The outer extent of the forced vortex region coincides with the radial distance from the centerline at which u_θ reaches its maximum value, $r = \delta_c$. Accordingly, the value of δ_c may be deduced by setting the first radial derivative of u_θ equal to zero. Due to the transcendental nature of the ensuing equation, a succinct asymptotic solution for δ_c may be pursued in a manner that is at

least as accurate as Eq. (5.35) itself. After some algebra, one extracts

$$\delta_c \approx \frac{2\sqrt{\frac{1+\sqrt{7}}{3}}}{\sqrt{c\lambda_1 \mathrm{Re}\,\kappa^*}} \approx 2.2048(c\lambda_1 \mathrm{Re}\,\kappa^*)^{-1/2} \tag{5.48}$$

Given that the basic definition of the vortex Reynolds number is $V = 2\pi\kappa\mathrm{Re}$ [112] and that other "modified" or problem-specific definitions, such as $V_0 = 2\pi\,\csc(\pi\beta^2)\kappa\mathrm{Re}$ [96], share the same operative component, $(\mathrm{Re}\,\kappa)$, the quantity $c\lambda_1 \mathrm{Re}\,\kappa^*$ appears to be yet another form of the vortex Reynolds number: namely, one that takes sidewall injection into account in addition to the effects of viscosity and swirl. Thus, the outcome in Eq. (5.48) is consistent both with prior literature as well as the laminar theory for swirling flows in that the thickness of the forced core scales with the reciprocal of the square root of the vortex Reynolds number. The backward substitution of δ_c into Eq. (5.22) returns the maximum value of the tangential velocity as $(u_\theta)_{\max} \approx 0.31902\sqrt{c\lambda_1 \mathrm{Re}\,\kappa^*}$. For further clarity, the forced core thickness is illustrated in Fig. 5.6, where δ_c is plotted against $\mathrm{Re}\,\kappa^*$. As noted above, this formulation for δ_c appears to be consistent with laminar flow theory and so the caution of Maicke and Majdalani [114] is repeated: a turbulent eddy viscosity should be used in place of the molecular viscosity under high speed conditions to avoid overpredicting the maximum velocity in the core.

5.3.2 Boundary Layer Thickness

In addition to the forced core, the thickness of the boundary layer that develops at the wall may be quantified. The location r_w of the boundary layer edge may be specified, as usual, by the relationship $0.99u^{(o)}(r_w) = u^{(w)}(r_w)$. The actual thickness of the boundary layer δ_w, which is measured from the wall, may be related to this edge using $\delta_w = 1 - r_w$. In the axial direction, one may set

$$0.99c\kappa^*\lambda_1 z J_0(\lambda_1 r_w) = c\kappa^*\lambda_1 z J_0(\lambda_1 r_w)\left\{1 - \exp\left[-\tfrac{1}{2}\left(\sqrt{\zeta^2 + 4\xi} + \zeta\right)\sqrt{\mathrm{Re}\,\kappa^*}(1 - r_w)\right]\right\}$$

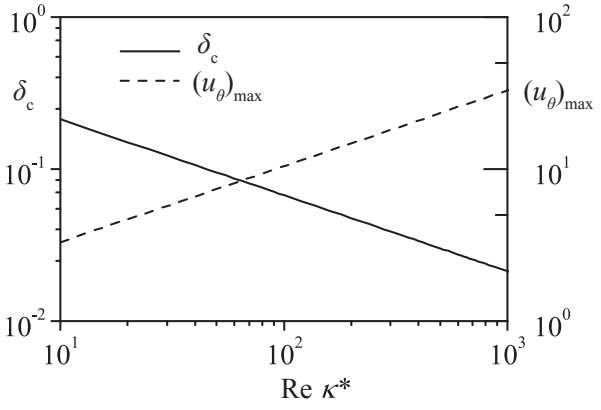

Figure 5.6. Variation of the forced core thickness and maximum tangential velocity with Re κ^*.

which simplifies straightforwardly into a form that admits one exact root, namely,

$$\delta_w = -\ln(0.01)\left[\tfrac{1}{2}\left(\sqrt{\zeta^2+4\xi}+\zeta\right)\sqrt{\mathrm{Re}\,\kappa^*}\right]^{-1} \approx 9.2103\left(\sqrt{\zeta^2+4\xi}+\zeta\right)^{-1}(\mathrm{Re}\,\kappa^*)^{-1/2} \tag{5.49}$$

which once again scales with the multiplicative inverse of the square root of the vortex Reynolds number. In the azimuthal direction, a similar analysis may be performed, but the transcendental nature of the ensuing relationship does not admit an exact solution. Nonetheless, an expansion of the outer solution results in the recovery of an expression for the tangential boundary layer that proves to be identical to that of the axial layer. One gets

$$\delta_w \approx 9.2103\left(\sqrt{\zeta^2+4\xi}+\zeta\right)^{-1}(\mathrm{Re}\,\kappa^*)^{-1/2} \tag{5.50}$$

As such, the constant thickness of the two layers is found to be identical in both axial and tangential directions, which stands in strong agreement with previous studies [96].

5.4 Application of Regression Rate Model and Comparison to Experiments

Now that the velocity field for the bidirectional vortex engine is characterized, it is possible to apply the regression rate model from Chapter 4 to an engine like the VIHRE. Knuth et al. [25 54] have published a small amount of test data from the initial bidirectional vortex engine investigations by Orbitec. Although critical operation parameters are deliberately obscured

Table 5.1. Motor information for experimental tests from Knuth et al. [25]

Dataset	Fuel	$\dot{m}_{ox}$ [kg/s]	L [m]	D_0 [m]	U [m/s]	$\dot{r}_{avg}$ [mm/s]
Test 2	HTPB	0.0177	0.0762	0.0508	~92	0.753
Test 10	HTPB	~0.032	0.0762	0.0508	~166	1.269
Test 17	HTPB	~0.023	0.0762	0.0508	~119	1.020

(injection angles are described as "small" or "large" in lieu of providing the numerical measurement) or omitted entirely (burn times are not specified for any of the tests) to protect the proprietary design, these data allow for rough comparisons. In particular, there are two available tests to evaluate the regression rate model based on the available data: first, the model may be manually calibrated to the data in order to compare the axial trends and, second, the model prediction can then be compared to a non-swirling equivalent motor to ascertain the net regression rate increase due to the novel flowfield. Since Knuth et al. [25] perform a similar comparison, the regression rate increase predicted by the model can be validated in a simplified, quantitative manner.

To this end, data and operating conditions for "Test 2", "Test10", and "Test 17" from [25] are chosen for comparison since these tests are discussed in greater detail than most of the others within that publication. Both axially-resolved and space-time-averaged results are published, and the actual mass flow rate for "Test 2" is provided as well as target mass flow rates for all three. Table 5.1 lists the relevant motor information from the VIHRE tests. The MATLAB simulation scheme described in Sec. 4.2 is configured with the appropriate inputs and then run to manually adjust the regression rate to the level indicated by the data. Values of 0.6 and 0 are chosen for n and m, leading to $a = 2.89 \cdot 10^{-5}$. Furthermore, the swirl number coefficient a_1 is reduced to 0.6, on the grounds that the effective axial mass flux for a bidirectional flow should be calculated using only the cross-sectional area of the outer vortex region. For the Beltramian class of solution, the mantle is located at a normalized radius of 0.628 and the outer vortex occupies 60% of the total cross-sectional area. The swirl exponent n_1 remains 0.18 as determined from the Tamura et al. [29] data in Sec. 4.3.2. Figure 5.7 shows that the axial trend predicted by the swirling regression rate model does not match the experimental data.

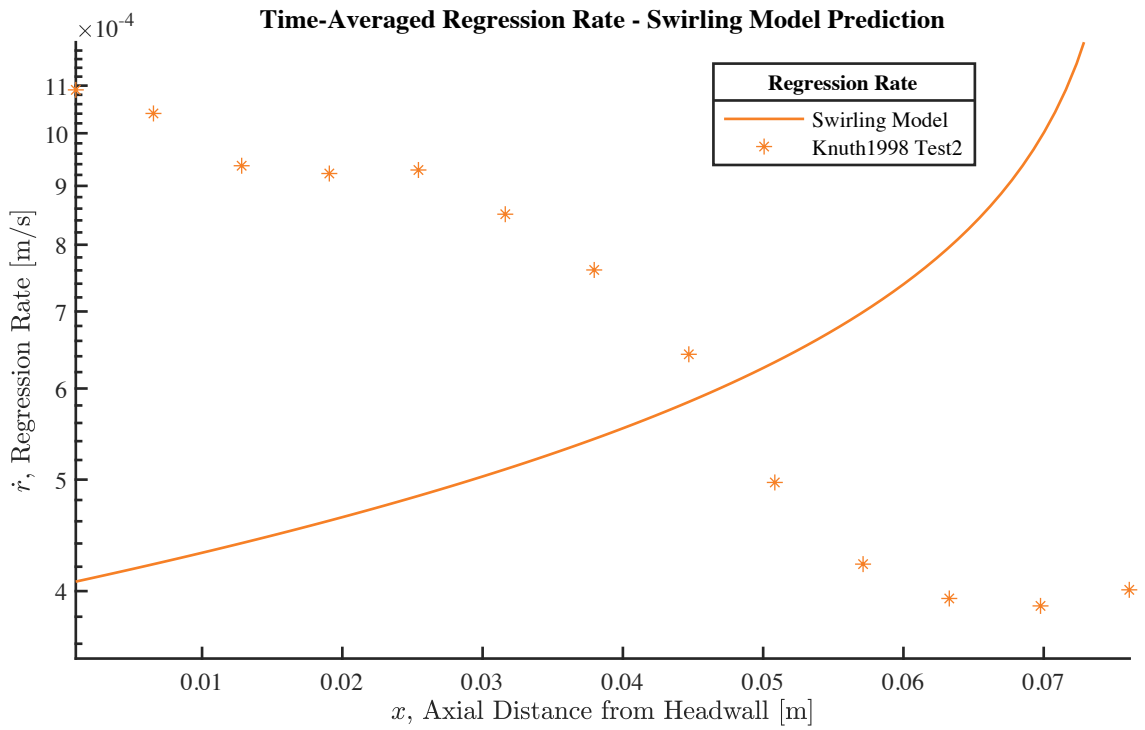

Figure 5.7. Locally-resolved regression rate prediction compared to "Knuth1998 Test2" test data. The prediction is manually adjusted to line up with this set of data so that the axial trends can be compared.

The overall range in the predicted regression rate is largely consistent with the data, but the curvature and direction of the regression trends are completely opposite.

The data in Fig. 5.7 display three clear regions: First, the regression profile on the left-hand side (near the injectors) drops off only slightly, which Knuth et al. [25] attribute to a combination of turbulent wall jet structure and possible oxidizer attack. As the jets dissipate and the oxidizer-to-fuel ratio drops, the regression rate rapidly decreases throughout most of the remainder of the port. Finally, the second region of flatter regression near the headwall (on the right) most likely occurs as a consequence of a ring-shaped recirculation zone in the corners of the engine [25]. Unfortunately, these effects are not explicitly incorporated in the Beltramian velocity field solution.

The primary discrepancy between theory and experiment is the way that fluid injection is modeled. In the Beltramian model, and indeed in all analytical models of the same family for the bidirectional vortex, oxidizer injection is accomplished as an inlet condition over the aft surface of the outer region. Although boundary condition (*d*) in Sec. 5.1.2 for tangential injection at

the exit plane is defined *at the wall* as $\bar{u}_\theta(a, L) = U$, the mathematical conditions used in the problem do not allow for injection solely along a line. Thus, the boundary conditions ultimately define the entire aft surface of the chamber as being open, with a demarcation between inlets and outlets according to the sign of the axial velocity so that the dividing surface delimits the mantle. This is a deficiency of the bulk flow model that, while not significant downstream or within the core, leads to obvious discrepancies with experiments near the injectors. This is true of the velocity field prediction in general, which means that it is also true of regression rate predictions that depend on the velocity field. Since the tangential velocity varies less than the axial velocity according to the analytical solution, the swirl number is largely controlled by the magnitude of the axial component. The regression model thus predicts that the effect of swirl is minimal near the injectors, where the velocity field solution starts with a maximum axial speed and then increases in swirl strength and fuel regression rate as the flow approaches the head end. This trend is clearly in opposition to the reality of the experimental data and the phenomenological description that accompanies it.

To overcome this paradoxical behavior, the z coordinate may be reversed so that the axial velocity begins with a value of zero at the injectors and grows to a maximum at the headwall. While this rectified profile is not entirely physical either, it offers a significant improvement over the foregoing solution at the base of the chamber and is able to match the experimental data quite well at both ends when the coefficient a is adjusted to $a = 2.1 \cdot 10^{-5}$, as evidenced in Fig. 5.8. In comparison, the complex-lamellar solution published by Fleischmann and Majdalani [96], when similarly rectified, predicts regression rates that are much lower for the same constant a. The precision of the complex-lamellar predictions improves when this coefficient is increased to a value of $a = 3.00 \cdot 10^{-5}$. Even so, Fig. 5.9 shows that these predictions continue to slightly underpredict the experimental data for VIHRE.

Notwithstanding any difficulties with the axial trend prediction, the overall improvement predicted by the swirl model is much more successful. Running each simulation again (with the axial velocity given by Eq. (5.47), as in Fig. 5.7) for a traditional motor with identical operating conditions produces an estimate for the average regression rate in the absence of swirl. Knuth et al. [25] reports increases of 5.67, 6.20, and 6.43 times the equivalent non-swirling motor

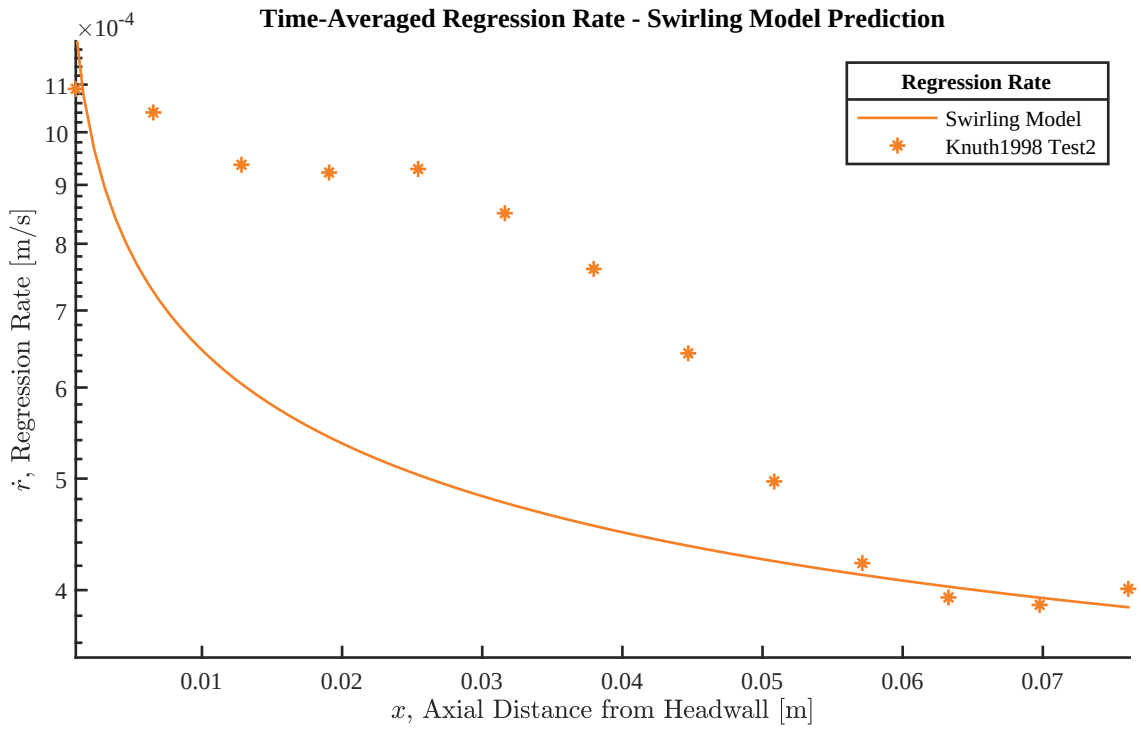

Figure 5.8. Locally-resolved regression rate prediction compared to "Knuth1998 Test2" test data for a rectified axial velocity profile. The prediction is manually adjusted to line up with this set of data so that the axial trends can be compared.

Table 5.2. Average regression rate improvement for the bidirectional vortex engine configuration as compared to equivalent axial-injection motors. VIHRE test data and predictions from Knuth et al. [25] are compared to the results of numerical simulations based on the new swirl model presented in Chapter 4

Dataset	Experimental $\dot{r}_{sw}/\dot{r}_0$	Analytical $\dot{r}_{sw}/\dot{r}_0$	Relative Error
Test 2	5.67	6.23	9.8%
Test 10	6.20	5.82	-6.1%
Test 17	6.43	6.04	-6.1%
Average	6.10	6.03	-1.1%

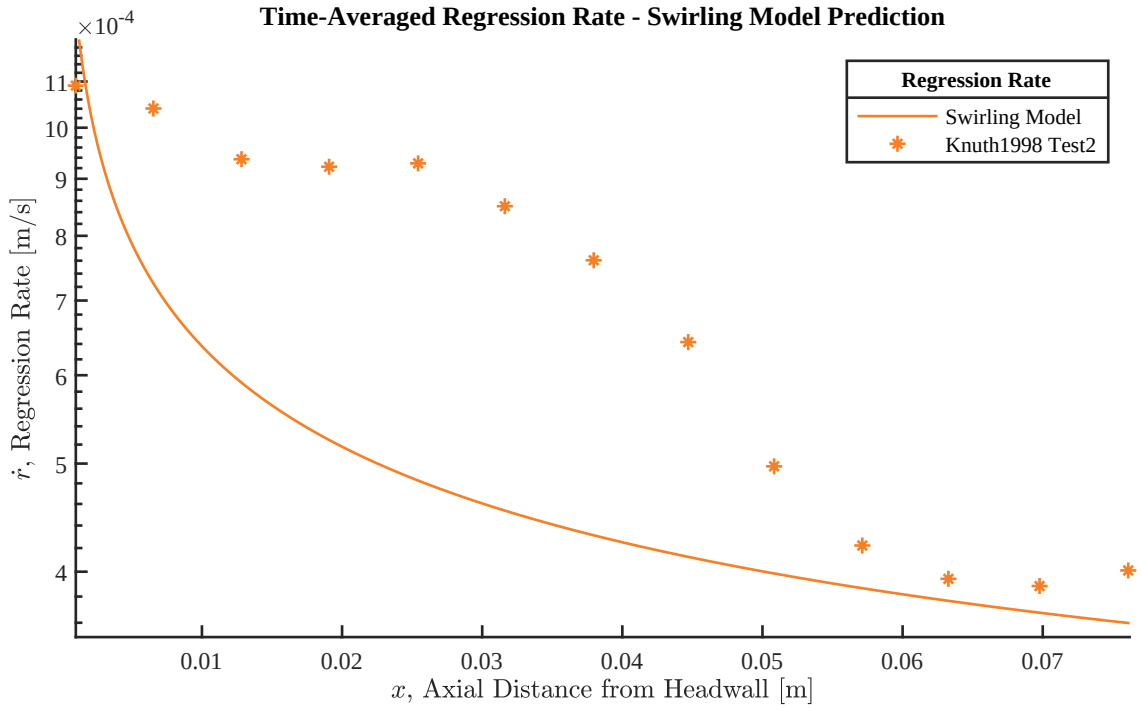

Figure 5.9. Locally-resolved regression rate prediction, computed using the complex-lamellar solution of Fleischmann and Majdalani [96], compared to "Knuth1998 Test2" test data for a rectified axial velocity profile. The prediction is manually adjusted to line up with this set of data so that the axial trends can be compared.

for the three tests, as described in Table 5.2. The swirl model presented in Chapter 4 predicts 6.23-, 5.82-, and 6.03-fold improvements for these same cases, which all agree to within ten percent relative error of the published values. Since all three motors share the same geometric and injection characteristics, differing only in mass flow rates, it is reasonable to consider them as a group. By averaging the three regression rates, Knuth et al. [25] report that an engine of this design should produce a regression rate 6.10 times greater than a traditional, axial-injection motor. Meanwhile, the numerical simulations performed here indicate an average increase of 6.03 times the traditional regression rate. The agreement between these two figures is remarkably good, with a relative error of only 1.1%. This is quite reassuring considering the appreciable jump in injection momentum ratio from 20.9 ($Sg = 19.4$) for most of the SOFT motors to 112.2 for the VIHRE. In fact, the disagreement falls within the estimated 5% measurement error associated with the experiment in question [25]. This result suggests that, despite near-complete disagreement in the predicted and observed local flow structure, the swirling regression rate model performs well in an average sense as long as the momentum ratio of the flow is correctly identified.

5.5 Summary

In this chapter, a cyclonic solution of the Beltramian type, which describes the mean flowfield of a non-reactive bidirectional vortex engine with sidewall mass addition, is extended so as to capture the effects of viscous damping both in the rotational core and wall layers. The technique relies on first establishing an inviscid model for the mean flow velocities under the assumption of axisymmetry. This assumption allows the use of the Bragg-Hawthorne equation as a starting point. The expressions for the outer, free-stream velocity components, along with the fundamental assumptions about the flow behavior, are subsequently used to simplify the incompressible Navier-Stokes equations into a set of suitable equations that prescribe the viscous motion in both the core and wall regions. Leading-order approximations to these boundary layer equations are then retrieved and mated to the inviscid, farfield solution using the method of matched-asymptotic expansions. Throughout this chapter, the ratio of sidewall-to-tangential injection speeds, ε, is employed as the primary perturbation parameter. This ensures that

the ensuing approximation remains valid as long as the magnitude of the tangential injection velocity remains significantly higher than the wall injection speed, which is guaranteed by the relatively modest grain regression rates in hybrid motors and the high injection velocities required to sustain a bidirectional vortex flowfield. Consequently, the correction in the tangential direction gives rise to a uniformly valid, triple-deck, composite expansion that secures the no-slip condition at the sidewall, suppresses the unbounded behavior at the centerline, and still displays free vortex characteristics in the intermediate, free-stream region. Along similar lines, the boundary layer, which develops along the sidewall in the axial direction, is treated using matched-asymptotic perturbative tools. After undergoing an intermediate variable transformation, a composite formulation for the axial velocity is achieved with a viscous correction near the wall that mirrors its tangential counterpart. This result confirms the consistent thickness of the wall boundary layer in both axial and tangential directions. As for the radial direction, a boundary layer analysis is precluded at leading order because of the assumedly uniform and orthonormal ejection of mass along the sidewall. Although a boundary layer correction can still be obtained, it only leads to a minor smoothing of the radial profile in the close vicinity of the wall. The sensitivity of the flow to variations in the swirl parameter, injection ratio, and Reynolds number is subsequently explored. In this process, expressions for the wall boundary layer thickness as well as the radial extent of the forced core region are retrieved. The subsequent application of the swirling regression model from Chapter 4 uncovers a weakness of the present flow solution, but the combination proves capable of analytically predicting the average improvement in regression rate for motors of this type with great success. In summary, the present solution stands as an essential counterpart to the article by Fleischmann and Majdalani [96] and advances the theoretical understanding of wall-bounded cyclonic motions by offering a uniformly valid Beltramian formulation on which future research may be based.

Chapter 6

Investigation of the Quadrupole Vortex Engine Concept

6.1 Introduction

In each of the vortex engine concepts shown in Fig. 1.2, the vortex motion produces temperature stratification as a consequence of centrifugal forces pushing the heavier, low-temperature gases outward. The circulation of cold gases in the vicinity of the wall may reduce the diffusion flame efficiency, thus impeding fuel regression and propulsive performance by preventing the heat transfer rate to the grain from reaching its full potential. To overcome this limitation of unidirectional or bidirectional vortex motions, swirl-induced quadrupoles can also be used to significantly enhance surface combustion and, as such, the fuel regression rate in hybrid propellant grains. The main objective of this chapter is therefore to explore the performance of a Quadrupole Vortex (QpV) in a right-cylindrical cavity by deriving a closed-form analytical solution that can mathematically describe its motion. The advent of a flowfield solution for the QpV engine is a crucial first step that precedes the execution of other essential research investigations incorporating: (i) the heat transfer enhancement entailed by the QpV motion using both theory and experiments; (ii) the inception, precession, and breakdown of the QpV flowfield; (iii) the overall impact of QpV

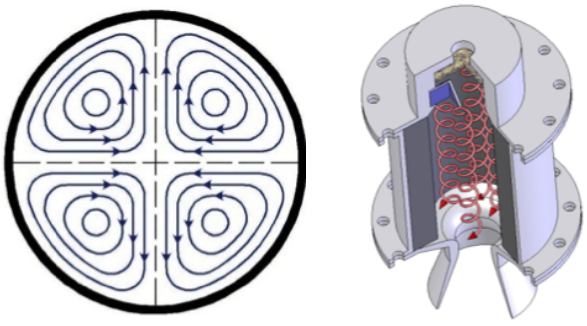

Figure 6.1. Four coaxial, counter-rotating vortices along the length of a right-cylindrical chamber.

motion on hybrid rocket engine performance at varying scales; and (iv) the benefits of QpV motion relative to conventional configurations.

In principle, a QpV-driven hybrid rocket chamber can combine simplicity and efficiency through an optimal core flow configuration, delivery system, and grain composition. According to Dake [135] and Dake and Majdalani [136], the establishment of a quadrupole vortex set appears to be among the simplest mechanisms capable of maximizing the rate of heat transfer in channel flow (Fig. 6.2(*a*)). Their findings also confirm the observations of Gak [137] and Pleshanova [138] in oval tubes (Fig. 6.2(*b*)), as well as other researchers who deliberately introduce vortices in cooling and heating applications [139–141].

In principle, the presence of four vortex cells promotes better mixing between the wall boundary layer and the flow along the chamber axis. This effect is induced by the continual circulatory motion that shuffles any unburnt, vaporized fuel into the turbulent and oxidizer-rich chamber core. The resulting motion also draws the hot gases from the center of the chamber and scrubs them across the grain surface, thus furthering the heat transfer and fuel erosion rates. This unique intercoiling stands to outperform the bidirectional vortex hybrid concept where a cool oxidizer is swirled along the chamber wall and a hot mixture is confined to the core region [17, 25, 36–39, 95]. Another advantage of the unidirectional QpV lies in its inherent simplicity, particularly in regard to injection systems. While more elegant options exist, vortex pairs may be initiated by simply affixing forward-swept tabs to the walls of a flow passage [135].

According to preliminary experiments conducted by Dake and Majdalani [136], the clover-leaf velocity pattern produced by the quadrupole vortex offers the potential for a dramatic

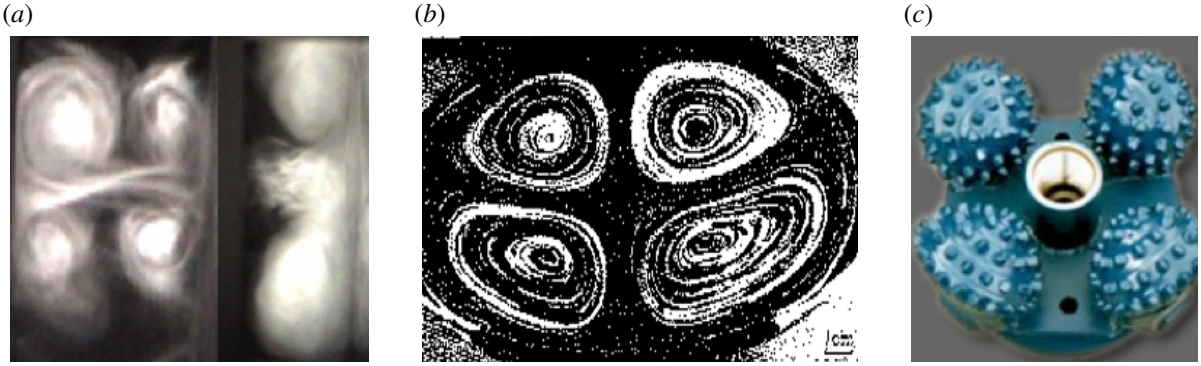

Figure 6.2. Quad vortices with common downwash produced within a) a tall channel [135] and b) a shallow oval tray [137, 138]. In part c) , the mechanically analogous rotary drill used in surface digging is depicted.

increase in the fuel regression rate. The high burning rate may be linked to the efficient scrubbing action associated with a motion similar to that of quad-cone petroleum drills (Fig. 6.2(c)): their four, circulating bits permit the passage of a hydraulic mixture that improves drilling rates and allows for the removal of slurry. In the case of a hybrid rocket, this role is assumed by the hot recirculating mixture. According to this analogy, the QpV clover-leaf pattern will maximize the heat transfer rate by ensuring that the grain surface is not swept by the low temperature oxidizer, as in the case of VIHRE, but rather the high temperature gases that originate from the turbulent core. The improved heat transfer rate will significantly enhance fuel vaporization while promoting the efficient transport of freshly ejected fuel particles from the wall boundary layer into the turbulent core, where intense mixing will, in turn, enhance combustion efficiency. To compensate for the scarcity of data on QpV behavior, this chapter aims at establishing a basic mathematical model that captures the character of the QpV flowfield in an effort to better understand and describe its benefits.

6.2 Mean Flow Analysis

6.2.1 Complex Potential Function

The starting point of this analysis is a description of the complex potential function used to derive the QpV flowfield in a polar plane. The analysis is launched by assuming that the vortices induced at the head end of the engine do not affect the streamwise velocity component, i.e., that the flow has a transversely-uniform velocity component in the z-direction. This one-way coupling assumption simplifies the analysis by locating all of the meaningful motion on the z-plane in the vicinity of the engine headwall region, where the swirl parameters are defined by virtue of the imposed flow circulation. However, it also introduces significant error if tab-style vorticators are used to induce the vortices as is likely for practical engines. Figure 6.3 illustrates the relevant geometry and coordinate system, showing the axes used in the upcoming analysis. Although the following approach may seem counter-intuitive, defining z to represent a variable in the complex plane, with u_x and u_y denoting the real and imaginary parts, simplifies the

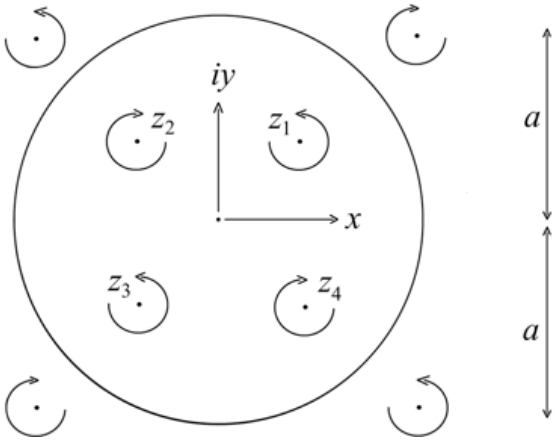

Figure 6.3. Coordinate system used in a z-plane.

analysis by permitting the use of the complex potential function in conjunction with the Milne-Thomson Circle Theorem. Proceeding in this manner also yields the benefit of collapsing the two velocity components into a single variable, which proves convenient when implementing the results of this analysis using a numerical solver over a mesh of grid points. By letting $z = x + iy$, the complex potential $f(z) = \phi + i\psi$ for a point vortex located at z_n may be expressed according to the Milne-Thomson Theorem [142] using

$$f(z) = ik \ln(z - z_n) \tag{6.1}$$

where the vortex strength k may be defined in terms of the core radius r_R and the solid-body angular velocity ω of the forced vortex core and, hence, the flow circulation Γ viz.

$$k = \frac{1}{2} r_R^2 \omega = \frac{1}{2\pi} \Gamma \tag{6.2}$$

According to the Milne-Thomson Circle Theorem, when the complex potential of an inviscid, incompressible flow with no boundaries is given by $f(z)$, the introduction of a circular-port cylinder of radius a normal to the z-plane gives rise to a new complex potential within the boundary of the cylinder such that

$$F(z) = f(z) + \bar{f}\left(\frac{a^2}{z}\right) \tag{6.3}$$

Finally, from the definitions of the stream function, potential function, and complex potential comes the expression

$$\frac{\mathrm{d}F}{\mathrm{d}z} = -u_x + iu_y \tag{6.4}$$

which facilitates a straightforward bulk flow representation of the velocity field once the complex potential is determined.

6.2.2 Potential Flow Solution

Using the method described heretofore, the complex potential for a flow consisting of four vortices that are anchored at four dissimilar points, z_1, z_2, z_3, and z_4, may be synthesized using the concept of superposition, namely,

$$f(z) = ik_1 \ln(z - z_1) + ik_2 \ln(z - z_2) + ik_3 \ln(z - z_3) + ik_4 \ln(z - z_4) \tag{6.5}$$

Then based on the Milne-Thomson Circle Theorem, the complex potential for four vortices enclosed by a circular boundary with radius a may be represented by

$$\begin{aligned} F(z) = {} & ik_1 \ln(z - z_1) - ik_1 \ln\left(z - a^2/\bar{z_1}\right) + ik_2 \ln(z - z_2) - ik_2 \ln\left(z - a^2/\bar{z_2}\right) \\ & + ik_3 \ln(z - z_3) - ik_3 \ln\left(z - a^2/\bar{z_3}\right) + ik_4 \ln(z - z_4) - ik_4 \ln\left(z - a^2/\bar{z_4}\right) \end{aligned} \tag{6.6}$$

At this juncture, the determination of explicit expressions for the axial and normal velocity components will depend on the differentiation and separation of both real and imaginary parts of Eq. (6.6). This process may be carried out in either order, with the first operation being less labor intensive than the other. For example, differentiating Eq. (6.6) gives

$$\begin{aligned} iu_y - u_x = \frac{\mathrm{d}(\phi + i\psi)}{\mathrm{d}z} = \frac{\mathrm{d}F(z)}{\mathrm{d}z} = {} & \frac{ik_1}{z - z_1} - \frac{ik_1}{z - a^2/\bar{z_1}} \\ & + \frac{ik_2}{z - z_2} - \frac{ik_2}{z - a^2/\bar{z_2}} + \frac{ik_3}{z - z_3} - \frac{ik_3}{z - a^2/\bar{z_3}} + \frac{ik_4}{z - z_4} - \frac{ik_4}{z - a^2/\bar{z_4}} \end{aligned} \tag{6.7}$$

Equation (6.7) may be relegated to a symbolic program or evaluated numerically for the real and imaginary parts of the right-hand-side fractional members. When it is preferable to

obtain explicit expressions for the velocity components and their potential function, this may be achieved by temporarily writing the complex numbers in modulus-amplitude form. The real parts may be then deduced from the resulting logarithm and the velocity potential equation identified as

$$\phi(x,y) = \sum_{n=1}^{4} \left\{ k_n \tan^{-1} \left[\left(y - \frac{y_n a^2}{x_n^2 + y_n^2} \right) \left(x - \frac{x_n a^2}{x_n^2 + y_n^2} \right)^{-1} \right] - k_n \tan^{-1} \left(\frac{y - y_n}{x - x_n} \right) \right\} \tag{6.8}$$

Due to the superimposed nature of this model, the form of Eq. (6.8) is not restricted to the present case of a quadrupole with $n \in [1,4]$. It may be modified to describe an arbitrary number of vortices contained in a cylindrical chamber by altering the upper bound on the summation term to reflect the number of desired vortices.

Up to this point, the position of each vortex has been left arbitrary, so long as it satisfies the geometric requirement of being located within the cylindrical boundary given by $x_n^2 + y_n^2 < a^2$. However, Eq. (6.8) may be further reduced by applying the physical conditions associated with quad symmetry in order to achieve a balanced quadrupole configuration, namely,

$$\begin{aligned} k_1 &= -k_2 = k_3 = -k_4 && \text{(counter-rotation, equal strength)} \\ x_1 &= -x_2 = -x_3 = x_4 && \text{(symmetry about the } y\text{-axis)} \\ y_1 &= y_2 = -y_3 = -y_4 && \text{(symmetry about the } x\text{-axis)} \end{aligned} \tag{6.9}$$

These equalities transform Eq. (6.8) into

$$\begin{aligned} \phi(x,y) = k_1 \Bigg\{ &- \tan^{-1} \left(\frac{y - y_1}{x - x_1} \right) + \tan^{-1} \left(\frac{y - y_1}{x + x_1} \right) - \tan^{-1} \left(\frac{y + y_1}{x + x_1} \right) + \tan^{-1} \left(\frac{y + y_1}{x - x_1} \right) \\ &+ \tan^{-1} \left(\frac{y - \Lambda y_1}{x - \Lambda x_1} \right) - \tan^{-1} \left(\frac{y - \Lambda y_1}{x + \Lambda x_1} \right) + \tan^{-1} \left(\frac{y + \Lambda y_1}{x + \Lambda x_1} \right) - \tan^{-1} \left(\frac{y + \Lambda y_1}{x - \Lambda x_1} \right) \Bigg\} \end{aligned} \tag{6.10}$$

where $\Lambda \equiv a^2/(x_1^2 + y_1^2)$ is introduced in the interest of brevity. With $\phi(x, y)$ in hand, it is a straightforward matter to extract the corresponding velocity components by taking

$$u_x = \frac{\partial \phi}{\partial x} = k_1 \left[\frac{y - y_1}{(x - x_1)^2 + (y - y_1)^2} - \frac{y - y_1}{(x + x_1)^2 + (y - y_1)^2} + \frac{y + y_1}{(x + x_1)^2 + (y + y_1)^2} \right.$$
$$- \frac{y + y_1}{(x - x_1)^2 + (y + y_1)^2} - \frac{y - \Lambda y_1}{(x - \Lambda x_1)^2 + (y - \Lambda y_1)^2} + \frac{y - \Lambda y_1}{(x + \Lambda x_1)^2 + (y - \Lambda y_1)^2}$$
$$\left. - \frac{y + \Lambda y_1}{(x + \Lambda x_1)^2 + (y + \Lambda y_1)^2} + \frac{y + \Lambda y_1}{(x - \Lambda x_1)^2 + (y + \Lambda y_1)^2} \right] \quad (6.11)$$

and

$$u_y = \frac{\partial \phi}{\partial y} = k_1 \left[- \frac{x - x_1}{(x - x_1)^2 + (y - y_1)^2} + \frac{x + x_1}{(x + x_1)^2 + (y - y_1)^2} - \frac{x + x_1}{(x + x_1)^2 + (y + y_1)^2} \right.$$
$$+ \frac{x - x_1}{(x - x_1)^2 + (y + y_1)^2} + \frac{x - \Lambda x_1}{(x - \Lambda x_1)^2 + (y - \Lambda y_1)^2} - \frac{x + \Lambda x_1}{(x + \Lambda x_1)^2 + (y - \Lambda y_1)^2}$$
$$\left. + \frac{x + \Lambda x_1}{(x + \Lambda x_1)^2 + (y + \Lambda y_1)^2} - \frac{x - \Lambda x_1}{(x - \Lambda x_1)^2 + (y + \Lambda y_1)^2} \right] \quad (6.12)$$

6.2.3 Piecewise Solution

It should be noted that Eq. (6.7) and Eqs. (6.11–6.12) are incomplete as stated due to the presence of singularities within the circular boundary; these free-vortex singularities violate the feasibility conditions for the Circle Theorem unless they are carefully suppressed. One avenue available to make headway is to follow the example of Park et al. [143] and patch a solid-body core over the vortex center to create a piecewise Rankine vortex [144]. The resulting vortices produce a velocity distribution that may be specified relative to the vortex centers according to:

$$\begin{aligned} u_r &= 0, \qquad u_\theta = k \frac{r}{r_R^2} \qquad \text{for} \qquad r \leq r_R \\ u_r &= 0, \qquad u_\theta = k \frac{1}{r} \qquad \text{for} \qquad r > r_R \end{aligned} \quad (6.13)$$

In reference to the origin of the present reference frame, these expressions yield

$$\begin{aligned} u_x^{(\mathrm{i})} &= k_n \frac{(y-y_n)}{r_R^2}, \qquad u_y^{(\mathrm{i})} = k_n \frac{(x-x_n)}{r_R^2} \qquad \text{for} \qquad \sqrt{(x-x_n)^2+(y-y_n)^2} \le r_R \\ u_x^{(\mathrm{o})} &= u_x, \qquad u_y^{(\mathrm{o})} = u_y \qquad \text{for} \qquad \sqrt{(x-x_n)^2+(y-y_n)^2} > r_R \end{aligned} \tag{6.14}$$

where $u_x^{(\mathrm{i})}, u_y^{(\mathrm{i})}$ and $u_x^{(\mathrm{o})}, u_y^{(\mathrm{o})}$ refer to the inner and outer vortex segments, respectively.

While the method of patching seems to be effective, certain precautions are necessary to ensure the validity of the model. Firstly, no vortex should be positioned within one core radius from the boundary in order to avoid possible interference from exterior singularities; furthermore, while oblique vortex collisions can typically be handled with acceptable accuracy, the inviscid nature of the solution allows for seemingly unrealistic collisions when adjacent vortices meet head-on. In practice, these restrictions do not prove to be too obtrusive, especially in what concerns the initial placement of the vortices. If, on the other hand, a dynamic simulation is attempted (as described below) with an insufficiently fine mesh, the model's inability to accurately reconcile vortex collisions will prescribe the stopping criteria for the simulation.

Naturally, the underlying assumption of uniform axial flow transforms the motion's dependence on time and space to a time-dependence only. This idealization, in turn, enables an iterative approximation of the velocity field down the bore. This may be achieved by computing the velocity of the vortex centers and incrementing the solution by a finite time step to calculate the new vortex location at a correspondingly small distance downstream. In a similar fashion, the model may be amended to account for a uniformly regressing grain surface by allowing the radius $a(t)$ to expand as a function of time. In fact, any of the inputs may be assumed to be variables with respect to time such that, for example, a vortex radius is increased while the flow is progressing downstream. Conveniently, the addition of grain regression does not alter the process of obtaining a mean flow expression because the correction may be applied after a fixed-parameter solution has already been derived. However, the unification of spatial and temporal dependence engenders a new imperative: when effects that are truly time-dependent, such as wall regression, are modeled concurrently with axially-dependent effects, such as vortex

expansion, care must be taken not to conflate the spatial and temporal interpretations of the time step used by each approximation. Failure to define independent time steps will lead to a model that corresponds to a conical rather than a cylindrical chamber.

6.2.4 Equilibrium Points

One of the primary motivations for choosing to use four vortices, when an arbitrary number can be described by Eq. (6.8), is the balanced nature offered by a quadrupole vortex configuration. Any even-numbered arrangement allows for each vortex to be bordered by a neighbor with opposite rotationality, which is essential to prevent the onset of imbalanced motion. A set of four in particular offers distinct advantages regarding the establishment and maintenance of the vortices. Just as importantly, a stable configuration is achievable for a quadrupole set. Specifically, there exists a set of equidistant equilibrium points about which the vortex centers tend to gyrate for a balanced set, when the circulation and spacing of each vortex is uniform as described by Eq. (6.9). If initiated exactly at these points, each of the vortices will exert an influence on the others so that the resultant velocity at each vortex center is identically zero. In this case, the position of the vortices will remain fixed in time. If initiated in the vicinity of these equilibrium points, the vortices gyrate around the point but remain confined to their quadrants in a repeating pattern that is effectively neutrally stable. If the vortices are initiated too far from the equilibrium points, the configuration is unstable and the vortex centers travel in increasingly wide paths around their quadrants until they are pushed up against the wall or each other. Although not accurately modeled by the present potential flow model, this situation is clearly not tenable in actual, viscous flow and will rapidly result in the dissolution of the flow structure. For this reason, an understanding of the location of the equilibrium points is highly desirable as a precursor to the design of any QpV motor.

Fortunately, the possession of a complete solution for the velocity field makes the derivation of these equilibrium points trivially easy. Starting with either Eq. (6.11) or Eq. (6.12), the velocity term is set to zero and the location of the vortices is simplified for a balanced and equidistant configuration by setting $x = y = x_1 = y_1$. Then, solving for x (or y) will give the position of the equilibrium point. Performing this procedure and reducing the resulting

expression leads to a surprisingly simple fourth-order algebraic equation for Λ:

$$0 = \Lambda^4 - 8\Lambda^2 - \Lambda \tag{6.15}$$

Solving Eq. (6.15) and converting back to one of the coordinate variables returns the exact solution for the equilibrium points in terms of the chamber radius:

$$x = y = a\sqrt{\frac{1}{2\sqrt{4+\sqrt{17}}}} \approx 0.418846101a \tag{6.16}$$

This solution is confirmed numerically to five decimal places using the code described in Sec. 6.3, which solves Eq. (6.7) rather than Eq. (6.11) and Eq. (6.12), in order to provide independent verification.

Whether an ideal motor should be designed with the vortices in perfect equilibrium is an open question. On one hand, this configuration will result in steady, predictable fuel regression. On the other hand, the regression will not be spatially uniform. It may not even be possible to maintain a QpV engine in perfect equilibrium for long burns or small diameter fuel grains, when the boundary will become appreciably non-circular as a result of uneven burning. The optimum solution is more likely to result from initializing the vortices at or near their equilibrium points and then allowing the configuration to drift toward a neutrally stable behavior as the port geometry gradually shifts and turbulence introduces chaotic perturbations. Such a configuration will maximize the coherence of the QpV structure and the accompanying benefits while still alleviating the pitfalls of uneven fuel consumption.

6.2.5 Pressure and Temperature Distributions

Once the velocity field is determined, the incompressible nature of the model also allows for a nearly effortless evaluation of the thermodynamic properties within the chamber. Using Bernoulli's equation, the pressure ratio may be obtained directly from

$$\frac{P}{P_0} = 1 - \frac{1}{2P_0}\rho_0 u^2 \tag{6.17}$$

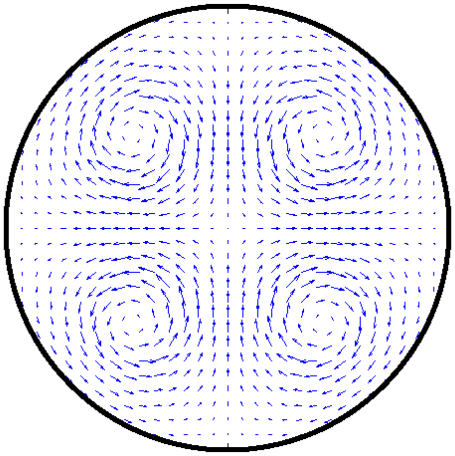

Figure 6.4. Potential flow solution for the quadrupole vortex engine.

Similarly, since the fluid under consideration is effectively inviscid and adiabatic, the isentropic relationships may be used to deduce the temperature ratio viz.

$$\frac{T}{T_0} = \left(\frac{P}{P_0}\right)^{\frac{\gamma-1}{\gamma}} = \left(1 - \frac{\rho_0 u^2}{2P_0}\right)^{\frac{\gamma-1}{\gamma}} \tag{6.18}$$

where ρ_0, P_0, and T_0 represent the total stagnation values taken at a common reference point. Equation (6.18) is, of course, only valid for the cold-flow case under consideration and not for realistic, combusting flow.

6.3 Theoretical Simulation Results

The formulation of Sec. 6.2.3 is used to write a program in MATLAB that calculates and displays the velocity field based on the specified inputs with the help of a custom function written by Long [145]. Figure 6.4 shows the results of a static simulation in which the distances are normalized by the cylinder radius and velocities are normalized by the maximum initial velocity, which is located at the edge of each vortex core. The vortices are located at $(\pm 0.4, \pm 0.4)$ and have core radii of 0.2. For the creation of Fig. 6.4, the mesh is left deliberately coarse, with $\Delta x = \Delta y = 0.067$, to avoid cluttering the display. Moreover, the non-dimensional value of the circulation is arbitrarily set to $\pm 2\pi$. The general pattern of the velocity field displays the expected behavior seen in experiments and CFD simulations, with stagnation points appearing

at the center as well as along the wall at the vertical and horizontal extremes, where opposing vortices cancel each other. The bulk flowfield is evenly divided into four cells corresponding to the four quadrants of the circular port with circulation that is confined solely within these cells.

In general, the tangential velocity near the wall varies greatly with the initial placement of the vortices and is not always applied evenly around the circumference of the chamber. The non-uniformity of the velocity near the wall has the potential to promote correspondingly non-uniform burning of the fuel in a QpV hybrid rocket, although it is important to keep in mind that burning will remain stable because regression retains a double symmetry. Simulations show that a disturbance in the tangential direction, such as a single vortex that is initialized slightly out of place, will cause the four vortices to rotate in unison around the axis of the chamber. Their orbiting motion will assuredly promote circumferentially uniform burning and reduce sliver formation, although the axial trend of fuel regression in this scenario is not well characterized by the simulations.

Next, a simulation is carried out to approximate the flowfield downstream of the initialization plane in order to draw qualitative conclusions about the nature of the QpV engine configuration. Using the same initial conditions as in Fig. 6.4 and a uniform axial component of velocity equal to the maximum velocity in the z-plane, the MATLAB code is run for successive stations, with the results indicating that the vortex centers follow spiraling paths in the same direction as the flow within their respective cells, as described in Sec. 6.2.4 and expected for vortices that are not in equilibrium. Figure 6.5 displays the resulting velocity vector fields at four evenly spaced stations between 2 and 2.75 radii downstream of the headwall. The vortex centers are pictured at various positions during their second cycle of revolution within the four quadrants.

The spiraling motion of the poles may be further illuminated by visualizing the flow in three dimensions. In this vein, Fig. 6.6 is used to display the three-dimensional streamlines of the flow corresponding to Fig. 6.5. Note that with the sole exception of the centerline, all streamlines make at least one helical rotation before reaching the aft end of the chamber. The evolution of a similar flow, displayed in Fig. 6.7(a), is compared to a flow where vortices are imposed in two tightly grouped pairs on opposing sides of the chamber (Fig. 6.7(b)). The

latter flow configuration is of interest due to the possibility of mounting triangular tabs to the chamber walls as a vortex generation mechanism. Evidently, imposing quad symmetry leads to highly stable and coherent vortices with good mixing characteristics. On the other hand, imposing vortices close together and near the wall results in high initial wall velocities that eventually dissipate their momentum to create lower velocity circulation cells that fill the entire chamber. In the absence of viscous damping and irrespective of the widely varying input values, the results of MATLAB simulations consistently predict a rotary motion of the poles that increases in both tangential speed and magnitude as the flow progresses downstream. This QpV characteristic should lead to a very efficient scrubbing effect when implemented in a hybrid motor. Additionally, perturbing the initial location of one or more vortices by a

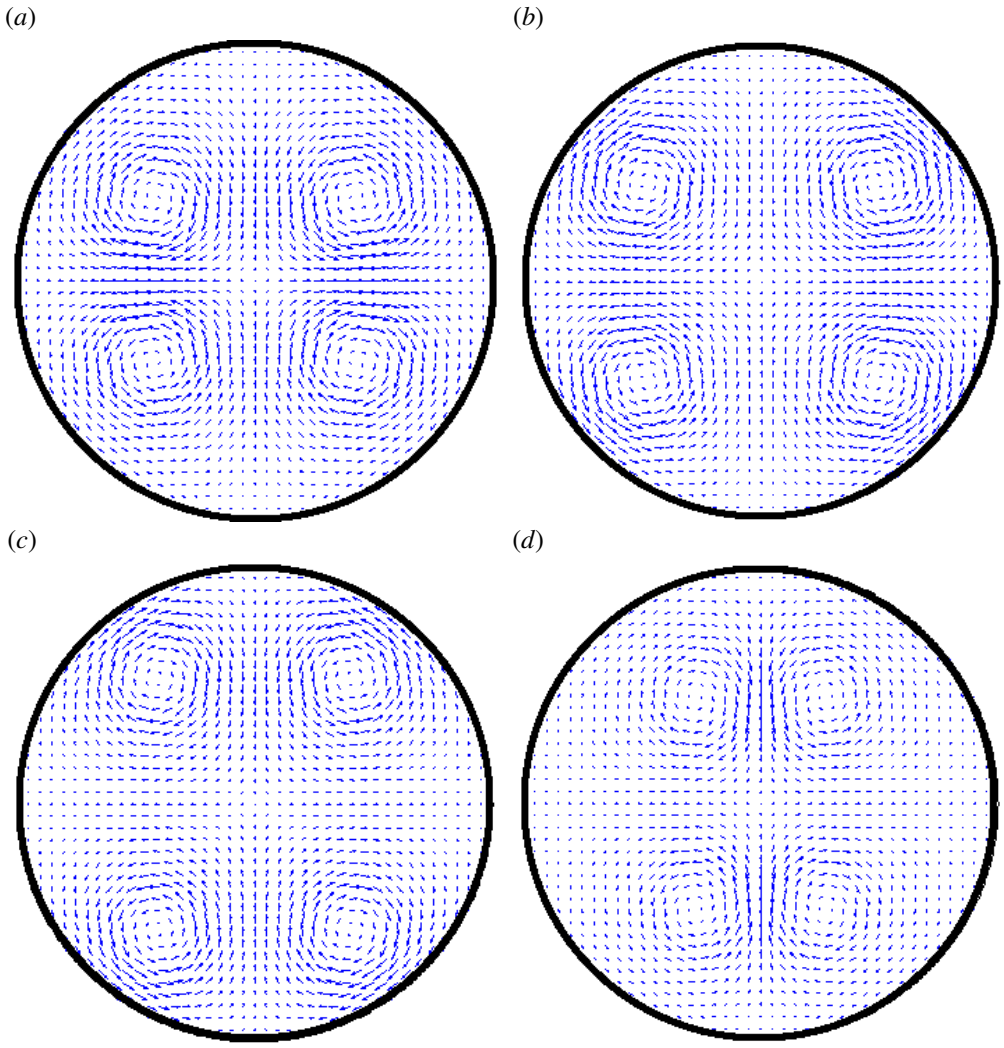

Figure 6.5. Normalized velocity fields at stations located a) $2a$, b) $2.25a$, c) $2.5a$, and d) $2.75a$ downstream of the chamber headwall.

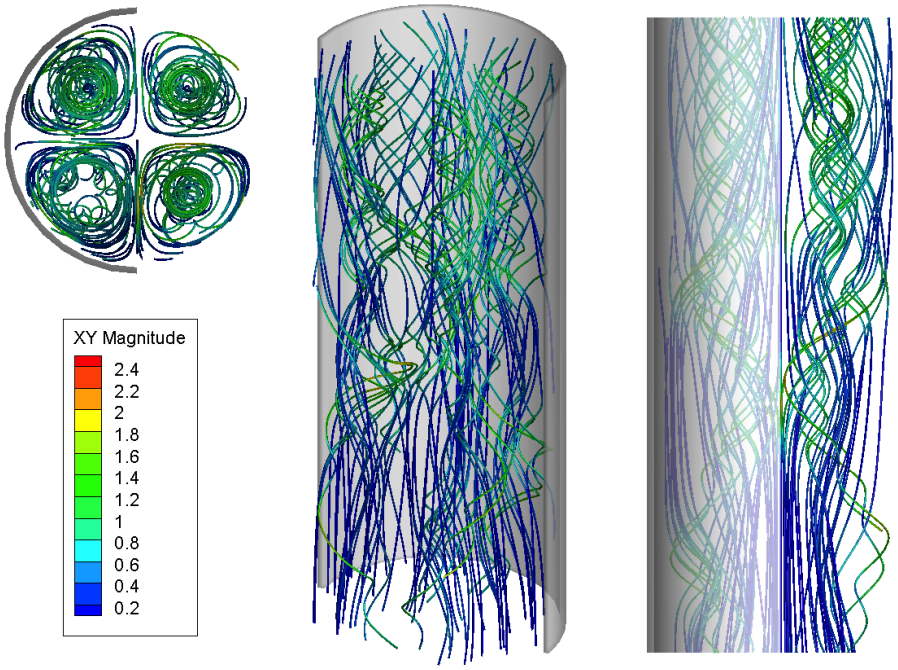

Figure 6.6. Streamlines of the flow corresponding to Fig. 6.5.

(*a*) (*b*)

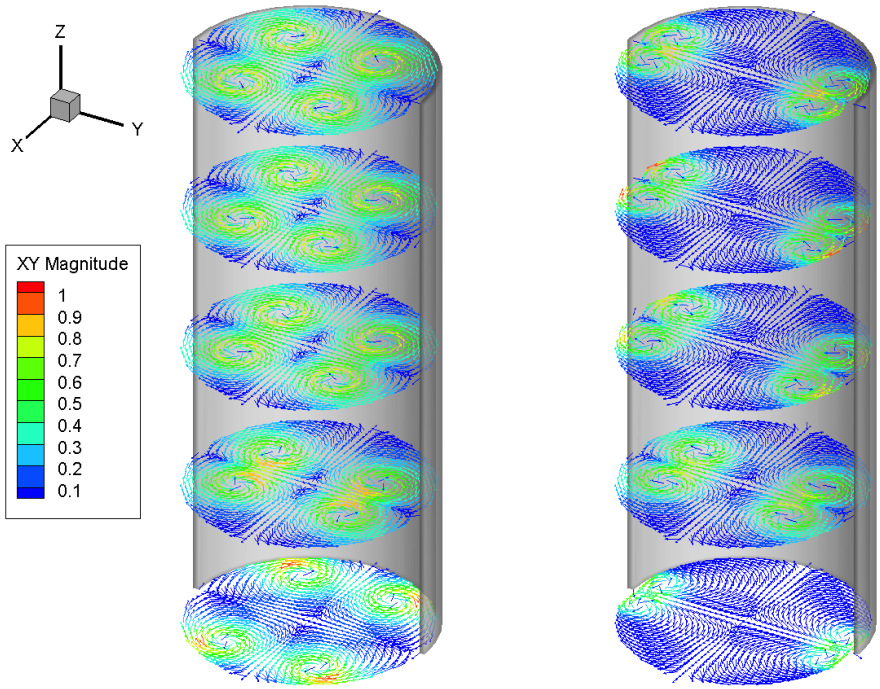

Figure 6.7. Normalized transverse velocity vectors for initial conditions representative of a) approximate quad symmetry and b) vortices induced by a pair of triangular vortex trippers.

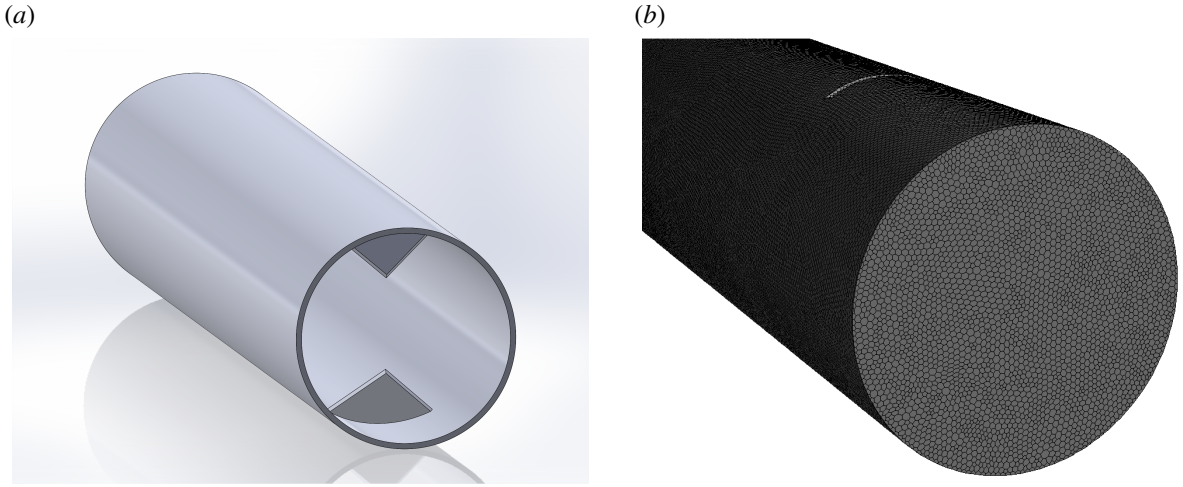

Figure 6.8. Configuration used in the CFD simulation with a) surface rendering of the chamber and triangular vorticators and b) the unstructured polyhedral mesh used to capture the quadrupole vortex evolution.

small distance leads to continuing asymmetric behavior over time that is characterized by strong cellular rotation as seen in the symmetric case. Otherwise, the simulated vortex motion displays effective mixing characteristics with very stable, dynamic structures.

6.4 CFD Simulation Results

Following prior work by Godfrey and Majdalani [146], a simple CFD simulation using the ANSYS suite of fluid dynamics software is used to validate the analytical solution provided here. The geometry for this analysis consists of a right cylinder that is 5.08 cm in diameter and 38.1 cm long, with two open ends (Fig. 6.8). Rather than the tangential injection scheme used in the previous study [146], the quadrupole vortex motion is induced by inserting a pair of triangular vortex trippers into the flow at an aggressive angle of attack of 60 degrees toward the inlet, as recommended by Dake and Majdalani [136]. Each vorticator consists of an isosceles triangle with a 2.54 cm base and a 1.9 cm height, thus subtending an apex angle of 67.4 degrees and two 2.29 cm sides. The base of each vorticator tab is positioned 5.08 cm downstream of the inlet. The geometry is created using SolidWorks and imported into ANSYS Workbench for further processing. Surfaces are defined based on the imported geometry, and then filled with an unstructured tetrahedral mesh. The default element size is 0.8 mm and the elements are permitted to grow to a maximum size of 0.16 cm at a growth rate of 1.2. Overall, the

mesh is very finely refined for the type of simulation being performed, with over 3.4 million tetrahedral elements that are reduced to approximately 634,000 polyhedral elements within Fluent. Figure 6.8 shows the relevant geometry both before and after meshing. As for the boundary conditions, they are imposed as follows: air with a uniform axial velocity of 1 m/s enters through the inlet while the outlet is set to atmospheric pressure. The simulation employs the realizable $k - \varepsilon$ viscous model. These conditions allow for a comparison of the potential flow model laid out in Sec. 6.2 to a more realistic, viscous case. Convergence of the simulation is quickly accomplished, with the continuity residual falling below 10^{-3}, which is the default and generally applicable threshold, after only 270 iterations. All other residuals are on the order of $5 \cdot 10^{-5}$ or lower.

The data derived from CFD simulations is qualitatively compared to the results obtained using the potential flow model in Fig. 6.9. The input parameters for the potential flow analysis

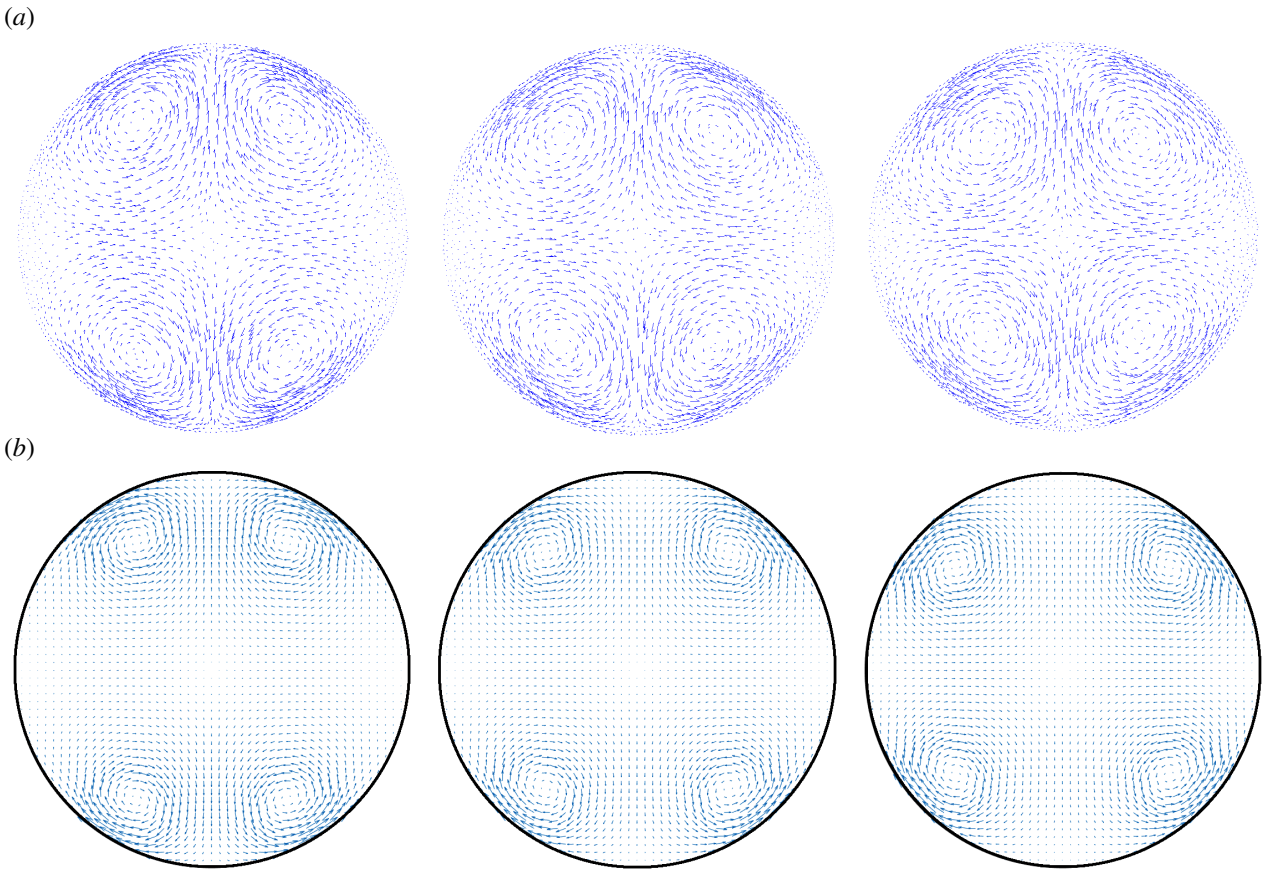

Figure 6.9. Comparison between a) the CFD results at three different axial stations of 6, 8, and 10 radii from the headwall and b) the corresponding potential flow predictions at the same locations. The MATLAB predictions are initialized 4 radii from the headwall with $r_R = 0.18a, \Gamma = \pm 2\pi/5$, and $z_n = (\pm 0.32a, \pm 0.75a)$.

are chosen to match the CFD solution four radii from the headwall (two radii downstream of the vortex trippers) in order to establish a common initial condition. The potential flow model is then used to predict the flow velocities for the remainder of the engine. Overall, the agreement is quite satisfactory. The CFD solution shows vortices that are evenly paired and move outward from their initial locations, which stands in good agreement with the MATLAB simulation. The flow near the walls agrees quite well between the two cases in light of the opposing boundary conditions applied to each model. One key distinction can be made between the two: transverse velocities in the CFD simulation exhibit definite axial decay as viscous forces act on the fluid. Whereas the theoretical vortices are ideally imposed and remain strong far downstream in the potential model, the optimum vortex occurs near the middle of the chamber in the viscous model, where balance is struck between full development and eventual dissipation. The structure of the vortices remains coherent over nearly the entire length of the chamber, but the magnitude of the swirling velocity falls off almost exponentially. On account of this effect, the plots in Fig. 6.9 are rescaled individually in order to maintain legibility. Despite this expected difference, the potential flow model seems capable of capturing the essential bulk motion of four vortices gyrating within their respective quadrants with a reasonable degree of accuracy, at least as far as the transverse velocities are concerned.

6.5 Regression Rate Prediction

Finally, the regression rate improvement that can be expected from the use of a quadrupole vortex configuration may be roughly estimated based on the regression rate model from Chapter 4 and using a technique from Sec. 5.4. Whereas this process benefits from reference data in the case of the BV engine, there is no such reference available for a QpV hybrid rocket engine. It is thus important to keep in mind that the predictions in this section are estimates that do not take into account the heat transfer enhancement caused by the rotary motion and increased temperature of the gaseous mixture. The exemplary performance that the swirl model has already demonstrated, for two dissimilar motor configurations relative to a wide range of experimental data, suggests that the prognostication may be reliable.

Three motors with identical operating conditions, two with QpV sets and one without any type of tangential velocity component, are simulated so that the relative increase in regression rate due to the application of the novel configuration may be ascertained. The reduced-order, quasi-one-dimensional regression rate model is applied to a dummy motor based on the "Sakurai2017 5-1" test from Chapter 4. This ensures that the general scaling is similar to other motors considered here and thus realistic. One key difference is that the mass flow rate is reduced so that the vortex strengths can likewise remain smaller than their practical values while scaling appropriately. This change is made in order to improve the stability of the simulation code, which tends to experience much higher numerical errors when simulating strong vortices. At each step within the main simulation code, a two-dimensional slice of the engine is discretized and solved, as in Sec. 6.3. The resulting velocity is then averaged circumferentially at the wall to calculate a mean swirl number for the regression rate prediction. According to these simulations, the fuel grain in a QpV engine with an equilibrium vortex placement will regress, on average, 46% faster than the non-swirling case. By switching the vortex placement to match that created by the triangular tabs in Sec. 6.4, the improvement is increased to 59%. The magnitude of these improvements depends on several parameters that are estimated, and so the results should be regarded as representative rather than authoritative.

Besides these predictions, two key aspects of the flow may be examined in a meaningful way: first, the difference in average swirl number based on initial vortex placement can be quantified, and, second, the vortex strength required to produce a certain average swirl number may be ascertained. Generally speaking, the performance of the QpV depends on the strength of the swirling motion in the same way as does the performance of a SOFT motor. In fact, the axial velocity is assumed to obey the same continuity-based governing equation given by Eq. (4.12) for all of the regression rate simulations since both motor types share the same geometry and combustion heating characteristics. Therefore, a combination of vortex strength and axial velocity that produces a certain swirl number will produce the same regression rate improvement in the QpV engines as in a SOFT engine, at least according to the simplified swirl model given by Eq. (4.19). Unfortunately, this discounts one of the primary motivations for developing a QpV engine, namely, the improved mixing between the core and boundary layer

fluid regions. On the other hand, it is true that a uni-directional swirl injection will produce a much higher concentration of mass flux close to the fuel grain, where it can have the greatest effect on the regression rate. A more complete evaluation of the unique benefits of the QpV flowfield will have to wait on the development of a more detailed regression model or fuller CFD simulations.

Returning to what *can* be deduced about the performance of a QpV engine from the available models, it is easily seen that three factors influence the average swirl strength in the z-plane. For a Rankine vortex, the maximum velocity occurs at the edge of the forced-vortex core:

$$u_{\max} = \omega r_R \tag{6.19}$$

This relation shows that the angular velocity (or any other measure of vortex strength, such as the circulation) and size of the core region control the maximum velocity of a single vortex within the engine. In an idealized scenario where vortices may be generated arbitrarily, Eq. (6.19) provides a simple avenue to control the interrelation between these first two factors. The interactions between multiple vortices and the boundary are much more complicated and so numerical evaluation of Eq. (6.7) is used to characterize the influence of initial vortex placement on the average swirl strength at the wall. Comparing the vortex placement from Fig. 6.9 to an identical set (with the same value of $u_{\max}$) placed in equilibrium permits a quantitative comparison of the two most likely initialization options. Within a single cross-sectional plane, the flowfield generated using vortex trippers produces an average velocity along the circumference of the chamber that is 99% higher than that of an equilibrium set. Since the vortices are placed near the wall, the velocities are high as the flow is forced to pass through a small space. This effect is sufficient to overcome the low velocities on the sides of the chamber furthest from the vortex centers. The equilibrium configuration produces a much more even distribution of velocities at the wall, but the distance from the vortices to the wall results in a lower overall average value.

When this effect is integrated into a regression rate prediction for a motor with the operating conditions of the "Sakurai2017 5-1" test and the vortex conditions from Fig. 6.9, the difference between vortex placements is almost non-existent. This difference depends heavily on the axial

velocity profile within the chamber by way of the mass flux, which in turn is sensitive to the regression rate, especially at the head end of the port. Decreasing the mass flow rate brings the difference between the two cases into sharper focus, as evidenced by the earlier predictions that deviate by 13%. In any case, the difference remains much smaller than would be expected by examining a single cross-sectional plane. The lesson to be learned here is that the difference in average regression caused by vortex placement is dampened by the self-regulating tendency of increased regression to diminish the swirl number downstream. Another key takeaway is that vortex placement will greatly impact the local (circumferential) burning trend in a manner reflective of the local velocity trends at the grain surface. Once again, the tab vortex trippers produce a higher axially-averaged regression rate at the expense of a much less uniform burning profile. It thus seems likely that it will be possible to tailor the desired regression profile and rate of a QpV engine by setting the vortex strengths and positions, even though the two are coupled. If an even-burning grain is desired, then a stable or neutrally-stable vortex placement will likely produce the best results. On the other hand, partially-symmetrical configurations such as those corresponding to the pattern created by a pair of opposed triangular tabs may have niche utility in non-circular ports. The inverse problem may also be solved: a knowledge of the flowfield created by the vortex generators will allow for the grain thickness to be customized to reduce sliver formation for any arrangement.

In terms of improvement over a non-swirling motor, the performance of a QpV engine once again depends heavily on the mass flow rates and vortex strength. As previously discussed, the best indication currently available is the vortex strength required to produce a certain average swirl number; this may then be taken as equivalent to a SOFT motor of identical strength. For the tab vorticator configuration studied, the ratio between the maximum velocity in a vortex and the average transverse velocity at the wall is 0.65. In comparison, the ratio for the equilibrium configuration is only 0.33. Comparing these ratios is equivalent to restating the aforementioned discovery that the tab generators are roughly twice as effective at translating imparted swirl to average swirl at the fuel surface. Accordingly, the angular velocity of each vortex that is required to produce a wall-average swirl equivalent to a geometric swirl number of 19.4, as in the experiments of Sakurai et al. [44] or Yuasa et al. [4], is 286 rad/s for the tab generators

and 568 rad/s for the equilibrium case. In comparison, the in-plane angular velocity created by the vorticator tabs in the CFD simulation of Sec. 6.4 is about 61 rad/s. This results in an equivalent injection swirl number of about 4.4, which, according to Tamura et al. [29], should result in an improvement of a little more than 50% compared to an identical, non-swirling motor. This projection aligns well with the earlier prediction by the numerical simulation scheme of a 59% increase based on the vortex strengths and positioning from the CFD simulation. Since the axial and transverse velocity components are highly coupled within this method of vortex generation, significant improvements in swirl number and hence regression rate beyond this level are unlikely using tabs unless the effect of a higher flame temperature is somehow accounted for in the regression rate swirl modifier. If a QpV set can be reliably created using another method with independent control of velocity components, then the outlook is more favorable. For example, generating each vortex in its own cylinder and then allowing them to collide in the port, as in [146], would only require tangential injection speeds of 1.43 m/s in order to achieve an $Sg = 19.4$ equivalent condition at the motor scale under consideration.

Throughout this discussion, the regression rate predictions are based on the assumption that the diffusion-limited model developed in Chapter 4 is applicable to the QpV engine. However, it is important to note that the unique characteristics of the QpV flowfield are not fully captured by this model and its underlying assumptions. In particular, the fact that the flow scrapes along the walls with high localized velocities before turning inward and carrying combustion products to the core of the motor has implications beyond the destratification of the mixture temperature. It is possible that the rapid entrainment of gasses from the boundary layer into the center of the engine will include reactants as well as products, thus effectively creating the opportunity for combustion to occur outside of a diffusion-limited environment. This behavior would represent a gaseous analog to the well-known droplet entrainment phenomenon observed in paraffin fuels [20] to which their heightened regression rates and present popularity may be ascribed. The unburned fuel in a QpV motor with sufficient vortex strength is convected to the core as a ready-to-burn gaseous to burn with available oxidizer in a kinetically limited process that is not impeded by the slow rate of species diffusion or droplet evaporation. Meanwhile, combustion products from the hot central core region will continue to be brought into contact

with the solid fuel in a strongly swirling vortex motion. It may be speculated that the strong mixing of oxidizer and fuel in the core region, coupled with the intense sweeping motion across the grain surface, can lead to much higher regression rates, namely, rates that are typically associated with a pre-mixed combustion process. As such, a hybrid QpV engine can potentially offer regression rates that exceed the present diffusion-limited model predictions by an entire order of magnitude, thus rivaling the burning rates of solid rockets while retaining the unique benefits that hybrid rockets continue to offer.

6.6 Summary

In this chapter, a velocity field solution for the quadrupole vortex is derived using the Milne-Thomson Circle Theorem. The resulting two-dimensional, potential flow model predicts that a quadrupole set of vortices confined to a cylindrical chamber can be made hydrodynamically stable and may indeed provide an alternative to other unidirectional and bidirectional vortex engines. An important product of this initial investigation is an analytical solution for the equilibrium points of a quadrupole vortex set. The velocity field solution and equilibrium point expression together reveal a great deal about the general behavior of a QpV flow and permit qualitative demonstrations of the bulk motion and the tendecy of the vortex positions to rotate within the chamber when initialized in an off-equilibrium arrangement. Although the analysis is greatly simplified and neglects many important physical realities, it represents an important first step on the journey toward fully evaluating the potential application of the QpV concept. Furthermore, a CFD simulation is performed and shows good qualitative agreement with the analytical mean flow approximation. This agreement indicates that, within the expected limitations dictated by its underlying assumptions, the predicitons generated by the potential flow model can indeed prove informative for the design of real motors. Finally, the application of the regression rate model from Chapter 4 reveals that a QpV engine will likely produce a modest improvement in regression rate over traditional motors. For the motor scale and conditions studied, this improvement is predicted to be about 60%, which is roughly equivalent to that offered by a SOFT engine with a geometric swirl number of approximately 4.4. It is expected that the actual improvement will be further boosted by the circulation of combustion gasses and

destratification offered by the QpV design, although this remains to be shown experimentally. If the establishment of coherent vortices using tangential injection can be demonstrated, then the QpV concept shows great promise for further increasing the regression rate in hybrid rockets in a highly customizable fashion.

Chapter 7

Summary and Conclusions

The field of hybrid rocketry is currently enjoying a resurgence of interest sparked by technological advances in propellant composition and chamber design. Swirl-driven hybrids stand to offer significant performance improvements over traditional motors without restricting propellant combinations or other design choices. As such, there is growing interest in developing predictive capabilities for the fuel regression rates of these engines. This dissertation attempts to address several sub-problems within this area so that the full potential of this promising technology may be realized. In the first chapter, an overview of the benefits and downsides to hybrid rocket technology is provided by way of introduction. Marxman's diffusion-limited regression rate model is then re-derived and thoroughly reviewed in the second chapter to set the stage for further extensions of the underlying concepts to swirl-driven hybrid rocket engines. Although other comprehensive reviews of classical regression rate modeling exist, the exposition given in this work offers a unique blend of brevity and detail that makes it ideal as a self-contained primer on the subject.

In the third chapter, an extensive literature review of existing analytical regression rate models is undertaken along with a summary of a few complementary numerical and experimental studies. Besides providing the community with an abridged compendium of related research efforts, this review permits a snapshot of the current state of the field of regression rate modeling in swirl-driven hybrid rockets, encompassing both areas of accord and points of contention. Key findings include the existence of unanimous agreement regarding the critical role of the swirl number in characterizing these engines, an ongoing schism over how best to measure and report the swirl number, and the importance of understanding the axial

variation of the swirl strength within a combustion chamber. A general agreement is also found that swirl-driven hybrids are controlled by convective heat transfer to an even greater extent than their axial-flow counterparts. Several research groups successfully employ modified versions of Marxman's model to describe solid fuel regression trends within their engines, usually by altering the mass flux term to account for the additional velocity component. The axial mass flux is observed by all researchers to relinquish its traditional role as the primary driver of regression rates in favor of some form of the ratio of tangential to axial momentum, expressed most often as a swirl number or an injection (tangential) mass flux. Various interpretations of the effect of increasing swirl strengths are put forward, including an argument that increasing swirl is functionally equivalent to augmenting the overall mass flux. More nuanced investigations reveal that non-uniformity of regression profiles along the length of the chamber is the prevalent condition in swirl-driven hybrids, although different factors are highlighted in the various explanations that accompany these studies. Phenomenological descriptions of the burning trends range in focus from the turbulent wall jet structure of the flow near the injectors, to the effect of central recirculation zones on the coherence of swirl, to axial acceleration as a result of combustion-driven flow heating. An attempt is made to unify these perspectives in the course of their discussion, and several key questions are identified for future investigation.

With a foundational understanding of the elements involved in hybrid rocket combustion established by the first three parts of the work, the fourth chapter proceeds onward to the derivation and validation of a simplified regression rate model for swirl-driven hybrid rockets. This model takes the form of a multiplicative modifier to the most common regression rule for non-swirling engines. This arrangement provides benefits in the form of conceptual simplicity and universal applicability and also offers the ability to conveniently calibrate predictions of swirl-driven engines based on data from test firings of their traditional counterparts. Fundamentally, the model is rooted in the same concept of an effective mass flux that has been successfully demonstrated by other researchers and produces a deceptively simple general expression. In order to retain this generality, the underlying development philosophy transfers the burden of detailed motor description away from the regression model itself and instead imposes the requirement of a two-dimensional velocity field solution for the motor under

consideration. For cylindrical engines with tangential injection and unidirectional swirl, this velocity field solution is accomplished through a quasi-one-dimensional solution of the compressible continuity equation and further consideration of the conservation of angular momentum within an idealized chamber. By taking into account the changes in flow composition and temperature, reasonable representations of the swirl number over the course of the burn are shown to permit accurate predictions of the associated regression rate profiles. To this end, a custom, fully-featured numerical simulation package is developed in order to mimic the progression of the combustion process in detail and without the need for more time-consuming CFD simulations. Once properly calibrated, the new regression rate expression shows comparable accuracy to the current state-of-the-art model. This accuracy is maintained over a wider set of experimental reference data than other regression models, proving that the new model is not restricted to any one test campaign.

The portability of the regression rate model developed in Chapter 4 is further demonstrated in Chapter 5, where the bidirectional vortex engine is studied in detail. The majority of the chapter is dedicated to the derivation of viscous corrections to improve an existing Beltramian flow solution for a hybrid bidirectional vortex engine similar to the one developed in the mid-1990s by Orbital Technologies Corporation. Starting with an appropriately simplified version of the Navier-Stokes equations for flow in the viscous regions of the engine, matched-asymptotic perturbation tools are employed to establish leading-order solutions for the tangential and axial velocity components near the centerline and wall of the engine. These asymptotic solutions remain valid as long as the blowing velocity from the fuel surface along the walls remains significantly smaller than the oxidizer injection velocity, which is already a necessary condition for the establishment of a coherent bidirectional vortex flowfield. In the process of developing the velocity field solution, expressions for the boundary layer thickness, extent of the forced core region, mantle location, and maximum tangential velocity are uncovered. All are found to depend on a new form of the vortex Reynolds number, which, along with the velocity solution itself, is shown to be a generalized version of an existing result for the flow in an analogous liquid rocket engine. After the velocity field is characterized, the new regression rate model is applied in order to test its extensibility. Although deficiencies in the underlying velocity

field solution preclude an accurate representation of the axial trends, the average regression rate improvement due to the bidirectional vortex configuration is predicted to within approximately one percent of the value published by the original investigators of the concept.

Finally, the sixth chapter introduces a new quadrupole vortex engine concept and initiates investigation into its prospects. As a first step, a potential-flow velocity field solution is derived to describe the motion of the fluid within a cross-sectional plane of the engine. While crude in comparison to the flowfield solution of the preceding chapter, the resulting set of expressions nevertheless proves sufficient to provide insight into the nature of a quadrupole vortex set. The hydrodynamic stability of vortex placement is given special attention, with dynamic simulations and an analytical solution for the equilibrium points combining to paint a picture of a stable flowfield with good mixing characteristics. A comparison of numerical evaluations of the analytical solution to a CFD simulation shows that the velocity field expressions are indeed capable of capturing the bulk characteristics of a real, viscous flow. However, this same CFD simulation identifies the sharp axial decay of in-plane vortex strength, even in the absence of combustion heating, as a potential obstacle to the practical application of the concept. Lastly, the new regression rate model is applied to this third engine type in order to quantify the effect of the engine design on the fuel regression. In particular, a vortex set placed in equilibrium is compared to an equivalent set generated by a pair of inclined tabs mounted within the chamber, opposite one another. While absolute statements are precluded by the absence of any solid reference, direct application of the model to a representative set of motors predicts an improvement of approximately 50-60% over a traditional motor. This figure is supported by a second, more general look at the vortex strength necessary to generate an effective swirl number that matches the better-studied unidirectional swirl motors that are discussed at length in earlier sections. As a rule, the tab method of vortex generation produces higher but distinctly less uniform regression rate profiles than the equilibrium arrangement. Many important aspects of the quadrupole vortex concept require further investigation, but the work presented in this document suggests that it shows promise as a viable design option if the vortices can be reliably maintained as the flow moves downstream.

Overall, this work represents a small part in the greater effort to fully characterize swirl-driven hybrid rockets so that their performance can be predicted and their designs better optimized. From the literature reviews, to the development of an improved regression rate model, to the establishment of analytical solutions for fluid flow within novel engine concepts, the efforts presented herein are all aimed at filling the need for an improved theoretical understanding of a technology that is being pushed forward largely by experiment and simulation. Hybrid rockets are poised to play a larger role in the future of chemical propulsion due to their safety and suitability for long-duration space missions, although their success in this area is not yet guaranteed. Rather, it will come about only as a result of continuous efforts to advance their capabilities. It is hoped that the findings brought to light in the course of this investigation will prove useful to other researchers and engineers in pursuit of similar objectives.

Bibliography

[1] Altman, D. and Humble, R., *Space Propulsion Analysis and Design*, McGraw Hill, 1995.

[2] Ronningen, J.-E. and Kubberud, N., "Hybrid Rocket Testing at NAMMO Raufoss A/S," *17th ESA Symposium on European Rocket and Balloon Programmes and Related Research*, edited by B. Warmbein, ESA SP-590, Sandefjord, Norway, 30 May - 2 June 2005, pp. 381–387.

[3] Yuasa, S., Shimada, O., Imamura, T., Tamura, T., and Yamoto, K., "A Technique for Improving the Performance of Hybrid Rocket Engines," *35th AIAA/ASME/SAE/ASEE Joint Propulsion Conference and Exhibit*, AIAA Papaer 1999-2322, June 1999. doi:10.2514/6.1999-2322.

[4] Yuasa, S., Shiraishi, N., and Hirata, K., "Controlling Parameters for Fuel Regression Rate of Swirling-oxidizer-flow-type Hybrid Rocket Engine," AIAA Paper 2012-4106, July 2012. doi:10.2514/6.2012-4106.

[5] Karabeyoglu, M., Cantwell, B., and Altman, D., "Development and testing of paraffin-based hybrid rocket fuels," *37th AIAA/ASME/SAE/ASEE Joint Propulsion Conference and Exhibit*, AIAA Paper 2001-4503, July 2001. doi:10.2514/6.2001-4503.

[6] Boiocchi, M., Maggi, F., Paravan, C., and Galfetti, L., "Paraffin-based Fuels and Energetic Additives for Hybrid Rocket Propulsion," *51st AIAA/SAE/ASEE Joint Propulsion Conference*, AIAA Paper 2015-4042, July 2015. doi:10.2514/6.2015-4042.

[7] Putnam, S. G., *Investigation of Non-Conventional Bio-Derived Fuels for Hybrid Rocket Motors*, Ph.D. dissertation, University of Tennessee - Knoxville, 2007.

[8] Altman, D., "Hybrid Rocket Development History," *27th AIAA/ASME/SAE/ASEE Joint Propulsion Conference and Exhibit*, AIAA Paper 1991-2515, June 1991, pp. 1–19. doi:10.2514/6.1991-2515.

[9] Marxman, G. and Gilbert, M., "Turbulent Boundary Layer Combustion in the Hybrid Rocket," *Eleventh Symposium (International) on Combustion*, Vol. 9, Ithaca, NY, USA, Aug. 1963, pp. 371–383. doi:10.1016/S0082-0784(63)80046-6.

[10] Marxman, G. A., Wooldridge, C. E., and Muzzy, R. J., "Fundamentals of Hybrid Boundary Layer Combustion," *Progress in Aeronautics and Astronautics*, Vol. 15, 1964, pp. 485–522. doi:10.1016/B978-1-4832-2730-6.50025-7.

[11] Marxman, G. A., "Combustion in the Turbulent Boundary Layer on a Vaporizing Surface," *Tenth Symposium (International) on Combustion*, Vol. 10, Cambridge, England, Aug. 1965, pp. 1337–1349. doi:10.1016/S0082-0784(65)80268-5.

[12] Marxman, G. A. and Wooldridge, C. E., "Research on the Combustion Mechanism of Hybrid Rockets," *Advances in Tactical Rocket Propulsion, AGARD Conference Proceedings No. 1*, La Jolla, California, USA, Aug. 1968, pp. 421–477.

[13] Marquardt, T. A. and Majdalani, J., "Advanced Manufacturing Enxtends the Operational Boundaries of Hybrids," *Aerospace America*, Vol. 57 (11), Dec. 2019, pp. 50.

[14] Marquardt, T. A. and Majdalani, J., "Toward Bigger and Better Hybrid Rockets," *Aerospace America*, Vol. 56 (11), Dec. 2018, pp. 26.

[15] Institution News Team, "James Clayton Lecture - BLOODHOUND SSC: The next stage. Interview with Richard Noble," *Institution of Mechanical Engineers*, 29 Nov 2017.

[16] Majdalani, J., "Analytical Models for Hybrid Rockets," *Fundamentals of Hybrid Rocket Combustion and Propulsion*, edited by M. J. Chiaverini and K. K. Kuo, Progress in Astronautics and Aeronautics, Chapter 5. AIAA Progress in Astronautics and Aeronautics, 1801 Alexander Bell Drive, Reston, Virginia 20191-4344, 2007, pp. 207–246. doi:10.2514/5.9781600866876.0207.0246.

[17] Majdalani, J., "Vortex Injection Hybrid Rockets," *Fundamentals of Hybrid Rocket Combustion and Propulsion*, edited by M. J. Chiaverini and K. K. Kuo, Progress in Astronautics and Aeronautics, Chapter 6. AIAA Progress in Astronautics and Aeronautics, 1801 Alexander Bell Drive, Reston, Virginia 20191-4344, 2007, pp. 247–276. doi:10.2514/5.9781600866876.0247.0276.

[18] Shotwell, R., "History of Mars Ascent Vehicle Development Over the Last 20 Years," *2016 IEEE Aerospace Conference*, IEEE, March 2016. doi:10.1109/aero.2016.7500823.

[19] Casillas, E., Shaeffer, C., Trowbridge, J., Casillas, E., Shaeffer, C., and Trowbridge, J., "Cost and Performance Payoffs Inherent in Increased Fuel Regression Rates," *33rd AIAA/ASME/SAE/ASEE Joint Propulsion Conference and Exhibit*, AIAA Paper 1997-3081, July 1997. doi:10.2514/6.1997-3081.

[20] Karabeyoglu, M. A., *Transient Combustion in Hybrid Rockets*, Ph.D. dissertation, Stanford University, 1998.

[21] Karabeyoglu, A., Zilliac, G., Cantwell, B. J., DeZilwa, S., and Castellucci, P., "Scale-Up Tests of High Regression Rate Paraffin-Based Hybrid Rocket Fuels," *Journal of Propulsion and Power*, Vol. 20, No. 6, Nov. 2004, pp. 1037–1045. doi:10.2514/1.3340.

[22] Karabeyoglu, A., Zilliac, G., Cantwell, B., Zilwa, S. D., and Castellucci, P., "Scale-up Tests of High Regression Rate Liquefying Hybrid Rocket Fuels," *41st Aerospace Sciences Meeting and Exhibit*, AIAA Paper 2003-1162, Jan. 2003. doi:10.2514/6.2003-1162.

[23] Story, G. T., Schnell, A., Yaghoubi, D., Karp, A. C., Nakazono, B., and Zilliac, G. G., "A Single Stage to Orbit Design for a Hybrid Mars Ascent Vehicle," *AIAA Propulsion and Energy 2019 Forum*, AIAA Paper 2019-3840, Aug. 2019. doi:10.2514/6.2019-3840.

[24] Evans, B. J. and Karabeyoglu, A. M., "Development and Testing of SP7 Fuel for Mars Ascent Vehicle Application," *53rd AIAA/SAE/ASEE Joint Propulsion Conference and Exhibit*, AIAA Paper 2017-4831, July 2017. doi:10.2514/6.2017-4831.

[25] Knuth, W. H., Chiaverini, M. J., Gramer, D. J., and Sauer, J. A., "Experimental Investigation of a Vortex-Driven High-Regression Rate Hybrid Rocket Engine," *34th AIAA/ASME/SAE/ASEE Joint Propulsion Conference and Exhibit*, AIAA Paper 1998-3348, July 1998. doi:10.2514/6.1998-3348.

[26] Cantwell, B. J., "Similarity solution of fuel mass transfer, port mass flux coupling in hybrid propulsion," *Journal of Engineering Mathematics*, Vol. 84, No. 1, June 2013, pp. 19–40. doi:10.1007/s10665-013-9624-y.

[27] Ozawa, K. and Shimada, T., "Performance of Mixture-Ratio-Controlled Hybrid Rockets Under Uncertainties in Fuel Regression," *Journal of Propulsion and Power*, Oct. 2020, pp. 1–14. doi:10.2514/1.b37970.

[28] Boardman, T. and Sutton, G., "Hybrid Propellant Rockets," *Rocket Propulsion Elements*, Chapter 15. John Wiley & Sons, Inc., 7th ed., 2001, pp. 579–607.

[29] Tamura, T., Yuasa, S., and Yamamoto, K., "Effects of Swirling Oxidizer Flow on Fuel Regression Rate of Hybrid Rockets," *35th AIAA/ASME/SAE/ASEE Joint Propulsion Conference and Exhibit*, AIAA Paper 1999-2323, June 1999. doi:10.2514/6.1999-2323.

[30] Paccagnella, E., Barato, F., Pavarin, D., and Karabeyoglu, A., "Scaling Parameters of Swirling Oxidizer Injection in Hybrid Rocket Motors," *Journal of Propulsion and Power*, Vol. 33, No. 6, Nov. 2017, pp. 1378–1394. doi:10.2514/1.b36241.

[31] Messineo, J., *Modélisation des instabilités hydrodynamiques dans les moteurs-fusées hybrides*, Ph.D. dissertation, Institut Supérieur de l'Aéronautique et de l'Espace (ISAE), Oct. 2016.

[32] Batterson, J. W. and Majdalani, J., "Biglobal Instability of the Bidirectional Vortex. Part 1: Formulation," *47th AIAA/ASME/SAE/ASEE Joint Propulsion Conference and Exhibit*, AIAA Paper 2011-5648, July 2011. doi:10.2514/6.2011-5648.

[33] Batterson, J. W. and Majdalani, J., "Biglobal Instability of the Bidirectional Vortex. Part 2: Complex Lamellar and Beltramian Motions," *47th AIAA/ASME/SAE/ASEE Joint Propulsion Conference and Exhibit*, AIAA Paper 2011-5649, July 2011. doi:10.2514/6.2011-56949.

[34] Pucci, J., "The Effects of Swirl Injector Design on Hybrid Flame-Holding Combustion Instability," *38th AIAA/ASME/SAE/ASEE Joint Propulsion Conference and Exhibit*, AIAA Paper 2002-3578, July 2002. doi:10.2514/6.2002-3578.

[35] Gloyer, P. W., Knuth, W. H., and Goodman, J., "Overview of Initial Research into the Effects of Strong Vortex Flow on Hybrid Rocket Combustion and Performance," *CSTAR Fifth Annual Symposium Paper N96-16953*, Jan. 1993.

[36] Knuth, W. H., Bemowski, P. A., Gramer, D. J., Majdalani, J., and Rothbauer, W. J., "Gas-Fed, Vortex Injection Hybrid Rocket Engine," SBIR Phase I, NASA Final Technical

Contract No. NAS8-40679, Orbital Technologies Corporation, Madison, Wisconsin, Aug. 1996.

[37] Knuth, W. H., Chiaverini, M. J., Sauer, J. A., and Gramer, D. J., "Solid-Fuel Regression Rate Behavior of Vortex Hybrid Rocket Engines," *Journal of Propulsion and Power*, Vol. 18, No. 3, 2002, pp. 600–609. doi:10.2514/2.5974.

[38] Knuth, W. H., Chiaverini, M. J., Gramer, D. J., Sauer, J. A., Clair, C. P. S., Whitesides, R. H., and Dill, R. A., "Preliminary Computational Fluid Dynamics Analysis of the Vortex Hybrid Rocket Chamber and Nozzle Flowfield," *34th AIAA/ASME/SAE/ASEE Joint Propulsion Conference and Exhibit*, AIAA Paper 1998-3351, July 1998. doi:10.2514/6.1998-3351.

[39] Knuth, W., Gramer, D., Chiaverini, M., and Sauer, J., "Development and testing of a vortex-driven, high-regression rate hybrid rocket engine," *34th AIAA/ASME/SAE/ASEE Joint Propulsion Conference and Exhibit*, AIAA Paper 1998-3507, July 1998. doi:10.2514/6.1998-3507.

[40] Chiaverini, M. J., Malecki, M. J., Sauer, J. A., Knuth, W. H., and Majdalani, J., "Vortex Thrust Chamber Testing and Analysis for O2-H2 Propulsion Applications," *39th AIAA/ASME/SAE/ASEE Joint Propulsion Conference and Exhibit*, AIAA Paper 2003-4473, July 2003. doi:10.2514/6.2003-4473.

[41] Knuth, W. K., Sauer, J. A., Malecki, M. J., Hall, C. D., and Chiaverini, M. J., "Final Report on Vortex Universal Stoichiometric Preburner (VUSP) - A Phase I SBIR Project," SBIR Phase I, NASA Final Technical Contract No. NAS8-02021, OTC-GS0120-FR-02-1, Orbital Technologies Corporation, Madison, Wisconsin, May 2002.

[42] Rice, E. E., Chiaverini, M. J., Malecki, M. J., St. Clair, C. P., Knuth, W. H., Gustafson, R. J., and Gramer, D. J., "Status Report on Mars ISRU CO/O2 Hybrid Engine Development and Testing," NASA Interim Technical Contract No. NASA CP-2001-210826, Orbital Technologies Corporation, Madison, Wisconsin, May 2001, pp. 189-192.

[43] Yuasa, S., Yamamoto, K., Hachiya, H., Kitagawa, K., and Oowada, Y., "Development of a Small Sounding Hybrid Rocket with a Swirl-Oxidizer Type Engine," *37th AIAA/ASME/SAE/ASEE Joint Propulsion Conference and Exhibit*, AIAA Paper 2001-3537, July 2001. doi:10.2514/6.2001-3537.

[44] Sakurai, T., Yuasa, S., Ando, H., Kitagawa, K., and Shimada, T., "Performance and Regression Rate Characteristics of 5-kN Swirling-Oxidizer-Flow-Type Hybrid Rocket Engine," *Journal of Propulsion and Power*, Vol. 33, No. 4, July 2017, pp. 891–901. doi:10.2514/1.b36239.

[45] Masugi, M., Ide, T., Sakurai, T., Yuasa, S., Shiraishi, N., and Shimada, T., "Visualization of Flames in Combustion Chamber of Swirling-Oxidizer-Flow-Type Hybrid Rocket Engines," *46th AIAA/ASME/SAE/ASEE Joint Propulsion Conference and Exhibit*, AIAA Paper 2010-6546, July 2010. doi:10.2514/6.2010-6546.

[46] Lee, C., Na, Y., and Lee, G., "The Enhancement of Regression Rate of Hybrid Rocket Fuel by Helical Grain Configuration and Swirl Flow," *41st AIAA/ASME/SAE/ASEE Joint Propulsion Conference and Exhibit*, July 2005. doi:10.2514/6.2005-3906.

[47] Lee, C., Na, Y., Hwang, Y. C., and Lee, S. T., "Turbulent Flow in the Helical Grain of Hybrid Rocket Fuel," *42nd AIAA/ASME/SAE/ASEE Joint Propulsion Conference and Exhibit*, July 2006. doi:10.2514/6.2006-4344.

[48] Walker, S. D., *High Regression Rate Hybrid Rocket Fuel Grains with Helical Port Structures*, Master's thesis, Utah State University, Logan, Utah, 2015.

[49] Caravella, Jr., J. R., Heister, S. D., and Wernimont, E. J., "Characterization of Fuel Regression in a Radial Flow Hybrid Rocket," *Journal of Propulsion and Power*, Vol. 14, No. 1, 1998, pp. 51–56. doi:10.2514/2.5265.

[50] Netzer, D. W., "Hybrid Rocket Internal Ballistics," Technical report, Chemical Propulsion Information Agency, Jan. 1972.

[51] Chiaverini, M. J., "Review of Solid-Fuel Regression Rate Behavior in Classical and Nonclassical Hybrid Rocket Motors," *Fundamentals of Hybrid Rocket Combustion and Propulsion*, edited by M. J. Chiaverini and K. K. Kuo, Vol. 218 of *Progress in Astronautics and Aeronautics*, Chapter 2. AIAA Progress in Astronautics and Aeronautics, 1801 Alexander Bell Drive, Reston, Virginia 20191-4344, 2007, pp. 37–126. doi:10.2514/5.9781600866876.0037.0126.

[52] Lees, L., "Convective Heat Transfer with Mass Addition and Chemical Reactions," *Combustion and Propulsion, Third AGARD Colloquium*, Palermo, Sicily, Italy, 1958, p. 451.

[53] Schlichting, H., *Boundary-Layer Theory*, McGraw-Hill Book Company, 7th ed., 1979. doi:10.1007/978-3-662-52919-5, Trans. J. Kestin.

[54] Knuth, W., Chiaverini, M., Gramer, D., and Sauer, J., "Solid-Fuel Regression Rate and Combustion Behavior of Vortex Hybrid Rocket Engines," *35th AIAA/ASME/SAE/ASEE Joint Propulsion Conference and Exhibit*, AIAA Paper 1999-2318, June 1999. doi:10.2514/6.1999-2318.

[55] Mickley, H. S. and Davis, R. S., "Momentum Transfer for Flow Over a Flat Plate with Blowing," Technical report, NACA TN-4017, 1957.

[56] Tewfick, O. E., "Some Characteristics of the Turbulent Boundary Layer with Air Injection," *AIAA Journal*, Vol. 1, No. 6, June 1963, pp. 1306–1312. doi:10.2514/3.1785.

[57] Lengellé, G., "Model Describing the Erosive Combustion and Velocity Response of Composite Propellants," *AIAA Journal*, Vol. 13, No. 3, March 1975, pp. 315–322. doi:10.2514/3.49697.

[58] Zilliac, G. and Karabeyoglu, M., "Hybrid Rocket Fuel Regression Rate Data and Modeling," *42nd AIAA/ASME/SAE/ASEE Joint Propulsion Conference and Exhibit*, AIAA Paper 2006-4504, July 2006. doi:10.2514/6.2006-4504.

[59] Bellomo, N., Barato, F., Faenza, M., Lazzarin, M., Bettella, A., and Pavarin, D., "Numerical and Experimental Investigation of Unidirectional Vortex Injection in Hybrid Rocket Engines," *Journal of Propulsion and Power*, Vol. 29, No. 5, Sept. 2013, pp. 1097–1113. doi:10.2514/1.b34506.

[60] Estey, P., Altman, D., and McFarlane, J., "An Evaluation of Scaling Effects for Hybrid Rocket Motors," *27th AIAA/ASME/SAE/ASEE Joint Propulsion Conference and Exhibit*, AIAA Paper 1991-2517, June 1991. doi:10.2514/6.1991-2517.

[61] Marxman, G. A., "Boundary Layer Combustion in Propulsion," *Eleventh Symposium (International) on Combustion*, Vol. 11, Berkely, CA, USA, Aug. 1967, pp. 269–289. doi:10.1016/S0082-0784(67)80153-X.

[62] Chiaverini, M. J., Serin, N., Johnson, D. K., Lu, Y.-C., Kuo, K. K., and Risha, G. A., "Regression Rate Behavior of Hybrid Rocket Solid Fuels," *Journal of Propulsion and Power*, Vol. 16, No. 1, Jan. 2000, pp. 125–132. doi:10.2514/2.5541.

[63] Wooldridge, C. E., Marxman, G. A., and Kier, R. J., "Investigation of Combustion Instability in Hybrid Rockets," Technical report, NASA Langley Research Center, Hampton, Virginia 23365, 1969.

[64] Miller, E., "Hybrid Rocket Combustion Regression Rate Model," *AIAA Journal*, Vol. 4, No. 4, 1966, pp. 752–753. doi:10.2514/3.3540.

[65] Smoot, L. D. and Price, C. F., "Regression Rates of Nonmetalized Hybrid Fuel Systems," *AIAA Journal*, Vol. 3, No. 8, 1965, pp. 1408–1413. doi:10.2514/3.3160.

[66] Smoot, L. D. and Price, C. F., "Regression Rates of Metalized Hybrid Fuel Systems," *AIAA Journal*, Vol. 4, No. 5, 1965, pp. 910–915. doi:10.2514/3.3566.

[67] Smoot, L. D. and Price, C. F., "Pressure Dependence of Hybrid Fuel Regression Rates," *AIAA Journal*, Vol. 5, No. 1, 1966, pp. 102–106. doi:10.2514/3.3914.

[68] Kosdon, F. J. and Williams, F. A., "Pressure Dependence of Nonmetalized Hybrid Fuel Regression Rates," *AIAA Journal*, Vol. 5, No. 4, April 1967, pp. 774–778. doi:10.2514/3.4061.

[69] Wooldridge, C. E. and Muzzy, R. J., "Internal Ballistic Considerations in Hybrid Rocket Design," *Journal of Spacecraft*, Vol. 4, No. 2, 1967, pp. 255–262. doi:10.2514/3.28844.

[70] Muzzy, R. J., "Applied Hybrid Combustion Theory," *8th Joint Propulsion Specialist Conference, AIAA-1972-1143*, New Orleans, LA, USA, Dec. 1972. doi:10.2514/6.1972-1143.

[71] Kumar, R. N. and Stickler, D. B., "Polymer-Degradation Theory of Pressure-Sensitive Hybrid Combustion," *Thirteenth Symposium (International) on Combustion*, Vol. 13 (1), Salt Lake City, UT, USA, 1971, pp. 1059–1072. doi:10.1016/S0082-0784(71)80104-2.

[72] Favaro, F. M., Sirignano, W. A., Manzoni, M., and DeLuca, L. T., "Solid-Fuel Regression Rate Modeling for Hybrid Rockets," *Journal of Propulsion and Power*, Vol. 29, No. 1, 2013, pp. 205–215. doi:10.2514/1.b34513.

[73] Ozawa, K. and Shimada, T., "A Theoretical Study of Combustion Stability in Vortex Injection Hybrid Rocket Engine," *Transactions of the Japan Society for Aeronautical and Space Sciences, Aerospace Technology Japan*, Vol. 12, No. ists29, 2014, pp. 53–61. doi:10.2322/tastj.12.pa_53.

[74] Ozawa, K. and Shimada, T., "Linear Combustion Stability Analysis of Uni-directional Vortex Injection Hybrid Rocket Engines," *50th AIAA/ASME/SAE/ASEE Joint Propulsion Conference and Exhibit*, AIAA Paper 2014-3455, July 2014. doi:10.2514/6.2014-3455.

[75] Ozawa, K. and Shimada, T., "Theoretical Prediction of Regression Rates in Swirl-Injection Hybrid Rocket Engines," *Progress in Propusion Physics*, 2016. doi:0.1051/eucass/201608283.

[76] Ozawa, K. and Shimada, T., "Performance of Mixture-Ratio-Controlled Hybrid Rockets for Nominal Fuel Regression," *Journal of Propulsion and Power*, March 2020. doi:10.2514/1.b37665.

[77] Greatrix, D. R., "Regression Rate Estimation for Standard-Flow Hybrid Rocket Engines," *Aerospace Science and Technology*, Vol. 13, No. 7, Oct. 2009, pp. 358–363. doi:10.1016/j.ast.2009.07.003.

[78] Wongyai, P. and Greatrix, D. R., "Regression Rate Estimation for Swirling-Flow Hybrid Rocket Engines," *50th AIAA/ASME/SAE/ASEE Joint Propulsion Conference and Exhibit*, AIAA Paper 2014-3750, July 2014. doi:10.2514/6.2014-3750.

[79] Wongyai, P. and Greatrix, D., "Regression Rate Estimation for Swirling-Flow Hybrid Rocket Engines," *Journal of Propulsion and Power*, 2016. doi:10.2514/1.B35761.

[80] Roy, B. J. and Frederick, R. A., "Overview of Vortex Injected Hybrid Rocket Engines-Regression Rate Modeling," *52nd AIAA/SAE/ASEE Joint Propulsion Conference*, AIAA Paper 2016-4530, July 2016. doi:10.2514/6.2016-4530.

[81] Dhir, V. and Chang, F., "Heat Transfer Enhancement Using Tangential Injection," *ASHRAE Transactions*, Vol. 98, 01 1992, pp. 383–390.

[82] Merkle, C. L. and Venkateswara, S., "Fundamental Phenomenon Fuel Decomposition and Boundary-Layer Combustion Processes with Applications to Hybrid Rocket Motors: Part II," Technical report, Final Contractor's Report to NASA, 1996.

[83] Chiaverini, M., Kuo, K., Peretz, A., and Harting, G., "Regression rate and heat transfer correlations for HTPB/GOX combustion in a hybrid rocket motor," *34th AIAA/ASME/SAE/ASEE Joint Propulsion Conference and Exhibit*, AIAA Paper 1998-3185, July 1998. doi:10.2514/6.1998-3185.

[84] Launder, B. and Rodi, W., "The Turbulent Wall Jet," *Progress in Aerospace Sciences*, Vol. 19, Jan. 1979, pp. 81–128. doi:10.1016/0376-0421(79)90002-2.

[85] Launder, B. E. and Rodi, W., "The Turbulent Wall Jet - Measurements and Modeling," *Annual Review of Fluid Mechanics*, Vol. 15, No. 1, Jan. 1983, pp. 429–459. doi:10.1146/annurev.fl.15.010183.002241.

[86] Barenblatt, G. I., Chorin, A. J., and Prostokishin, V. M., "The turbulent wall jet: A triple-layered structure and incomplete similarity," *Proceedings of the National Academy of Sciences*, Vol. 102, No. 25, June 2005, pp. 8850–8853. doi:10.1073/pnas.0503186102.

[87] Karabeyoglu, A., Zilwa, S. D., Zilliac, G., and Cantwell, B., "Transient Modeling of Hybrid Rocket Low Frequency Instabilities," *39th AIAA/ASME/SAE/ASEE Joint Propulsion Conference and Exhibit*, AIAA Paper 2003-4463, July 2003. doi:10.2514/6.2003-4463.

[88] Motoe, M., *Numerical Simulations of Combustive Flows in a Swirling-Oxidizer-Flow-Type Hybrid Rocket*, Ph.D. dissertation, The University of Tokyo, Bunkyo-ku, Tokyo, Japan, 2014.

[89] Motoe, M. and Shimada, T., "Numerical Simulations of Combustive Flows in a Swirling-Oxidizer-Flow-Type Hybrid Rocket," *52nd AIAA Aerospace Sciences Meeting*, AIAA Paper 2014-0310, Jan. 2014. doi:10.2514/6.2014-0310.

[90] Ozawa, K. and Shimada, T., "Flight Performance Simulations of Vertical Launched Sounding Rockets Using Altering-Intensity Swirling-Oxidizer-Flow-Type Hybrid Motors," *51st AIAA/ASME/SAE/ASEE Joint Propulsion Conference and Exhibit*, AIAA Paper 2015-3832, July 2015. doi:10.2514/6.2015-3832.

[91] Shimada, T., Yuasa, S., Nagata, H., Aso, S., Nakagawa, I., Sawada, K., Hori, K., Kanazaki, M., Chiba, K., Sakurai, T., Morita, T., Kitagawa, K., Wada, Y., Nakata, D., Motoe, M., Funami, Y., Ozawa, K., and Usuki, T., "Hybrid Propulsion Technology Development in Japan for Economic Space Launch," *Chemical Rocket Propulsion: A Comprehensive Survey of Energetic Materials*, edited by L. D. Luca, T. Shimada, V. P. Sinditskii, and M. Calabro, Springer Aerospace Technology. Springer International, Switzerland, 2017, pp. 545–575. doi:10.1007/978-3-319-27748-6.

[92] Mickley, H. S., Ross, R. C., Squyers, A. L., and Stewart, W. E., "Heat, Mass, and Momentum Transfer for Flow Over a Flat Plate with Blowing or Suction," Technical report, NACA TN-3208, 1954.

[93] Greatrix, D. R., "Model for Predicting Fuel Regression Rate in Hybrid Rocket Engines," *43rd AIAA/ASME/SAE/ASEE Joint Propulsion Conference and Exhibit*, AIAA Paper 2007-5346, July 2007. doi:10.2514/6.2007-5346.

[94] Beér, J. M. and Chigier, N. A., *Combustion Aerodynamics*, Krieger, Malabar, FL, 1983.

[95] Majdalani, J. and Vyas, A. B., "Rotational Axisymmetric Mean Flow for the Vortex Injection Hybrid Rocket Engine," *40th AIAA/ASME/SAE/ASEE Joint Propulsion Conference and Exhibit*, AIAA Paper 2004-3475, July 2004. doi:10.2514/6.2004-3475.

[96] Fleischmann, J. and Majdalani, J., "Complex Lamellar Helical Solution for Cyclonically Driven Hybrid Rocket Engines," *53rd AIAA Aerospace Sciences Meeting*, AIAA Paper 2015-0372, Jan. 2015. doi:10.2514/6.2015-0372.

[97] Marquardt, T. A. and Majdalani, J., "Beltramian Solution for Cyclonically Driven Hybrid Rocket Engines," *53rd AIAA/SAE/ASEE Joint Propulsion Conference*, AIAA Paper 2017-4638, July 2017. doi:10.2514/6.2017-4638.

[98] Greatrix, D. R., "Geometric Swirl Number and Hybrid Rocket Engine Performance," *54th AIAA/SAE/ASEE Joint Propulsion Conference*, AIAA Paper 2018-4442, July 2018. doi:10.2514/6.2018-4442.

[99] Hikone, S., Maruyama, S., Isiguro, T., and Nakagawa, I., "Regression Rate Characteristics and Burning Mechanism of Some Hybrid Rocket Fuels," *46th AIAA/ASME/SAE/ASEE Joint Propulsion Conference and Exhibit*, AIAA Paper 2010-7030, July 2010. doi:10.2514/6.2010-7030.

[100] Lee, T. S. and Potapkin, A., "The Performance of a Hybrid Rocket with Swirling GOx Injection," *Proceedings of the 11th International Conference on Methods of Aerophysical Research*, Defense Technical Information Center, Fort Belvoir, VA, July 2002, pp. 126–132.

[101] Franco, M., Barato, F., Paccagnella, E., Santi, M., Battiston, A., Comazzetto, A., and Pavarin, D., "Regression Rate Design Tailoring Through Vortex Injection in Hybrid Rocket Motors," *Journal of Spacecraft and Rockets*, Vol. 57, No. 2, March 2020, pp. 278–290. doi:10.2514/1.a34539.

[102] Motoe, M. and Shimada, T., "Head-End Injected Swirling Gas Flow in a Chamber," *45th AIAA/ASME/SAE/ASEE Joint Propulsion Conference and Exhibit*, AIAA Paper 2009-5025, Aug. 2009. doi:10.2514/6.2009-5025.

[103] Chang, F. and Dhir, V. K., "Turbulent flow field in tangentially injected swirl flows in tubes," *Int. J. Heat and Fluid Flow*, Vol. 15, No. 5, Oct. 1994, pp. 346–356. doi:10.1016/0142-727X(94)90048-5.

[104] Lengellé, G., "Solid-Fuel Pyrolysis Phenomena and Regression Rate, Part 1: Mechanisms," *Fundamentals of Hybrid Rocket Combustion and Propulsion*, edited by M. J. Chiaverini and K. K. Kuo, Vol. 218 of *Progress in Astronautics and Aeronautics*, Chapter 3. AIAA Progress in Astronautics and Aeronautics, 1801 Alexander Bell Drive, Reston, Virginia 20191-4344, 2007, pp. 127–166. doi:10.2514/5.9781600866876.0127.0166.

[105] Karabeyoglu, A., Cantwell, B., and Zilliac, G., "Development of Scalable Space-Time Averaged Regression Rate Expressions for Hybrid Rockets," *41st AIAA/ASME/SAE/ASEE Joint Propulsion Conference and Exhibit*, AIAA Paper 2005-3544, July 2005. doi:10.2514/6.2005-3544.

[106] ter Linden, A. J., "Investigations into Cyclone Dust Collectors," *Proceedings of the Institution of Mechanical Engineers*, Vol. 160, 1949, pp. 233–251. doi:10.1243/PIME_PROC_1949_160_025_02.

[107] Dahlstrom, D. A., "Cyclone Operating Factors and Capacities on Coal and Refuse Slurries," *Transactions of the American Institute of Mining and Metallurgical Engineers*, Vol. 184, No. 9, 1949, pp. 331–344.

[108] Falconer, S. A., "Some Recent Investigations with the Dutch State Mines Cyclone Separator on Fine Coal Slurries," *Transactions of the American Institute of Mining and Metallurgical Engineers*, Vol. 187, No. 11, 1950, pp. 790–800.

[109] Rietema, K., "Performance and Design of Hydrocyclones - I: General Considerations," *Chemical Engineering Science*, Vol. 15, No. 3-4, Sept. 1961, pp. 298–302. doi:10.1016/0009-2509(61)85033-1.

[110] Bloor, M. I. G. and Ingham, D. B., "The Flow in Industrial Cyclones," *Journal of Fluid Mechanics*, Vol. 178, No. 1, May 1987, pp. 507–519. doi:10.1017/S0022112087001344.

[111] Vyas, A. B. and Majdalani, J., "Exact Solution of the Bidirectional Vortex," *AIAA Journal*, Vol. 44, No. 10, Oct. 2006, pp. 2208–2216. doi:10.2514/1.14872.

[112] Majdalani, J. and Rienstra, S. W., "On the Bidirectional Vortex and Other Similarity Solutions in Spherical Coordinates," *Journal of Applied Mathematics and Physics (ZAMP)*, Vol. 58, No. 2, March 2007, pp. 289–308. doi:10.1007/s00033-006-5058-y.

[113] Majdalani, J. and Chiaverini, M. J., "On Steady Rotational Cyclonic Flows: The Viscous Bidirectional Vortex," *Physics of Fluids*, Vol. 21, No. 10, 2009, pp. 103603–15. doi:10.1063/1.3247186.

[114] Maicke, B. A. and Majdalani, J., "A Constant Shear Stress Core Flow Model of the Bidirectional Vortex," *Proceedings of the Royal Society of London, Series A*, Vol. 465, No. 2103, March 2009, pp. 915–935. doi:10.1098/rspa.2008.0342.

[115] Batterson, J. W. and Majdalani, J., "Sidewall Boundary Layers of the Bidirectional Vortex," *Journal of Propulsion and Power*, Vol. 26, No. 1, 2010, pp. 102–112. doi:10.2514/1.40442.

[116] Majdalani, J., "Exact Eulerian Solutions of the Cylindrical Bidirectional Vortex," *45th AIAA/ASME/SAE/ASEE Joint Propulsion Conference and Exhibit*, AIAA Paper 2009-5307, Aug. 2009. doi:10.2514/6.2009-5307.

[117] Majdalani, J., "Helical Solutions of the Bidirectional Vortex in a Cylindrical Cyclone: Beltramian and Trkalian Motions," *Fluid Dynamics Research*, Vol. 44, No. 6, Oct. 2012, pp. 065506–38. doi:10.1088/0169-5983/44/6/065506.

[118] Batterson, J. W. and Majdalani, J., "On the Viscous Bidirectional Vortex. Part 1: Linear Beltramian Motion," *46th AIAA/ASME/SAE/ASEE Joint Propulsion Conference and Exhibit*, AIAA Paper 2010-6763, July 2010. doi:10.2514/6.2010-6763.

[119] Batterson, J. W. and Majdalani, J., "On the Viscous Bidirectional Vortex. Part 2: Nonlinear Beltramian Motion," *46th AIAA/ASME/SAE/ASEE Joint Propulsion Conference and Exhibit*, AIAA Paper 2010-6764, July 2010. doi:10.2514/6.2010-6764.

[120] Batterson, J. W. and Majdalani, J., "On the Viscous Bidirectional Vortex. Part 3: Multiple Mantles," *46th AIAA/ASME/SAE/ASEE Joint Propulsion Conference and Exhibit*, AIAA Paper 2010-6765, July 2010. doi:10.2514/6.2010-6765.

[121] Akiki, G. and Majdalani, J., "On the Bidirectional Vortex with Arbitrary Endwall Velocity," *46th AIAA/ASME/SAE/ASEE Joint Propulsion Conference and Exhibit*, AIAA Paper 2010-6652, July 2010. doi:10.2514/6.2010-6652.

[122] Akiki, G. and Majdalani, J., "On the Viscous Bidirectional Vortex with Arbitrary Endwall Injection," *47th AIAA/ASME/SAE/ASEE Joint Propulsion Conference and Exhibit*, AIAA Paper 2011-5692, July 2011. doi:10.2514/6.2011-5692.

[123] Maicke, B. A. and Majdalani, J., "On the Compressible Bidirectional Vortex. Part 1: A Bragg-Hawthorne Stream Function Formulation," *50th AIAA Aerospace Sciences Meeting*, AIAA Paper 2012-1103, Jan. 2012. doi:10.2514/6.2012-1103.

[124] Maicke, B. A. and Majdalani, J., "On the Compressible Bidirectional Vortex. Part 2: A Beltramian Flowfield Approximation," *50th AIAA Aerospace Sciences Meeting*, AIAA Paper 2012-1104, Jan. 2012. doi:10.2514/6.2012-1104.

[125] Barber, T. A. and Majdalani, J., "Exact Eulerian Solution of the Conical Bidirectional Vortex," *45th AIAA/ASME/SAE/ASEE Joint Propulsion Conference and Exhibit*, AIAA Paper 2009-5306, Aug. 2009. doi:10.2514/6.2009-5306.

[126] Barber, T. A. and Majdalani, J., "New Exact Solution of the Bidirectional Vortex in a Conically-Shaped Cyclonic Chamber," *50th AIAA/ASME/SAE/ASEE Joint Propulsion Conference and Exhibit*, AIAA Paper 2014-3676, July 2014. doi:10.2514/6.2014-3676.

[127] Barber, T. A., Cecil, O., and Majdalani, J., "Complex-Lamellar Cyclonic Vortex in a Cylindrical Chamber with a Hollow Core," *51st AIAA/ASME/SAE/ASEE Joint Propulsion Conference and Exhibit*, AIAA Paper 2015-3848, July 2015. doi:10.2514/6.2015-3848.

[128] Smith, J. L., "An Experimental Study of the Vortex in the Cyclone Separator," *Journal of Basic Engineering âĂŞ Transactions of the ASME*, Vol. 84, No. 4, Dec. 1962, pp. 602–608. doi:10.1115/1.3658721.

[129] Smith, J. L., "An Analysis of the Vortex Flow in the Cyclone Separator," *Journal of Basic Engineering âĂŞ Transactions of the ASME*, Vol. 84D, No. 4, Dec. 1962, pp. 609–618. doi:10.1115/1.3658722.

[130] Wall, N. J., *Characterisation of Multiple Concentric Vortices in Hybrid Rocket Combustion Chambers*, Ph.D. dissertation, University of Sheffield, 2013.

[131] Bragg, S. L. and Hawthorne, W. R., "Some Exact Solutions of the Flow through Annular Cascade Actuator Disks," *Journal of the Aeronautical Sciences*, Vol. 17, No. 4, 1950, pp. 243–249. doi:10.2514/8.1597.

[132] Batchelor, G. K., "Axial Flow in Trailing Line Vortices," *Journal of Fluid Mechanics*, Vol. 20, No. 4, 1964, pp. 645–658. doi:10.1017/S0022112064001446.

[133] Majdalani, J., "Unified Framework for Modeling Swirl Dominated Helical Motions," *50th AIAA/ASME/SAE/ASEE Joint Propulsion Conference and Exhibit*, AIAA Paper 2014-3677, July 2014. doi:10.2514/6.2014-3677.

[134] Nayfeh, A. H., *Perturbation Methods*, Wiley-VCH Verlag GmbH & Co., Mörlenbach, Germany, 2004. doi:10.1002/9783527617609.

[135] Dake, T. J., *Application of Vortical Airflow to Electronics Thermal Management Systems*, Master's thesis, Marquette University, 2004.

[136] Dake, T. J. and Majdalani, J., "Improving Flow Circulation in Heat Sinks Using Quadrupole Vortices," *ASME 2009 InterPACK Conference, Volume 2*, ASME, 2009. doi:10.1115/interpack2009-89211.

[137] Gak, M. Z., "Laboratory Investigation of a Self-Excited Oscillation in a System of Four Vortices," *Izvestiya, Atmospheric and Oceanic Physics*, Vol. 17, No. 2, 1981, pp. 147–150.

[138] Pleshanova, L. A., "Self Oscillations in a Four Vortex System," *Izvestiya, Atmospheric and Oceanic Physics*, Vol. 18, No. 4, 1982, pp. 263–269.

[139] Fiebig, M., "Vortex Generators for Compact Heat Exchangers," *Journal of Enhanced Heat Transfer*, Vol. 2, No. 1-2, 1995, pp. 43–61. doi:10.1615/JEnhHeatTransf.v2.il-2.60.

[140] Fiebig, M., "Vortices, Generators and Heat Transfer," *Chemical Engineering Research and Design*, Vol. 76, No. 2, Feb. 1998, pp. 108–123. doi:10.1205/026387698524686.

[141] Jacobi, A. and Shah, R., "Heat transfer surface enhancement through the use of longitudinal vortices: A review of recent progress," *Experimental Thermal and Fluid Science*, Vol. 11, No. 3, Oct. 1995, pp. 295–309. doi:10.1016/0894-1777(95)00066-u.

[142] Milne-Thomson, L. M., *Theoretical Aerodynamics*, St. Martins Press, New York, NY, 1966.

[143] Park, J., Heister, S. D., and Sullivan, J., "Development of a Counter-Rotating Vortex Pair (CVP) Mixer for Aerospace Applications," *49th AIAA/ASME/SAE/ASEE Joint Propulsion Conference and Exhibit*, AIAA Paper 2013-3832, July 2013. doi:10.2514/6.2013-3832.

[144] Rankine, W. J. M., *A Manual of Applied Mechanics*, Richard Griffin and Co., London, UK, 1858.

[145] Long, W., "mat2tecplot: Program to create tecplot binary file (.plt)," CFD Online Forums, June 2012.

[146] Godfrey, B. and Majdalani, J., "CFD Modelling of a Quadrupole Vortex Inside a Cylindrical Channel for Research into Advanced Hybrid Rocket Designs," *Journal of Physics: Conference Series*, Vol. 548, Nov. 2014, pp. 012067. doi:10.1088/1742-6596/548/1/012067.

Appendix A

Derivation of Marxman's Blowing Correction

Close to the wall, $u \approx 0$ and $\partial u/\partial x \approx 0$ so that continuity becomes $\rho v = \rho_w v_w$ and, in the absence of an axial pressure gradient, the momentum equation can be written as

$$\tau = \tau_w + \rho_w v_w u \tag{A.1}$$

Substitution of $B = 2(\rho_w v_w)/(\rho_e u_e C_f)$ and $\tau_w = \frac{1}{2} C_f \rho_e u_e^2$ into Eq. (A.1) leads to

$$\tau = \tau_w (1 + B\phi) \tag{A.2}$$

where $\phi \equiv u/u_e$. Next, one may equate Eq. (A.2) to the definition of shear stress for a turbulent boundary layer:

$$\tau = (\mu + \rho\varepsilon) \frac{\partial u}{\partial y} \tag{A.3}$$

where ε represents the turbulent eddy diffusivity. This produces

$$\tau_w (1 + B\phi) = (\mu + \rho\varepsilon) \frac{\partial u}{\partial y} \tag{A.4}$$

Fully nondimensionalizing using $\mathrm{Re}_\delta \equiv \rho_e u_e \delta/\mu$, $\eta = y/\delta$, ϕ, and τ_w gives

$$\frac{1}{2} C_f (1 + B\phi) = \mathrm{Re}_\delta^{-1} \left(1 + \frac{\rho\varepsilon}{\mu}\right) \frac{\partial \phi}{\partial \eta} \tag{A.5}$$

According to Prandtl's mixing length concept, $\varepsilon \propto \eta^2 \partial\phi/\partial\eta$, where for the purpose of estimating ε, a power law profile such as $\phi = \eta^n$ may be used for the range of Reynolds numbers typical

of hybrid motors [20]. Then $\partial\phi/\partial\eta$ may be approximated as $n\eta^{n-1}$. Furthermore, since n is usually small ($\sim 1/7$), the eddy diffusivity becomes

$$\varepsilon \approx c\eta^{1+n} \approx c\eta \tag{A.6}$$

where c represents a constant that is proportional to the mixing length – its exact value proves immaterial to this analysis. Substituting Eq. (A.6) into Eq. (A.5) yields

$$\frac{1}{2}C_f\,(1+B\phi) = \mathrm{Re}_\delta^{-1}\left(1+\frac{\rho}{\mu}c\eta\right)\frac{\partial\phi}{\partial\eta} \tag{A.7}$$

Integration from the wall to the boundary layer edge, i.e., from 0 to 1 for both η and ϕ, leads to an expression for the skin friction coefficient as a function of Re_δ and B only:

$$\frac{1}{2}C_f = G\,(\mathrm{Re}_\delta)\,\frac{\ln(1+B)}{B} \tag{A.8}$$

Marxman [11] argues that since the Reynolds number and blowing parameter dependencies can be neatly separated in the expression for C_f, the functional form of $G\,(\mathrm{Re}_\delta)$ may be obtained by comparing Eq. (A.8) to known results in the absence of blowing, namely,

$$\frac{1}{2}C_{f_0} = G\,(\mathrm{Re}_\delta) = 0.0225\mathrm{Re}_\delta^{-0.25} \tag{A.9}$$

where a suitable empirical expression from Schlichting [53] is used. Thus,

$$\frac{1}{2}C_f = 0.0225\mathrm{Re}_\delta^{-0.25}\frac{\ln(1+B)}{B} \tag{A.10}$$

Evaluating Eq. (A.10) for the case of no blowing makes it obvious that

$$\frac{C_f}{C_{f_0}} = \left(\frac{\delta_0}{\delta}\right)^{0.25}\frac{\ln(1+B)}{B} \tag{A.11}$$

where (δ_0/δ) accounts for the thickening effect of mass addition and differentiates Marxman's expression from that of Lees in Eq. (2.17). At this point, one is left with the task of determining a

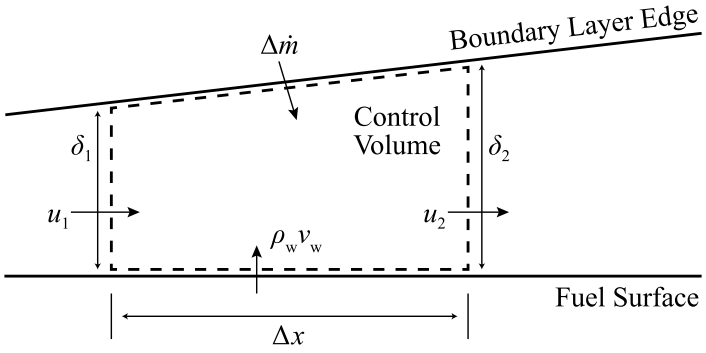

Figure A.1. Sketch of the control volume for the momentum integral analysis.

relation to describe δ in terms of B in Eq. (A.11). Such a relation may be obtained by performing a control volume analysis of the boundary layer to deduce an appropriate momentum integral expression. A sketch of a suitable control volume is provided in Figure. A.1. In this context, a statement of mass conservation (per unit thickness) across the control volume leads to

$$\Delta\dot{m} + \int_0^{\delta_1} \rho u_1 \mathrm{d}y - \int_0^{\delta_2} \rho u_2 \mathrm{d}y + \rho_w v_w \Delta x = 0 \tag{A.12}$$

Similarly, a statement of axial momentum conservation yields

$$u_e \Delta\dot{m} + \int_0^{\delta_1} \rho u_1^2 \mathrm{d}y - \int_0^{\delta_2} \rho u_2^2 \mathrm{d}y - \tau_w \Delta x = 0 \tag{A.13}$$

Rearranging and nondimensionalizing produces

$$\text{Mass:} \qquad \begin{aligned} \Delta\dot{m} + \frac{1}{2} C_f \rho u_e B \Delta x &= \rho u_e \delta_2 \int_0^1 \phi \mathrm{d}\eta - \rho u_e \delta_1 \int_0^1 \phi \mathrm{d}\eta \\ \frac{\Delta\dot{m}}{\rho u_e \Delta x} + \frac{1}{2} C_f B &= \frac{\delta_2 - \delta_1}{\Delta x} \int_0^1 \phi \mathrm{d}\eta \end{aligned} \tag{A.14}$$

$$\text{Momentum:} \qquad \begin{aligned} u_e \Delta\dot{m} + \frac{1}{2} C_f \rho u_e^2 \Delta x &= \rho u_e^2 \delta_2 \int_0^1 \phi^2 \mathrm{d}\eta - \rho u_e^2 \delta_1 \int_0^1 \phi^2 \mathrm{d}\eta \\ \frac{\Delta\dot{m}}{\rho u_e \Delta x} - \frac{1}{2} C_f &= \frac{\delta_2 - \delta_1}{\Delta x} \int_0^1 \phi^2 \mathrm{d}\eta \end{aligned} \tag{A.15}$$

Combining the expressions for conservation of mass, Eq. (A.14), and momentum, Eq. (A.15), produces

$$\frac{\delta_2 - \delta_1}{\Delta x} = \frac{1}{2} C_f \frac{1 + B}{\int_0^1 \phi\,(1 - \phi)\,\mathrm{d}\eta} = \frac{1}{2} C_f \frac{1 + B}{\beta} \tag{A.16}$$

where $\beta = \int_0^1 \phi\,(1 - \phi)\,\mathrm{d}\eta$ is related to the momentum thickness of the boundary layer by $\beta = \theta/\delta$. In the limit as $\Delta x \to 0$, the control volume becomes infinitesimal such that

$$\frac{\mathrm{d}\delta}{\mathrm{d}x} = \frac{1}{2} C_f \frac{1 + B}{\beta} \tag{A.17}$$

Substituting the expression for the skin friction found earlier as Eq. (A.10) into Eq. (A.17) leads to

$$\frac{\mathrm{d}\delta}{\mathrm{d}x} = 0.0225 \mathrm{Re}_\delta^{-0.25} \frac{\ln(1 + B)}{B} \frac{1 + B}{\beta} = 0.0225 \frac{\ln(1 + B)}{B} \frac{1 + B}{\beta} \left(\frac{\rho u_\mathrm{e}}{\mu} \right)^{-0.25} \delta^{-0.25} \tag{A.18}$$

Subsequent integration over the boundary layer yields

$$\frac{\delta}{x} = \left[0.02813 \frac{\ln(1 + B)}{B} \frac{1 + B}{\beta} \right]^{0.8} \mathrm{Re}_x^{-0.2} \tag{A.19}$$

and so

$$\frac{\delta_0}{\delta} = \left[\frac{\beta}{\beta_0} \frac{B}{(1 + B)\ln(1 + B)} \right]^{0.8} \tag{A.20}$$

Finally, combining Eq. (A.20) with Eq. (A.11) leads to an expression for the blowing correction in terms of the blowing parameter, specifically

$$\frac{C_f}{C_{f_0}} = \left[\frac{\beta}{\beta_0} \frac{B}{(1 + B)\ln(1 + B)} \right]^{0.2} \frac{\ln(1 + B)}{B} = \left[\frac{\beta}{\beta_0} \frac{1}{(1 + B)} \right]^{0.2} \left[\frac{\ln(1 + B)}{B} \right]^{0.8} \tag{A.21}$$

where β depends on the velocity profile ϕ, which may be approximated rather straightforwardly. Starting with Eq. (A.4), it is easy to show that

$$\frac{\partial \phi}{\partial \eta} = \frac{\tau_\mathrm{w} \delta}{u_\mathrm{e}\,(\mu + \rho\varepsilon)} (1 + B\phi) = f\,(y, B)\,(1 + B\phi) \tag{A.22}$$

When $\beta = 0$, the assumption of a power law profile $\phi = \eta^n$ is again made such that $\partial\phi/\partial\eta = n\eta^{n-1}$, which simplifies the unknown function $f(y, B)$ to the assumed form $f(B)\, n\eta^{n-1}$ with the requirement that $f(0) = 1$. For $n = \frac{1}{7}$, Eq. (A.22) becomes

$$\frac{\partial\phi}{\partial\eta} = f(B)\,\eta^{-6/7}\left(1 + B\eta^{1/7}\right) \tag{A.23}$$

Integrating Eq. (A.23) and evaluating at the boundaries, as with Eq. (A.7), leads to

$$\phi = \frac{\eta^{1/7}\left(1 + \frac{1}{2}B\eta^{1/7}\right)}{1 + \frac{1}{2}B} \tag{A.24}$$

Finally, the expression for ϕ permits the evaluation of β from its definition:

$$\beta = \frac{7\left(1 + \frac{13B}{10} + \frac{4B^2}{11}\right)}{72\left(1 + \frac{B}{2}\right)^2} \tag{A.25}$$

It is clear that in the case with no blowing (with $B = 0$), β reduces to $\beta_0 = \frac{7}{72}$ such that

$$\frac{\beta}{\beta_0} = \frac{\left(1 + \frac{13B}{10} + \frac{4B^2}{11}\right)}{\left(1 + \frac{B}{2}\right)^2} \tag{A.26}$$

Appendix B

Regression Rate Plots for Space-Time-Averaged Data

This appendix contains plots comparing each of the available space-time-averaged regression rate datasets to the prediction produced by

$$\dot{r} = aG^n x^m \left[1 + (3.75S)^2\right]^{0.18} \qquad \text{(4.19 Revisited)}$$

The remaining calibration constants a, n, and m vary from one set of data to another and are listed in Table 4.3. All plots have a logarithmic ordinate and linear abscissa. A complete summary of the error data for these plots appears in Table 4.6. The quality of the predictions is discussed in Sec. 4.3.3.

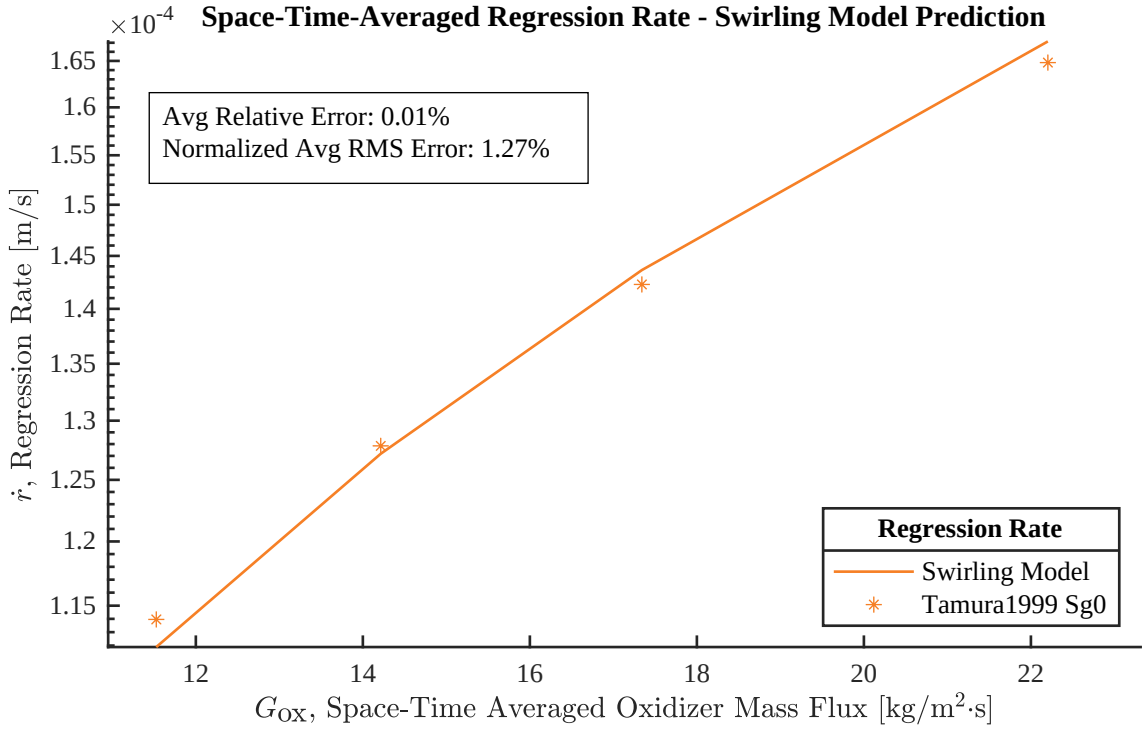

Figure B.1. Regression rate prediction compared to "Tamura1999 Sg0" test data.

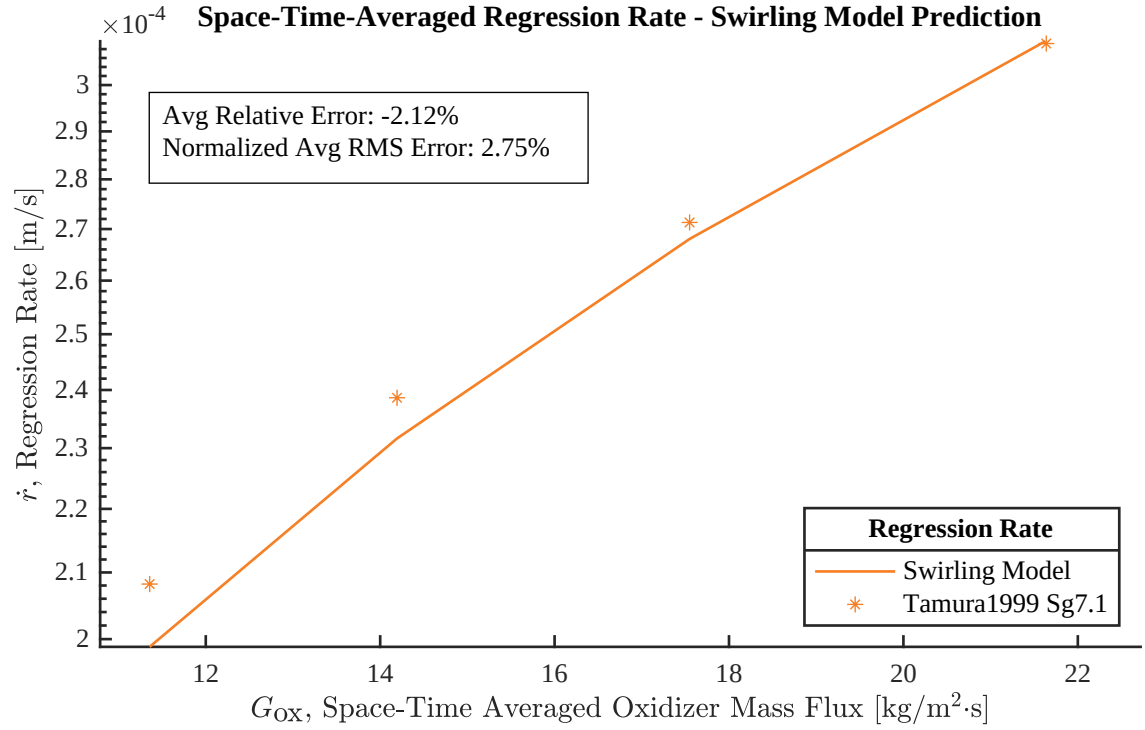

Figure B.2. Regression rate prediction compared to "Tamura1999 Sg7.1" test data.

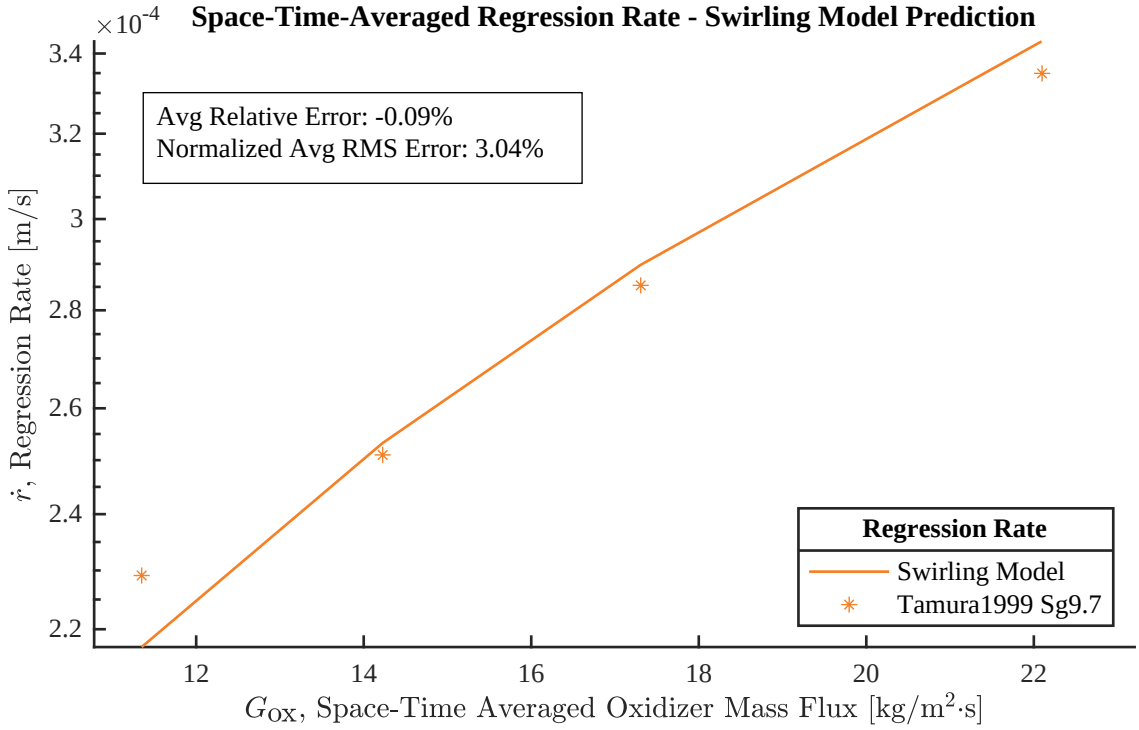

Figure B.3. Regression rate prediction compared to "Tamura1999 Sg9.7" test data.

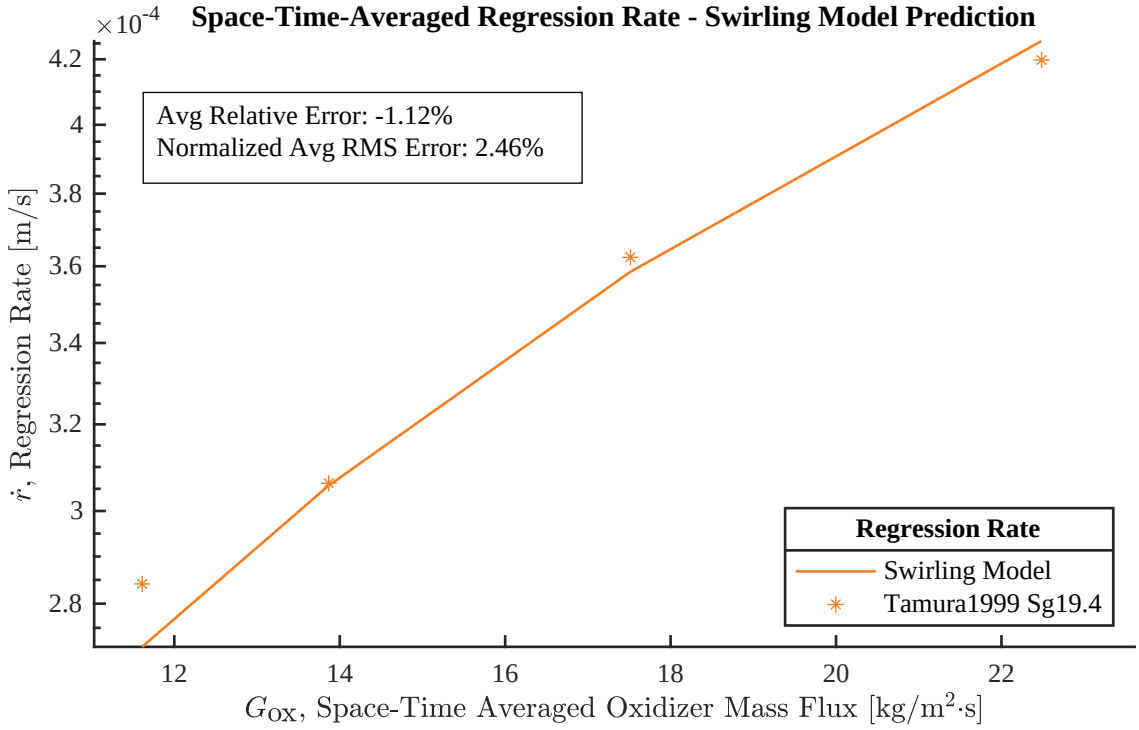

Figure B.4. Regression rate prediction compared to "Tamura1999 Sg19.4" test data.

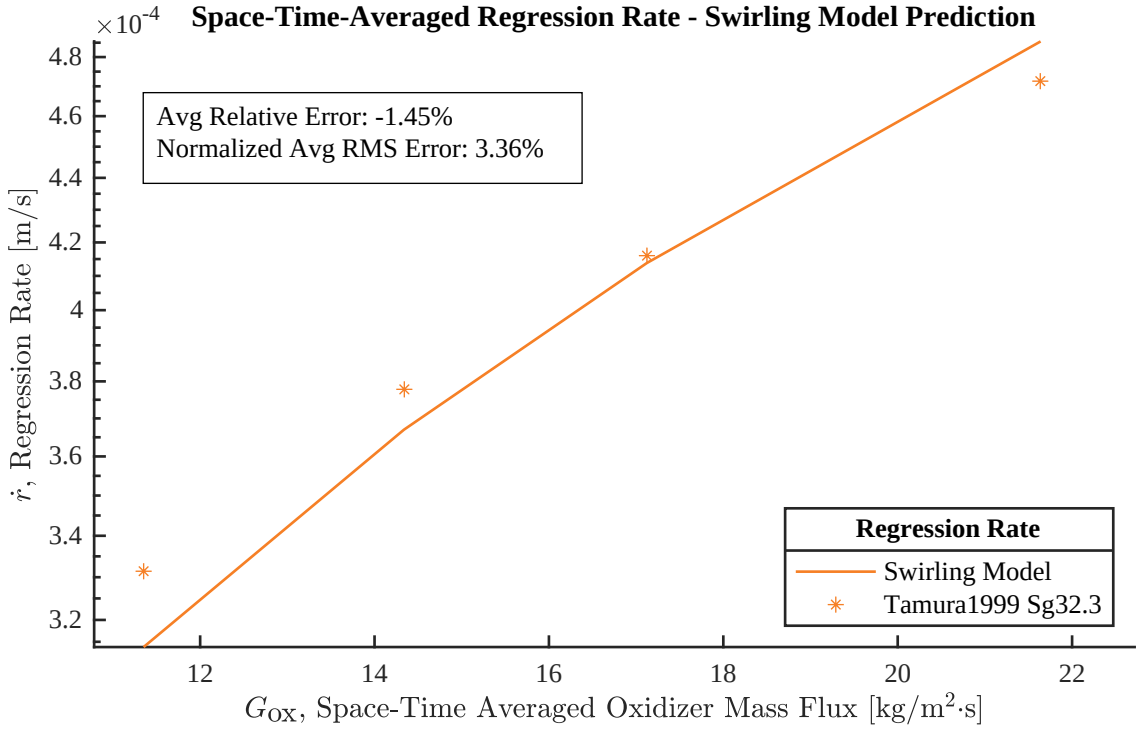

Figure B.5. Regression rate prediction compared to "Tamura1999 Sg32.3" test data.

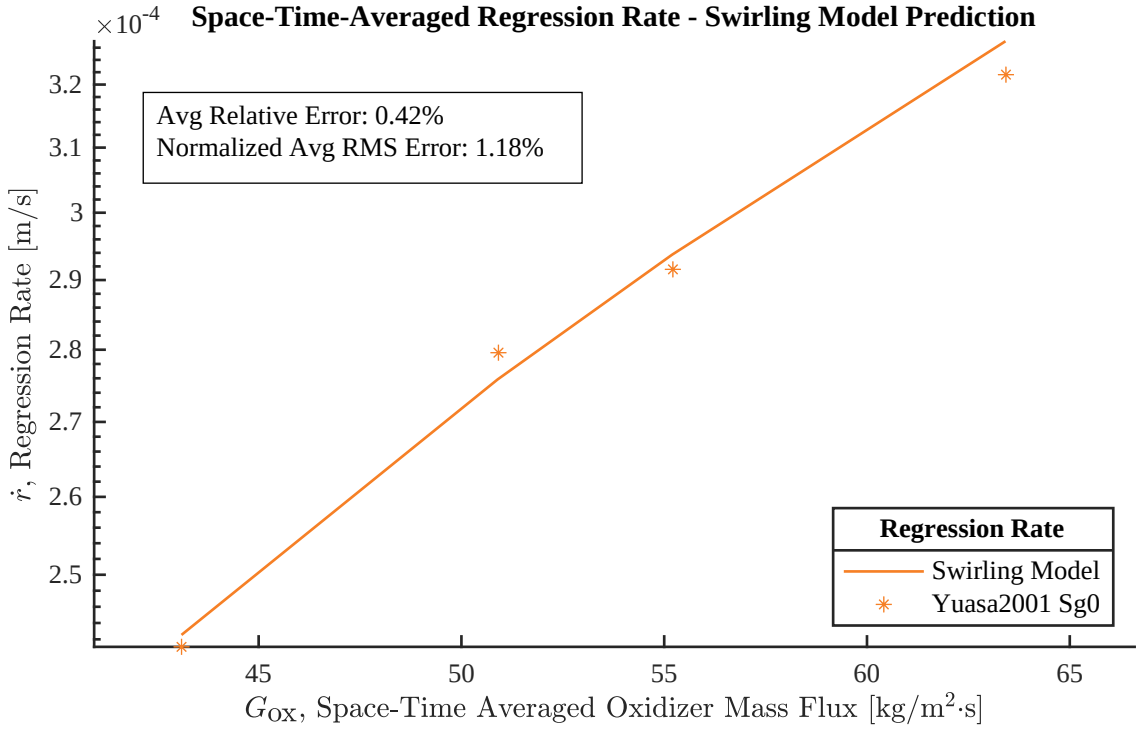

Figure B.6. Regression rate prediction compared to "Yuasa2001 Sg0" test data.

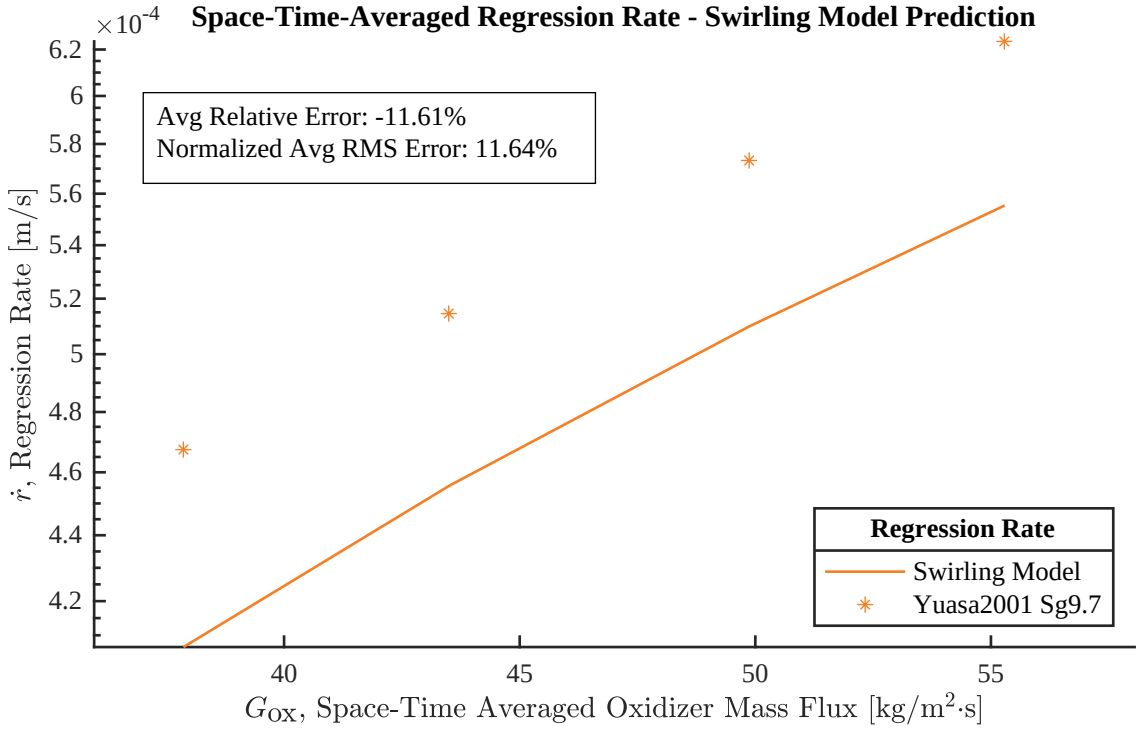

Figure B.7. Regression rate prediction compared to "Yuasa2001 Sg9.7" test data.

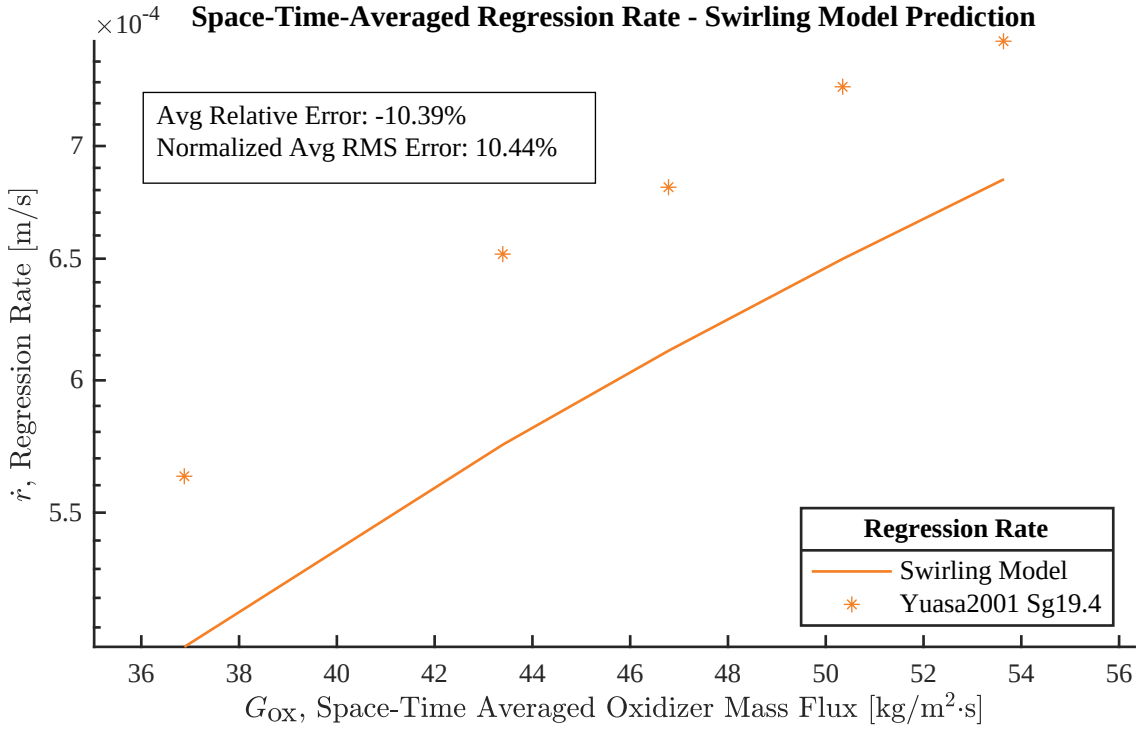

Figure B.8. Regression rate prediction compared to "Yuasa2001 Sg19.4" test data.

Appendix C

Regression Rate Plots for Locally Resolved Data

This appendix contains plots comparing each of the available axially-resolved regression rate datasets to the prediction produced by

$$\dot{r} = aG^n x^m \left[1 + (3.75S)^2\right]^{0.18} \qquad \text{(4.19 Revisited)}$$

The remaining calibration constants a, n, and m vary from one set of data to another and are listed in Table 4.3. All plots have a logarithmic ordinate and linear abscissa. A complete summary of the error data for these plots appears in Table 4.7. The quality of the predictions is discussed in Sec. 4.3.4, where several of the plots from this appendix are also reproduced.

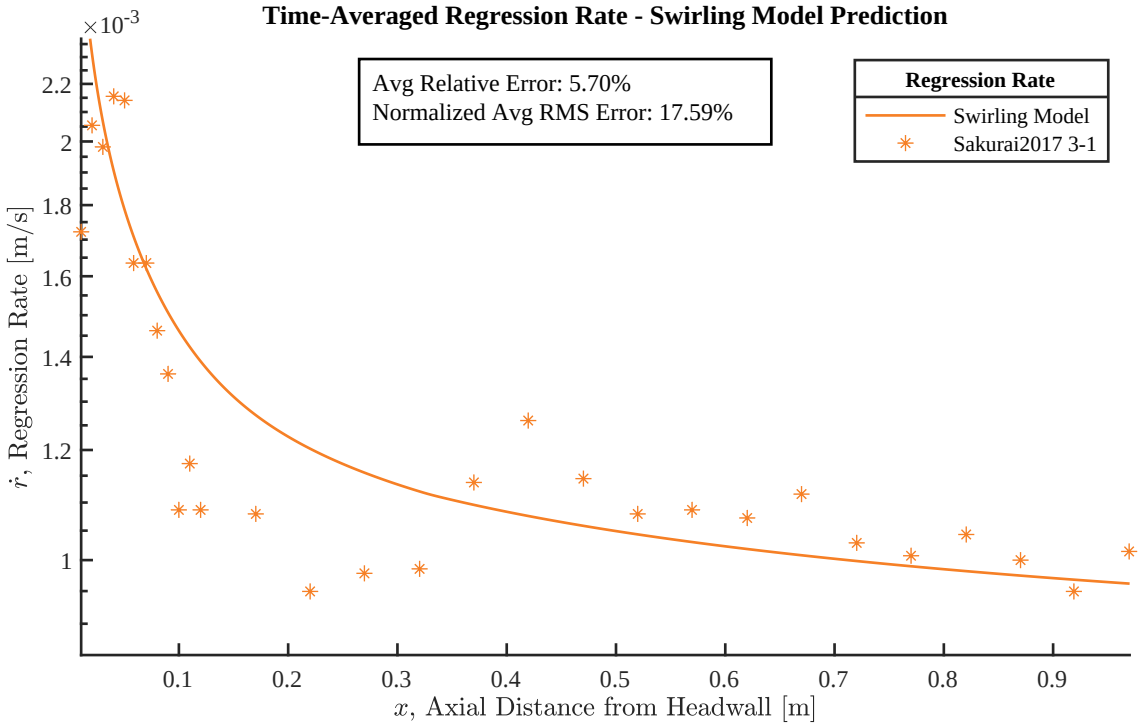

Figure C.1. Regression rate prediction compared to "Sakurai2017 3-1" test data.

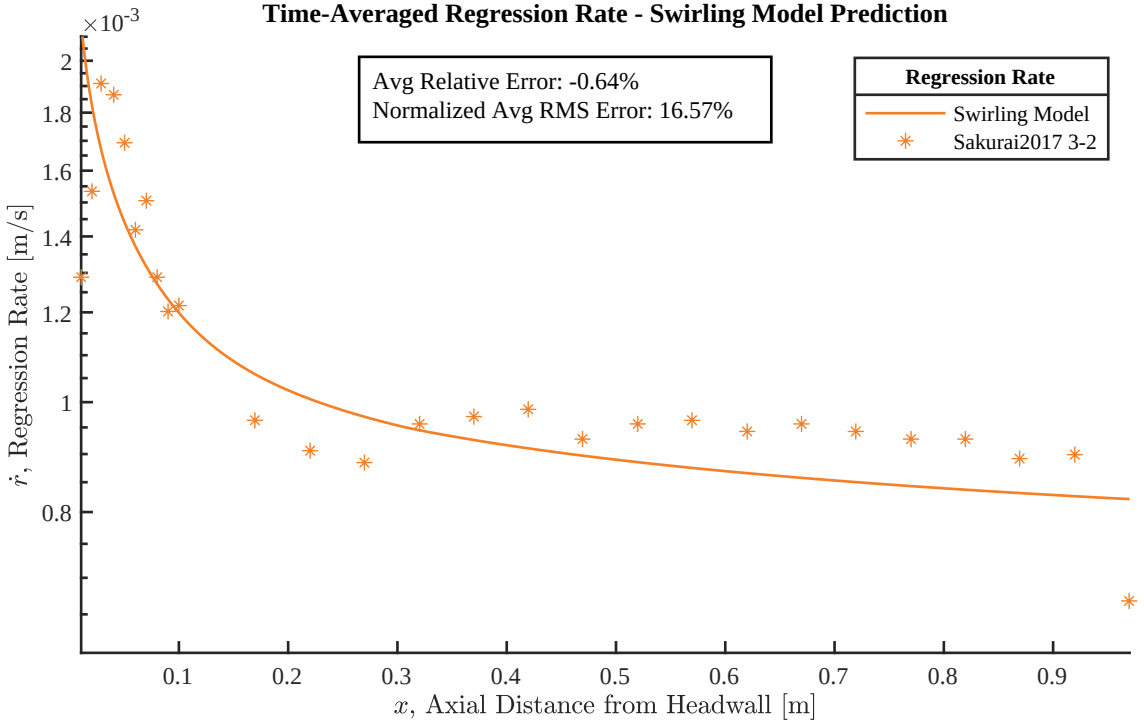

Figure C.2. Regression rate prediction compared to "Sakurai2017 3-2" test data.

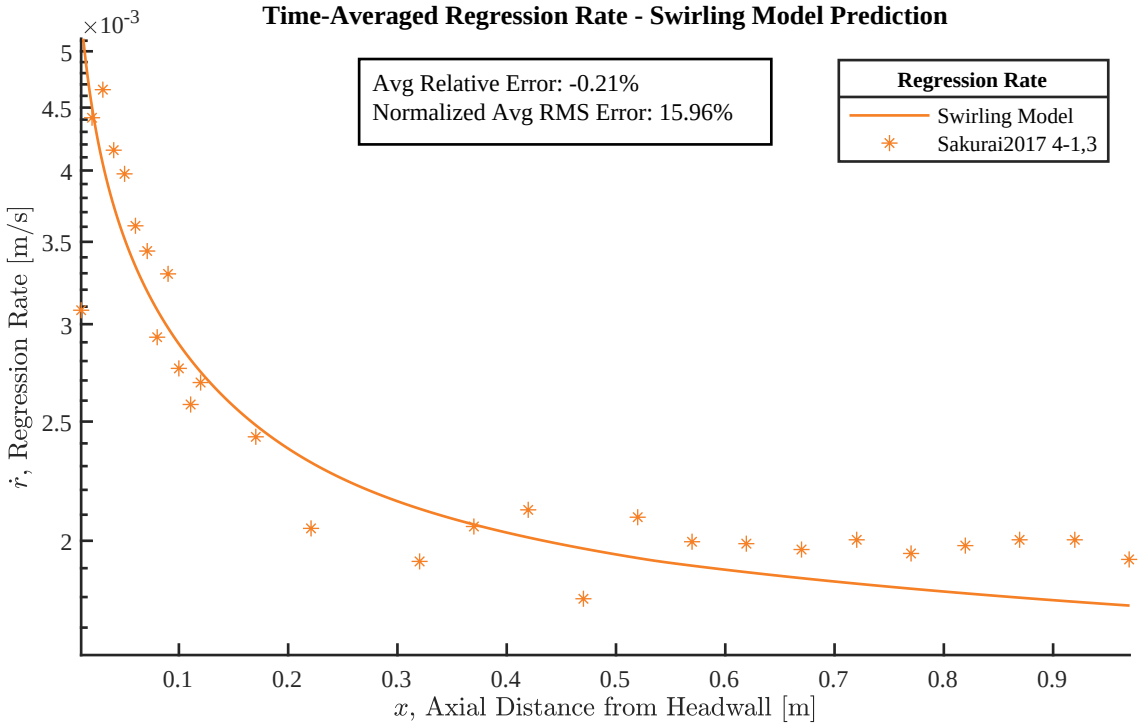

Figure C.3. Regression rate prediction compared to "Sakurai2017 4-1,3" test data.

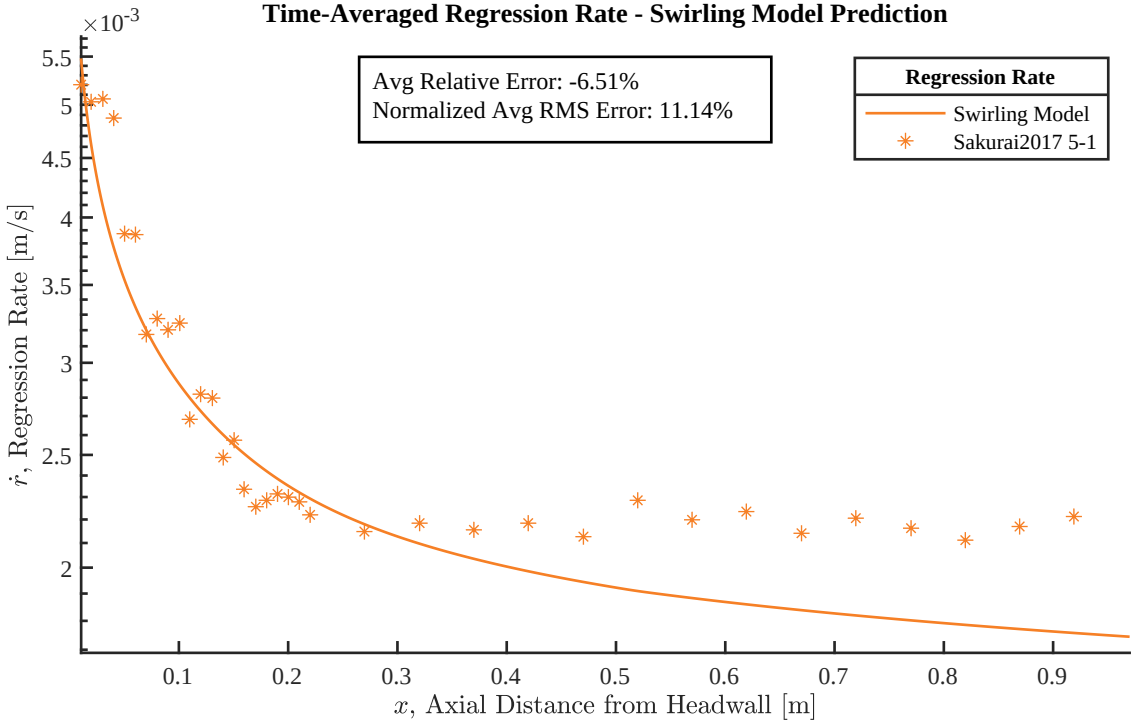

Figure C.4. Regression rate prediction compared to "Sakurai2017 5-1" test data.

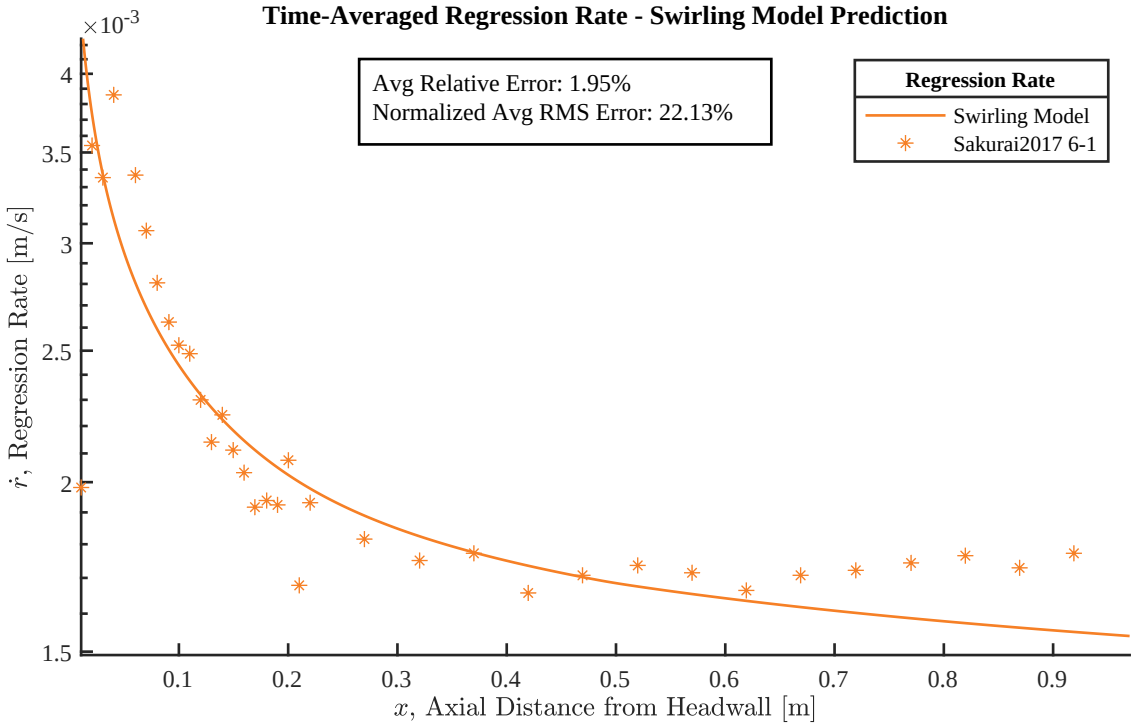

Figure C.5. Regression rate prediction compared to "Sakurai2017 6-1" test data.

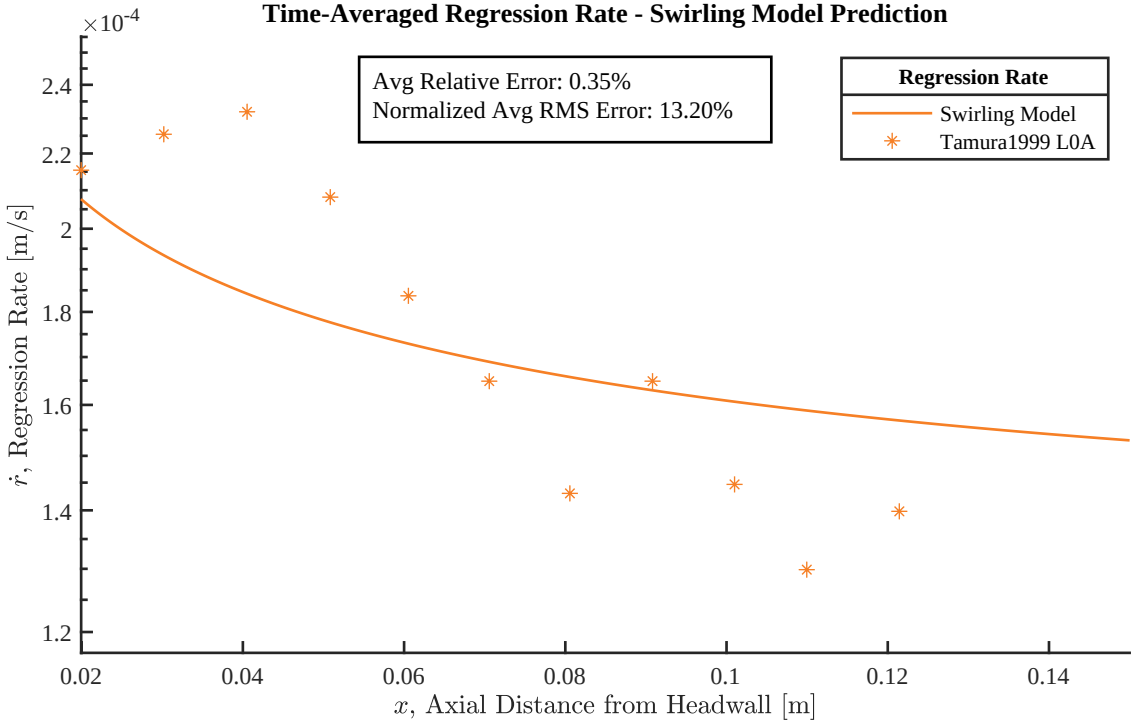

Figure C.6. Regression rate prediction compared to "Tamura1999 L0A" test data.

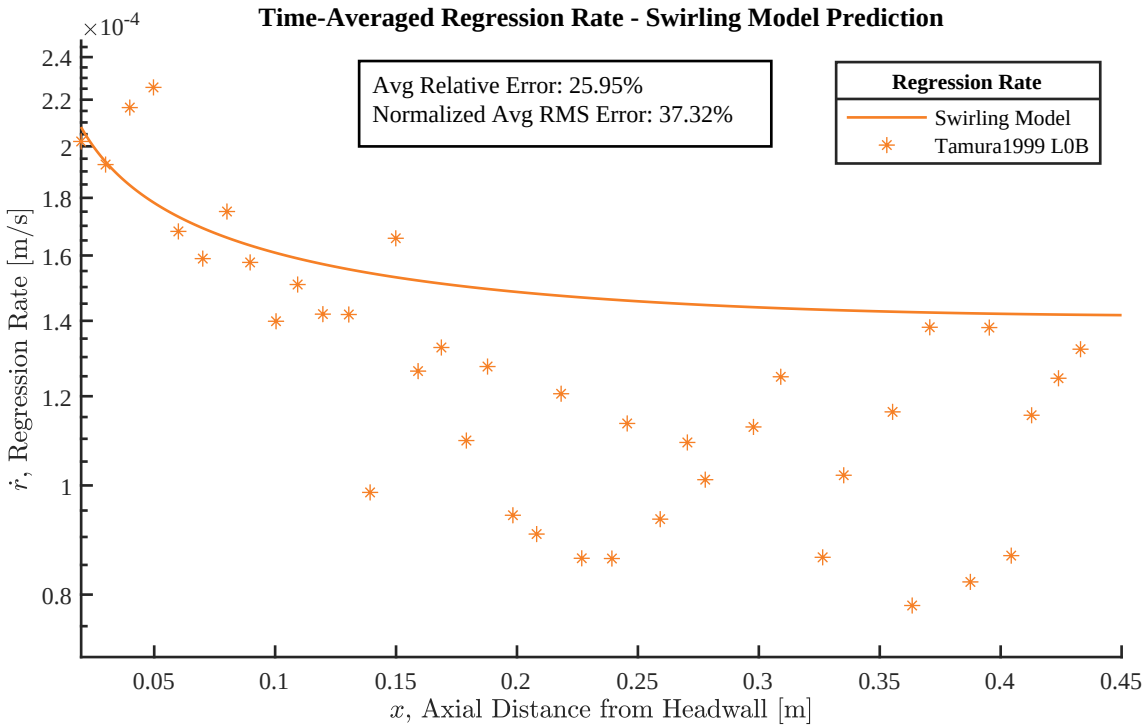

Figure C.7. Regression rate prediction compared to "Tamura1999 L0B" test data.

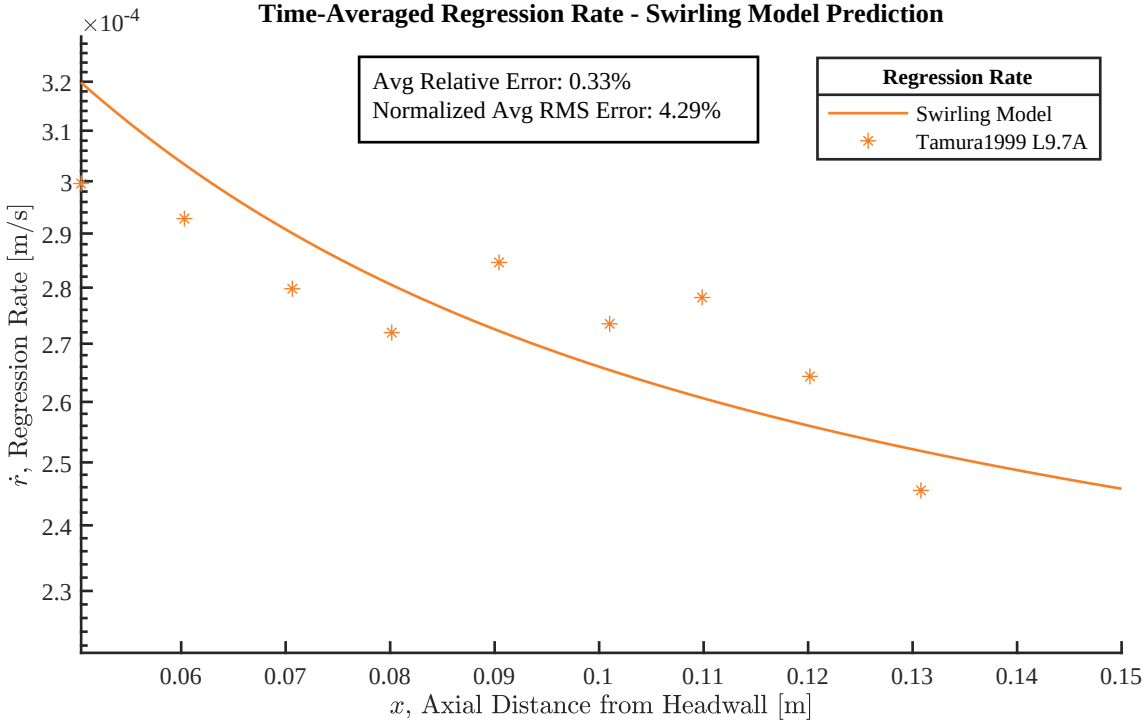

Figure C.8. Regression rate prediction compared to "Tamura1999 L9.7A" test data.

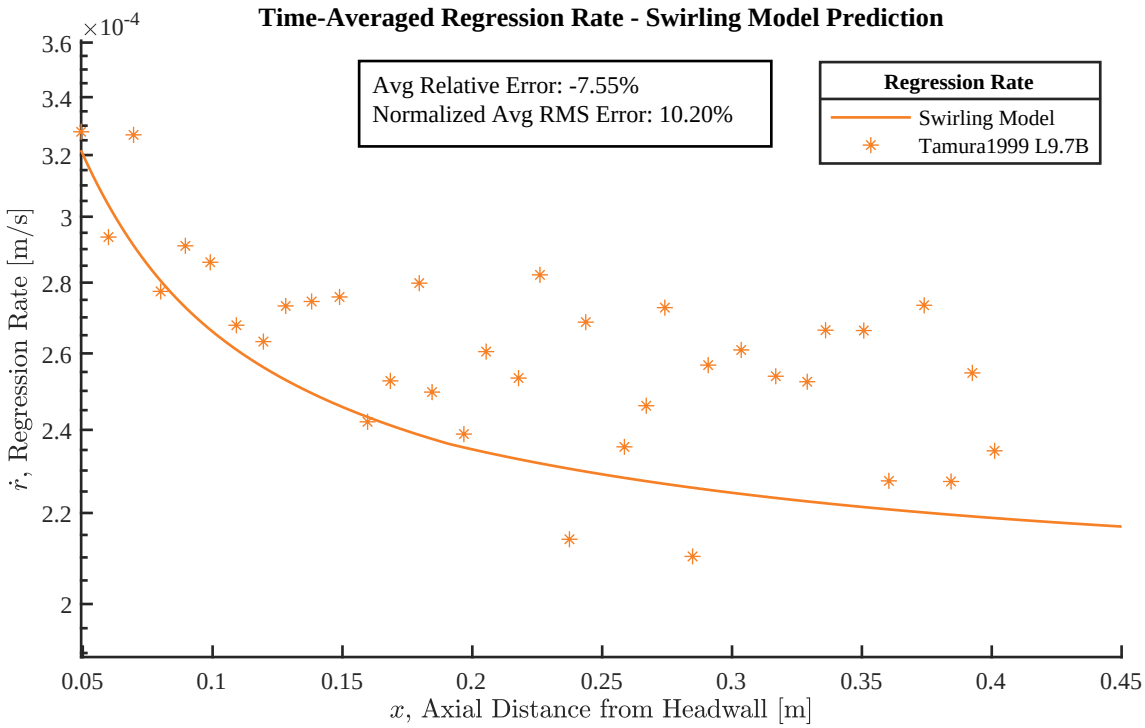

Figure C.9. Regression rate prediction compared to "Tamura1999 L9.7B" test data.

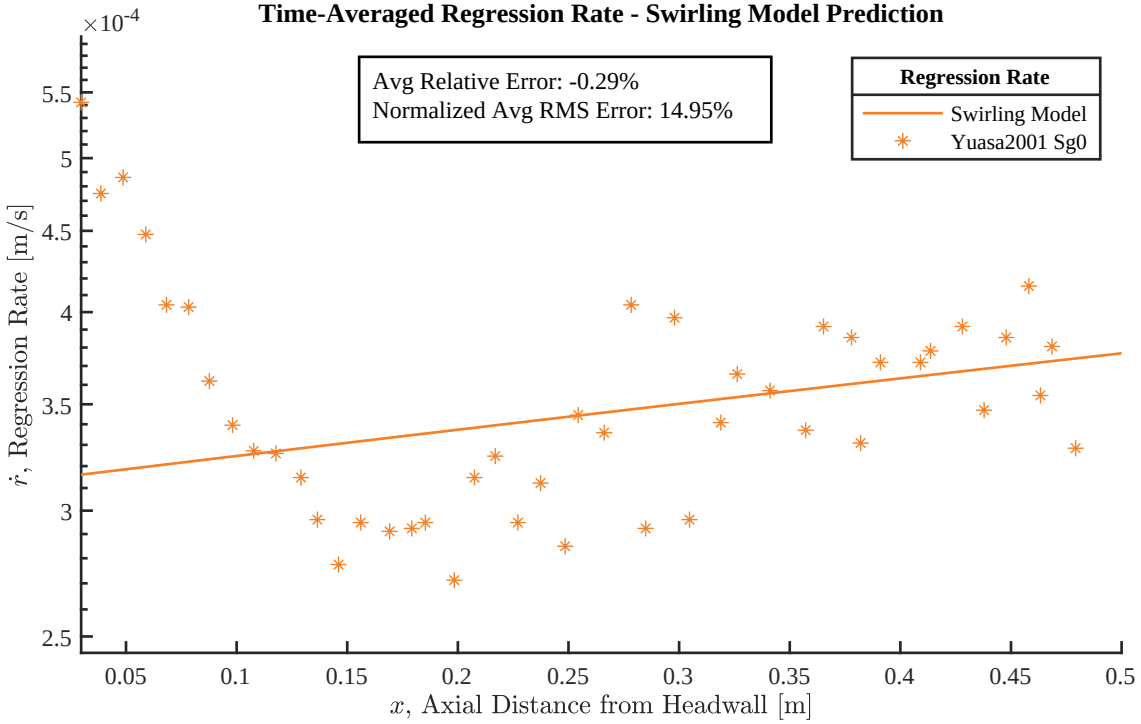

Figure C.10. Regression rate prediction compared to "Yuasa2001 L0" test data.

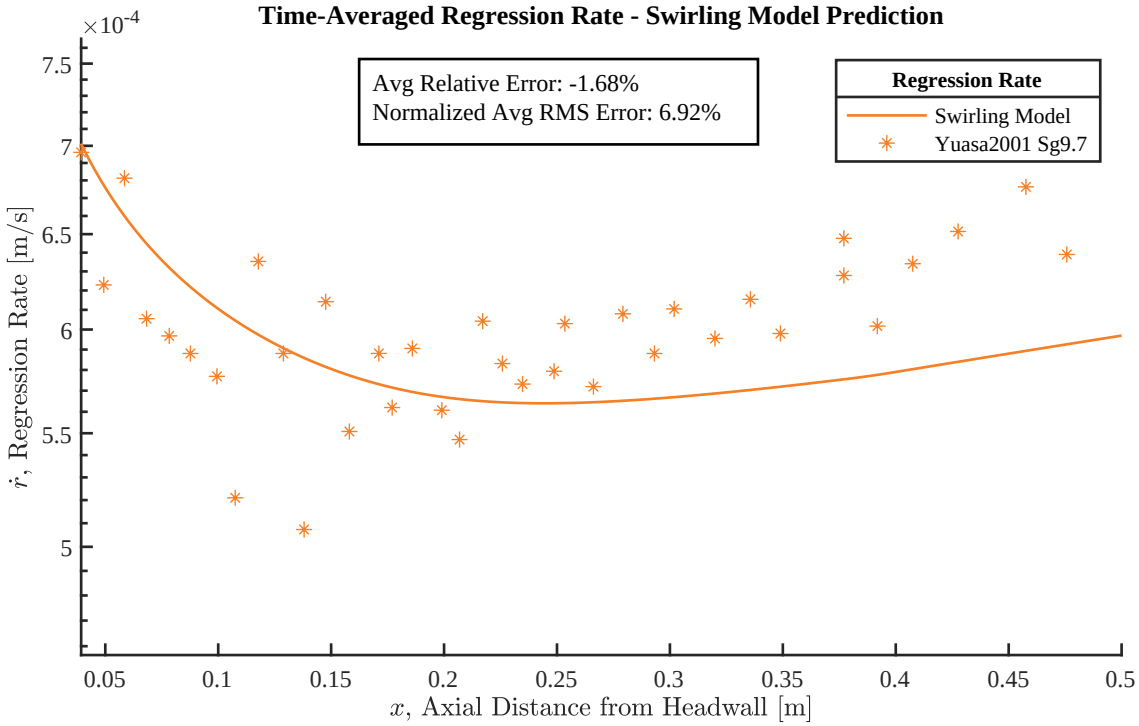

Figure C.11. Regression rate prediction compared to "Yuasa2001 L9.7" test data.

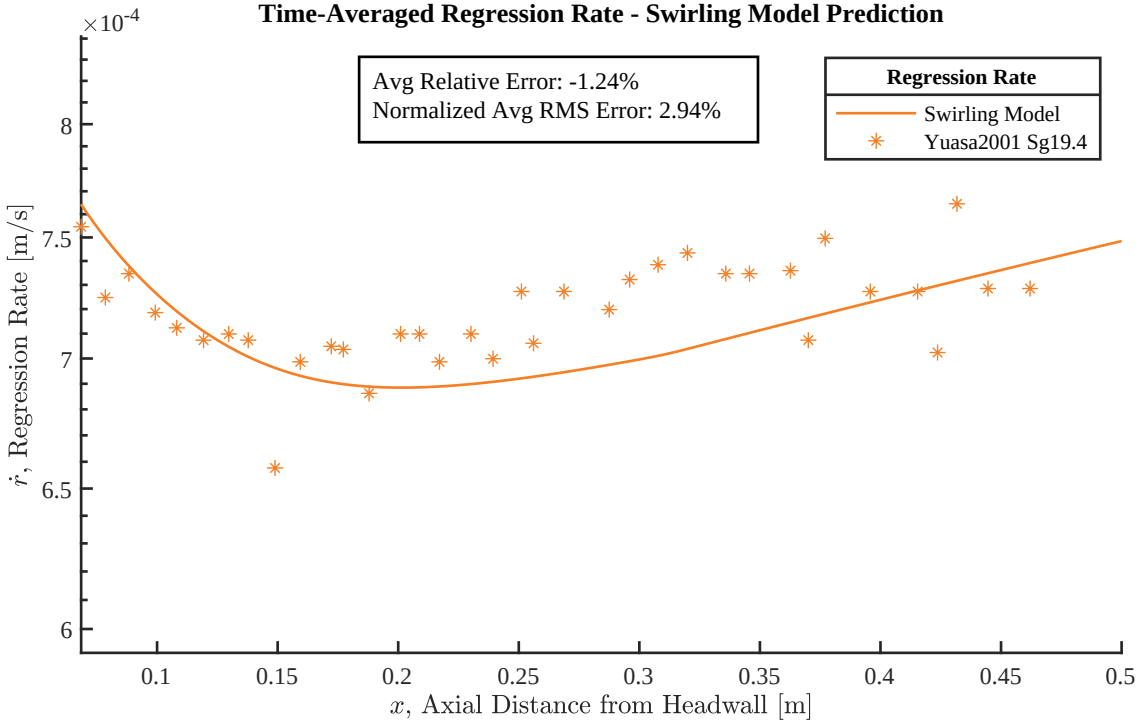

Figure C.12. Regression rate prediction compared to "Yuasa2001 L19.4" test data.

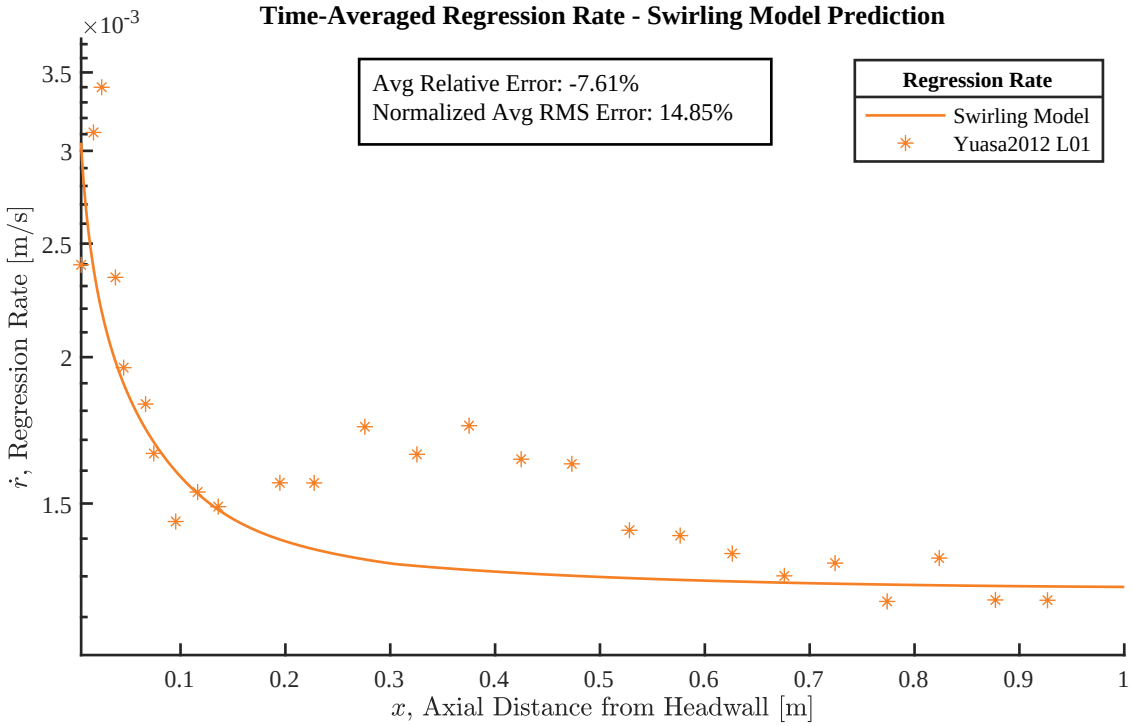

Figure C.13. Regression rate prediction compared to "Yuasa2012 L01" test data.

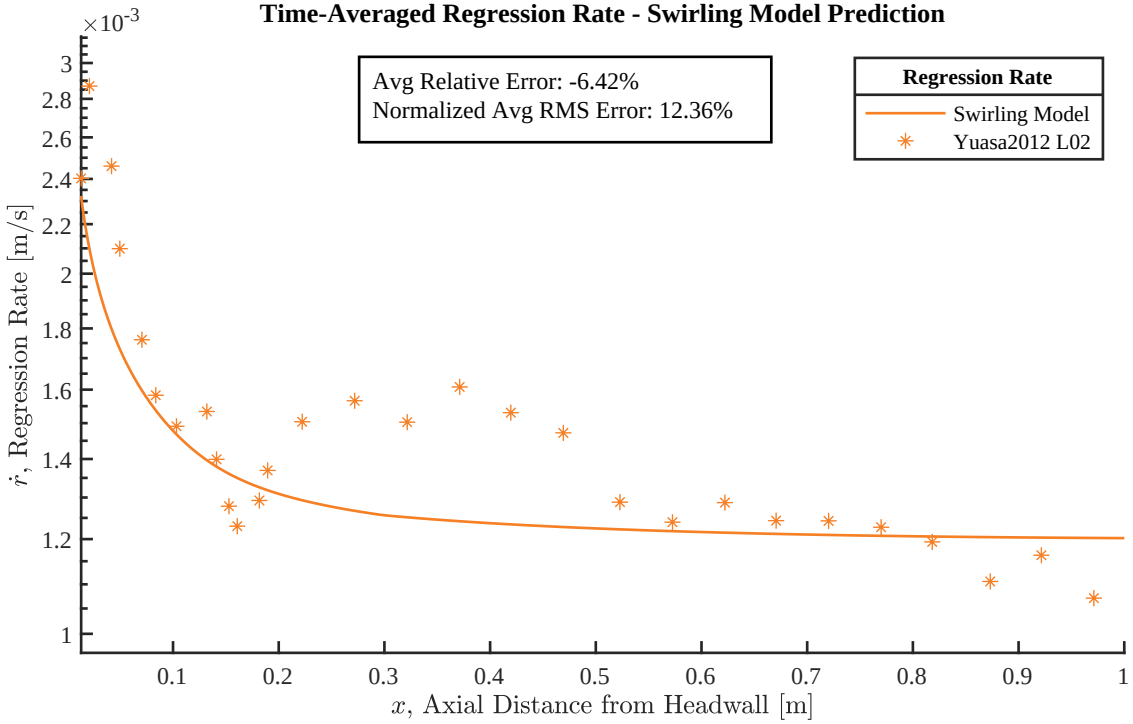

Figure C.14. Regression rate prediction compared to "Yuasa2012 L02" test data.

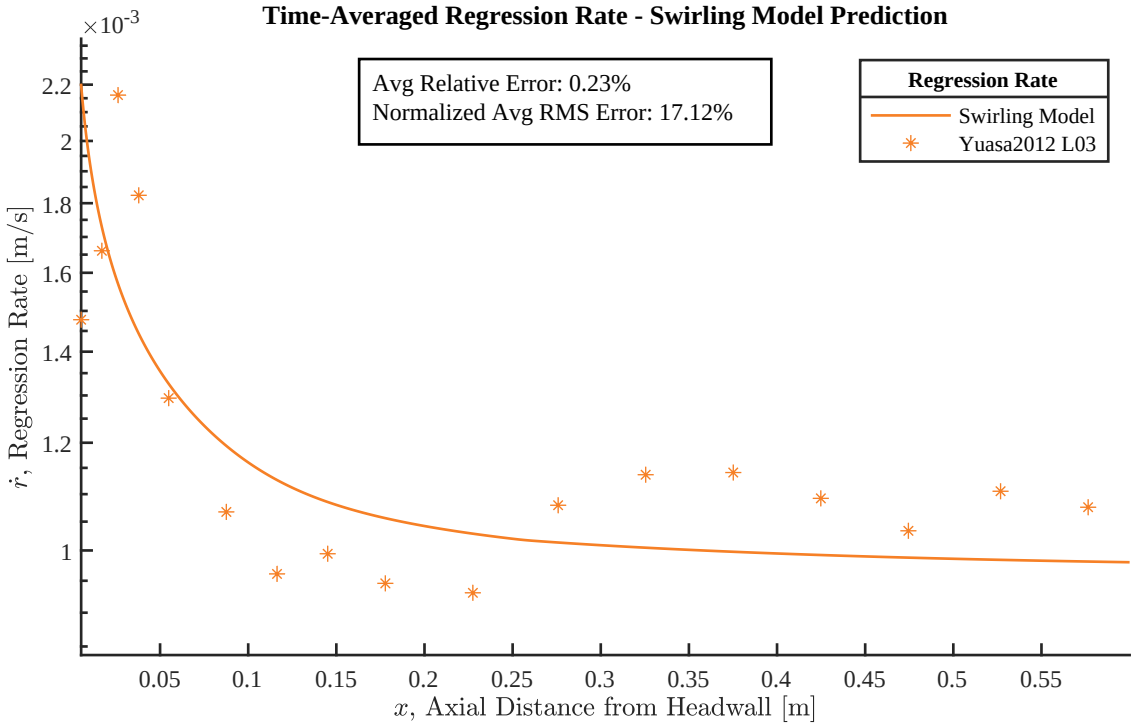

Figure C.15. Regression rate prediction compared to "Yuasa2012 L03" test data.

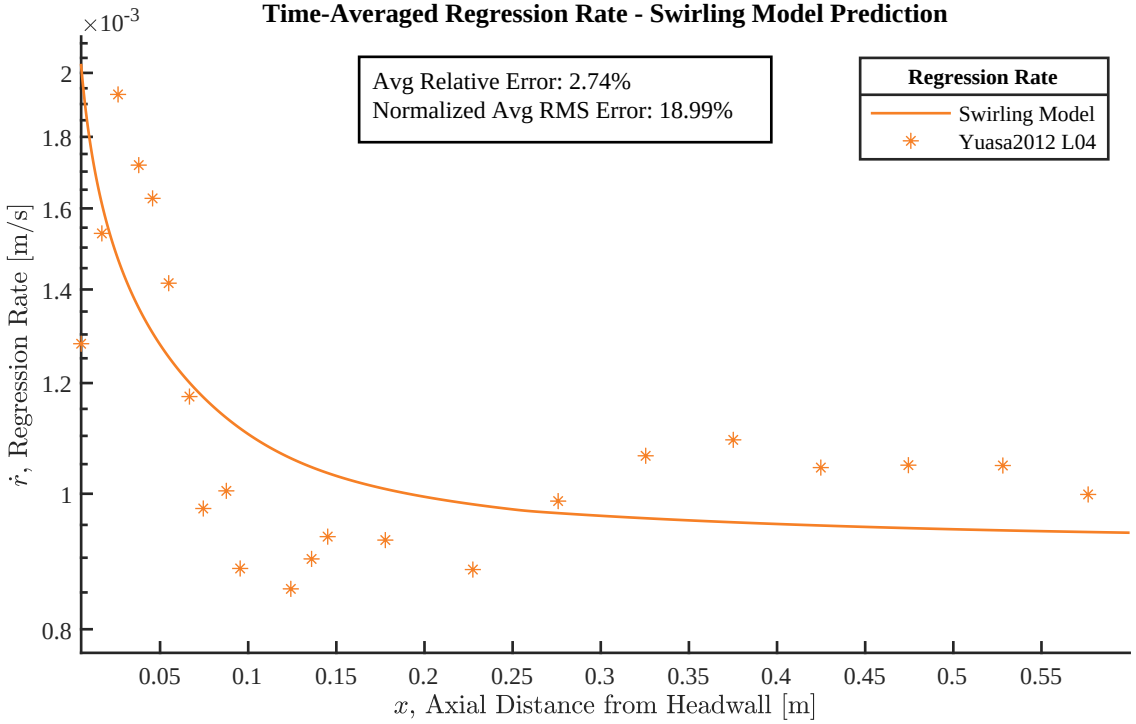

Figure C.16. Regression rate prediction compared to "Yuasa2012 L04" test data.

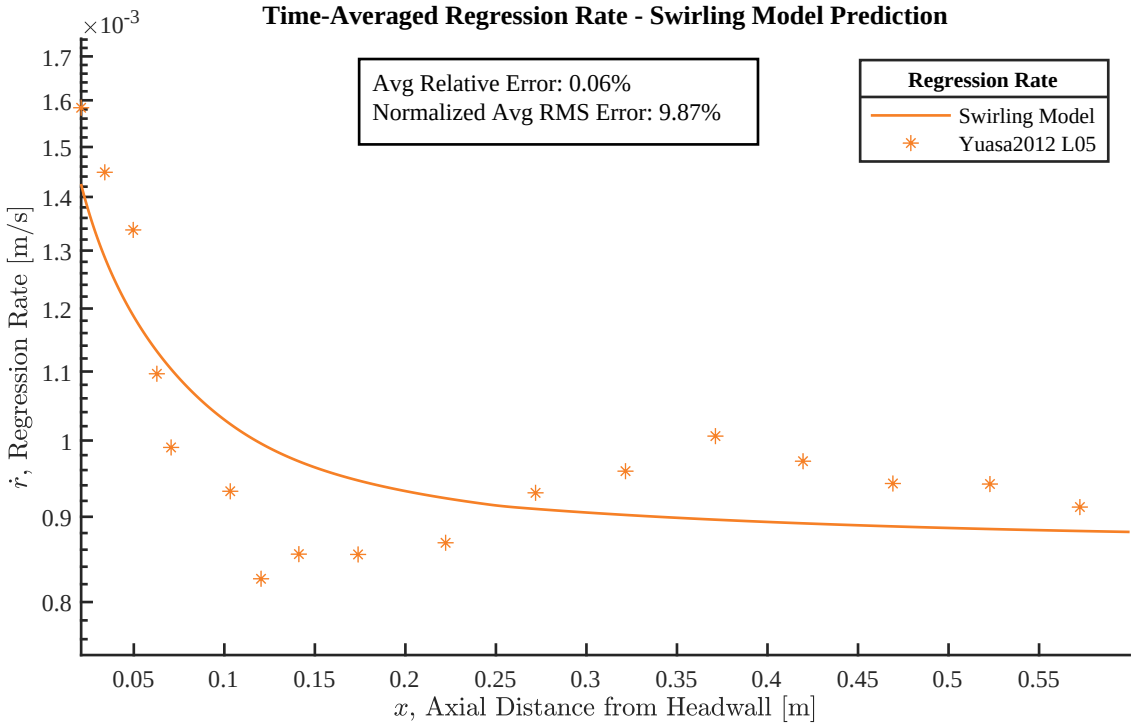

Figure C.17. Regression rate prediction compared to "Yuasa2012 L05" test data.

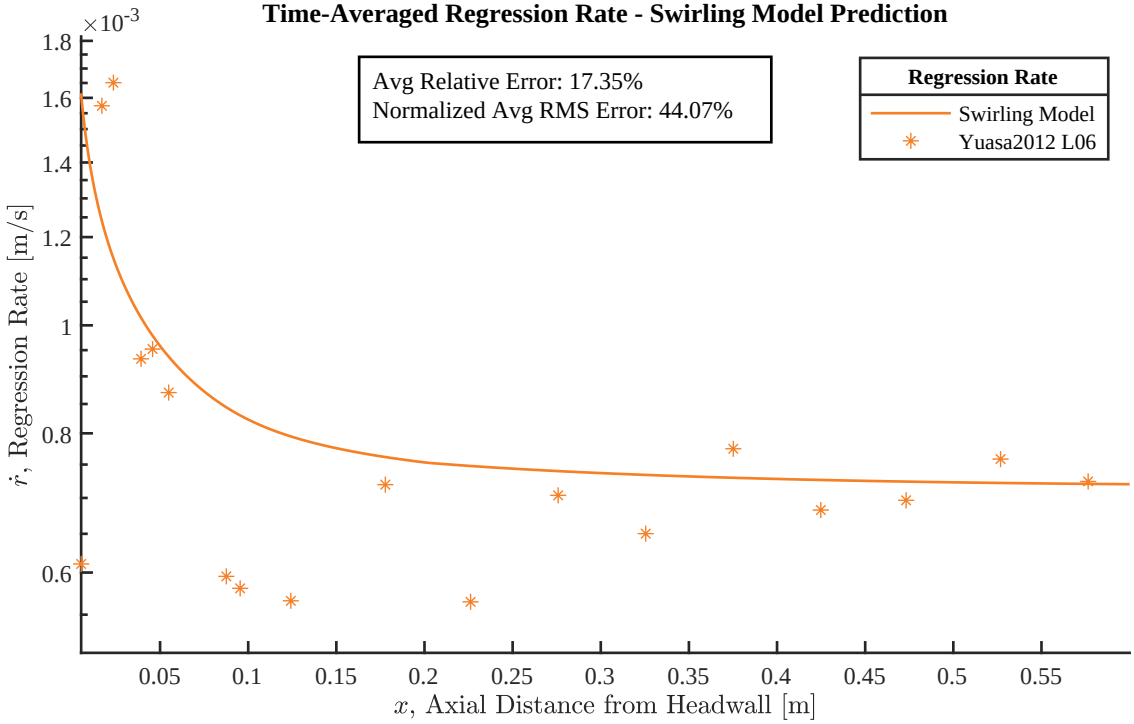

Figure C.18. Regression rate prediction compared to "Yuasa2012 L06" test data.

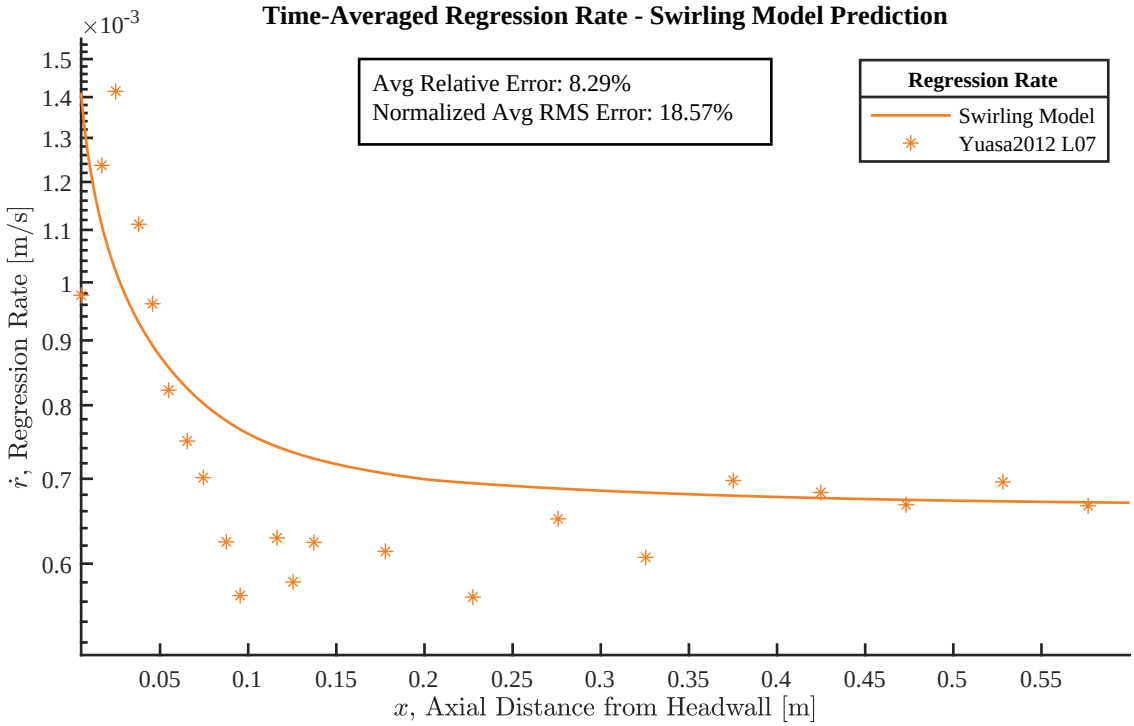

Figure C.19. Regression rate prediction compared to "Yuasa2012 L07" test data.

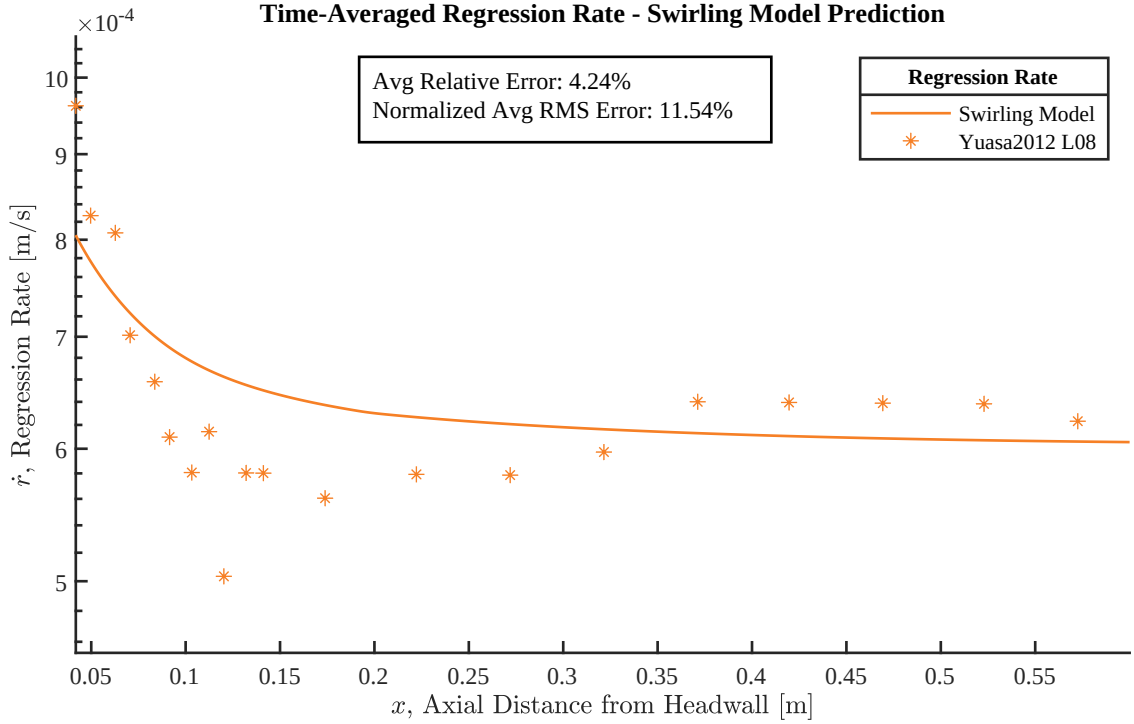

Figure C.20. Regression rate prediction compared to "Yuasa2012 L08" test data.